The internal structure, mechanics, and fluid flow properties of low-angle normal faults a case study from the island of Elba, Italy

Steven A. F. Smith

The Internal Structure, Mechanics, and Fluid Flow Properties of Low-Angle Normal Faults: A Case Study from the Island of Elba, Italy

A thesis submitted to the University of Durham
for the degree of Doctor of Philosophy
in the Faculty of Science

Steven A.F. Smith

2009

Abstract

Low-angle normal faults have been extensively documented in areas of regional extension, in both continental and oceanic lithosphere, but their existence as seismically active structures remains controversial. Low-angle normal faults do not conform to 'traditional' frictional fault theory, and large earthquakes on low-angle normal faults appear to be rare. Their enigmatic nature suggests that they may hold important clues regarding the rheology of fault zones in general, controls on frictional behaviour, and the deformation histories of the mid- to upper-crust. In this study, I investigate the internal structure, mechanical properties, and fluid flow conditions along a large-displacement low-angle normal fault exposed on the Island of Elba, Italy. Using field relationships, microstructural analysis, stable isotope geochemistry, and rock deformation experiments, I document the most important characteristics of the fault zone, and test hypotheses concerning the mechanical behaviour and evolution of low-angle normal faults.

The Zuccale low-angle normal fault crosscuts and displaces a lithologically heterogeneous sequence of wall rocks. Field relationships suggest that it was active in the upper crust during the emplacement of large plutonic complexes. On a regional-scale, the Zuccale fault appears to have a long-wavelength domal morphology, which may have resulted from the intrusion of an upper-crustal igneous pluton in to the shallow footwall of the fault. Pluton intrusion strongly influenced the fluid flow regimes and fault rock evolution along the Zuccale fault.

Geometric and kinematic relationships between the Zuccale fault and a network of minor footwall faults suggest that the Zuccale fault slipped at a low-angle throughout most of its history. The footwall faults were active broadly contemporaneously with movement along the Zuccale fault, and controlled the distribution and connectivity of different fault rock components. This imparted a distinct mechanical structure to the fault core, potentially influencing fault zone rheology.

The central core of the Zuccale fault contains a sequence of fault rocks that deformed by a variety of deformation mechanisms, and formed during progressive exhumation of the fault zone. Triaxial deformation experiments indicate that the frictional strength of many of the fault rocks is too high to explain slip along the Zuccale fault. However, several

potential mechanisms of fault zone weakening have been identified, including fluid-assisted dissolution-precipitation creep, grain-size sensitive creep in calcite mylonites, frictional sliding within phyllosilicate-rich areas of the fault core, high fluid pressures, and particulate flow accommodated by fine-grained clay minerals.

Fluids associated with the Zuccale fault were derived from two main sources. During the relatively early stages of movement, and particularly during the intrusion of plutonic complexes, fluids were of meteoric-hydrothermal origin. During the late stages of exhumation, fluids were derived from a seawater source that infiltrated downwards through faulted and fractured wall rocks. Sub-horizontal tensile veins carrying both fluid signatures are found adjacent to and within the fault core, suggesting that supra-lithostatic fluid pressures were able to develop throughout the exhumation history. One of the consequences of high fluid pressures was the development of a suite of fluidized fault breccias, a newly recognized type of fault rock that may be indicative of the interseismic stage of the earthquake cycle.

Table of Contents

Chapter 1:

Chapter 2:

Using Footwall Structures to Constrain the Evolution of Low-Angle Normal Faults

Chapter 3:

Recognizing the Seismic Cycle Along Ancient Faults: CO_2-Induced Fluidization of Breccias in the Footwall of a Sealing Low-Angle Normal Fault

Chapter 4:

Interactions Between Low-Angle Normal Faulting and Plutonism in the Upper Crust: Insights from the Zuccale Fault, Elba Island, Italy

Chapter 5:

Laboratory measurements of the Frictional Strength of a Natural Low-Angle Normal Fault: The Zuccale Fault, Elba Island, Italy

Chapter 6:

Fault Rock Development and Weakening Mechanisms During Exhumation of a Continental Low-Angle Normal Fault: The Zuccale Fault, Elba Island, Italy

Chapter 7:

Future Work

List of Figures

Chapter 2:

Chapter 3:

Chapter 4:

Chapter 5:

Chapter 6:

List of Tables

Chapter 3:

Chapter 4:

Chapter 5:

Chapter 6:

Acknowledgements

Firstly I'd like to express my thanks to Bob Holdsworth and Cris Collettini, whose guidance and encouragement over the last few years have had a particularly large role to play in this thesis. Bob has been a supervisor since my undergraduate days in Durham, and despite having rather a large number of other tasks to perform as head of department (and take care of 4 children), he has always had time to discuss new ideas, promptly edit manuscripts and presentations, and spend time in the field. Collaboration with Cris has been fruitful at every stage, and I am indebted to him for introducing me to the geology of Elba, and for many discussions that have resulted in big improvements to this work. I hope that both Bob and Cris remain close colleagues in the future.

Richard Jones has entertained and embarrassed at various stages over the last few years, and generally kept me on my toes! He has been a great colleague, cycling and running partner, and close friend. It's clear that old age is now creeping up on him, but in between nappy duties I hope he can find time to stay in touch.

More recently, Dan Faulkner at Liverpool University has introduced me to the world of experimental rock deformation, and Colin Macpherson has been working closely on stable isotope analysis. I am grateful to both of them for providing me the opportunity to broaden my experience.

I am also indebted to the following people in Durham and elsewhere who have guided and discussed various parts of this research, or provided invaluable help with all sorts of technical and administrative issues: Jonny Imber, Ken McCaffrey, Nic de Paola, Ruth Wightman, Woody Wilson, Dave Healy, Phil Clegg, Mark Allen, Dougal Jerram, Mark Pearce (Liverpool), Janice Oakes, Karen Atkinson, Carole Blair, Dave Sales, Gary Wilkinson, and Dave Stevenson.

Many other postgrad and postdoc students have shared the trials and tribulations of starting and finishing a PhD. Thanks to all of the following for keeping me sane, and making each day in the office a fun one: Fabio 'Apache' Domingos, Jiulin 'My Boy' Guo, Nicola '5 screens' Marsh, Adam 'the Professor' Pugh, Tom Challands, Mike Mawby, Chris Dale (who gets a special mention for sharing some 'testing' times out on the fell), Pippa Whitehouse, Sharon Jefferies, Rich Walker, and Dave Moy.

Thanks to many other friends and family who have helped out enormously over the past few years. In particular my parents, sister, and nana have remained supportive throughout, and I will always be indebted to them for their constant encouragement.

Fieldwork at various stages was funded by The Geological Society of London, The American Association of Petroleum Geologists, The Mineralogical Society of Great Britain and Ireland, The Geologists Association, The Edinburgh Geological Society, Hatfield College, and The John Ray Trust. This thesis was supported by a Doctoral Fellowship from the University of Durham.

DECLARATION

No part of this thesis has previously been submitted for a degree at this or any other university. The work described in this thesis is entirely that of the author, except where reference is made to previously published or unpublished work.

Steven A.F. Smith

University of Durham

Department of Earth Sciences

February 2009

Chapter 1

1.1. Introduction

Since their recognition in the Basin and Range province, western USA, low-angle[1] normal faults (also termed 'detachment faults') have been at the centre of a heated debate [*Coney*, 1980, *Wernicke*, 1981, *Axen*, 2004, *Anders et al.*, 2006, *Axen*, 2007, *Walker et al.*, 2007]. Some examples of low-angle normal faults have clearly been rotated from higher-dip angles [*Proffett*, 1977, *Buck*, 1988, *Garces and Gee*, 2007], but others appear to have accommodated large-magnitude displacement during crustal extension at dips of <30° [*Axen*, 1988, *Wernicke*, 1995, *Axen*, 2004]. The latter examples pose a problem for traditional frictional fault theory, and give rise to the well known 'mechanical paradox' of low-angle normal faults [e.g. *Burchfiel et al.*, 1982, *Westaway*, 1999, *Axen*, 2004, *Axen*, 2007].

Anderson's theory of faulting assumes that one of the principal stresses is vertical near the surface of the Earth, and that faulting is controlled by a Mohr-Coulomb type failure criterion, where slip occurs when the applied stresses reach the failure criterion [*Anderson*, 1942]. In a fluid-saturated, isotropic rock the effective principal stresses are $\sigma'_1 = (\sigma_1 - P_f) > \sigma'_2 = (\sigma_2 - P_f) > \sigma'_3 = (\sigma_3 - P_f)$, where P_f is the pore fluid pressure [*Hubbert and Rubey*, 1959]. Brittle faulting of intact rock can be described by the Coulomb criterion for shear failure:

[1] Low-angle is typically defined (as in this thesis) as <30°

$$\tau = C + \mu_i \sigma'_n = C + \mu_i(\sigma_n - P_f),$$

where τ is the shear stress, σ_n is the normal stress, C is the cohesive strength, and μ_i is the coefficient of internal friction. Typical values for the coefficient of internal friction range from 0.5-1.0, indicating that conjugate sets of brittle faults should form at angles of 22°-32° to the maximum principal stress [*Jaeger and Cook*, 1979, *Collettini and Sibson*, 2001]. In an extending crust, where the maximum principal stress is vertical [*Anderson*, 1942], normal faults are thus predicted to form at dip angles of 58°-68°.

Once faults have initiated, slip occurs on pre-existing cohesionless planes with coefficients of sliding friction, μ_s, governed by Amonton's law (Figure 1.1):

$$\tau = \mu_s \sigma'_n = \mu_s(\sigma_n - P_f).$$

This equation is particularly important in the study of fault mechanics and seismogenesis, because most earthquakes occur on pre-existing faults [*Scholz*, 2002]. Assuming laboratory-derived friction coefficients of 0.6-0.85 [*Byerlee*, 1978], *Sibson* [1985] showed that optimal reactivation of pre-existing faults containing the σ_2 axis occurs when the angle between the fault plane and the maximum principal stress is 25°-30° i.e. close to the initial 'Andersonian' dips. Frictional lock-up is expected to occur when the angle is greater than ~60°. Thus, in a crust characterized by a vertical maximum principal stress, slip along pre-existing normal faults is expected to cease if the faults are rotated to dip angles of less than 30°.

To illustrate the mechanical difficulty in reactivating low-angle normal faults, consider the Mohr diagrams shown in Figures 1.1a and 1.1b [modified from *Collettini and Barchi*, 2002, which contains details of Mohr circle construction]. Both figures show: i) a failure envelope for reactivation of a pre-existing cohesionless fault, assuming a coefficient of sliding friction (μ_s) of 0.6, at the lower end of the Byerlee range [0.6-0.85; *Byerlee*, 1978], ii) a composite Coulomb-Griffith failure envelope for intact rocks,

assuming a coefficient of internal friction (μ_i) of 0.75, in the middle of the range for typical crustal rocks given by *Jaeger and Cook* [1979] and, iii) differential stress states on faults containing the σ_2 axis. Fault loading is assumed to take place by increases in pore fluid pressure, which reduces the magnitudes of σ_1 and σ_3 by equal amounts. In Figure 1.1a, increases in fluid pressure leads to the development of a new fault dipping at ~60° (2θ = 120°) as the Mohr circle intersects the Coulomb criterion (point A on blue circle). This occurs before reactivation of a low-angle normal fault dipping at 20° (2θ = 40°). In Figure 1.1b, increases in fluid pressure leads to the formation of extensional fractures or hybrid-extensional fractures as the Mohr circle intersects the Griffith parabola (point B on blue circle). This leads to draining of fluid, and increases in the principal effective normal stresses. Again, this occurs before reactivation of a low-angle normal fault dipping at 20° (2θ = 40°).

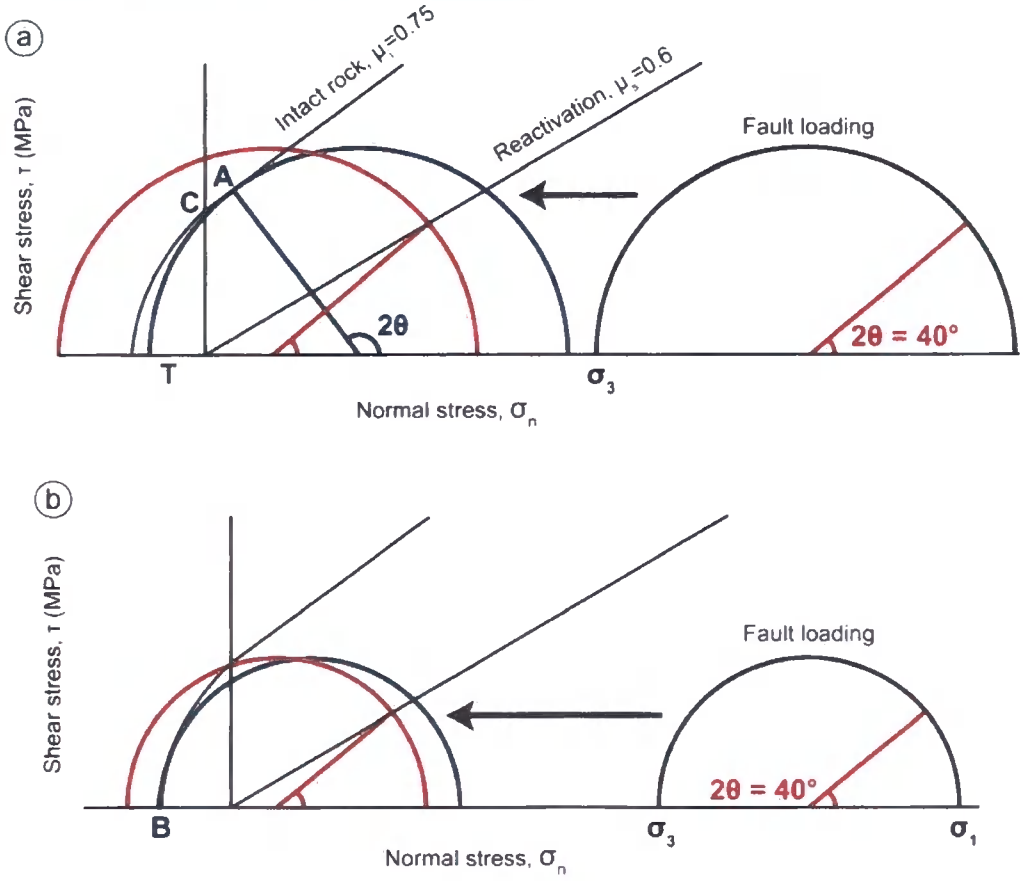

Figure 1.1) Schematic Mohr diagrams illustrating the difficulties in reactivating a low-angle normal fault dipping at 20°, $2\theta = 40°$, and containing the σ_2 axis [modified from *Collettini and Barchi*, 2002]. C is cohesion and T is tensile strength. Fault loading takes place by increases in fluid pressure, which decreases σ_1 and σ_3 by equal amounts, **a)** The Mohr circle intersects the Coulomb criterion (at point A) before reactivation of the low-angle normal fault, leading to formation of a new, steeply dipping fault, **b)** The Mohr circle intersects the Griffith parabola (at point B) before reactivation of the low-angle normal fault, leading to formation of extensional or hybrid-extensional shear fractures, and draining of high-fluid pressures.

To overcome these mechanical difficulties, and promote slip on severely misoriented faults such as low-angle normal faults, two principal mechanisms have been suggested. The first possibility is a decrease in the coefficient of sliding friction within the fault zone, resulting from the presence of frictionally weak minerals (e.g. some clays). In a Mohr-Coulomb framework, this decreases the gradient of the failure envelope for reactivation, meaning that in certain situations slip can occur on low-angle normal faults before the formation of new faults or extensional fracturing. The second possibility was highlighted in a seminal paper by *Rice* [1992], and applied specifically to low-angle normal faults by *Axen* [1992]. *Rice* suggested that slip may occur on severely misoriented faults due to high pore fluid pressures alone, but extensional fracturing and subsequent draining of fluids might be prevented by rotation of the regional stresses within the altered and saturated central fault core. More recent work suggests that such stress rotations might also occur within the damaged wall rocks surrounding fault cores [*Faulkner et al.*, 2006].

The mechanical paradox of low-angle normal faults is seemingly confounded by the apparent lack of unambiguously identified earthquake ruptures on low-angle normal faults in the seismological record [*Jackson and White*, 1989, *Collettini and Sibson*, 2001]. Potential examples of large earthquakes and triggered sub-events do exist, but all of them remain controversial. For example, *Abers* [1991] and *Wernicke* [1995] suggested that 3 large earthquakes with magnitudes between 5.7 and 6 occurred along a low-angle normal fault dipping at 10°-25° in the Papua New Guinea region, but recent seismic imaging

shows that the normal fault in question dips at around 30° [*Floyd et al.*, 2001]. Only recently have high-resolution microseismic campaigns begun to document compelling evidence for seismic activity on active, shallowly-dipping structures in the mid- to upper-crust [e.g. *Rigo et al.*, 1996, *Chiaraluce et al.*, 2007].

Low-angle normal faults have now been documented in a wide range of tectonic settings in both continental and oceanic lithosphere, prompting a re-evaluation of current fault mechanical theory [e.g. *Coney*, 1980, *Wernicke*, 1981, *Lister*, 1984, *Wernicke*, 1995, *Cann et al.*, 1997, *Smith et al.*, 2006, *Axen*, 2007, *Cottle et al.*, 2007]. They are typically associated with many, or all, of the following characteristics: 1) Slip magnitudes between a few kilometres and a few tens of kilometres; 2) Broadly domal fault surfaces across which there may be a significant metamorphic break. In such cases, the low-angle normal faults are part of 'metamorphic core complexes'; 3) Broadly synchronous magmatic activity; 4) A sequence of ductile, semi-brittle, and brittle fault rocks that may record progressive exhumation of the fault zone and its footwall. Although such characteristics appear to be common to many low-angle normal faults, their origin and evolution remains highly controversial, and low-angle normal faults remain a poorly understood class of tectonic fault.

Low-angle normal faults could contribute in a fundamental way to our understanding of weak fault zones in general, and they are also important for understanding seismicity [e.g. *Axen*, 1999, 2007]. The lack of large earthquakes along low-angle normal faults suggests that either: the recurrence interval of low-angle normal faults is long, in which case rare examples of low-angle normal fault earthquakes may be large and destructive [*Wernicke*, 1995]; or low-angle normal faults slip by a combination of aseismic creep and small ruptures, possibly driven by transient increases in fluid pressure [*Collettini*, 2002, *Collettini and Holdsworth*, 2004, *Chiaraluce et al.*, 2007]. If this is the

case, they may represent a special class of tectonic fault, and probably hold important clues about frictional stability versus instability in general [*Axen*, 2007]. Low-angle normal faults and their footwalls expose complex fault rock sequences, and hence they can provide a window in to the nature and evolution of deformation mechanisms, environmental conditions, and fluid-flow regimes over a wide range of crustal levels.

Motivated by the need to advance our understanding of this enigmatic class of tectonic fault, the purpose of this study is to examine a regionally-significant low-angle normal fault exposed on the Island of Elba, Italy. A series of detailed case studies will be used to document the most important characteristics of the fault zone and to test hypotheses concerning the mechanical behaviour and evolution of low-angle normal faults. The Zuccale fault on Elba was chosen for this study because the geological framework is relatively well established. Importantly, it has also been proposed as an exhumed analogue for currently active low-angle normal faults beneath central Italy, and the fault zone itself is spectacularly exposed in a number of key outcrops. The latter condition is particularly important, because few previous studies have focussed on the significance that grain- to fault zone-scale processes may have on the mechanics of low-angle normal faults. Primary data comprises field mapping and structural analysis, microscopic investigation, stable isotope analysis, and triaxial rock deformation experiments. Principal aims of the study include:

- To describe the internal structure of the Zuccale fault and its constituent fault rocks, and assess the relationships between the Zuccale fault and the local wall rocks.
- To document the relationships between the Zuccale fault and a series of upper-crustal igneous bodies that are broadly related to regional extension.
- To determine the significance and origins of fluid flow along the Zuccale fault.

- To document in detail the textural and geochemical characteristics of the fault zone and its constituent fault rocks, and assess the implications that this may have for fault zone rheology (e.g. fault zone weakening, strengthening).

1.2. Thesis outline and style

Chapters 2-6 of this thesis are described individually below. Each chapter has been written as a standalone manuscript, and each has been published in, or submitted to, a peer-reviewed scientific journal. As such, each chapter contains a separate abstract and introduction, and separate sections dealing with the geological setting, discussion of data, and conclusions. Chapter 7 includes some suggestions for future work. Inevitably there is some overlap in the content of chapters 2-6, particularly in the sections dealing with the geological setting. Each of the chapters was published or submitted with a number of co-authors. Consequently, chapters 2-6 are written in the third person ('we') throughout. However, I am first author on each of the papers, and I am responsible for greater than 90% of the primary data collection, data interpretation, and paper writing. Co-authors provided scientific advice and discussion, assistance with data collection in some instances, and normal levels of editorial guidance.

Chapter 2 – Published article included in Appendix I

Published as S.A.F. Smith, R.E. Holdsworth, C. Collettini & J. Imber (2007) Using footwall structures to constrain the evolution of low-angle normal faults, *Journal of the Geological Society, London*, **164**, 1187-1191

This chapter describes the relationships between the Zuccale fault and a network of subsidiary extensional faults that occur in its immediate footwall. Detailed mapping and structural analysis are used to document the distribution of different fault rock components within the central core of the Zuccale fault. This distribution is used to evaluate the timing relationships between the Zuccale fault and the footwall faults, with important implications for the interpretation of the Zuccale fault as a low-angle structure. The observations and conclusions presented in this chapter are used as a framework for subsequent chapters.

Chapter 3 – Published article included in Appendix II

Published as S.A.F. Smith, C. Collettini, R.E. Holdsworth (2008) Recognizing the seismic cycle along ancient faults: CO_2-induced fluidization of breccias in the footwall of a sealing low-angle normal fault, *Journal of Structural Geology*, **30**, 1034-1046

This chapter describes an unusual and newly recognized suite of fault breccias associated with the Zuccale fault. Detailed mapping and microstructural analysis are used to document the fabrics of the breccias, and the relationships between the breccias and the Zuccale fault. Observations are used to propose a model for the formation and evolution of the breccias that has implications for the mechanics of low-angle normal faults, and the recognition of fault rocks that represent particular phases of the seismic cycle.

Chapter 4

A modified version of this chapter was submitted to the *Bulletin of the Geological Society of America* in February 2008 and is currently in revision. Co-authors are R.E. Holdsworth and C. Collettini.

This chapter focuses on the outcrop- to regional-scale relationships between the Zuccale fault and a series of upper-crustal igneous bodies that are broadly associated with regional extension. Detailed mapping and structural analysis are used to document the temporal and spatial relationships between the Zuccale fault and the igneous bodies, and to evaluate the geometric consequences of pluton intrusion associated with low-angle normal faulting. Stable isotope analysis is used to elucidate the origins of fluid flow along the Zuccale fault, with implications for the mechanical behaviour of the fault zone.

Chapter 5

This chapter is to be submitted to the *Journal of Geophysical Research* in December 2008. D.R. Faulkner is co-author.

This chapter presents the results of triaxial rock deformation experiments carried out on powdered fault rock material from the core of the Zuccale fault. The experiments are used to test the hypothesis that mineralogical weakening alone may explain prolonged slip on low-angle normal faults.

Chapter 6

A modified version of this chapter is to be submitted to *Geochemistry, Geophysics, Geosystems* in December 2008. Co-authors are C. Collettini, R.E. Holdsworth and M.A. Pearce.

Previous research carried out by *Collettini and Holdsworth* [2004] suggested that the Zuccale fault was characterized by a distinctive and complex fault rock 'stratigraphy'.

Building on this, and the results of chapters 2-5, this chapter focuses on the microstructural and geochemical characteristics of the fault rocks in detail. Optical- and scanning-electron microscopy, coupled with X-ray diffraction and X-ray fluorescence analyses, are used to describe each of the main fault rock components within the core of the Zuccale fault. The results have important implications for evaluating the exhumation history and mechanical behaviour of low-angle normal faults.

Chapter 2

Using Footwall Structures to Constrain the Evolution of Low-Angle Normal Faults

*This chapter was published as: S.A.F. Smith, R.E. Holdsworth, C. Collettini & J. Imber (2007) Using footwall structures to constrain the evolution of low-angle normal faults, Journal of the Geological Society, London, **164**, 1187-1191*

Abstract

Controversy exists over the presence of normal faults that initiate and slip at low angles (<30°). Evidence from the Zuccale fault, which dips *c.* 15° east on the island of Elba, Italy, indicates that the early stages of low-angle faulting were synchronous with the development of subsidiary high-angle footwall faults. These footwall structures controlled fault rock distribution and caused the development of flow folds similar to those produced in analogue studies of synchronous high- and low-angle faulting. The current configuration of footwall structures indicates that the Zuccale fault cannot have originally dipped greater than *c.* 20° east, and represents a primary low-angle normal fault.

2.1 Introduction

Normal faults that currently dip at low angles (<30°, often <15°) are recognized worldwide in both continental and oceanic settings, and have frequently played an important role in accommodating large-magnitude extension in zones of rifting [e.g. *Wernicke*, 1981, *Davis et al.*, 1986, *Wernicke*, 1995, *Axen*, 2004, *Smith et al.*, 2006]. Despite this, unambiguous recognition in the geological record of primary low-angle normal faults, that initiated and slipped at a low angle, remains problematic. *Axen* [2004] summarized several compelling examples of large-displacement (5–50 km) primary low-angle normal faults, but because of the apparent mechanical paradox of these structures [*Sibson*, 1985, *Jackson and White*, 1989, *Collettini and Sibson*, 2001] many geoscientists still strongly favour the idea that such faults are formed by passive rotation of high-angle structures, during either footwall isostatic rebound [*Buck*, 1988] or rotation within 'domino' or listric fault sets [*Proffett*, 1977, *Davis*, 1983a, b]. One commonly encountered problem is that it can be difficult to discern the temporal relationships between low-angle normal faults and subsidiary high-angle structures, that commonly cross-cut hanging-wall rocks [e.g. *Cichanski*, 2000]. This leads to ambiguity regarding the dip history of the main low-angle structure, and whether or not high-angle subsidiary structures formed early or late in the faulting sequence. Part of the problem results from the fact that hanging-wall faults rarely interfere with the well-defined fault rock 'stratigraphy' common to many Cordilleran-type metamorphic core complexes [*Davis and Lister*, 1988], typically consisting of (from bottom to top): mylonites with gently inclined fabrics, foliated cataclasites and gouges, and chlorite breccias or microbreccias [*Coney*, 1980, *Cowan et al.*, 2003]. In contrast, high-angle footwall faults that lie immediately below low-angle normal faults have received little attention, and in this paper we investigate the interactions

between such high angle structures and fault rocks found along the shallowly dipping Zuccale fault on the island of Elba, Italy. Our findings demonstrate that the Zuccale fault must have been active as a low-angle structure throughout its slip history and that it has not experienced a decrease in dip value on a regional scale of more than *c.* 5°. This suggests that, whenever they are present, such footwall faults can be used as indicators of low-angle extensional slip along detachment faults worldwide, and that they can also be used to place constraints on the amount of post-slip rotation experienced by low-angle normal faults.

2.2 Geological Setting

The northern Tyrrhenian–Apennine region of Italy has experienced two phases of eastward-migrating deformation since the Cretaceous [*Elter et al.*, 1975, *Jolivet et al.*, 1998, *Pauselli et al.*, 2006]. An early stage of Cretaceous to Pliocene shortening and thrusting was closely followed by a later stage of Miocene–Recent post-collisional extension, which continues in the Umbria–Marche region of Italy. The current stress field in central Italy is characterized by a subvertical σ_1 and an east–west to NE–SW-trending, subhorizontal σ_3 [*Montone et al.*, 2004]. Extension is largely accommodated along shallowly east-dipping normal faults, including the currently microseismically active Altotiberina Fault, and the older exhumed Zuccale fault on Elba, which dips regionally *c.* 15° east [*Collettini et al.*, 2006b].

The geology of Elba comprises five thrust sheets stacked towards the NE during the Late Cretaceous to Early Miocene [Complexes I-V, Figure 2.1; *Trevisan et al.*, 1967, *Keller and Coward*, 1996, *Bortolotti et al.*, 2001a]. The Zuccale fault does not appear to reactivate any of the earlier thrust faults, but instead cross-cuts the entire pre-existing

thrust stack. *Collettini and Holdsworth* [2004] defined a distinct sequence of fault rocks produced during prolonged slip along the Zuccale fault. An initial phase of cataclasis and fluid influx was followed by profound weakening as a result of the onset of pressure-solution accommodated deformation within the fault core, and the development of macroscopically ductile phyllonites and foliated cataclasites. Further brittle deformation led to the formation of coarse fault breccias and fault gouges. Shear sense along the Zuccale fault is consistently top-to-the-east, and overall extensional offsets are *c.* 6km. The relationship between movements along the low angle Zuccale fault and subsidiary high-angle footwall faults is best displayed in 100% exposed coastal sections at the type locality for the fault zone, Punta Di Zuccale (Figures 2.1–2.3).

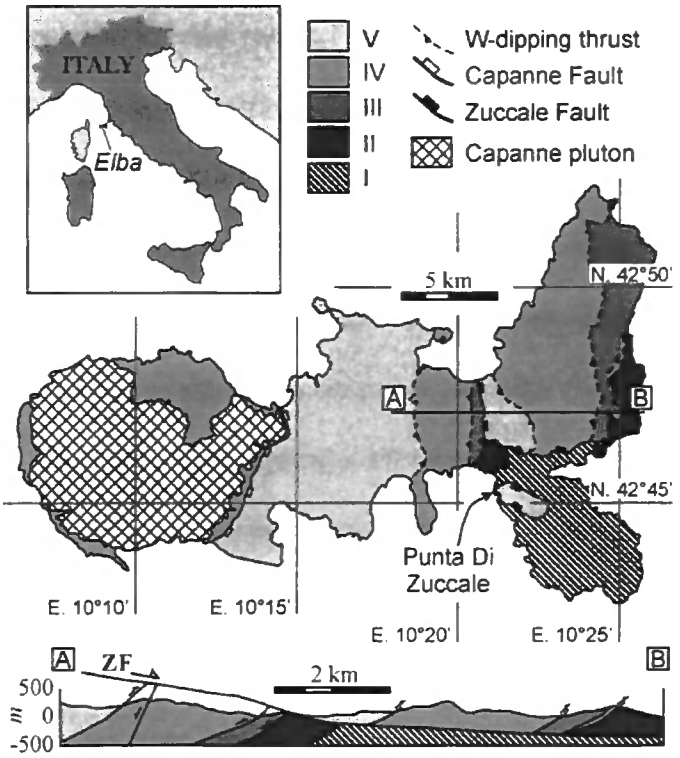

Figure 2.1) Simplified geological map of Elba, and cross-section through central and eastern Elba showing the geometry of the Zuccale low-angle normal fault. I, Complex I basement schists; II, Complex II Tuscan metamorphic sequence; III, Complex III Tuscan limestone sequence; IV, Complex IV Ligurian ophiolite sequence; V, Complex V Cretaceous and Eocene flysch [*Trevisan et al.*, 1967].

2.3 Footwall faulting patterns, Punta Di Zuccale

At Punta Di Zuccale, Complex V Cretaceous flysch in the hanging wall of the Zuccale fault is juxtaposed against Complex I basement schists in the footwall (Figure 2.1). Extension-related deformation in the footwall and hanging wall is exclusively brittle, and the footwall of the Zuccale fault is everywhere pervasively faulted. Footwall faults located in Complex I schists are widely spaced, but occur in geometrically distinct sets (Figure 2.2). Kinematic patterns appear to be relatively simple, with a large majority of faults accommodating east–west-directed extension. Faults that trend east–west or NW–SE (e.g. Area 1 in Figure 2.2) contain shallowly to moderately east-plunging slickenline lineations, accommodate east-directed extension, and represent oblique or strike-slip faults.

Faults that trend north–south (e.g. Area 2 in Figure 2.2) contain steeply plunging slickenline lineations and represent dip-slip normal faults. Fault dip values in Area 2 vary widely between 22° and 88°, but major faults that link upwards into the fault core commonly dip *c.* 70°–90° east (Figure 2.2 inset, Figure 2.3). Displacements on footwall structures are typically tens of centimetres to several metres. Overall, this fault pattern divides the upper surface of the footwall into a 3D block-and basin topography. Large footwall structures cut upwards into the lower part of the main low-angle fault zone (e.g. Figure 2.3), and frequently host, or are linked to, major steeply dipping to subvertical hydrofracture veins filled with carbonate (labelled 'V' in Figure 2.2), suggesting that footwall structures were able to periodically tap and release fluids stored beneath the low-permeability fault core.

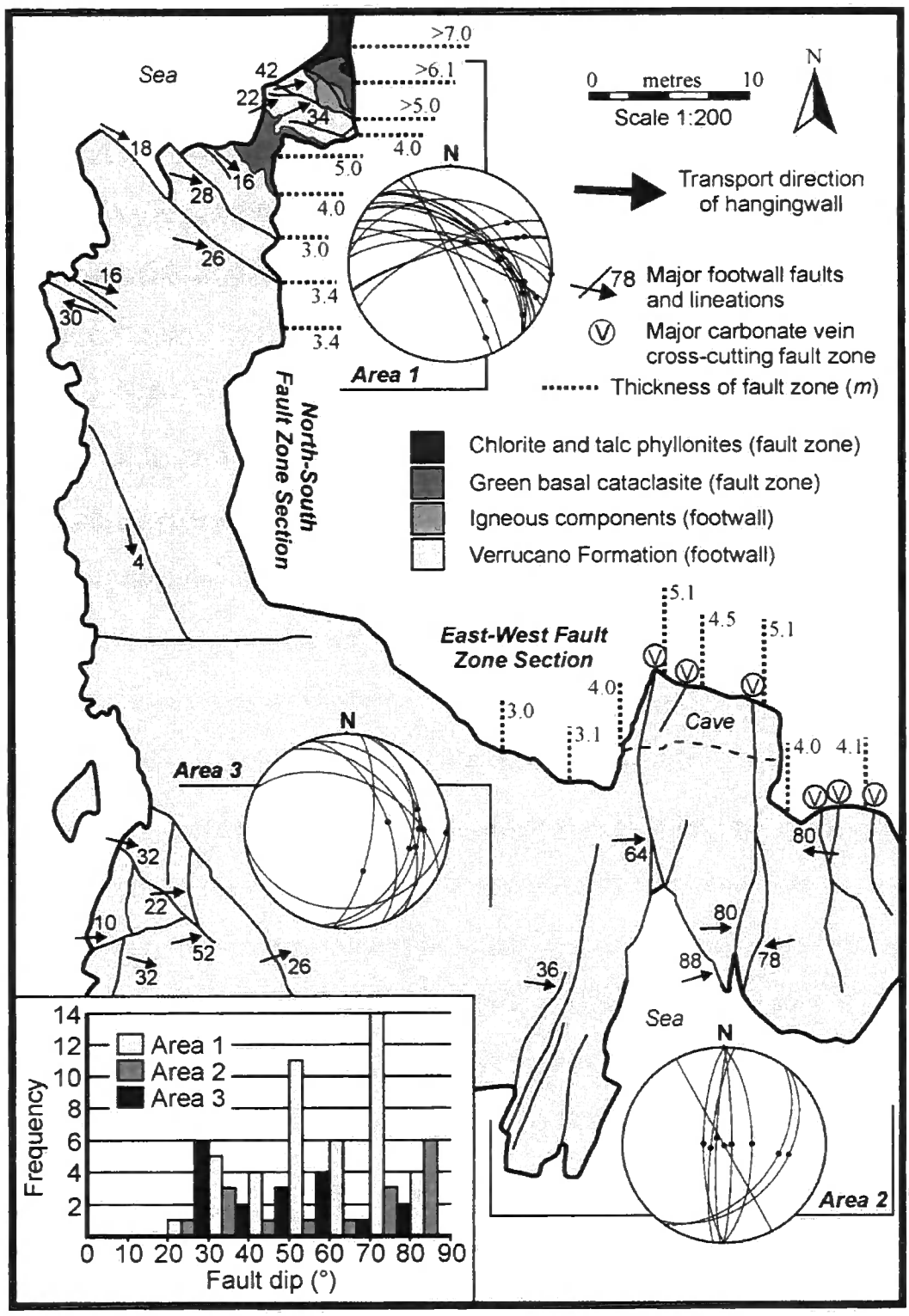

Figure 2.2) Detailed geological map of faulting in the footwall of the Zuccale low-angle normal fault at Punta Di Zuccale. Stereonets show fault-plane orientations and slickenline lineations. Only major faults are shown on the map and stereonets. All measured faults are included in the dip histograms (inset).

2.4 Fault zone architecture, Punta Di Zuccale

New mapping (Figures 2.2, 2.3) demonstrates that the distribution of fault rocks within the Zuccale fault is controlled significantly by footwall faulting, and that a complete fault rock sequence is not preserved everywhere at Punta Di Zuccale. Major footwall structures cut directly up into the base of the Zuccale fault and cause the fault core to increase in thickness from *c.* 3 to *c.* 8m (Figures 2.2, 2.3). This occurs along both east–west (parallel to transport direction) and north–south (orthogonal to transport direction) sections. Figure 2.3(b and d) shows that chlorite- and talc-rich phyllonites, that formed early during the evolution of the Zuccale fault, are found only as elongate lenses in areas where the fault core is unusually thick. In other words, these phyllonites are found only where they lie in the hanging wall (or 'lee' side) of footwall faults where they locally thicken the fault core. Along the east–west section at Punta Di Zuccale, the phyllonites are found as an isolated lens *c.* 8 m long by 3 m high (Figure 2.3b). Along the north–south section the phyllonites are interlayered with green schists, and occur in a lens at least 20 m long by 5 m high (Figure 2.3d). In areas where the footwall is not down-faulted, the fault rock sequence is dominated by carbonate rich foliated cataclasites, with a notable absence of phyllonite. In the field, the base of the carbonate-rich foliated cataclasite is marked by a discrete brittle fault surface, that either cross-cuts and terminates all high-angle footwall faults, or causes a rapid decrease in their offsets across it (e.g. Figure 2.3a). This suggests that during the development of the extensional fault zone, large-offset low-angle and smaller-offset high-angle fault movements have alternated. As we explain below, the alternating low-angle and high-angle scenario provides a compelling explanation for the current preservation or excision of the early formed phyllonites in the core of the Zuccale fault.

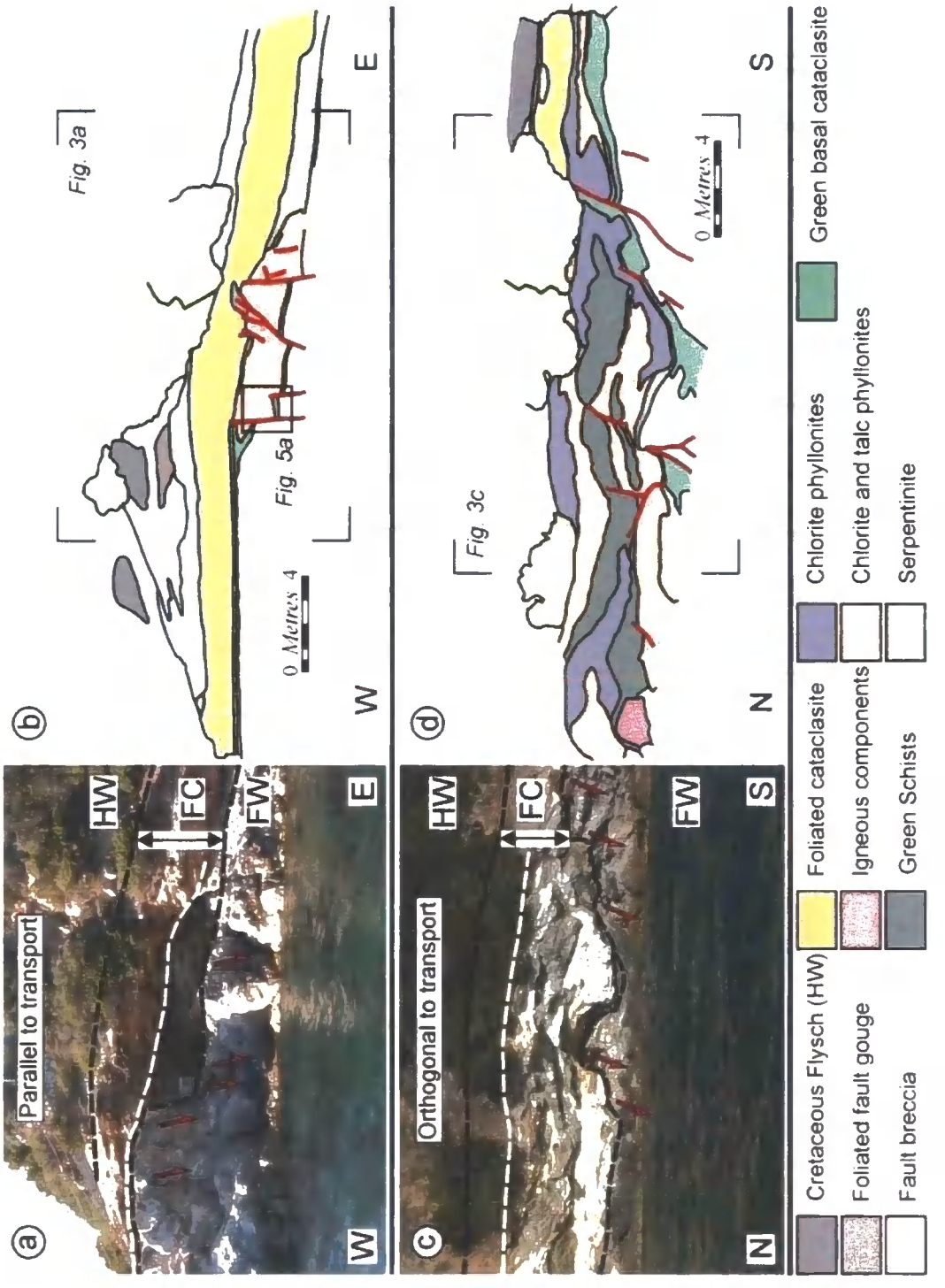

Figure 2.3a, b) Photograph and detailed sketch illustrating the internal architecture of the Zuccale low-angle normal fault (top-to-the-east), and the position of footwall faults, along an east–west coastal section (Area 2 in Figure 2.2). Double-headed arrows in (a) indicate 4.0 m thickness, **(c, d)** North–south coastal section (including Area 1 in Figure 2.2). Double-headed arrows in (c) indicate 3 m thickness. HW, hanging wall of Zuccale fault; FC, fault core; FW, footwall of Zuccale fault. White dashed lines mark the location of a late brittle detachment.

2.5 Fault zone evolution

The sequence of structures and distribution of fault rocks preserved within the core of the Zuccale fault suggests the following deformation history (Figure 2.4). Early fault rocks including phyllonites developed along the low-angle Zuccale fault. It is unclear whether low-angle faulting then ceased for some period during which high-angle footwall (and hanging-wall) structures initiated, or whether this occurred synchronously with low-angle displacements (as shown in Figure 2.4a). The footwall faults grew and eventually cut up into the base of the fault zone, causing thickening of the phyllonitic fault core in directions parallel and perpendicular to transport (Figure 2.4b). Significantly, in three areas at Punta Di Zuccale, the phyllonites contain east-verging asymmetric folds, all of which are located directly above footwall structures (Figures 2.4b, 2.5). These folds have amplitudes of *c.* 1–3 m, exhibit moderately west-dipping axial planes and subhorizontal or shallowly plunging fold axes, and possess geometries that closely resemble those produced in analogue experiments of synchronous low-angle detachment-slip and high angle oblique-slip [Figure 2.5c; *Fossen and Rykkelid*, 1992]. All of the observed folds have overturned western limbs, suggesting that they are not simply extensional forced folds produced by 'draping' of phyllonitic material above a footwall ramp [Figure 2.5; *Maurin and Niviere*, 2000, *Withjack and Callaway*, 2000]. Further low-angle faulting resulted in the formation of carbonate-rich foliated cataclasites and a sequence of brittle fault breccias and gouges (Figure. 2.4c), that probably represent progressive exhumation of the fault zone (Chapter 6). Infrequent reworked clasts of phyllonitic material are found within the overlying foliated cataclasites, indicating that the phyllonites predate the formation of foliated cataclasites at Punta Di Zuccale. The phyllonites were excised from many parts of the main fault zone by a late brittle detachment in the Punta Di Zuccale and other areas, but

remain preserved in isolated lenses down-faulted in the hanging wall 'lee regions' of high-angle footwall faults (Figure 2.4c).

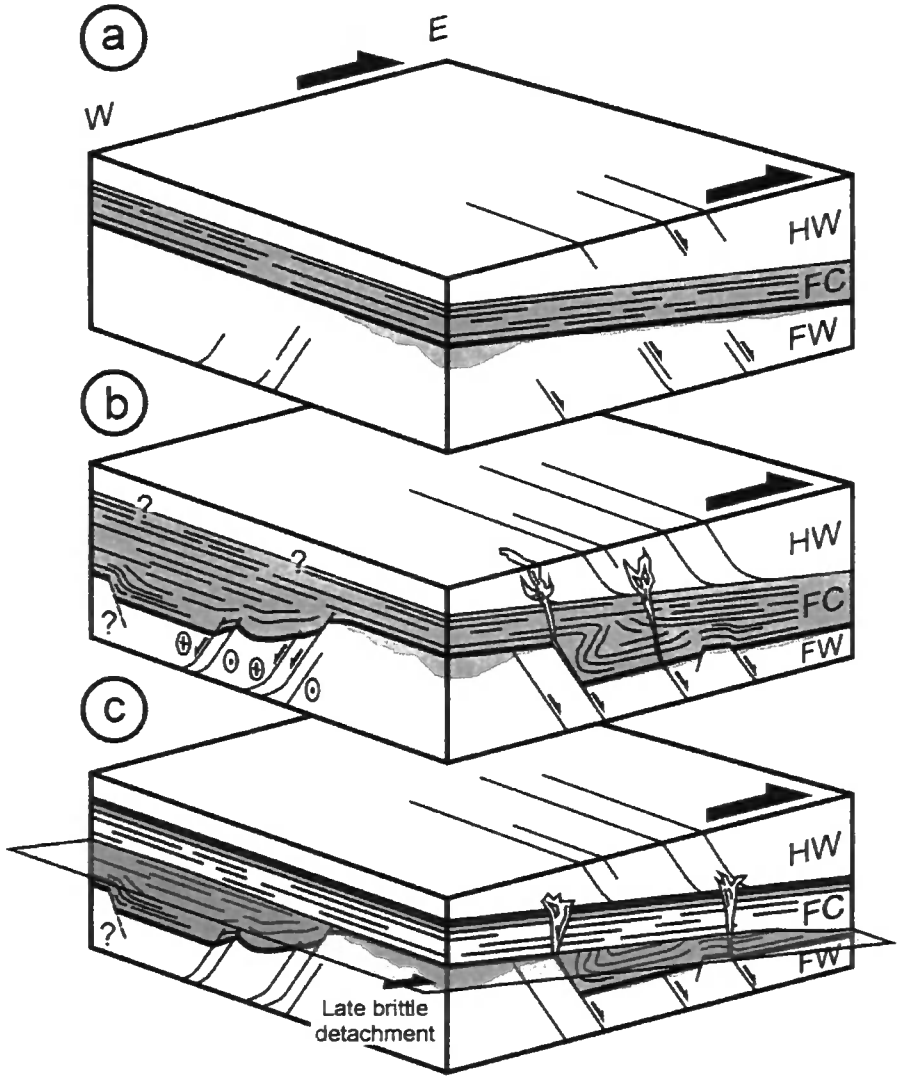

Figure 2.4) Synoptic 3D diagram of fault slip history, **a)** Development of early fault rocks and incipient growth of high-angle subsidiary structures, **b)** Footwall faulting causes thickening of the main fault zone, and folding of early formed phyllonitic fault rocks. Fluids are periodically released by footwall structures to form carbonate hydrofracture veins, **c)** Present-day geometry. A late brittle detachment excises the early phyllonitic sequence, which is 'protected' in thickened areas of the fault core.

2.6 Discussion

The footwall extension recognized during the present study could conceivably originate in several ways, including flexural forces associated with isostatic rebound [*Buck*, 1988], the progression of a 'rolling hinge' [*Axen and Bartley*, 1997], or stress concentration at the margins of a larger, curviplanar ('wavy') fault zone [*Chester and Chester*, 2000]. Alternatively, footwall faulting may simply be the natural consequence of overall regional extension in areas outside the weakened low-angle fault core.

Many of the large footwall structures that formed contemporaneously with early displacements on the Zuccale fault have dips greater than 80° (e.g. Area 2, Figures 2.2, 2.3). This makes it unlikely that the Zuccale fault has experienced a post-slip decrease in dip of more than *c.* 5° in this area, because this would require that the steep footwall structures were originally reverse faults. Synchronous movement along a major extensional fault and a suite of reverse faults in the footwall would represent a highly unusual situation, and one that would introduce major compatibility problems within both the fault core and the adjacent wallrocks. In other localities, successive footwall faulting and interaction with igneous bodies (Chapter 4) has caused the Zuccale fault to rotate more than 5°, so that locally the fault zone dips westward. However, the key relationships preserved at Punta Di Zuccale indicate that on a regional scale the Zuccale fault cannot originally have dipped more than *c.* 20° east.

Footwall faults played a key role in the preservation of early formed fault rock assemblages, materials that carry vital evidence concerning the initial weakening mechanisms that may facilitate movements along high-displacement low-angle normal faults, and the early kinematic history of the fault zone (Chapter 6). In addition, many footwall faults lying immediately beneath the main core of the Zuccale fault are filled with

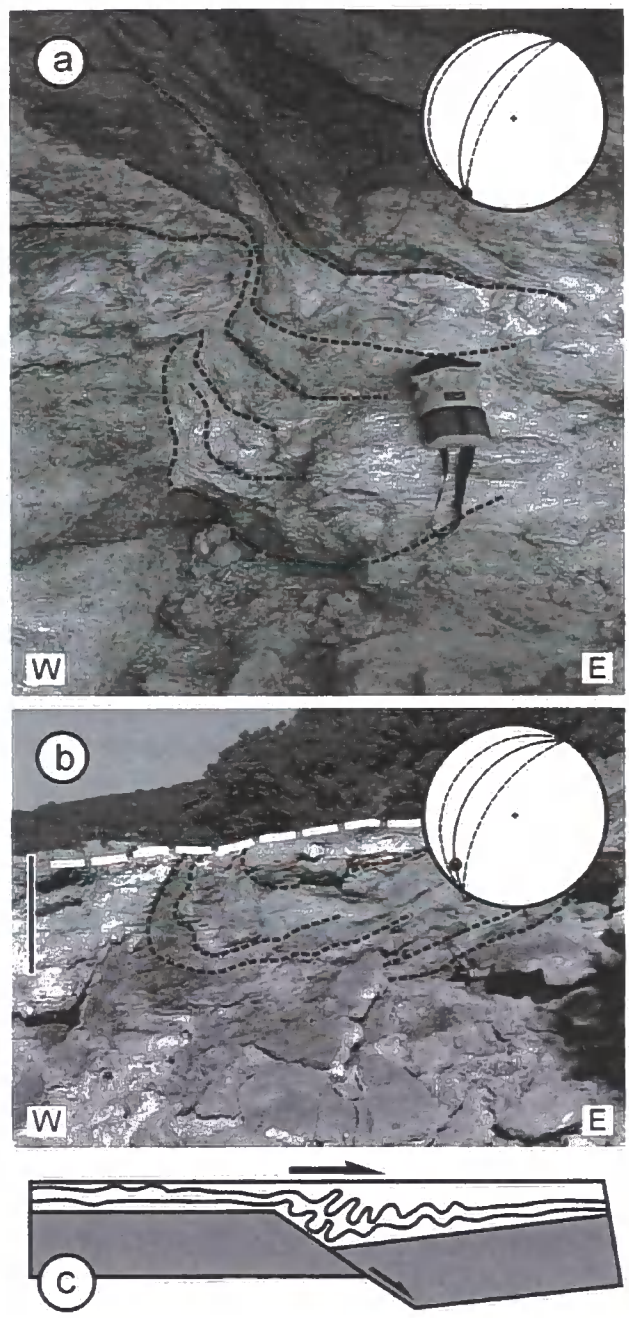

Figure 2.5a) Photograph of asymmetric east-verging fold developed in phyllonites within the east–west section of thickened fault core. Location is shown in Figure 2.3b, **b)** East-verging asymmetric fold within phyllonites to the north of the mapped area. White dashed line marks the location of a late brittle detachment. Scale bar represents c. 2 m. (c) Sketch of analogue model of synchronous layer-parallel and oblique shear after *Fossen and Rykkelid* [1992]. Stereonets show orientations of fold axial planes (continuous lines) and fold axes. Mean orientations of fold limbs are shown as dashed lines.

vein carbonate or act as the origin for subvertical hydrofracture veins, some of which currently cross-cut the complete fault zone stratigraphy. This relationship strongly suggests

that overpressured fluids that accumulated in the footwall region below the foliated fault core seal were periodically released and that, once formed, footwall faults acted as long-lived preferential conduits for fluid flow.

It seems likely that movements along high-angle footwall faults have acted as a first-order control on fault rock distribution and fluid circulation in other areas where low-angle normal faults are known to be important. For example, there is a noticeable similarity between the geometry and distribution of fault rocks presented in this paper and the example given by *Hayman* [2006, figure 3], from the Black Mountain low-angle normal faults in Death Valley. The orientation of footwall structures found along other low-angle normal faults may help in placing constraints on the amount of post-slip rotation caused by mechanisms such as isostatic rebound. Subsidiary faulting patterns over a range of scales are likely to affect the distribution of fault rocks in a wide range of extensional, compressional and strike-slip regimes, and we believe that understanding these patterns has important implications for reconstructing fault zone histories and fault zone permeability properties, and for transmitting the effects of grainscale weakening mechanisms up to the fault and crustal scales.

2.7 Conclusions

The Zuccale fault on the island of Elba slipped as a low-angle (*c.* 15°) extensional structure throughout its history. Subsidiary high-angle footwall faults strongly controlled the distribution of phyllonites that formed early within the fault core, indicating that the footwall structures themselves must have formed early. The phyllonites also contain a series of inclined asymmetric folds that resemble those produced in analogue experiments, suggesting that low-angle and high-angle faulting were synchronous, or alternated with

one another. On a regional scale the Zuccale fault has not experienced a decrease in dip of more than *c.* 5° and its current geometry cannot be explained by significant passive reorientation. The outcrop-scale field relationships described in this paper can be applied to detachment faults worldwide to infer that the early stages of movement occurred at low angles.

Chapter 3

Recognizing the Seismic Cycle along Ancient Faults: CO_2-Induced Fluidization of Breccias in the Footwall of a Sealing Low-Angle Normal Fault

*This chapter was published as: S.A.F. Smith, C. Collettini & R.E. Holdsworth (2008) Recognizing the seismic cycle along ancient faults: CO_2-induced fluidization of breccias in the footwall of a sealing low-angle normal fault, Journal of Structural Geology, **30**, 1034-1046*

Abstract

The Zuccale low-angle normal fault exposed on the island of Elba, Italy, is a crustal-scale structure which contains a strongly foliated fault core. In the immediate footwall of the Zuccale fault, cohesive fault-related breccias that were initially deformed by typical frictional deformation mechanisms experienced fluidization over areas of at least 10^{-2}-10^{-3} km^2.

Three internal variants of fluidized breccia are recognized, with each related to a separate fluidization event. Characteristics of the fluidized breccias include: 1) A highly irregular 'intrusive' boundary with the overlying fault core; 2) no grain-scale evidence for typical frictional deformation mechanisms; 3) an association with carbonate cements indicating that fluids contained CO_2; and 4) a clast-preferred orientation suggesting that fluids were moving vertically and spreading laterally as they encountered the foliated fault core.

Our observations suggest that the fluidized breccias are representative of the interseismic period along the Zuccale low angle fault, and developed across small fault patches during build-ups in fluid overpressure. Attainment of a critical fluid overpressure triggered embrittlement and the formation of low-angle slip surfaces and sub-vertical tensile hydrofractures within the overlying fault core, which may account for the presence and the dimensions (10^{-1}-10^{-3} km^2) of rupture surfaces that produce microseismicity along active low-angle normal faults in central Italy.

3.1 Introduction

Fluids exert a fundamental control on the mechanical and chemical behaviour of all types of fault and shear zone. There is a voluminous literature detailing field, laboratory and theoretical work carried out in an attempt to understand the role of fluids in earthquake rupture, the formation of hydrothermal ore deposits, and the long-term evolution of faulted regions of the crust and lithosphere at all depths and scales [e.g. reviews by *Hickman et al.*, 1995, *Oliver*, 1996, *Sibson*, 2000, *Person et al.*, 2007]. Increasingly it is recognized that cycling of fluid pressure - e.g. 'fault-valve' models [*Sibson*, 1990] - within faults and shear zones strongly affects their mechanical behaviour, and can be intimately linked to the earthquake cycle [*Parry and Bruhn*, 1990, *Sibson*, 1992, *Cox*, 1995, *Henderson and Mccaig*, 1996, *Nguyen et al.*, 1998, *Famin and Nakashima*, 2005, *Sibson*, 2007].

Low-angle normal faults, that dip less than 30°, have received considerable attention since standard 'Andersonian' frictional fault theory does not predict such orientations and because large earthquakes on low-angle normal faults are rare or absent [*Anderson*, 1942, *Jackson and White*, 1989, *Wernicke*, 1995, *Collettini and Sibson*, 2001, *Axen*, 2004, *Axen*, 2007]. Low-angle normal faults may slip over prolonged periods of time if fault rock materials lining the fault surface possess a low friction coefficient [*Numelin et al.*, 2007], or if high fluid pressures are generated within, or adjacent to, the fault zone [e.g. *Axen*, 1992]. Attainment of tensile fluid overpressure ($P_f > \sigma_3$) is critical for reactivation and slip along low-angle normal faults, particularly in the upper 10km of the brittle crust. For example, *Collettini and Barchi* [2002] applied frictional reactivation theory to study the conditions necessary for reactivation of the Altotiberina fault, an active low-angle normal fault in central Italy. They found that the Altotiberina fault can be reactivated for low values of differential stress ($\sigma_1 - \sigma_3 < 28$ MPa), relatively high values of tensile strength of

the surrounding rocks (~10 MPa), and tensile fluid overpressure $P_f > \sigma_3$ (e.g. $\lambda_v > 0.93$). There is strong evidence from the footwalls of metamorphic core complexes and their associated low-angle normal faults, where vein and fracture networks are commonly observed, that tensile fluid overpressure is locally obtained [e.g. *Reynolds and Lister*, 1987]. However, the factors leading to focused fluid flow and to the development of fluid overpressure at specific sites are unknown, and there is still a paucity of direct geological evidence for any form of fluid cycling along low-angle normal faults.

The aim of this paper is to describe in detail the geological setting, microstructural characteristics, and evolution of a suite of frictional fault rocks (breccias) that we believe to have experienced widespread fluidization beneath the Zuccale fault, a low-angle normal fault exposed on the Island of Elba. We focus our attention on a single coastal outcrop that contains 100% exposure in the immediate footwall of the Zuccale fault, and use our observations to develop a conceptual model for fluidization. We discuss our observations in the context of fluid cycling, the development of fluid overpressure associated with low-angle normal faults, and the recognition of fault rocks that represent particular phases of the seismic cycle.

3.2. Geological Setting

3.2.1 The Northern Apennines

Elba lies ~20km to the west of Tuscany in the northern Tyrrhenian Sea. This area has experienced two contrasting phases of deformation, both of which migrated progressively from west to east [Figure 3.1a; *Elter et al.*, 1975, *Pauselli et al.*, 2006]. An earlier phase of Cretaceous to Quaternary collision was followed by a later phase of Miocene to currently active post-collisional extension. Geological and geophysical studies have highlighted that

a majority of post-collisional extension has been accommodated along shallowly east-dipping low-angle normal faults [Figure 3.1a; *Barchi et al.*, 1998, *Jolivet et al.*, 1998, *Collettini et al.*, 2006b, *Pauselli et al.*, 2006, *Chiaraluce et al.*, 2007]. Active extension presently occurs along the Altotiberina low-angle normal fault, that produces abundant microseismicity (M<2.3) at a rate of ~3 events $day^{-1}km^{-2}$ [*Chiaraluce et al.*, 2007] over a depth range of 4km-14km [Figure 3.1a; *Boncio et al.*, 1998, *Boncio et al.*, 2000]. Microseismic activity occurs on rupture surfaces in the size range of 10^{-1}-10^{-3} km^2 [*Sibson*, 1989, *Collettini and Barchi*, 2002, *Chiaraluce et al.*, 2007]. The active regional stress field in central Italy is characterized by a sub-vertical σ_1 and an east-west to NE-SW-trending, sub-horizontal σ_3 [*Montone et al.*, 2004]. Older, inactive low-angle normal faults are exhumed in western Tuscany and the Tyrrhenian islands, which includes the Zuccale fault exposed on Elba.

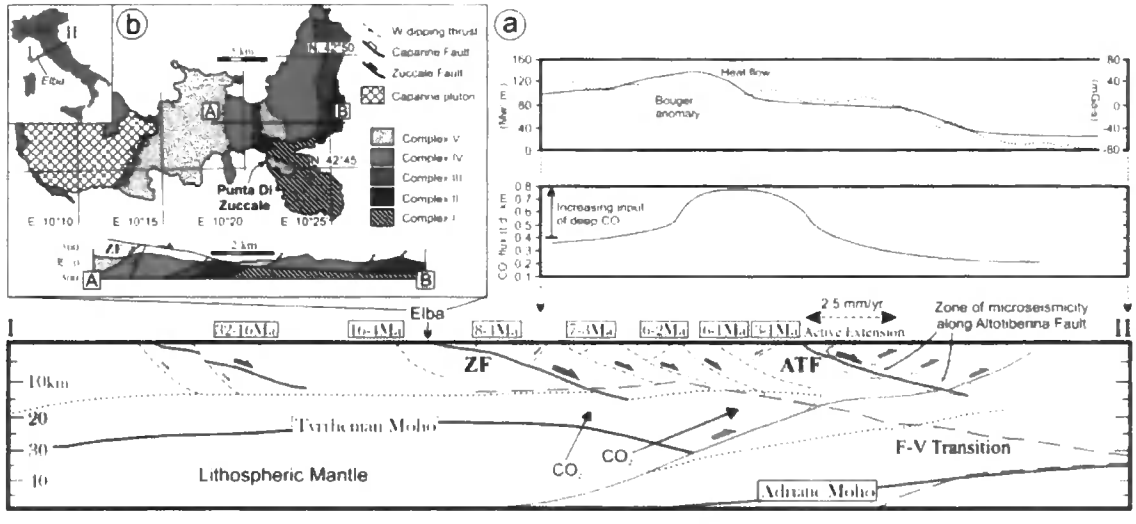

Figure 3.1a) Crustal-scale cross section from Corsica to the Adriatic coast based partly on the CROP03 deep seismic reflection profile [*Barchi et al.*, 1998]. Location of the cross section is shown in part b. The age ranges of syn-tectonic extensional basins are shown in white boxes. Extensional processes in the Tyrrhenian Sea and Tuscany have caused high average heat flows, a regional positive Bouger gravity anomaly, and a shallow Moho [*Collettini et al.*, 2006b]. Additionally, the area is associated with high fluxes of deeply-derived CO_2. Location of the frictional-viscous (F-V) transition after *Pauselli and Federico* [2002]. Zone of microseismicity along the Altotiberina Fault (ATF) after *Chiaraluce et al.* [2007]. ZF, Zuccale fault, **b)** Simplified geological map of Elba [after *Trevisan et al.*, 1967] and cross section through central and eastern Elba highlighting the geometry of the Zuccale fault. Complex I, Palaeozoic basement schists; Complex II, Tuscan metamorphic sequence; Complex III, Tuscan limestone sequence; Complex IV, Ligurian ophiolite sequence; Complex V, Cretaceous flysch.

Central Italy is characterized by an anomalously high flux of non-volcanic CO_2, focused specifically within the area that has experienced widespread post-collisional extension [Figure 3.1a; *Chiodini et al.*, 2004]. The flux of CO_2 reaches ~0.8 tonnes day^{-1}km^{-2}, whereas to the east of the active extensional front, the flux of CO_2 decreases rapidly. Based mainly on $^3He/^4He$ and $\delta^{13}C$ isotopic analysis, it appears that around 40% of the CO_2 gas discharged in central Italy is derived from the upper mantle, which acts as an important source of CO_2-bearing fluid to the base of the brittle crust [*Minissale et al.*, 2000, *Chiodini et al.*, 2004, *Minissale*, 2004]. Two deep boreholes (Santo Donato at 4750m below sea level and Santo Stefano at 3700m below sea level) that penetrated the active Altotiberina fault encountered fluid overpressures that were ~85% of the lithostatic load (λ_v=0.85), induced by trapped CO_2-bearing hydrous fluids in the footwall of the fault [*Chiodini and Cioni*, 1989]. Several authors have suggested that deeply derived CO_2-bearing fluids play a critical role in the nucleation of crustal earthquakes and the time-space evolution of aftershocks in central Italy [*Collettini and Barchi*, 2002, *Miller et al.*, 2004, *Chiaraluce et al.*, 2007].

3.2.2 The Zuccale fault on the Island of Elba

Elba consists of a series of 5 stacked thrust sheets (Complexes I-V) that formed during late Cretaceous-early Miocene shortening (Figure 3.1b). All of the thrust sheets currently dip moderately to the west and are crosscut and displaced by the shallowly east-dipping Zuccale fault [Figure 3.1b; *Trevisan et al.*, 1967, *Keller and Pialli*, 1990, *Bortolotti et al.*, 2001a]. Shear sense along the Zuccale fault is uniformly top-to-the-east, and overall extensional offsets are ~6km [*Keller and Coward*, 1996]. The movement history of the Zuccale fault is poorly constrained, but a majority of displacement is likely to have

occurred between ~8Ma and ~4Ma based on ages obtained for displaced granitic intrusions [*Dini et al.*, 2002], and for sediments deposited in extensional basins to the east [*Pascucci et al.*, 1999]. Extension on Elba was accompanied by intrusion of the Capanne (c.6.9Ma) and Porto Azzurro (c.5.9Ma) plutons, both of which were associated with significant hydrothermal fluid flow systems [*Taylor and Turi*, 1976, *Dini et al.*, 2002, *Maineri et al.*, 2003, *Gagnevin et al.*, 2004, *Rossetti et al.*, 2007].

The Zuccale fault is exposed particularly well at its type locality at Punta Di Zuccale (Figure 3.1b), where it juxtaposes a hangingwall of Cretaceous sandstone and mudstone flysch deposits (Complex V) against a footwall of Palaeozoic quartzites and quartz-mica schists (Complex I; Figure 3.2). *Collettini and Holdsworth* [2004] and *Smith et al.* [2007; Chapter 2] studied the fault rock sequence and internal structure of the Zuccale fault, and only a brief summary of necessary details is provided below.

From bottom to top, the sequence of fault rocks found along the Zuccale fault consists of five units: (1) Breccias and cataclasites derived exclusively from the Palaeozoic footwall rocks and containing clasts of quartzite and quartz-mica schist surrounded by a carbonate-chlorite-quartz matrix. These were deformed by frictional deformation mechanisms including fracture, grain fragmentation and grain rolling. Although their distribution is heterogeneous, they typically have a minimum thickness of ~3 meters. Below, we refer to them as *frictional breccias*; (2) Chlorite-talc-carbonate phyllonites; (3) Foliated tremolite-talc-chlorite schist with inclusions of serpentinite; (4) Carbonate-rich foliated cataclasites containing lenses of serpentinite, phyllonite, and calc-mylonite; (5) Coarse fault breccias and foliated fault gouges derived predominantly from the hangingwall units. Throughout this paper we refer to fault rock units 2-5 as the 'fault core'. The footwall and fault core are crosscut by abundant carbonate veins, often possessing crack-seal textures, and interpreted to represent hydrofractures formed due to periodic

build-ups in fluid overpressure [*Collettini et al.*, 2006a]. The largest hydrofracture veins link directly downwards in to subsidiary, steeply-dipping extensional faults present in the footwall of the Zuccale fault (Figure 3.2), strongly suggesting that such footwall faults focused and channelled fluid flow [*Smith et al.*, 2007; Chapter 2]. Along part of the north-south (transport-perpendicular) coastal section at Punta Di Zuccale, frictional breccias (fault rock unit 1) locally adopt a different, and unusual, appearance. Typically, these unusual breccias are grey to milky-white in colour and below we refer to them collectively as *grey breccias*.

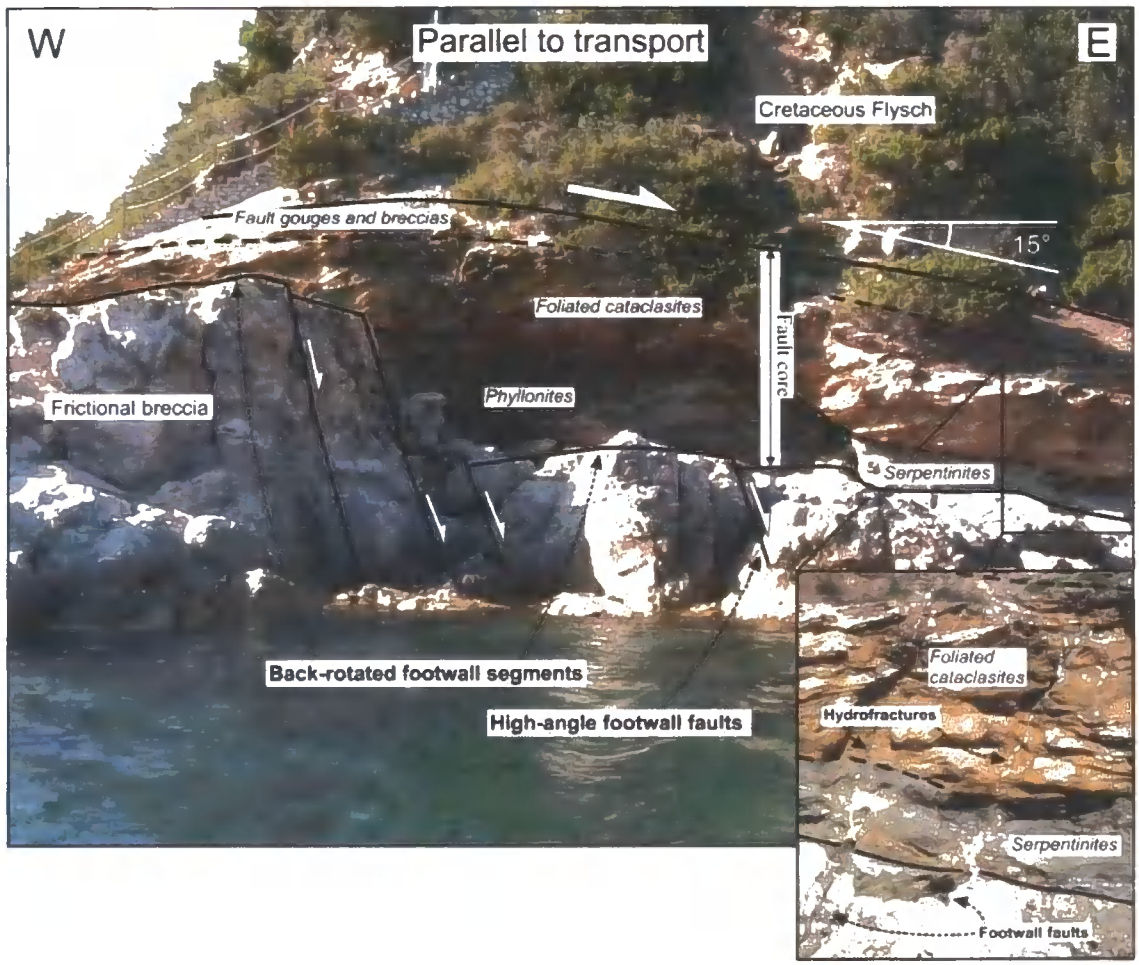

Figure 3.2) Characteristic geometry of the Zuccale fault observed along an east-west coastal section at Punta Di Zuccale, where it places Cretaceous flysch in the hangingwall against Palaeozoic schists in the footwall. Double headed arrow labelled "Fault Core" is 5 meters in thickness. Overall, the Zuccale fault dips ~15°E, but locally the base of the fault core has been

back-rotated by a series of high-angle footwall faults, which also strongly control the distribution of individual fault rock units. Hydrofracture veins cross-cut the footwall and fault core, and are always directly linked to high-angle footwall faults (see inset photograph).

3.3 Grey Breccias

3.3.1 Field relationships

Grey breccias occur in the immediate footwall of the Zuccale fault where they occupy a minimum area in plan view of ~70x40 meters, and occur over large areas of continuous outcrop and as a series of isolated windows that are eroded through the overlying fault rocks (Figures 3.3-3.5). The total vertical extent of the grey breccias is unknown, but they are present to a depth of at least 3 meters in the footwall of the Zuccale fault. Three internal variants of grey breccia are recognized and we refer to these as breccias A, B, and C (Figures 3.3, 3.4). They are differentiated in the field on the basis of colour, structural position beneath the Zuccale fault, textural features, and maximum clast size.

Grey breccia A is the most voluminous variant and occupies an area of ~40x40 meters in the southern half of the mapped outcrop (Figure 3.3). Compositionally and texturally it is highly heterogeneous, and is dominated by large blocks of basement quartzite and quartz-mica schist that can be up to several meters in diameter. The lithologies of clasts within this variant, and those in variants B and C, are indistinguishable from the local wallrock.

Variants B and C are texturally much more homogenous. Both are grey to milky-white in colour, and contain clasts of basement quartzite and quartz-mica schist not exceeding several tens of centimetres in diameter. Breccia C is differentiated from B on the basis of two specific macroscopic characteristics. Firstly, it occurs solely as discrete pods of material that sit at topographically and structurally higher levels than B (Figures 3.4, 3.5a).

Secondly, breccia C possesses a distinct honeycomb weathering texture, particularly noticeable towards its base, which appears to reflect erosion and removal of large clasts (Figure 3.5b).

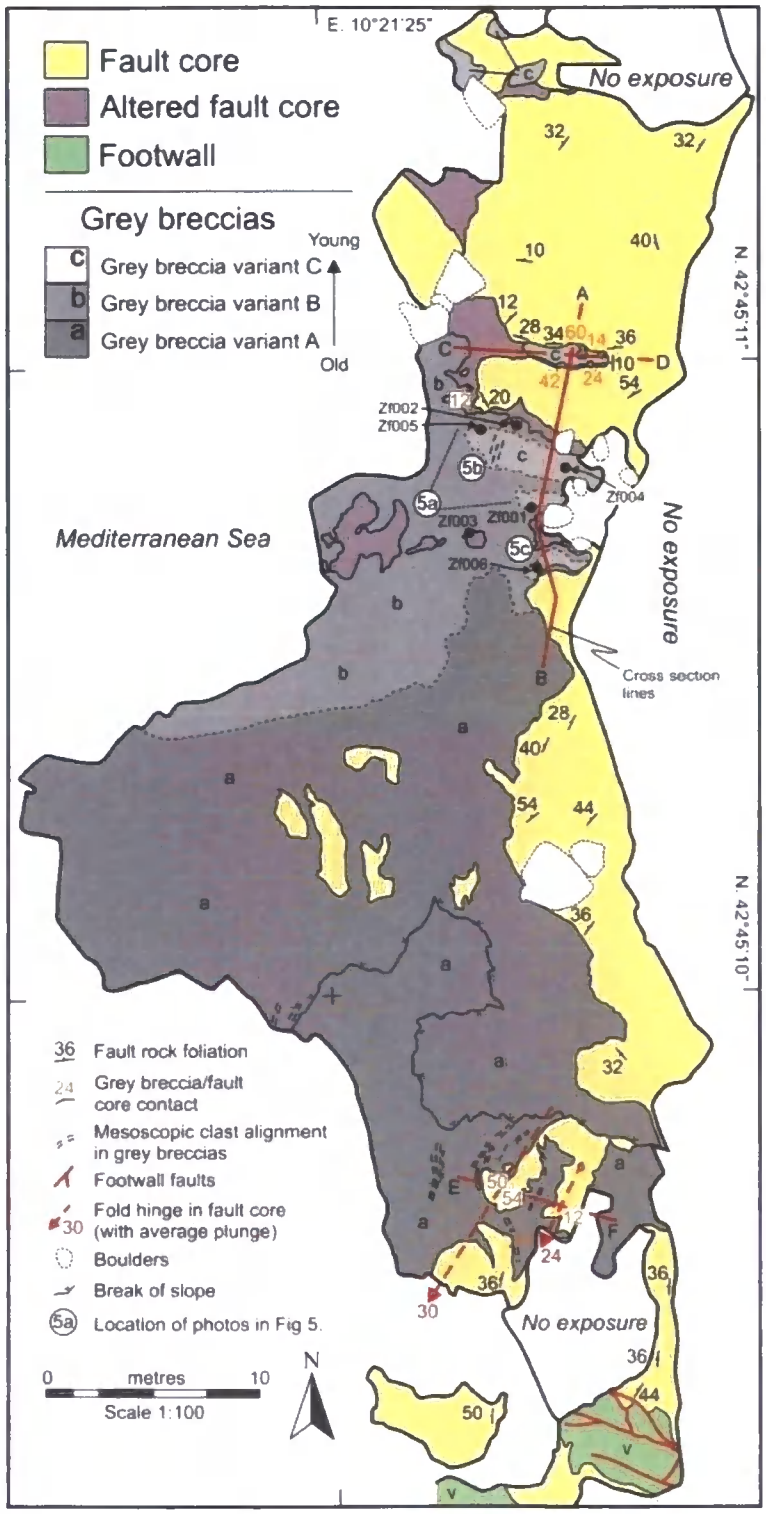

Figure 3.3) Detailed geological map of the north-south coastal section at Punta Di Zuccale where grey breccias are present. Also shown are the cross section lines in Figure 3.4, the locations of photographs in Figure 3.5, and the locations of samples Zf001-Zf006 discussed in section 3.4.2.

The three variants of grey breccia appear to have formed at different times based on their structural relationship to extensional slip surfaces within the overlying foliated core of the Zuccale fault. Slip surfaces are commonly highly polished and associated with a thin (<1mm) veneer of ultra-fine grained cataclastic material. Breccia A appears to be the oldest variant, because in places the upper surface of this breccia is defined by a cross-cutting extensional slip surface that contains well-developed east-west slickenlines. In turn, breccias B and C cross-cut the same slip surface and so, by definition, must be younger than A. Breccia C is interpreted to be younger than B because of its occurrence as isolated pods of material that sit on top of and appear to originate from within B (Figures 3.4, 3.5a).

Importantly, there is strong evidence that the coastal section containing the grey breccias is underlain by a major north-south trending high-angle extensional fault like those described in section 3.2 and shown in Figure 3.2. *Smith et al.* [2007; Chapter 2] showed that well exposed footwall faults are directly associated with (Figure 3.2): 1) The preservation of phyllonitic fault rocks as isolated lenses of material; 2) Inclined flow folds within the fault core; and 3) Back-rotation of footwall blocks so that locally they are sub-horizontal or dip westward. All of these structural relations are found in the area containing the grey breccias (Figure 3.3). Large flow folds are present within the fault core in the southern half of the mapped outcrop, and all the fault core rocks dip moderately to the west or north-west, indicating that the fault core has experienced local back-rotation.

3.3.2 The boundary between the grey breccias and the overlying fault core

All three variants of grey breccia appear to preserve 'intrusive' relationships with overlying foliated fault rocks within the core of the Zuccale fault (Figures 3.4, 3.5, 3.7b). The boundary between the grey breccias and the overlying fault core is well defined and typically has a highly irregular nature, preserving undulations with wavelengths between 10cm-5m, both parallel and perpendicular to the easterly transport direction within the Zuccale fault. These undulations are directly associated with warping and folding of the overlying fault core, so that the foliation within the overlying fault rocks closely follows the shape of the underlying boundary (Figure 3.4). In detail, the boundary has a cuspate-lobate nature (Figure 3.5c). Additionally, small fragments (<30cm in diameter) of heavily altered fault core material are commonly found 'floating' within the underlying grey breccias (Figure 3.5c). Within breccia variants A and C a macroscopic ~north-south alignment of elongate clasts of quartzite and quartz-mica schist can be observed on sub-horizontal (plan view) surfaces (Figure 3.6).

Figure 3.4) Cross sections through the grey breccias and overlying fault rocks within the core of the Zuccale fault. Key is the same as Figure 3.3. Note the presence of a macroscopic clast alignment within the grey breccias, and a layer of altered fault core overlying the grey breccias.

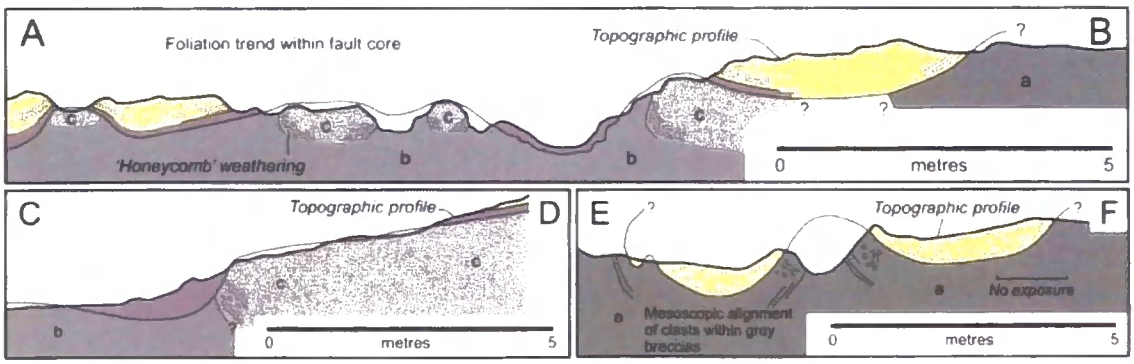

3.3.3 Microstructural observations

Frictional breccias are typically characterized by a mosaic texture [following the terminology of *Mort and Woodcock*, 2008], so that at any scale of observation, the textural framework appears to be 'clast-supported' (Figure 3.7a). The frictional breccias contain abundant cataclastic fractures that are commonly lined with fibrous chlorite. The matrix of the frictional breccias typically consists of fine-grained quartz, chlorite and sericite, derived from comminution of larger clasts. Qualitatively, clasts within the frictional breccias at any scale of observation have an angular to sub-angular appearance, and contain no visible shape-preferred orientation (Figure 3.7a). They appear relatively fresh and have not been overgrown by any late alteration or replacement products.

Grey breccias appear remarkably different on a grain-scale, and their overall texture does not readily fit into one of the breccia classes proposed by *Mort and Woodcock* [2008; Figure 3.7b]. At any scale of observation, the breccia framework appears to be 'matrix-supported'. Relatively large clasts of quartzite and quartz-mica schist (up to ~1000μm) are isolated within an ultra-fine grained matrix. There is a complete lack of any localized deformation features such as cataclastic fractures or shear bands.

Qualitatively, clasts within the grey breccias have a sub-rounded to rounded appearance and are commonly overgrown by euhedral crystals of colourless dolomite (Figure 3.8a). In thin section, the boundary between the grey breccias and the overlying fault core preserves a well defined, irregular nature (Figure 3.8b). Immediately above the boundary, in a layer 30 cm – 1 m thick, the fault core is highly altered and is dominated by fine-grained Fe-oxide phases and inter-grown calcite and dolomite crystals (Figures 3.3, 3.4, 3.5, 3.8b). These carbonate crystals are fresh and undeformed, and often preserve primary growth zoning (Figure 3.8c). In places, a relict breccia texture is overgrown by

undeformed, subhedral-anhedral calcite crystals (Figure 3.8d). Table 3.1 provides a summary of microstructural observations of frictional breccias and grey breccias.

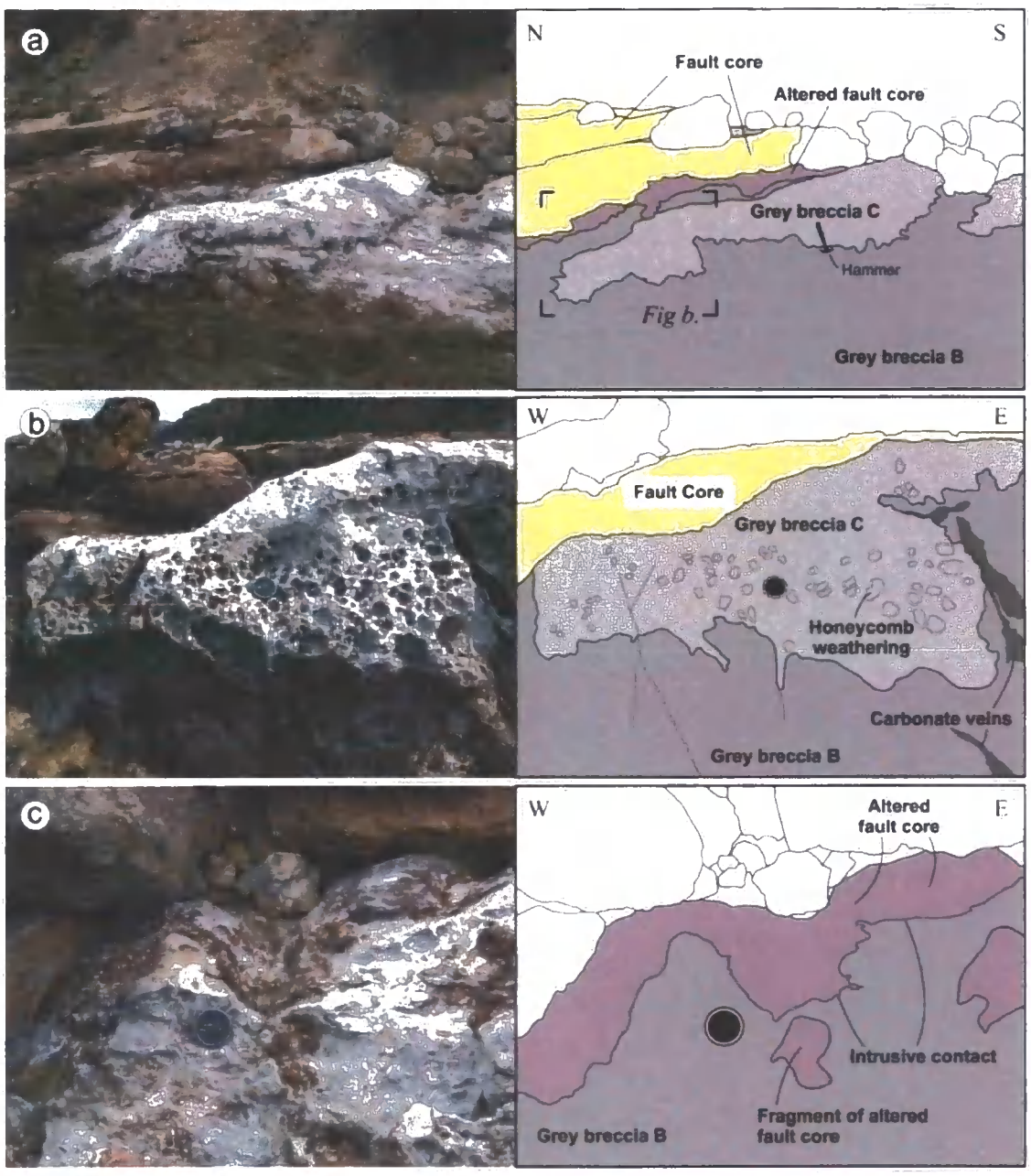

Figure 3.5) Photographs and detailed sketches of the grey breccias and overlying fault core. Locations of photographs are shown in Figure 3.3.

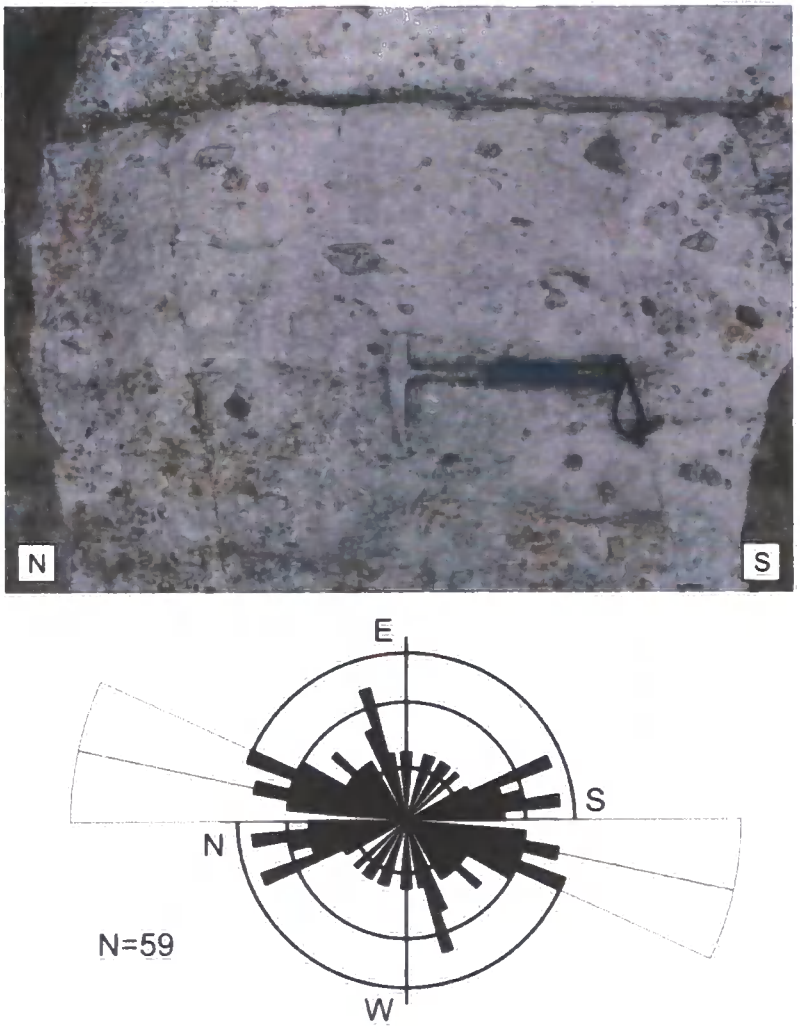

Figure 3.6) Photograph of horizontal surface showing an alignment of elongate clasts of quartzite and quartz-mica schist within grey breccia variant C. The clasts are aligned broadly north-south. See section 3.4.2 and the caption for Figure 3.11 for a description of the construction and labelling of the rose diagram. Orientation statistics were calculated for this example by tracing all visible clasts in the photograph. Mean vector orientation, 12° clockwise from north; Mean vector strength, 0.4; Mean aspect ratio of visible clasts, 2.17.

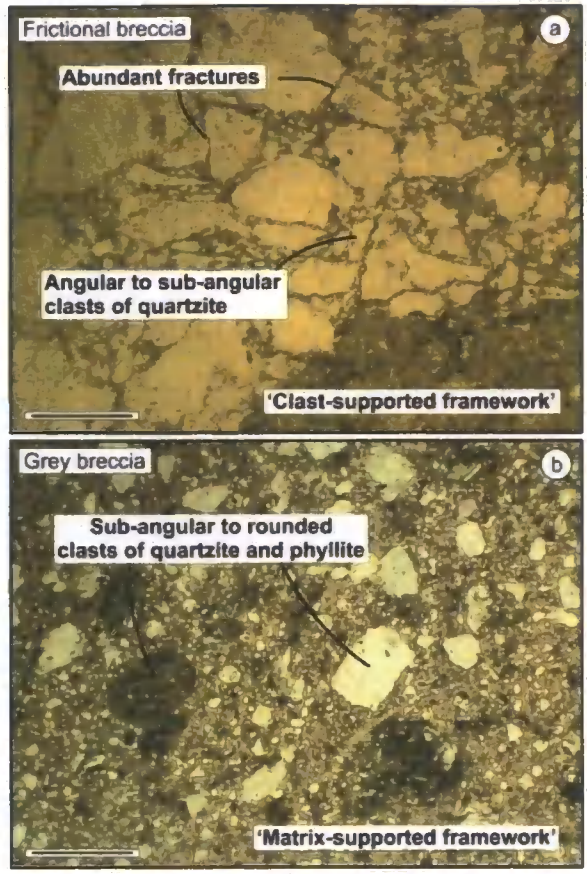

Figure 3.7) Photomicrographs showing grain-scale textures within typical frictional breccias **(a)** and grey breccias **(b)**. Note the 'matrix-supported' framework, and the lack of cataclastic fractures within the grey breccias. Scale bars are 1mm, and both images are taken in plane polarized light.

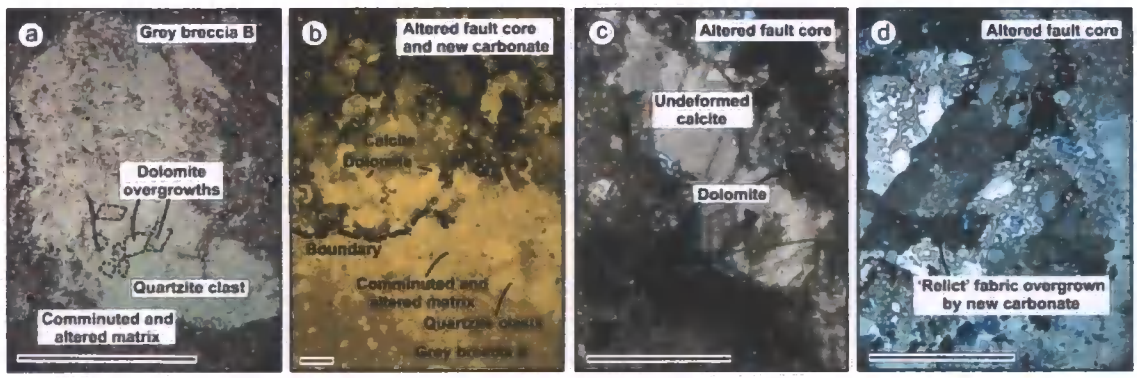

Figure 3.8) Photomicrographs showing details of grain-scale textures within grey breccias and overlying fault core. Scale bars are 1mm. Images a and b are taken in plane polarized light, c and d in crossed polarized light. **a)** Detail of quartzite clast within grey breccia B which is overgrown by abundant euhedral dolomite crystals, **b)** Irregular, well-defined boundary between grey breccia variant B and overlying altered fault rocks within the core of the Zuccale fault. The overlying fault rocks are dominated by fine-grained Fe-oxide phases and fresh growths of calcite and dolomite, **c)** Detail of calcite and dolomite intergrowths within altered fault core overlying the boundary. Note the primary growth zoning in both minerals, **d)** Relict breccia fabric overgrown by new subhedral-anhedral calcite crystals within the altered fault core.

Frictional Breccia
'Clast' supported mosaic texture Abundant cataclastic fractures Matrix is fine grained quartz and fibrous chlorite Upper boundary of breccias is commonly a fault contact Sub-angular to angular clasts
Grey Breccia
'Matrix' supported fabric No cataclastic fractures Matrix is ultra-fine grained quartz, sericite, and infrequent chlorite Abundant growth of undeformed calcite and dolomite Quartzite clasts frequently overgrown by dolomite. Upper boundary of breccias is intrusive in nature Sub-rounded to rounded clasts

Table 3.1) Summary of microstructural observations of typical frictional breccias and grey breccias at Punta Di Zuccale

3.4 Quantifying grain-scale deformation in the grey breccias

3.4.1 Analysis of fragmented counterparts

Monzawa and Otsuki [2003] and *Otsuki et al.* [2003] proposed a quantitative method to determine whether a particular granular fault rock has experienced fluidization. The key parameter analyzed using their method is the 'detection probability of fragmented counterparts' in thin sections of fault rock. A clast in thin section is considered a fragmented counterpart when it can be recognized that it was originally part of a larger clast. In other words, if two clast fragments are found adjacent to one another, and they evidently fit together like a jigsaw puzzle, they can be considered fragmented counterparts.

During frictional deformation, granular fault rocks such as breccias and cataclasites, that consist of packed and interlocking clasts, experience continuous fracturing due to high stresses at grain-grain contacts. Consequently, the probability that clasts will be fractured during frictional deformation is high.

Once a granular fault rock becomes fluidized, the only mechanism capable of generating new clast fragments is head-on collision between clasts, or between clasts and the wall rocks. However, *Monzawa and Otsuki* [2003] showed that in most circumstances the probability of fragmenting clasts smaller than a few millimeters during fluidization is virtually zero, because the collision velocities required are extremely high (e.g. 10 m s^{-1} for clasts of quartzite 1mm in diameter). Although only currently developed for 2-dimensional analysis, their simple theoretical treatment indicates that an assessment of the number of fragmented counterparts can yield important insights into whether a granular fault rock has experienced fluidization or not.

The analysis of fragmented counterparts involves scanning thin sections under the optical microscope and searching for fragmented counterparts with radius $r < r < r + \Delta r$ within a given area for a given magnification. During fault slip, fragmented counterparts will move away from one another. The total number of identifiable fragmented counterparts with radius r, $\Delta N_f(r)$, can be expressed as a percentage probability, $P(r)$, relative to the total number of clasts with radius r, $\Delta N_t(r)$. At this stage we define the parameter $R_f(r)$ as the fragmentation rate per clast per unit incremental fault slip, Δs. Therefore, the total number of fragmented counterparts produced during incremental fault slip is $N_t(r)R_f(r)\Delta s$. For a fragmented counterpart to remain identifiable, it must stay within a critical distance, d_c. The probability at which a pair of counterparts can be identified after fragmentation is proportional to $(d_c/v_r)/\Delta s$, where v_r is the mean residence 'time' for counterparts to stay within d_c. In summary, *Monzawa and Otsuki* [2003] show that the total number of identifiable fragmented counterparts is proportional to $N_t(r)R_f(r)\Delta s$ x $d_c/v_r\Delta s$, and the detection probability of fragmented counterparts is:

$$P(r) \equiv \frac{N_f(r)}{N_t(r)} \propto \frac{R_f(r)d_c}{v_r} \quad (1)$$

As noted above, $R_f(r)$ during fluidization is likely to be low, whereas in the frictional regime, it can be high due to grain-grain contact stresses. Additionally, v_r is likely to be considerably higher for the fluidization regime compared to the frictional regime because clasts are able to move more freely in a fluid phase. Consequently, $P(r)$ is expected to be small for fluidized fault rocks, but much larger for fault rocks produced during typical frictional deformation.

We measured $P(r)$ in 8 thin sections of breccia from the immediate footwall of the Zuccale fault (Figure 3.9). 4 thin sections were cut from 2 samples of breccia deformed by typical frictional mechanisms (PZ019, PZ020), and 4 thin sections were cut from 2 samples of grey breccia (PZ001 from variant C, PZ003 from variant B). Fragmented counterparts were analyzed over the size range 10μm to 4000μm, and 200-600 measurements were carried out on each thin section.

The P values of sample PZ020 are the highest, and reach 60-70% for clast diameters of ~1000μm, decreasing to <50% at clast diameters of <100μm. The average P value for this sample is 61%. Sample PZ019 also shows high values, with an average of 44.5%. Again, P values reach 50-70% for clast diameters of ~1000μm, decreasing to <40% for clast diameters of <100μm. In both cases, P clearly shows a strong clast size dependency. This is related to the fact that the tensile strength of clasts is strongly size dependent, and consequently the fragmentation rate $R_f(r)$ is also size dependent [*Monzawa and Otsuki*, 2003, *Otsuki et al.*, 2003]. This highlights the fact that when carrying out fragmented counterpart analysis it is necessary to consider clast sizes over as wide a size range as possible.

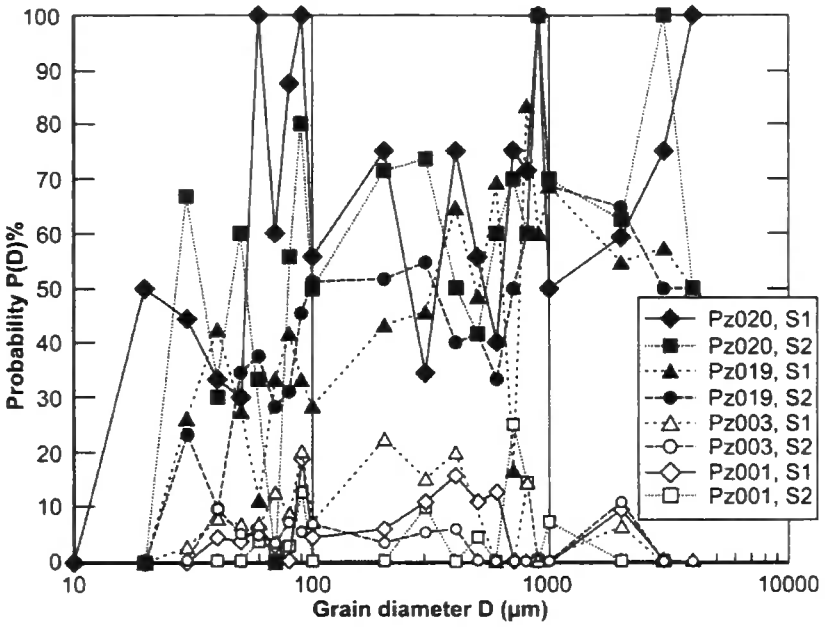

Figure 3.9) Detection probability of fragmented counterparts as a function of grain diameter (D) for 4 thin sections of frictional breccia (PZ019, PZ020) and 4 thin sections of grey breccia (PZ001, PZ003). Note the separation in the probability values between the frictional and grey breccias. See text for discussion.

In marked contrast, samples PZ001 and PZ003 show uniformly low P values and no obvious size dependency. The average values of P are 8% for PZ001 and 7.6% for PZ003. There are clearly 2 separate groups identifiable in our results, the first group consisting of PZ019 and PZ020, the second group consisting of PZ001 and PZ003.

3.4.2 Analysis of clast shape-preferred orientations

Field observations suggest that a mesoscopic shape-preferred orientation (SPO) of quartzite and quartz-mica schist clasts is visible in places within grey breccia variants A and C (Figure 3.6). This SPO is aligned roughly north-south on sub-horizontal (plan view) surfaces, but these surfaces only provide a 2-dimensional view of an inherently 3-dimensional SPO vector. To partly overcome this problem, we measured the SPO of clasts within thin sections of grey breccia cut in 3 orthogonal planes through oriented samples

collected at the outcrop. 6 oriented samples of grey breccia were collected from variants B and C (Figure 3.3). 3 orthogonal thin sections were cut from each sample, and each thin section is given reference indices to help with identification and analysis. We have followed the labelling convention of Hayman et al. [2004] and provide a description of this convention in the caption for Figure 3.11b. Using a BATY® Shadowmaster, thin sections were projected in plane polarized light at x1 magnification on to a large tracing table. All of the visible clasts within the breccias were traced at x1 scale. At least 300 clasts were traced in each thin section, although in most cases significantly more than 400 clasts were traced. The resulting images were scanned, processed and imported into ImageTool® textural analysis software (Figure 3.10). By tracing all the visible clasts, we eliminate clast selection bias that is usually implicit in manual measurements of SPO at the outcrop or on a grain-scale. Only clasts with an aspect ratio (L/S) greater than 1.5 were included in the final statistical analysis. Although this methodology forces us to restrict our analysis to x1 magnification, *Cladouhos* [1999b] found that the orientation of the SPO mean vector remains roughly constant at all magnifications.

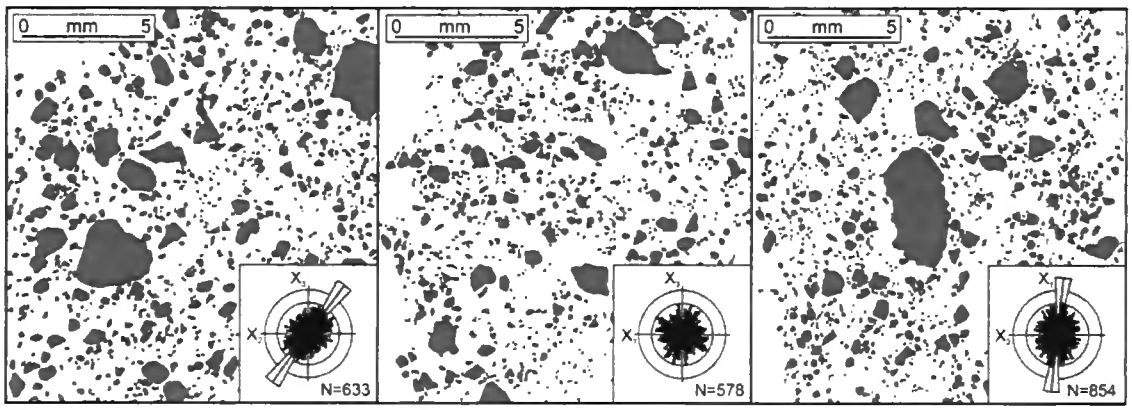

Figure 3.10) Examples of images which were used as input to ImageTool® textural analysis software, and the resulting rose diagrams calculated using EZ-ROSE [*Baas*, 2000]. The images represent tracings of 3 thin sections cut along orthogonal planes through one oriented sample. See text for discussion.

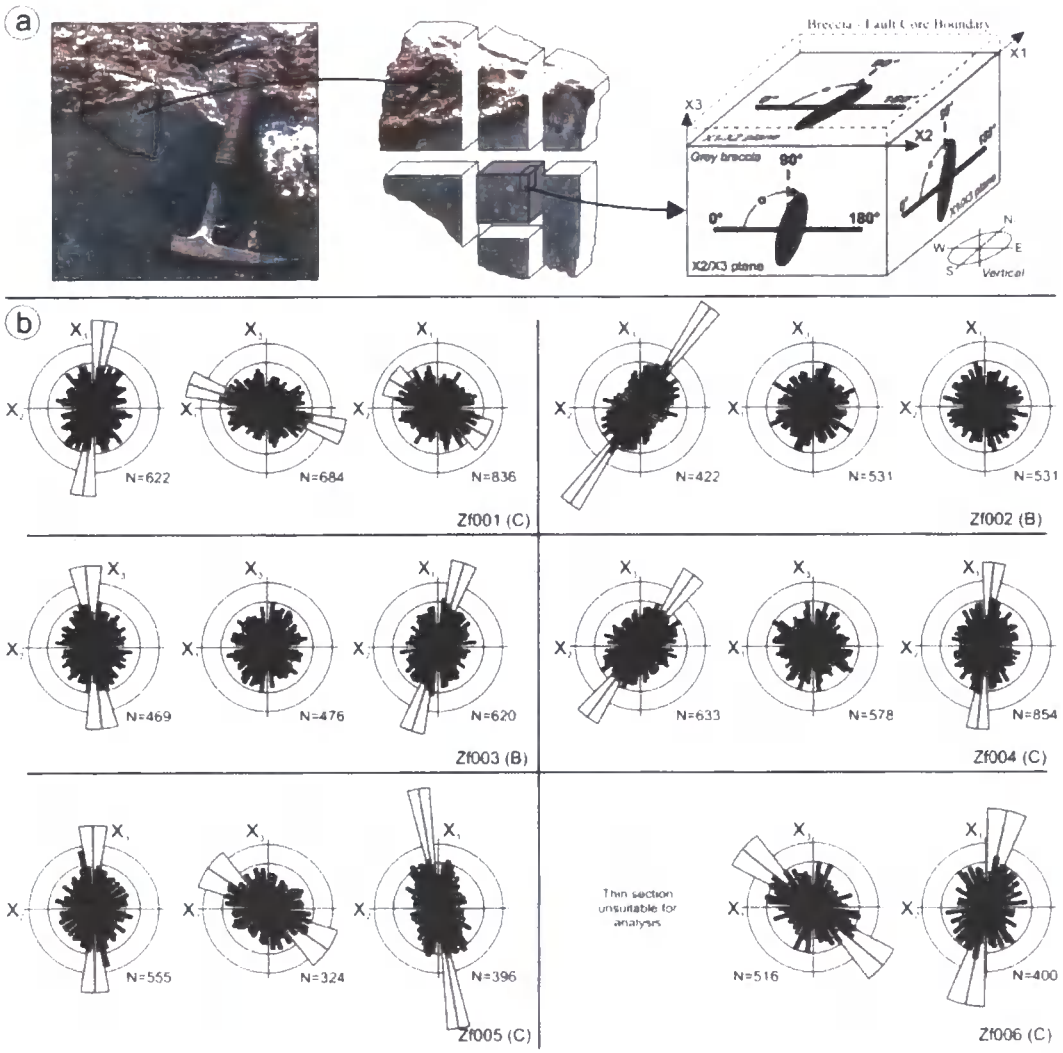

Figure 3.11a) Orientation conventions used for calculating grain-scale shape-preferred orientation (SPO). 3 orthogonal thin sections were cut from samples collected in the field. The X1/X2 thin section is sub-horizontal, and the edges of the thin section aligned with X1 (north-south) and X2 (east-west). The X2/X3 thin section is vertical, and the edges of the thin section aligned with X2 and X3. The X1/X3 thin section is vertical, and the edges of the thin section aligned with X1 and X3. α is the angle (0-180° measured clockwise) between the reference line indicated and the long-axis of the measured clast. **b)** Equal-area rose diagrams of the shape-preferred orientation of clasts within 6 samples of grey breccia (Zf001-Zf006; letters in brackets refer to the grey breccia variant from which the sample was taken). The rose diagrams were constructed using EZ-ROSE [*Baas*, 2000] and the data are plotted in 5° bin intervals. The outer circle represents 10% of the data. The grey sector in each rose diagram shows the mean vector orientation (black bisector line) and mean vector strength (length of grey sector). The angular confidence interval (95% confidence) is indicated by the width of the grey sector. N is the total number of clasts measured in each thin section. In all cases N>300, usually N>>400. Where no grey sector is present, the data has a uniform distribution and there is no statistically significant preferred orientation at 95% confidence. Measurements of all angles presented in Table 3.2 are clockwise from the reference line indicated in part a. One thin section from sample Zf006 was unsuitable for microscopic analysis.

The results of grain-scale SPO analyses are shown qualitatively as equal-area rose diagrams in Figure 3.11b. Quantitatively, the orientation of the mean vector, *M*, can be calculated using the semicircular vector mean [*Agterberg*, 1974, *Davis*, 2002]:

$$M = 0.5\tan^{-1}\left(\frac{\sum \sin 2\theta_i}{\sum \cos 2\theta_i}\right) \tag{2}$$

while the mean vector strength, *R*, is:

$$R = \frac{1}{N}\left\{\left(\sum \sin 2\theta_i\right)^2 + \left(\sum \cos 2\theta_i\right)^2\right\}^{\frac{1}{2}} \tag{3}$$

for *N* measurements with clast long axes oriented θ_i. Statistical results for all 6 samples of grey breccia are provided in Table 3.2.

	X2X3				X1X3				X1X2			
Sample	**M**	**R**	**L/S**	**N**	**M**	**R**	**L/S**	**N**	**M**	**R**	**L/S**	**N**
Zf001 (C)	97.08	0.19	2.04	622	17.73	0.16	1.92	684	30.6	0.08	1.89	836
Zf002 (B)	126	0.34	1.8	422			1.67	531			1.7	531
Zf003 (B)	84.35	0.16	1.84	469			1.89	476	107.6	0.19	1.84	620
Zf004 (C)	126.61	0.2	1.85	633			1.86	578	95.91	0.17	1.85	854
Zf005 (C)	89.392	0.181	1.82	555	34.64	0.12	1.70	324	80.48	0.358	1.84	396
Zf006 (C)					40.1	0.19	1.78	516	102.39	0.239	2.02	400

Table 3.2) Shape preferred orientation statistics for 6 samples (18 thin sections) of grey breccia (see Figure 11 for corresponding rose diagrams and orientation conventions). M, Mean vector orientation (α°); R, Mean vector strength; L/S, Mean aspect ratio; N, Number of clasts used in each thin section. Boxes are left blank where results were not statistically significant at 95% confidence.

The results indicate that there is a statistically significant SPO (at a 95% confidence level) of clasts present within the grey breccias. The SPO is strongest in the X1/X2 (horizontal) and X2/X3 (vertical, east-west) sections (Figure 3.11b). In the X1/X2 sections,

4 out of 6 samples show a vector strength varying between 0.17 and 0.36. In one sample (Zf002) there is no SPO in the X1/X2 section, and in another the vector strength is weak (Zf001). For those 4 samples that show a stronger SPO, the orientation of the mean vector is consistently ~north-south. Significantly, this vector orientation is similar to that observed in horizontal surfaces in the field, suggesting that the grain-scale measurements are reliable. In the X2/X3 sections, all 5 analyses show a vector strength varying between 0.16 and 0.34. One thin section was unsuitable for analysis because the entire slide was occupied by one large clast. All of the mean vector orientations are at a high angle (84°-127°) to horizontal. 3 out of 6 samples show a significant SPO in the X1/X3 sections (vertical, north-south). However, the vector strengths are generally weak (0.12-0.19) and subordinate to the SPO observed in the other 2 sections. In summary, the dominant shape-preferred orientations of clasts within the grey breccias are ~north-south in horizontal surfaces, and sub-vertical in east-west trending vertical surfaces.

3.5 Discussion

3.5.1 Generation of grey breccias

Several outcrop-scale observations suggest that the grey breccias have experienced fluidization. We define fluidization after *Monzawa and Otsuki* [2003] as "the state in which grains fly around with a mean free path like gaseous molecules". More precisely, we consider fluidization of grey breccias at Punta Di Zuccale to result in the constituent clasts experiencing particle transport in the presence of a fluid phase. Firstly, grey breccias preserve 'intrusive' relationships with foliated fault rocks lying within the core of the Zuccale fault. Secondly, the boundary between the grey breccias and the fault core is highly irregular and undulose in nature. Thirdly, fragments of altered fault core material

are found floating within the underlying grey breccias. Finally, a shape-preferred orientation of clasts is present within all variants of grey breccia. The grey breccias contain low values of fragmented counterparts, providing complementary grain-scale evidence that they experienced fluidization. In addition, the rounded to sub-rounded nature of clasts within the grey breccias has previously been suggested as indicating particle transport in the presence of a fluid [e.g. *Clark and James*, 2003].

Clasts of quartzite within the grey breccias are commonly overgrown by crystals of dolomite, and the red oxidized layer overlying the grey breccias is dominated by intergrowths of calcite and dolomite (Figure 3.7). Additionally, there are abundant carbonate hydrofracture veins that cross-cut the footwall and the core of the Zuccale fault. These observations indicate that the fluids which were circulating adjacent to the Zuccale fault contained CO_2. Sources of fluid and CO_2 may include mantle degassing, hydrothermal fluid flow associated with intrusion of the Porto Azzurro pluton, metamorphic fluid, or deeply-circulating meteoric fluid. Regardless of the source(s) of the fluids, recent experimental data [*Le Guen et al.*, 2007] has shown that CO_2-bearing fluids can cause rapid dissolution of carbonate and silicate minerals, particularly if the fluids are under high partial pressures.

3.5.1.1 Precursors to fluidization

Grey breccias are developed in the footwall of the Zuccale fault in an area that contains: a) Pre-existing frictional breccias; b) A north-south trending high-angle footwall fault (section 3.3.1); and c) A strongly foliated fault core dominated by phyllonites and foliated cataclasites (Figure 3.12a; section 3.2.2). Prior to fluidization, the migration of fluids containing CO_2 occurred that was controlled, at least in part, by fault and fracture

networks located in the footwall of the Zuccale fault (Figure 3.12a). We suggest that the fluids were forced to pond in structural traps or migrate laterally at the base of the Zuccale fault because of the likely impermeable nature of the foliated fault core [cf. *Faulkner and Rutter*, 2000, *Faulkner*, 2004]. At this stage, fluids were able to percolate along fracture networks within the pre-existing frictional breccias, causing dissolution of constituent quartzite and quartz-mica schist clasts, and eventually leading to a partial loss of cohesion within the frictional breccias.

3.5.1.2 Fluidization and the development of fluid overpressures

We interpret the clast-preferred orientations within the grey breccias as representative of a flow fabric generated by fluids moving through the breccias and causing transport and re-alignment of the constituent clasts. The SPO data are consistent with fluids moving upwards within the footwall from depth and spreading laterally in a north-south direction once they encountered the relatively impermeable fault core. This scenario would account for the sub-vertical SPO observed on vertical planes and the ~north-south SPO observed on horizontal planes.

All major hydrofracture veins that cross-cut the fault core link directly downwards into high-angle footwall faults, strongly suggesting that footwall structures act to focus and channel fluid flow (section 3.2.2, Figure 3.2). We believe that the SPO of clasts within the grey breccias can be explained by invoking fluidization during periodic slip events along high-angle footwall faults (Figure 3.12b). During such slip events, fault planes can experience dilation allowing short-term focused fluid flow at rates of up to several 10's cm's per second [*Eichhubl and Boles*, 2000, *Sibson*, 2000, *Sheldon and Ord*, 2005]. The overlying fault core in this case maintained its integrity, and its low-

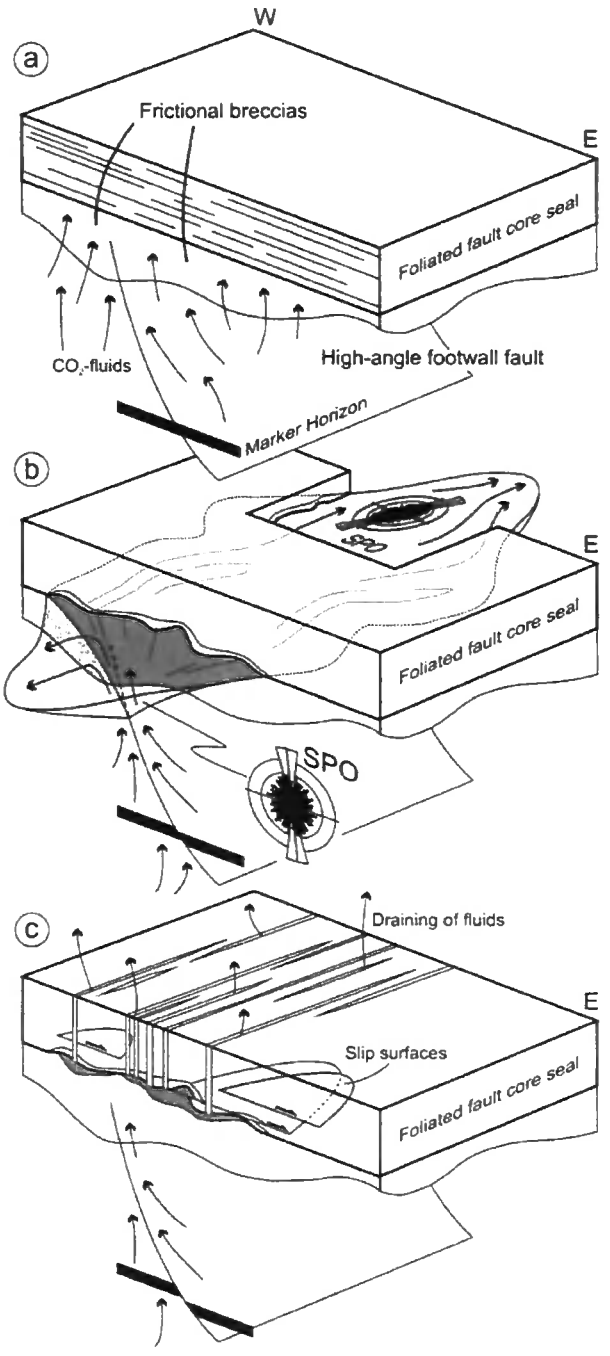

Figure 3.12) Generation of grey breccias, **a)** Precursors to fluidization: The Zuccale fault possesses a strongly foliated fault core which acts as a low-permeability seal to CO_2-bearing fluids migrating within the footwall. The fault core is underlain by a high-angle footwall fault. Fluids infiltrate pre-existing frictional breccias, leading to dissolution and a loss of cohesion, **b)** Fluidization: Periodic slip along high-angle footwall faults leads to focused and rapid fluid flow, causing fluidization of clasts within the frictional breccias. The fluid pulse spreads laterally as it encounters the fault core. Ponding of fluids, and deformation of the boundary, may occur during continued input of fluids, **c)** Hydrofracturing: Critical fluid overpressure leads to embrittlement within the core of the Zuccale fault, allowing fluids to drain from footwall to hangingwall. The fractures undergo healing processes returning to a low-permeability nature, allowing the fault-valve cycle to repeat.

permeability, by continuing to experience macroscopically-ductile deformation, meaning that the footwall-hosted fluid pulse was forced to spread laterally beneath the fault core, explaining the development of an SPO on horizontal (plan view) surfaces (Figure 3.12b). This scenario also satisfies a condition of *Bagnold's* [1954] experimental investigation into the generation of fluidized granular materials. He showed that the transition from frictional deformation to fluidization occurs when the Bagnold number decreases from infinity to a finite value (larger than 450), and that the most likely reason for this is a small decrease in the volume fraction of clasts. To explain this small decrease, *Monzawa and Otsuki* [2003] and *Otsuki et al.* [2003] invoked normal interface vibration [*Brune et al.*, 1993] and a resulting increase in the distance between fault wall rocks. In our model, a small decrease in the volume fraction of breccia clasts beneath the Zuccale fault could result directly from slip along high-angle footwall faults in one of two ways: 1) Fault plane dilation; or 2) The hangingwall of such faults would experience negative (tensional) static stress changes [*Nostro et al.*, 1997]. The most likely reason for ~north-south directed lateral flow beneath the fault core is enhanced permeability parallel to the σ_2 direction and the strike of the footwall fault [*Sibson*, 2000].

The ponding of fluids at the base of the Zuccale fault as a consequence of a waning in flow could result in the slow growth of fresh and undeformed carbonate within a thin alteration horizon overlying the grey breccias (Figure 3.4, 3.12b). This may also explain the fact that large clasts of quartzite and quartz-mica schist, now eroded to form a honeycomb texture, appear to have settled downwards towards the base of breccia variant C (Figure 3.5b). During successive slip events along the high-angle footwall fault, continued input of fluids would lead to a gradual increase in the concentration of CO_2, eventually leading to gas bubble formation. This would increase fluid overpressure, inducing deformation (warping and folding) of the boundary between the grey breccias

and the fault core, and promoting the incorporation of fault core material into the breccias (Figure 3.4, 3.5). Deformation of the boundary may also have been enhanced by reaction-weakening processes within the fault core, triggered by the presence of chemically active CO_2-bearing fluids.

3.5.1.3 Hydrofracturing and fault-valve behaviour

Once fluid overpressure in the footwall of the Zuccale fault reached a critical value (e.g. $Pf = \sigma_3+T$), this triggered hydrofracturing of the fault core and a significant increase in permeability, allowing fluids to drain from the footwall into the hangingwall (Figure 3.12c). We speculate that an increase in fluid overpressure also promoted movement along extensional slip surfaces within the fault core, because at Punta Di Zuccale, the concentration of these slip surfaces is greatest within the fault core immediately overlying the grey breccias. As described in section 3.3.1, grey breccia variant A is cross-cut along its upper margin by a low-angle slip surface. Draining of fluids from the footwall to the hangingwall resulted in a decrease in fluid overpressure. Hydrofractures and slip surfaces were mineralized, and the fault core underwent sealing processes returning to a low-permeability state [e.g. *Tenthorey and Cox*, 2006, *Gratier and Gueydan*, 2007]. The presence of multiple variants of grey breccia attests to the fact that fluid flow along the Zuccale fault was cyclic. The combined grey breccia-hydrofracture-slip surface association therefore represents an integrated example of fault-valve behaviour along low-angle normal faults.

3.5.2. Fluidized fault rocks and the seismic cycle

Fluidized fault rocks have been described on several occasions in the literature from a variety of tectonic settings. These include, but are not restricted to: decimeter-thick lenses of fluidized cataclasite found in association with pseudotachylytes within ancient accretionary complexes [*Rowe et al.*, 2005, *Ujiie et al.*, 2007]; centimetre-thick fluidized cataclasites and fault gouges from major intracontinental strike-slip faults in Japan [*Monzawa and Otsuki*, 2003, *Otsuki et al.*, 2003]; fluidized breccias found as meter-scale dyke- and pipe-like bodies around intrusions, faults and near ore deposits in eastern Australia [*Oliver et al.*, 2006] and South Africa [*Boorman et al.*, 2003]; and variably-sized fluidized breccias controlled by dilational fault jogs [e.g. *Clark and James*, 2003]. In each of these cases, the fluidized fault rocks are found as bodies that cross-cut wall rocks with sharp angular contacts, and are interpreted as forming due to single rapid events related to a sudden release, or increase, of fluid overpressure. The close link between fluidized cataclasites and pseudotachylytes found along exhumed subduction thrust faults prompted *Rowe et al.* [2005] and *Ujiie et al.* [2007] to suggest that this type of fluidized cataclasite may be used as an indicator of co-seismic slip.

We believe that fluidization of the grey breccias found at Punta Di Zuccale is related to the interactions between slip along the low-angle Zuccale fault (that accommodates ~6km of displacement), and slip along high-angle footwall faults (individually accommodating, at most, 5 meters of displacement). With respect to the Zuccale fault, we suggest that fluidization of the grey breccias is related to gradual build-ups of fluid overpressure in the footwall of the Zuccale fault during the interseismic stage of the earthquake cycle. It is important to note that build-ups of fluid overpressure were punctuated by co-seismic slip events along high-angle footwall faults, but not by slip

events within the low-angle core of the Zuccale fault itself. In other words, the fault-valve and seismic-cycle along the Zuccale fault were intimately related to, and dependent upon, the fault-valve and seismic cycle along the high-angle footwall faults.

During the interseismic stage along the Zuccale fault, the fault core likely possessed a low permeability and was deforming by mechanisms such as pressure-solution ('frictional-viscous') creep [*Bos and Spiers*, 2001, *Collettini and Holdsworth*, 2004]. Migration of CO_2-bearing fluids at this stage acted to corrode frictional breccias in the footwall. Both migration of fluids and corrosion of frictional breccias were essential precursors to fluidization. Build-ups of fluid overpressure in the footwall of the Zuccale fault, perhaps combined with reaction-weakening within the fault core, led to deformation and folding of the boundary between the grey breccias and the fault core. Only when fluid overpressure in the footwall obtained a critical value could hydrofracturing and brittle slip occur along the Zuccale fault. In our opinion, the size of the grey breccias, characteristics of the boundary with the overlying Zuccale fault core, and structural position *beneath* the fault core, are most compatible with fluidization having occurred during the interseismic period along the Zuccale fault. Comparison with the studies of fluidized fault rocks mentioned above suggests that fluidization of grey breccias during co-seismic slip along the Zuccale fault would have resulted in angular and sharp cross-cutting relationships with the fault core and local wall rocks, and/or formation of fluidized material formed by slip *within*, and emanating from, the core of the Zuccale fault.

The fluidization of grey breccias at Punta Di Zuccale occurred over areas of 10^{-3}-10^{-2} km^2. We suggested in section 3.5.1.3, based on field evidence, that attainment of critical fluid overpressures in the footwall of the Zuccale fault triggered the formation of low-angle extensional slip surfaces within the overlying fault core, and therefore it seems likely that the slip surfaces would possess dimensions roughly equal to those of the grey breccias.

We speculate that hydrofracturing and brittle slip processes, triggered by fluid overpressure, may represent co-seismic events along the low-angle Zuccale fault. Interestingly, microseismicity produced along the active Altotiberina low-angle normal fault occurs on rupture surfaces on the order of 10^{-3}-10^{-1} km^2.

Cowan [1999] concluded that, based on our current understanding, the only fault rocks that are unambiguous indicators of co-seismic slip are pseudotachylytes. More recently, *Han et al.* [2007a, 2007b] conducted high-velocity friction experiments and reported that at seismic slip velocities (up to 2m/s) calcite and siderite experienced thermal decomposition resulting in the formation of CO_2 + lime and CO_2 + magnetite, respectively. *Ujiie et al.* [2008] also suggested that stretching of fluid inclusions in calcite might indicate frictional heating associated with co-seismic slip. The present study shows that it is possible to identify distinctive fault rocks and fault structures that are characteristic of different parts of the seismic cycle. In order to do this, it is necessary to document geological evidence that constrains the likely fluctuations in fluid pressure that occur, as well as the ways in which different parts of the overall fault network (e.g. low angle fault core and high-angle footwall faults) may mutually interact through time. Ultimately this will lead to important advances in fault and earthquake mechanics, particularly along enigmatic structures such as low-angle normal faults.

Chapter 4

Interactions Between Low-Angle Normal Faulting and Plutonism in the Upper Crust: Insights from the Zuccale Fault, Elba Island, Italy

A modified version of this chapter was submitted to the Bulletin of the Geological Society of America in February 2008, and is currently in revision.

Abstract

Structural and geochemical data suggest that the Zuccale low-angle normal fault was fundamentally influenced on a regional- to microscopic- scale by the intrusion of upper-crustal igneous complexes, most notably the Porto Azzurro plutonic complex.

Detailed mapping of the kinematic relationships between the Zuccale fault and exposed parts of the Porto Azzurro pluton indicates that pluton emplacement and cooling occurred during movements along the Zuccale fault. Intrusion of minor dykes and sills related to the Porto Azzurro pluton resulted in short-lived pulses of thermal softening in the footwall of the Zuccale fault, which controlled the geometry of subsidiary fault and fracture networks. Structure contour analysis indicates that the Zuccale fault has a long-wavelength (7-10km) domal morphology. The overall shape, dimensions, and spatial location of the dome correlates with the likely sub-surface position of the Porto Azzurro pluton, and we propose that the most likely reason for doming was intrusion of the pluton by horizontal expansion followed by vertical inflation and roof uplift. Surface exposures of the Zuccale fault are not associated with any regional mylonitic fabrics, and it represents a domal fault morphology that developed entirely within the upper crust, during the late stages of fault movement, and as a direct result of pluton emplacement.

Oxygen, carbon, and strontium isotope analysis of carbonate vein material associated with the Zuccale fault indicates the presence of at least 2 distinct fluid sources. Syn-tectonic dolomite veins within the central core of the Zuccale fault were precipitated from a fluid of meteoric-hydrothermal origin, which interacted with upper crustal igneous bodies such as the Porto Azzurro pluton. Later calcite veins that cross-cut the fault core were precipitated from seawater that infiltrated downwards through the fractured footwall and hangingwall. Collectively, the isotopic data suggest a switch in fluid reservoir during progressive exhumation of the Zuccale fault. The presence of sub-horizontal tensile veins carrying both fluid signatures indicates that transient periods of near-lithostatic to supra-lithostatic fluid pressure may have developed throughout the exhumation history.

4.1. Introduction

More than three decades of research into metamorphic core complexes and their associated low-angle normal faults (also known as detachment faults) has shown that, in a large number of cases, such structures are broadly associated with igneous plutons or sill-like complexes that intrude the footwalls of the low-angle faults during extensional movements [*Davis*, 1983b, *Lister and Davis*, 1989, *Davis et al.*, 1993, *Lister and Baldwin*, 1993, *Daniel and Jolivet*, 1995, *Jolivet et al.*, 1998, *McCaffrey et al.*, 1999]. The magmatic bodies are commonly mylonitized close to their margins, suggesting that relatively short-lived intrusive events can promote thermal weakening and localized ductile deformation [*Lister and Baldwin*, 1993, *Pavlis*, 1996]. Broad correlations between core complex formation and magmatic activity are best described in the Basin and Range province [*Wright et al.*, 1974, *Holm*, 1985, *Gans et al.*, 1989] and the Cycladic islands in the Aegean Sea [*Faure et al.*, 1991, *Kumerics et al.*, 2005, *Ring and Collins*, 2005, *Brichau et al.*, 2007], but similar relationships have been documented in many other extensional settings worldwide. More recently, the discovery of gabbroic intrusions in the footwalls of oceanic core complexes points to a close and specific association between extension along low-angle normal faults and magmatism in these settings also [*Escartin et al.*, 2003, *Ildefonse et al.*, 2007]. Despite our improved understanding of the relationship between low-angle normal faults and magmatism, little is known about the direct structural consequences of magma emplacement, particularly in situations where final emplacement occurs in the upper 10km of the crust.

Fault rocks associated with large low-angle normal faults possess widespread evidence for extensive syn-tectonic fluid-rock interactions and the development of transiently high fluid pressures [Chapter 6; *Reynolds and Lister*, 1987, *Manatschal et al.*,

2000, *Collettini and Holdsworth*, 2004, *Hayman*, 2006, *Smith et al.*, 2008]. The development of elevated fluid pressures along low-angle normal faults may be a principal mechanism of fault zone weakening [*Axen*, 1992], so understanding fluid sources and fluid flow pathways is of fundamental importance in evaluating the long- and short-term mechanical behaviour of low-angle normal faults. Fluids derived from deep magmatic or metamorphic sources may be channelled up permeable fault zones from depth, facilitated by fracturing and brecciation of wall rocks within the upper crust, or highly anisotropic permeability within ductile shear zones in the mid- to lower-crust [*Reynolds and Lister*, 1987, *Wickham et al.*, 1993, *Floyd et al.*, 2001, *Famin and Nakashima*, 2005]. During exhumation, fluids derived from shallow meteoric or sedimentary sources are able to infiltrate faulted hangingwall strata, often resulting in late-stage formation of mineral deposits [*Reynolds and Lister*, 1987, *Losh et al.*, 2005]. Deciphering the sources of fault-controlled fluid flow in central Italy is particularly important, because a large source of mantle-derived CO_2 has been invoked to explain the time-space evolution of earthquake aftershock events during the 1997 Umbria-Marches seismic sequence [*Miller et al.*, 2004]. More recently, fault creep accompanied by the generation of microseismicity ($M<2.3$) along the Altotiberina low-angle normal fault has been speculatively attributed to an influx of mantle-derived CO_2 triggering transient fluid overpressures at depths of <10km [*Chiaraluce et al.*, 2007].

In this paper, we present a detailed case study from the Island of Elba, Italy, illustrating the geometric and kinematic consequences of pluton intrusion beneath the Zuccale low-angle normal fault. Additionally, we present carbon, oxygen, and strontium isotopic data to constrain the likely fluid sources that operated during faulting. Our results suggest that pluton intrusion fundamentally influenced the Zuccale fault at regional- to microscopic-scales.

4.2. Geological background

4.2.1. Regional geology

The northern Tyrrhenian-Apennine region of Italy has experienced two phases of deformation since the Cretaceous, both of which migrated from west to east [Figures 3.1, 6.1; *Elter et al.*, 1975, *Pauselli et al.*, 2006]. An early phase of Cretaceous to Quaternary compression related to collision between the Adria microplate and the European plate (Corsica-Sardinia block) was closely followed by Miocene-recent post-collisional extension, that continues at the present day in the Umbria-Marche region of Italy [Figures 3.1, 6.1; *Keller and Coward*, 1996, *Boncio et al.*, 1998, *Jolivet et al.*, 1998, *Hunstad et al.*, 2003, *Collettini et al.*, 2006b]. The eastward migration of post-collisional extension is recorded by a decrease in the ages of overlying syn-extensional sedimentary basins [Figures 3.1, 6.1; *Barchi et al.*, 1998, *Decandia et al.*, 1998]. Extension is also intimately associated with magmatism in both space and time, so that the ages of magmatic activity also decrease progressively from west to east. Typically, final emplacement of magmatic bodies occurs towards the end of the lifespan of extensional basins [*Serri et al.*, 1993, *Jolivet et al.*, 1998, *Collettini et al.*, 2006b].

Integration of geological and geophysical studies carried out over the past 10 years has shown that a majority of the post-collisional extension was likely accommodated by a series of 6 sub-parallel, east-dipping low-angle normal faults that penetrate the crust from surface levels to depths of ~15km [Figures 3.1, 6.1; *Carmignani and Kligfield*, 1990, *Keller et al.*, 1994, *Collettini and Barchi*, 2002]. Present-day extension occurs along the microseismically active Altotiberina low-angle normal fault, that slips at a rate of ~1mm/yr^{-1}, and along higher-angle synthetic and antithetic structures in its hangingwall [*Chiaraluce et al.*, 2007]. The Altotiberina low-angle normal fault slips in a stress field

characterised by a sub-vertical σ^1 and a sub-horizontal, SW-NE trending σ^3 [*Montone et al.*, 2004]. Eastwards migration of extension has progressively exhumed older, inactive low-angle normal faults in western Tuscany and the Tyrrhenian islands, that includes the Zuccale low-angle normal fault exposed on the Island of Elba [Figure 4.1; *Carmignani and Kligfield*, 1990, *Jolivet et al.*, 1998, *Rossetti et al.*, 1999, *Gueydan et al.*, 2003, *Collettini and Holdsworth*, 2004]. Extension to the west of the Umbria-Marche region has been active for a sufficiently long time to have affected the regional geophysical characteristics: the Tyrrhenian Moho is at a depth of 20-25km, regional heat flow is high (80-120mW/m^2), magmatism is widespread, and the area is characterised by a long-wavelength positive Bouger gravity anomaly [~30-40mGals; *Barchi et al.*, 1998, *Collettini et al.*, 2006b]. The extended sector of northern Italy is characterised by an unusually high flux of non-volcanic CO_2 (up to ~0.8 tonnes day^{-1}km^{-2}), around 40% of which is thought to be derived from a deep mantle source [*Chiodini et al.*, 2000, *Minissale et al.*, 2000, *Minissale*, 2004]. This is equivalent to ~10% of the global flux of CO_2 emitted from all of the sub-aerial volcanoes on Earth [*Kerrick*, 2001].

At least 4 large plutonic complexes have been documented in the northern Tyrrhenian Sea (part of the larger Tuscan Magmatic Province), including the Capanne and Porto Azzurro plutons on Elba, and the plutons that dominate the islands of Montecristo and Giglio [*Rossetti et al.*, 1999, *Dini et al.*, 2002, *Rocchi et al.*, 2002, *Gagnevin et al.*, 2004, *Dini et al.*, 2007, *Rossetti et al.*, 2007]. The high heat fluxes (locally exceeding 1000mW/m^2) around the Lardarello and Monte Amiata geothermal fields in western Tuscany have been attributed to the intrusion of multiple plutonic complexes at depths of <5km in the last 3.8Ma [*Dini et al.*, 2005, *Rossetti et al.*, 2008]. All of the exposed plutons are spatially and temporally associated with top-to-the-east movements along low-angle normal faults [*Barchi et al.*, 1998, *Jolivet et al.*, 1998, *Collettini et al.*, 2006b].

Additionally, shallow crustal reflectors that may represent active fault zones have been identified at Lardarello and Monte Amiata [e.g. *Brogi et al.*, 2005].

4.2.2. The Island of Elba and the Zuccale fault

Elba comprises a series of stacked thrust sheets that formed during late Cretaceous-early Miocene compression (Figure 4.1). *Trevisan et al.* [1967] recognized 5 thrust 'Complexes', composed of diverse lithological units that have continental ("Tuscan", Complexes I-III) or oceanic ("Ligurian", Complexes IV-V) affinities, all of which currently dip shallowly to the west (Figure 4.1). The entire thrust stack is offset ~6km eastwards by the shallowly east-dipping Zuccale fault, so that on Elba there is a clear repetition of Complexes II-V in the centre and in the east of the island [Figure 4.1; *Trevisan et al.*, 1967, *Keller and Pialli*, 1990, *Keller et al.*, 1994]. Complex V was intruded by the 8Ma Capo Bianco aplite and the 7.95Ma Portoferraio granite porphyry prior to extensional movements along the Zuccale fault [*Dini et al.*, 2002], and hence most (if not all) of the displacement across the Zuccale fault must have been accommodated after 7.95Ma. The fault can be recognized in seismic profiles crossing mainland Italy [e.g. CROP 03 profile; *Barchi et al.*, 1998] and also from seismic interpretations offshore, around 20km to the south of Elba [*Keller and Coward*, 1996]. In both cases it appears to dip ~15°E from the surface to depths of ~15km, with the Punta Ala and Montecristo basins lying in the immediate hangingwall of the fault in the region between Elba and mainland Italy [*Pascucci et al.*, 1999]. All other crustal-scale low-angle normal faults in the northern Apennines emerge near the surface at the western margins of similar extensional basins, and are known to have controlled the growth of such basins [e.g. Grosseto basin, Val D'Orcia basin, Siena Radicofani basin, Val di Chiana basin, Tiber basin; *Decandia et al.*,

1998, *Collettini and Barchi*, 2002, *Collettini et al.*, 2006b, *Pauselli et al.*, 2006; Figure 6.1]. The age range of syntectonic sediments deposited in the Punta Ala and Montecristo basins suggests that all extensional activity in the area had ceased by ~4Ma [*Keller and Coward*, 1996, *Pascucci et al.*, 1999].

4.2.3. Magmatism on Elba

Magmatic activity on Elba occurred between ~8.5Ma-5.9Ma and involved crustal-, hybrid-, and mantle-derived melts that reflect progressive thinning of the lithosphere during post-collisional extension [*Dini et al.*, 2002, *Rocchi et al.*, 2002]. Two large plutonic complexes are of particular interest because their emplacement must overlap in

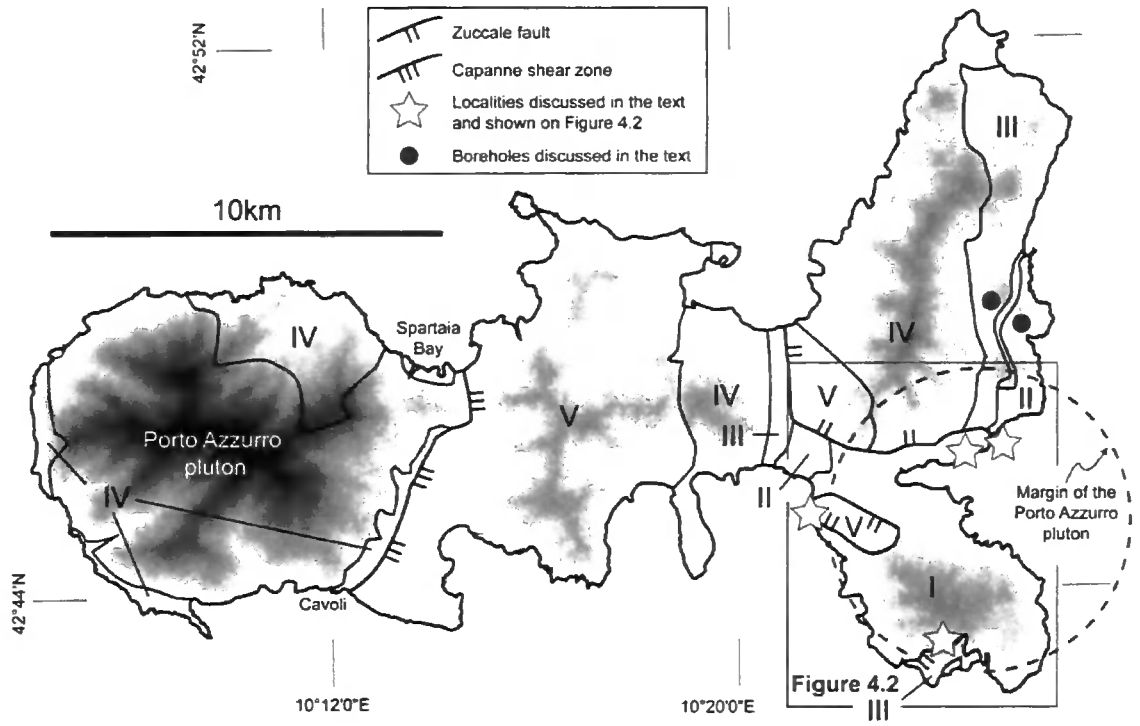

Figure 4.1) Simplified geological map and digital elevation model of Elba, highlighting the distribution of Complexes I-V and the locations of the Zuccale fault and Capanne shear zone, after *Trevisan et al.* [1967] and *Daniel and Jolivet* [1995]. The map also shows the location of Figure 4.2, the localities discussed in the text and shown on Figure 4.2, and the locations of 2 boreholes to the north of Figure 2 [from *Bortolotti et al.*, 2001a]. For the regional geological context, and the location of Elba in the northern Tyrrhenian Sea, consult Figures 3.1 and 6.1.

space and time with movements along top-to-the-east detachment faults: the Capanne pluton that dominates the western third of Elba, and the Porto Azzurro pluton that lies at shallow depths beneath the eastern third of Elba (Figures 4.1, 4.2).

Based on whole-rock Rb-Sr plagioclase-K-feldspar-biotite cooling ages, the Capanne monzogranite pluton was emplaced at c.6.9Ma [*Dini et al.*, 2002] as a composite, sheeted pluton with an overall laccolithic geometry [*Dini et al.*, 2007]. Metamorphic reactions preserved in the thermal aureole surrounding the pluton, coupled with geometric reconstructions of the overburden thickness at the time of emplacement, suggest that final emplacement occurred at ~4.5km depth [*Dini et al.*, 2002, *Rocchi et al.*, 2008]. *Daniel and Jolivet* [1995] used detailed structural analysis to suggest that intrusion of the pluton was accommodated by high-temperature, top-to-the-east detachment faulting along its eastern margin, an inference that is supported by measurements of the magnitude and anisotropy of magnetic susceptibility within the pluton [Figure 6.1; *Bouillin et al.*, 1993].

Much less is known about the Porto Azzurro monzogranitic pluton, which was intruded beneath south-east Elba at c.5.9Ma [*Saupe et al.*, 1982, *Maineri et al.*, 2003]. The Porto Azzurro pluton is poorly exposed, but a significant size is suggested by the extent of thermally metamorphosed Complex I schists around Monte Calamita (Figures 4.1, 4.2). *Duranti et al.* [1992] used petrological data to show that thermal metamorphism occurred at maximum pressures of ~2kbars, suggesting a final emplacement depth of <6km. Several important pieces of information are available that allow some additional constraints to be placed on the shape and dimensions of the pluton (Figure 4.2): 1) The pluton outcrops at the surface within Complex I schists over a small area 2km NNE of Punta Di Zuccale and 1km NW of Baia Di Mola; 2) two small isolated stocks that are related to, or part of, the pluton are found on the west side of Capo Bianco; 3) The pluton has been encountered in 4 boreholes to the north of Spiagge Nere at depths of between -20 and -320m [*Bortolotti et*

al., 2001a]. The boreholes suggest that the pluton roof becomes deeper to the north, and that it typically lies a few tens to a few hundreds of metres beneath the Zuccale fault. Two additional boreholes ~5km north of Spiagge Nere failed to encounter the pluton at depths of up to 500m (Figure 4.1), suggesting that the northern margin of the pluton lies several km to the north of Spiagge Nere. In addition, 1 borehole encountered monzogranite thought to be part of the pluton at a depth of -25m on the east side of Monte Calamita; 4) A dense network of tourmaline-bearing dykes and sills related to the Porto Azzurro pluton are present within Complex I basement schists along the east side of Monte Calamita, around La Serra, and around Porto Azzurro, suggesting that the pluton lies relatively close to the surface in all of these areas [*Dini et al.*, 2008]. Overall, the Porto Azzurro pluton seems to have a diameter of ~10km, similar in size to the better exposed Capanne pluton. Comparison with other large, late-Miocene to recent plutons in the northern Tyrrhenian area further suggests that the Porto Azzurro pluton is likely to have a circular or sub-circular shape, speculatively shown in Figures 4.1 and 4.2 [*Westerman et al.*, 1993, *Acocella and Rossetti*, 2002, *Dini et al.*, 2002, *Rocchi et al.*, 2002, *Dini et al.*, 2007, *Rossetti et al.*, 2008].

4.3. Methodology

To characterise the relationships between the Porto Azzurro pluton and the Zuccale fault, we initially carried out structure contour analysis of exposed surface traces of the Zuccale fault, based on the mapping of *Trevisan et al.* [1967], and new mapping carried out by the authors on the south side of Monte Calamita. The Porto Azzurro pluton itself is poorly exposed, but small igneous stocks, dykes, and sills, which are directly related to the Porto Azzurro pluton are well exposed around the town of Porto Azzurro, where they

intrude Complex I basement schists. We mapped several exposed igneous bodies and their basement host rocks at scales of 1:100 or 1:200, and supplemented the mapping with detailed structural analysis and petrographic examination of thin sections.

Carbon, oxygen, and strontium isotope analyses were carried out on two types of carbonate vein material associated with the Zuccale fault. All of the samples were collected from the Punta di Zuccale outcrop (Figure 4.2), where the central core of the Zuccale fault is well exposed (Chapters 2, 6). Powdered carbonate was prepared from hand samples and thick (100μm) sections using a dentist's drill or a high-resolution micromill, respectively.

Stable isotope analyses were performed using standard techniques in the Northern Centre for Isotopic and Elemental Tracing at Durham University, using a gas-bench coupled to a ThermoFinnigan MAT 253 mass spectrometer. Carbonate powders were placed in individual vials and reacted with phosphoric acid at 60°C in the gas bench. Typical sample size was ~150 micrograms, and the 1σ precision for $\delta^{13}C$ and $\delta^{18}O$ is <0.1‰. Standardisation was obtained by analysing standards NBS-18 and NBS-19, and all the data were corrected such that NBS-18 and NBS-19 gave values equivalent to those approved by the International Atomic Energy Agency (IAEA). All results are reported in the familiar per mil (‰) notation relative to the standards V-PDB (Vienna Pee-Dee Belemnite, for carbon isotopes) and V-SMOW (Vienna Standard Mean Ocean Water, for oxygen isotopes).

Sr isotope analyses were performed on carbonate powders that were repeatedly dissolved in nitric acid at temperatures of 60°-120°C. Residual material that remained after dissolution was removed by centrifuging for 15 minutes. Strontium was separated using standard column chemistry procedures. $^{87}Sr/^{86}Sr$ ratios were measured using a ThermoFinnigan MAT Neptune ICP-mass spectrometer in the Northern Centre for

Isotopic and Elemental Tracing at Durham University. Standardisation was obtained by analyzing NBS-987 which yielded $^{87}Sr/^{86}Sr = 0.710269 \pm 0.0000085$ (1σ precision). All the data were normalized to an accepted NBS-987 value of 0.710240. One standard was analyzed for every 5 samples. Age corrections for radiogenic decay of strontium are negligible in the case of the Zuccale fault, and thus were ignored.

4.4. Results

4.4.1. Regional geometry of the Zuccale fault

Structure contours constructed for the Zuccale fault show a systematic change in the orientation of the fault that correlates closely with its spatial position on Monte Calamita, and also the likely position of the underlying Porto Azzurro pluton (Figure 4.2). At Punta Calamita, the Zuccale fault dips steeply to the south (40°-70°) and separates Complex I schists from limestones and skarn deposits belonging to Complex III (Figure 4.2). It is likely that the southern margin of the Porto Azzurro pluton runs broadly east-west through this area. To the east of Punta Di Zuccale, close to the likely western margin of the Porto Azzurro pluton, the Zuccale fault separates Complex I from Complex V and dips moderately to the west or north-west (10°-30°; Figure 4.2). To the north of La Serra, the fault separates Complex I from Complexes IV and V and dips steeply NNE (Figure 4.2). Here, the fault is exposed at elevations of up to 130m. The increase in the elevation of the exposed fault trace between the Punta Di Zuccale area and La Serra correlates with the presence of two outcrops of the Porto Azzurro pluton exposed at elevations of between ~40-100m, suggesting that the pluton roof may be significantly higher here. At Capo Bianco and Spiagge Nere, the Zuccale fault appears to preserve a primary dip of ~10-15° east or NE. Borehole records to the north of Spiagge Nere [*Bortolotti et al.*, 2001a] suggest

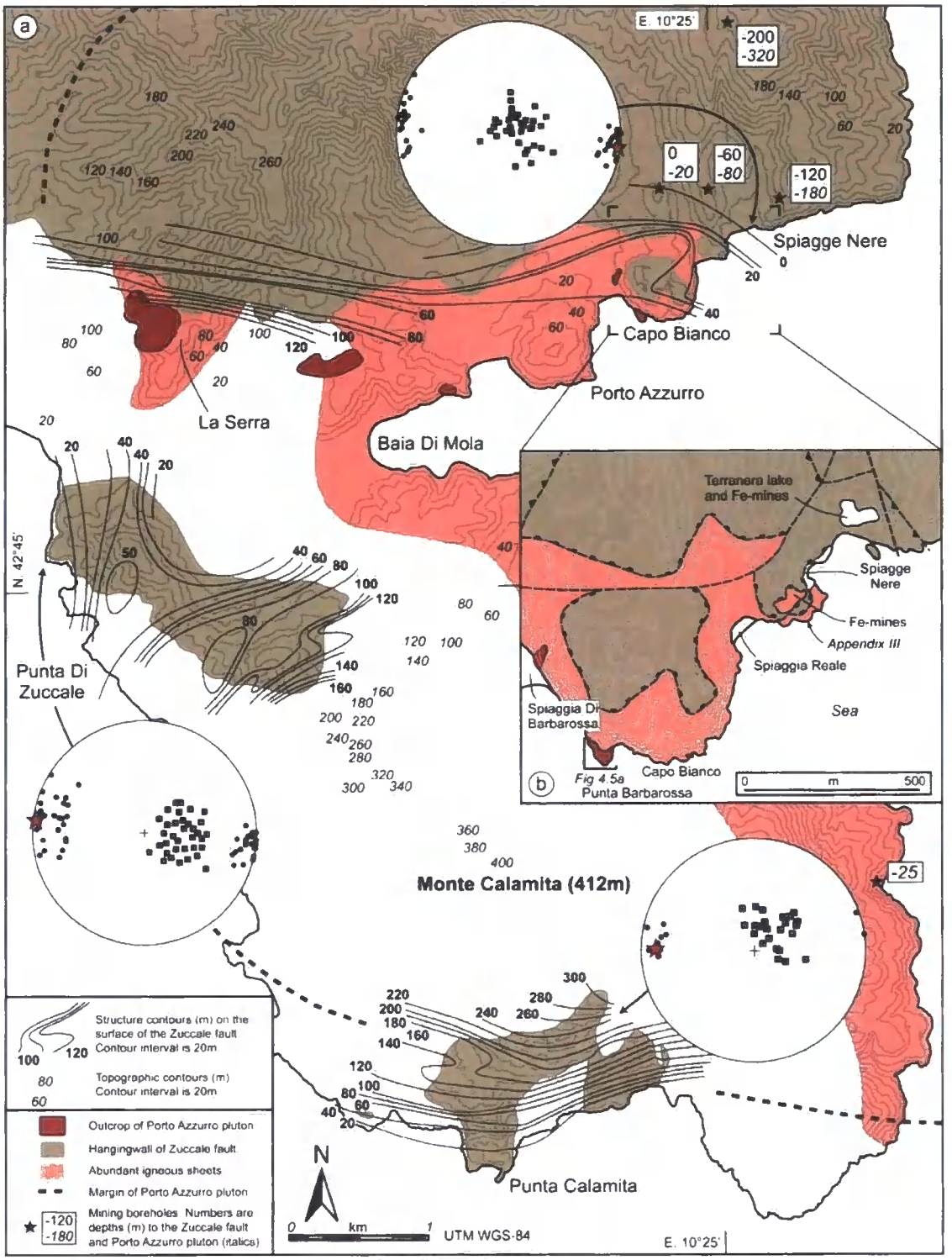

Figure 4.2a) Structure contour map constructed for the surface of the Zuccale fault. Hangingwall units are undifferentiated and their distribution is based on the mapping of *Trevisan et al.* [1967], *Bortolotti et al.* [2001a], and new mapping by the authors on the south side of Monte Calamita. The footwall of the Zuccale fault is uncoloured except where it contains abundant igneous sheets [distribution after *Trevisan et al.*, 1967]. Mining borehole data is from *Bortolotti et al.* [2001a]. Stereonets show the orientation of slickenlines (circles, mean values shown by red stars) and poles to foliation (squares) from the central core of the Zuccale fault in 3 areas discussed in the text. In

the Spiagge Nere area the mean foliation plane is 029°/14° W and the mean lineation (red star) is 2°-098°. **b)** Detailed geological map of Spiagge Nere and Capo Bianco, showing the locations of Figures 4.5 and the map included in Appendix III.

that the fault surface dips broadly to the north, and deepens towards the northern margin of the pluton. In all the areas we have studied (Punta Di Zuccale, Capo Bianco and Spiagge Nere, Capo Calamita) the Zuccale fault possesses shallowly-plunging lineations with a mean azimuth of ~90-100°/270-280° (Figure 4.2), and abundant top-to-the-east shear sense indicators.

4.4.2. Structure of minor igneous bodies related to the Porto Azzurro pluton

4.4.2.1. Igneous dykes and sills

Complex I basement schists in the footwall of the Zuccale fault carry a strong foliation, defined principally by a finely-spaced (sub-mm) compositional banding of quartz, biotite and muscovite horizons. The foliation strikes ~north-south and dips moderately to the west, and is thought to be related to pre-Mesozoic ductile deformation (Figure 4.3a). The foliation is widely overgrown by post-tectonic porphyroblasts of anhedral cordierite + biotite ± muscovite ± k-feldspar related to intrusion of the Porto Azzurro pluton [*Duranti et al.*, 1992, *Bortolotti et al.*, 2001a, *Garfagnoli et al.*, 2005]. The basement schists are intruded by igneous dykes and sills (herein referred to as igneous 'sheets') varying in thickness from a few mm to several meters. Intrusion of such igneous sheets appears to have occurred broadly parallel to the host rock foliation (Figure 4.3b), although in detail both concordant and discordant geometric relationships are common. All of these intrusions are most likely related to the underlying Porto Azzurro pluton [*Dini et al.*, 2008]. We have not found any igneous sheets related to the Porto Azzurro pluton within the core of the Zuccale fault, or anywhere within its hangingwall.

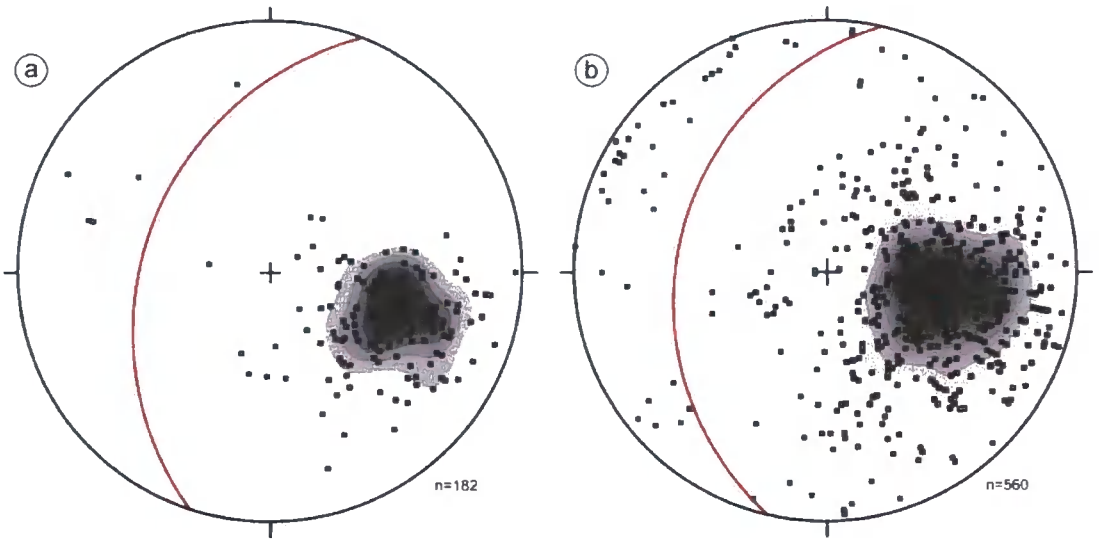

Figure 4.3a) Stereonet showing poles to the basement foliation at Spiagge Nere and Capo Bianco. Mean foliation plane (red great circle), 021°/44° W, **b)** Stereonet showing poles to igneous sheets intruded in to Complex 1 basement schists at Spiagge Nere and Capo Bianco. Mean igneous sheet (red great circle), 012°/40° W.

Many of the igneous sheets contain aligned, acicular tourmaline crystals (Figure 4.4a). Two dominant orientations of tourmaline-bearing igneous sheets are apparent: one set that dips sub-vertically and trends NNE-SSW, and one set that dips moderately to the west and trends NNE-SSW (parallel to the host rock foliation; Figure 4.4b). Both sets contain tourmaline crystals that plunge gently and are oriented ESE-WNW (Figure 4.4c), that we interpret as the direction of opening experienced during emplacement. Hence, the sub-vertical set of igneous sheets opened as tensile fractures, whilst the moderately west-dipping set opened as hybrid extensional-shear fractures. The ESE-WNW opening direction is similar to the transport direction recorded by slickenline lineations within the Zuccale fault (Figure 4.2).

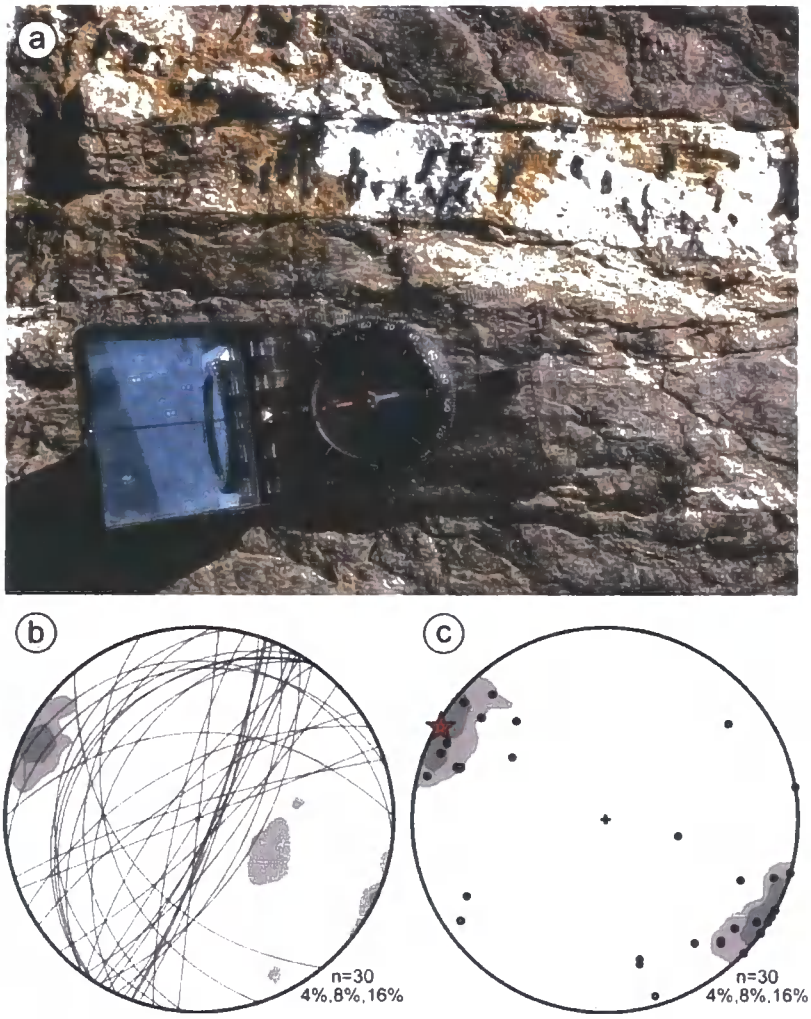

Figure 4.4a) Photograph of a minor igneous sheet which contains aligned, acicular tourmaline crystals, **b)** Stereonet showing great circles representing igneous sheets which contain strongly aligned tourmaline needles. Poles to igneous sheets are contoured, and display two dominant point maxima, representing a steeply east-dipping set and a moderately west-dipping set. **c)** Stereonet showing the orientation of acicular tourmaline needles from within the igneous sheets. Mean tourmaline lineation (red star), 2°-300°.

4.4.2.2. Igneous stocks

The footwall of the Zuccale fault is intruded by at least 2 isolated stocks of monzogranite that outcrop at Spiaggia Di Barbarossa and Punta Barbarossa (Figure 4.2b). The Barbarossa stock occupies a minimum area along the coast of ~50x50 meters, and lies approximately 40 vertical meters below the outcrop trace of the Zuccale fault (Figures

4.2b, 4.5a). The stock contains weakly aligned K-feldspar megacrysts up to 15 cm in length, set within a finer-grained groundmass of K-feldspar, quartz, biotite ± tourmaline. The stock contains a weak sub-horizontal solid-state foliation defined by a compositional banding of quartz, feldspar, and biotite horizons mm's in thickness, and weak sub-horizontal solid-state stretching lineations defined by an alignment of platy biotite crystals (Figure 4.5ai). The mean lineation plunges 9° towards 271°. The stock is crosscut by a suite of aplite dykes that vary in thickness from a few mm's to ~50cm (Figure 4.5a). The aplite dykes strike uniformly ~north-south, dip moderately to the west, and generally have sharp planar contacts with the host monzogranite (Figure 4.5aii). The orientation of the aplite dykes appears to have been controlled by the moderately west-dipping foliation within the surrounding basement schist host rocks.

Intrusion of the monzogranite stock, development of a pervasive solid-state foliation, and intrusion of the aplite dykes was followed by the development of narrow solid-state mylonitic shear zones, 15 of which are recognised at the outcrop (Figure 4.5a). Shear zones are developed within the host monzogranite, but in a majority of cases they exploit the intrusive contacts between the aplite dykes and the monzogranite stock, that represent a strong rheological anisotropy [Figure 4.5b; *Mancktelow and Pennacchioni*, 2005]. As the aplite dykes dip uniformly to the west (Figure 4.5aii), the later mylonitic shear zones also strike ~north-south and dip moderately to the west (Figure 4.5aiii). The shear zones are typically mm's to a few cm's in thickness, and are associated with a strong mylonitic foliation and approximately down-dip, east-west trending stretching lineations, defined by elongate quartz and biotite crystals (Figure 4.5c). Shear sense is uniformly top-to-the-west, defined by offset K-feldspar megacrysts and asymmetric sigmoidal foliations (Figure 4.5b). Although the top-to-the-west shear sense is opposite to that recorded in the central core of the Zuccale fault, it most likely reflects the orientation of the pre-existing

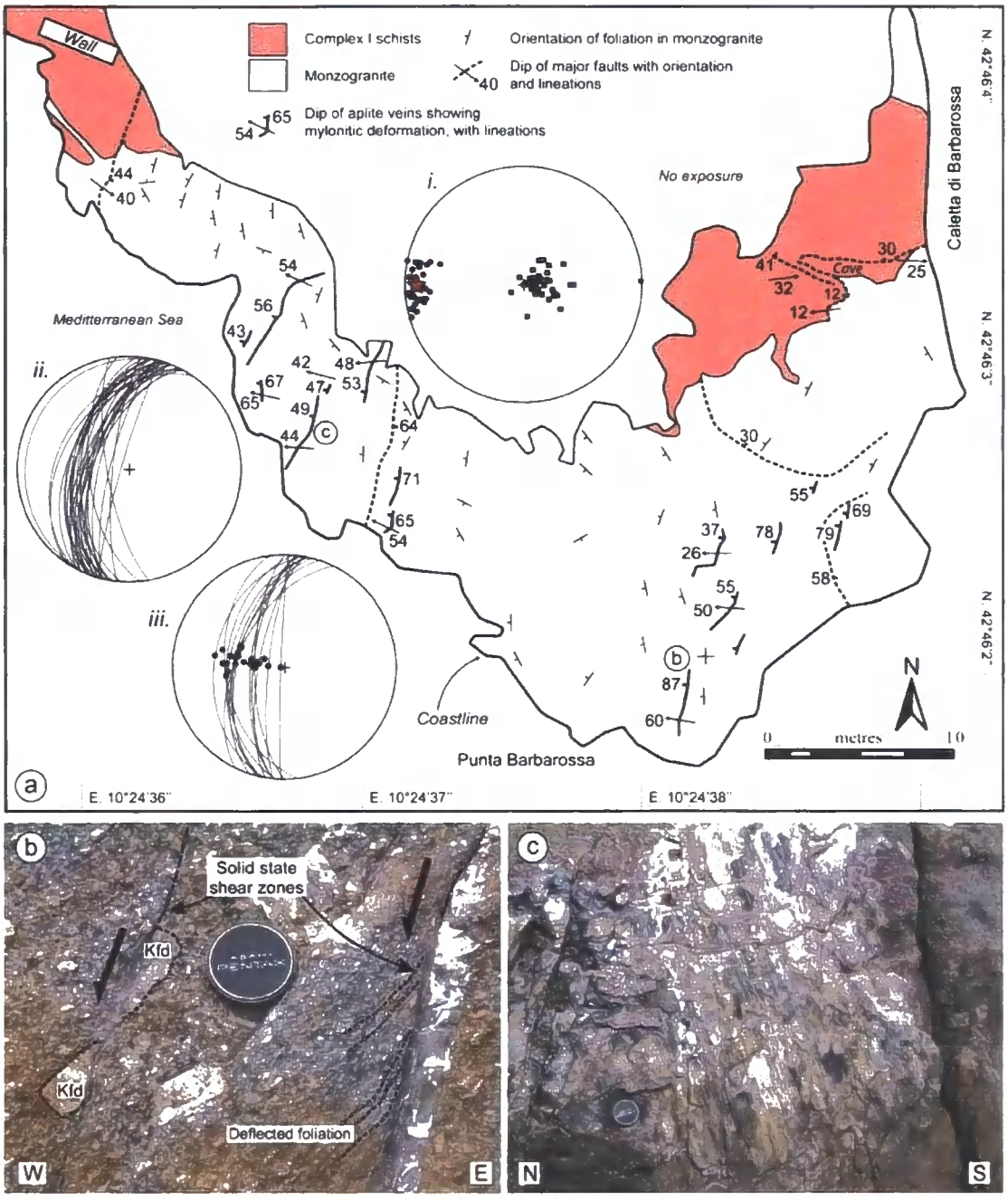

Figure 4.5a) Map of the Barbarossa monzogranite stock and surrounding host rocks, showing the location and orientation of solid state mylonitic shear zones, and the general trend of solid-state foliations within the stock. Stereonets show: i) poles to solid-state foliations within the stock (squares), and solid-state lineations (circles). Mean foliation, 000°/7° W. Mean lineation (red star), 7°-270°; ii) the orientation of aplite veins within the stock. Mean aplite vein, 016°/56° W; iii) the orientation of mylonitic shear zones and associated stretching lineations. Mean mylonitic shear zone, 009°/58° W. Mean lineation, 52°-278°, **b)** Photograph of two minor shear zones within the monzogranite stock. Shear zone to left offsets a K-feldspar megacryst indicating top-to-the-west shear sense. Shear zone to right formed preferentially along the western margin of a late-stage aplite vein. Deflection of the external foliation indicates a top-to-the-west shear sense, **c)** Photograph of down-dip mylonitic stretching lineations within a solid-state shear zone at the margin of a west-dipping aplite vein.

aplite dykes. The ~east-west extension direction within the shear zones (mean azimuth of lineations = 278°) is exactly the same as that recorded by slickenline lineations within the Zuccale fault at Spiagge Nere and Capo Bianco (mean azimuth of 098°).

On a grain-scale, the mylonitic foliation within the shear zones is defined by a compositional banding of quartz, K-feldspar, and biotite. Biotite is stable, and no retrogression to chlorite appears to have occurred. Magmatic quartz is pervasively recrystallised and occurs in elongate ribbons of uniform grain size (50-100μm) that possess no obvious grain-shape- or crystallographic-preferred orientation (determined by insertion of a sensitive tint plate). Plagioclase and K-feldspar typically occur as elongate porphyroclasts, and as fine-grained dynamically recrystallised products within the surrounding matrix. Large relict porphyroclasts are crosscut by intragranular fractures lined with recrystallised quartz or fine-grained muscovite. Deformation-induced flame perthite microstructures within K-feldspar are widely developed and, coupled with the other microstructural observations, suggest that deformation within the shear zones occurred at upper greenshist to lower amphibolite facies conditions [~450°C-500°C; *Hirth and Tullis*, 1992, *Passchier and Trouw*, 2005].

In the following section, we focus on ascertaining the geometries, linkages and kinematics of subsidiary fault networks developed in the immediate footwall of the Zuccale fault in a region directly overlying the Porto Azzurro pluton. We highlight evidence pointing to the development of numerous low- and high-angle fault arrays in the basement in this area and investigate field constraints concerning the timing of this faulting relative to plutonism. The best regions in which to study these relationships lie around Capo Bianco and Spiagge Nere (Figure 4.2b), where 100% exposed coastal sections are preserved in the immediate footwall region of the Zuccale fault.

4.4.3. Footwall faulting patterns during igneous intrusion

The central core of the Zuccale fault is characterized by broadly east-west trending lineations (Figure 4.2a) and abundant top-to-the-east shear sense indicators including asymmetric folding of the fault rock foliation and the development of Riedel shear fabrics. Appendix III includes a detailed map, cross section, and short description of representative faulting patterns in the immediate footwall of the Zuccale fault in the area between Spiagge Nere and Spiaggia Reale (location in Figure 4.2b). In this area, both the footwall and the hangingwall of the Zuccale fault are extensively faulted.

The hangingwall of the Zuccale fault is cut by steep normal faults, many of which have a listric geometry and sole directly into the main low-angle detachment, contain east-directed dip-slip lineations, and typically have displacements of tens of cm's [*Collettini and Holdsworth*, 2004].

The footwall of the Zuccale fault at Spiagge Nere and Capo Bianco contains a complex network of linked, predominantly extensional faults that have individual fault offsets ranging from a few mm's to several meters. Extension values in the footwall are variable, but the high density of faulting means that, locally, magnitudes of extension up to 60% occur over distances of 25 meters. Extensional footwall faults can be subdivided into two clear sets based on their orientation and fault rock associations: 1) faults and semi-brittle shear zones that are broadly sub-horizontal in orientation, and; 2) faults that dip moderately to steeply to the east. There is an absence of footwall faults with intermediate dips.

4.4.3.1. Sub-horizontal footwall faults

Sub-horizontal faults have a mean orientation of 006/10° W, which is broadly parallel to the current orientation of the Zuccale fault at these particular outcrops (Figure 4.6,

Appendix III). The faults are typically represented by discrete fault planes or wider (centimetres to tens of centimetres) semi-brittle shear zones composed of finely comminuted basement material (Figure 4.7). They have displacements of up to a few tens of centimetres. Sub-horizontal faults are easily recognisable, as they generally cut across the moderately west-dipping basement foliation (Figure 4.7a-d). Most faults are laterally discontinuous and occur within anastomosing sets, although some of the discrete fault planes are laterally continuous over several metres. Kinematic indicators are poorly developed, but the shear sense is consistently top-to-the-east, defined by deflections of minor igneous sheets within the surrounding basement, and by deflections of the basement foliation itself (Figure 4.7a-d). Microstructural fabrics within cataclastic zones, such as R-type riedel shears, are also consistent with top-to-the-east movements. Crucially, the observation that these structures deform igneous sheets related to the Porto Azzurro pluton (c.5.9Ma) indicates that they are not reverse faults inherited from early Miocene compressional events, but must broadly overlap in time with movements along the Zuccale fault.

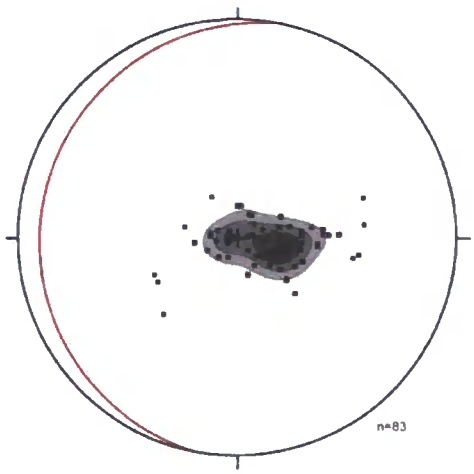

Figure 4.6) Stereonet showing poles to broadly sub-horizontal faults at Spiagge Nere and Capo Bianco. Mean fault (red great circle), 006°/10° W.

Sub-horizontal faults appear to preserve microstructural evidence for a 2-phase deformation history, described below from oldest to youngest (and from highest-temperature to lowest-temperature). 1) Igneous sheets can be traced into the sub-horizontal faults where they experience asymmetric boudinage, and typically preserve 'pinch and swell' geometries (e.g. Figure 4.7c). Igneous sheets are entrained into the faults and become stretched and smeared-out parallel to the fault margins to form elongate slivers or lenses, suggesting that intrusion and faulting overlapped in time (Figure 4.7a-d). Magmatic quartz found within the slivers and lenses of igneous material has experienced pervasive dynamic recrystallisation (Figure 4.7e, f). Equigranular subgrains (typically 50-100μm) are present throughout and possess both a grain-shape- and a crystallographic-preferred orientation (determined by insertion of a sensitive tint plate). Aggregates of subgrains are laterally continuous with newly recrystallised grains, that we interpret as forming due to subgrain-rotation recrystallisation [e.g. *Passchier and Trouw*, 2005]. In contrast, magmatic feldspars show no evidence for recrystallisation, but deform entirely by brittle fracture and/or kinking, indicating approximate deformation temperatures of 350°-450°C [*Hirth and Tullis*, 1992, *Passchier and Trouw*, 2005]. 2) Crystal-plasticity was followed by pervasive brittle cataclasis, that dominates the present-day fabric along the sub-horizontal faults (Figure 4.7e). Cohesive cataclastic fault rocks are mm to several cm in thickness and contain angular fragments of all sizes set within a matrix of ultrafine grained comminution products, sericite, and Fe-oxide phases.

4.4.3.2. East dipping footwall faults

The dominant sets of structures in the immediate footwall of the Zuccale fault are approximately north-south striking, discrete brittle faults that dip moderately to steeply to the east (mean orientation 000/43° E; Figure 4.8). Evidence summarized in Chapter 2 indicates that such footwall faults were active broadly synchronously with low-angle

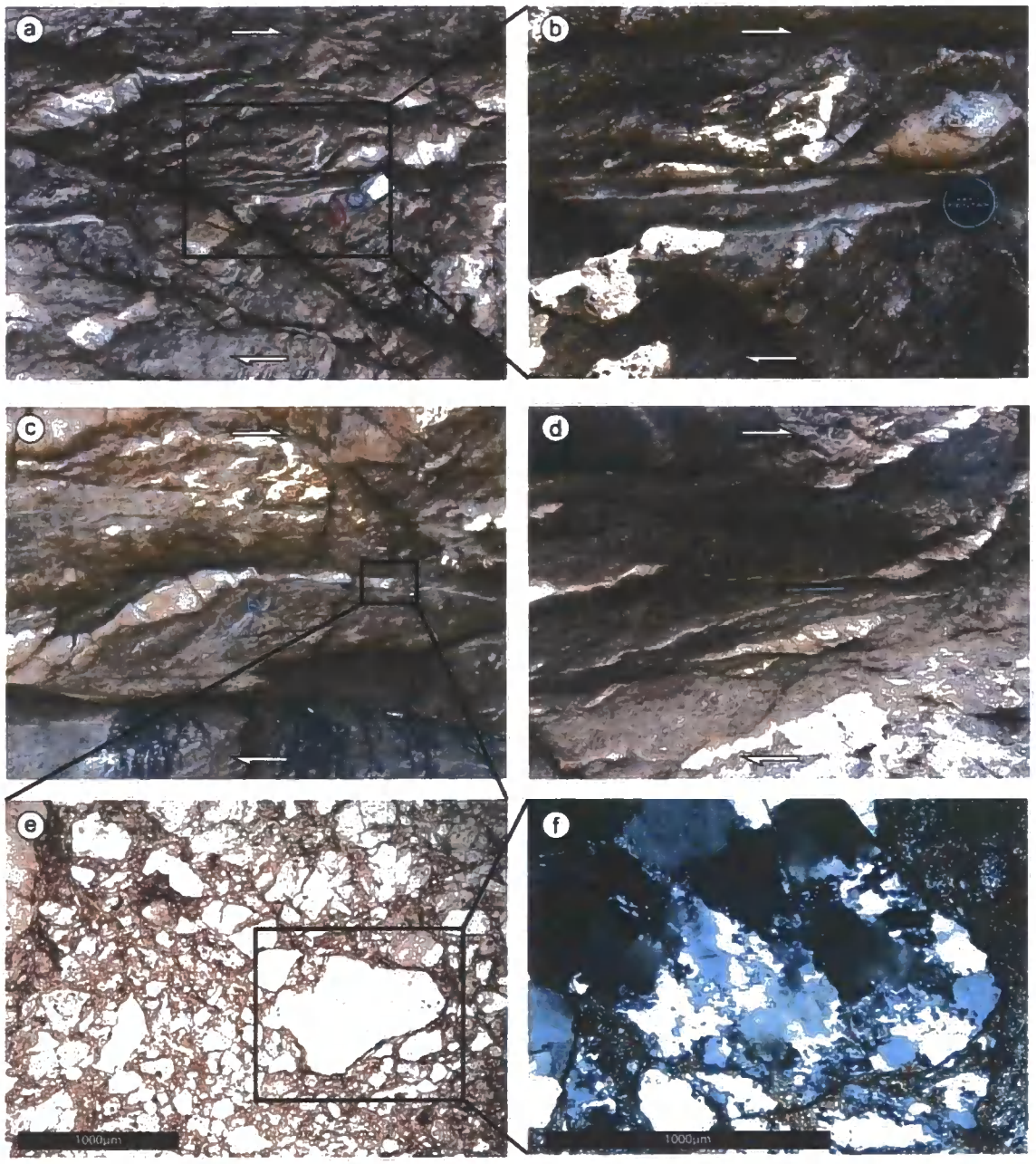

Figure 4.7a-d) Examples of sub-horizontal faults which deflect, stretch, and boudinage igneous sheets intruded in to Complex I basement schists. The fault in a and b is characterised by a relatively wide zone of shearing several centimetres in thickness, whilst the faults in c and d are represented by more discrete cataclastic fault planes, **e)** Photomicrograph in plane polarised light showing the pervasive cataclastic texture which dominates many of the sub-horizontal faults, **f)** Photomicrograph in crossed polarised light showing widespread evidence for crystal-plasticity and dynamic recrystallisation within individual clasts of quartz from the sub-horizontal faults.

movements along the Zuccale fault, and it is important to note that identical relationships to those described in Chapter 2 are present at Spiagge Nere and Capo Bianco. Kinematic indicators on exposed fault surfaces are well preserved and are typically defined by surface grooves and fine hematite striations that plunge moderately to steeply east to south-east (Figure 4.8). Shear sense indicators in the form of offset marker horizons uniformly indicate top-to-the-east extensional movements along east-dipping faults. In many cases, sequential 'bookshelf'-style rotation of east-dipping faults can be demonstrated from cross-cutting relationships (Figure 4.9, Appendix III). Faults that dip relatively shallowly to the east are consistently cross-cut by faults dipping relatively steeply to the east (Figure 4.9a, b, Appendix III).

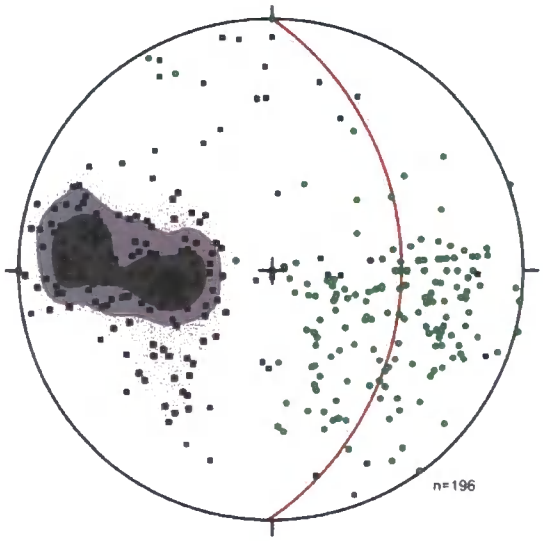

Figure 4.8) Stereonet showing poles to east-dipping faults (black squares) and associated lineations (green circles) at Spiagge Nere and Capo Bianco. Mean fault (red great circle), 000°/43° E. Mean lineation, 44°-111°.

East-dipping faults cross-cut igneous sheets within the basement to produce angular breccias and fault gouges (Figure 4.9c, d). Where present, fault rock materials are up to several centimetres in thickness but have a heterogeneous distribution along the strike and

dip of the fault surfaces. The boundaries between fault rock material, the host schists, and igneous sheets within the schists, are always sharp. Critically, east-dipping footwall faults are never observed to cause asymmetric boudinage of the igneous sheets, but instead result in fracturing and intense comminution. Elongate slivers and lenses of boudinaged igneous materials, like those observed along the sub-horizontal footwall faults, are not present, and there is no evidence on an outcrop or microscopic scale for crystal-plastic behaviour of fault rock material.

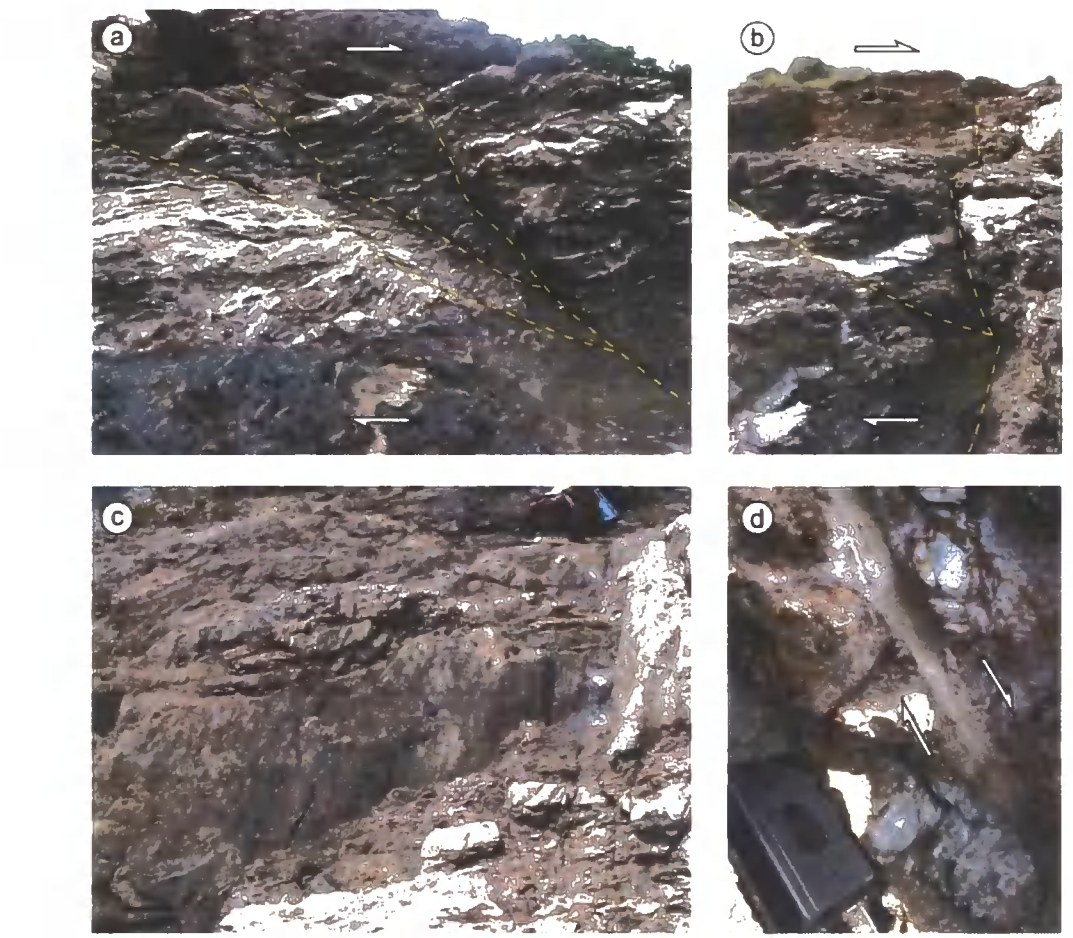

Figure 4.9a, b) Examples of east-dipping footwall faults showing typical cross-cutting relationships and sequential 'bookshelf'-style rotation. In both cases, faults which dip relatively shallowly to the east are cross-cut by faults which dip relatively steeply to the east, **c)** Surface grooves and slickenlines preserved on the polished surface of a steeply east-dipping fault, **d)** Foliated fault gouge and breccia preserved along a steeply east-dipping fault. All of the east-dipping faults show sharp contacts with the surrounding basement schists, and with igneous sheets intruded in to the basement schists.

4.4.3.3. Cross-cutting relationships between footwall faults

There are no consistent cross-cutting relationships between the sub-horizontal faults and the east-dipping faults. Mutual cross-cutting relationships can be documented in several areas, suggesting that movement across both sets of faults occurred broadly contemporaneously. Figure 4.10 illustrates one such example, where a sub-horizontal structure is cross-cut by two steeply east-dipping structures that in turn are crosscut by a younger, continuous sub-horizontal structure. The sub-horizontal faults in this example are defined by broad zones (tens of centimetres) of cataclasis that deflect and boudinage igneous sheets within the basement, whereas the steeply east-dipping structures are defined by discrete brittle fault planes that do not deflect or boudinage igneous sheets.

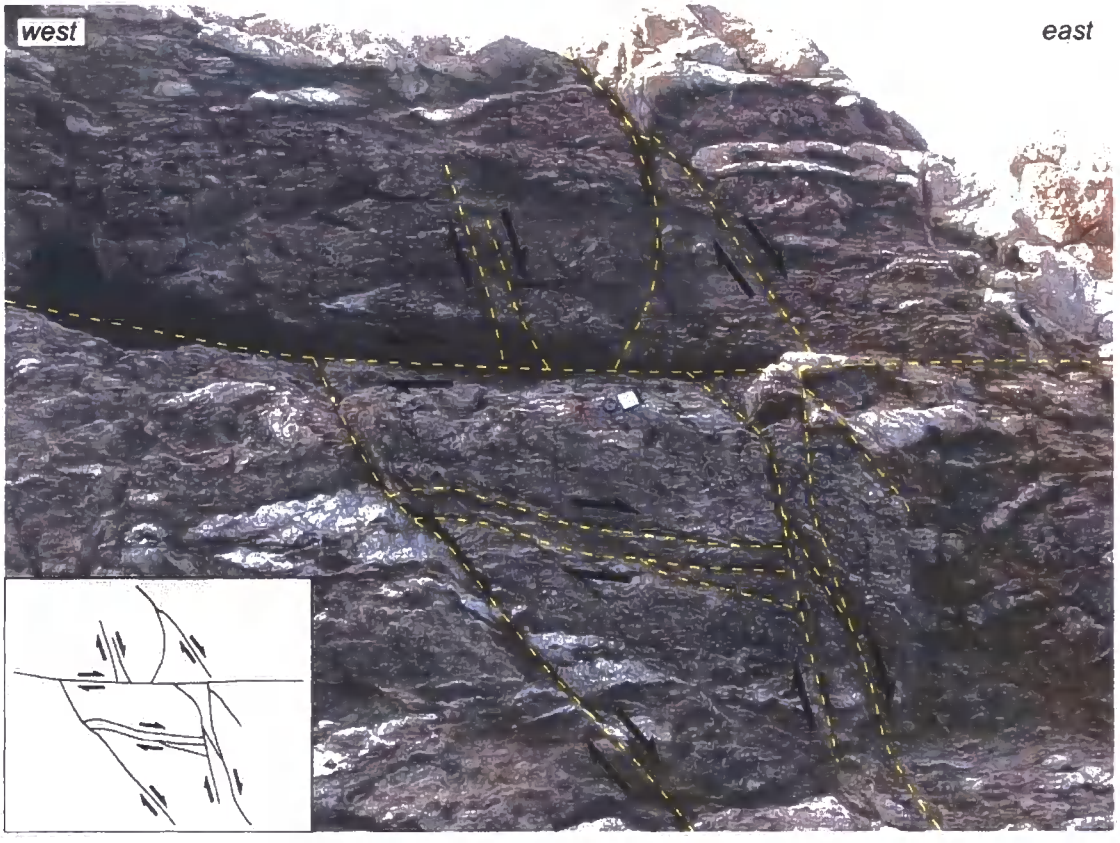

Figure 4.10) An example of the mutual cross-cutting relationships between sub-horizontal faults and east-dipping faults. The inset figure represents the overall fault network, and also shows the distribution of igneous sheets (grey shading) which can be reliably correlated from hangingwall to footwall across individual faults. In this example, a sub-horizontal fault is truncated at either end by steeply east-dipping faults (lower half of image), which in turn are truncated by a younger sub-horizontal fault running left to right through the middle of the photograph. The younger sub-horizontal fault offsets the two steeply east-dipping faults by ~1m, indicating a top-to-the-east shear sense. The sub-horizontal faults are broadly parallel to the main Zuccale fault in this area.

4.4.4. Carbon, oxygen, and strontium isotope analysis

The central core of the Zuccale fault is particularly well exposed at Punta di Zuccale, where it places Cretaceous deepwater flysch deposits in the hangingwall against Palaeozoic quartz-mica schists in the footwall (Figures 4.1, 4.2, 4.11a and Chapter 2). The fault core at Punta di Zuccale is several metres thick and contains a number of distinctive types of fault rock material, including talc- and chlorite-phyllonites, calcite-mylonites, and foliated cataclasites (Chapters 2, 6).

The foliated cataclasites within the fault core are dominated by fractured quartz and dolomite grains, but in places they are characterised by >90% dolomite vein material (Figure 4.11b). Dolomite veins are typically 1-2mm in width, closely spaced, and aligned parallel to a macroscopic P-foliation visible in the field. Dolomite within the veins has an elongate-blocky or blocky morphology and grows perpendicular to the vein margins. The veins only contain one generation of dolomite fill, and multiple crack-seal bands are rarely present. Most veins contain a thin median line, but they do not contain any optically resolvable twins or recrystallised material. The dolomite veins are crosscut and deflected by R^1-type riedel shears within the foliated cataclasites, indicating that they are syn-tectonic in origin. The $\delta^{18}O_{V\text{-}SMOW}$ signature of the dolomite veins is between 9.8‰ and 13.9‰, with a mean value of 12.5‰ (Figure 4.12, Table 4.1). $\delta^{13}C_{V\text{-}PDB}$ varies between -5.2‰ and -7.1‰, but 16 out of 17 analysed samples lie within the range -5.2‰ to -6.1‰

(Figure 4.12). The carbon isotopic values are strongly clustered around a mean value of -5.7‰. $^{87}Sr/^{86}Sr$ varies between 0.70958-0.71001 (Figure 4.13).

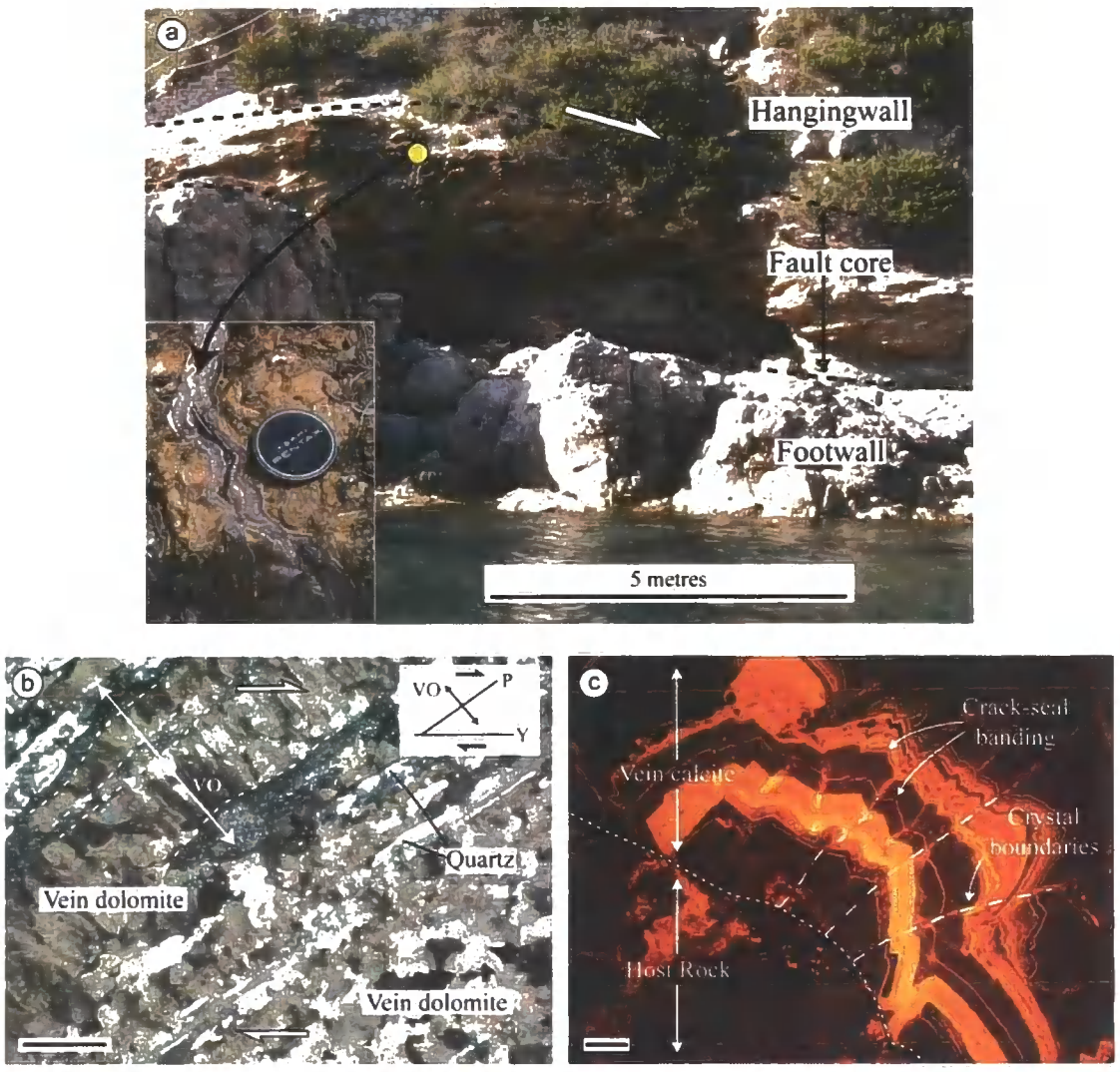

Figure 4.11a) Photograph of the central core of the Zuccale fault at Punta di Zuccale (location in Figure 4.2). The fault core contains foliated cataclasites with abundant syn-tectonic dolomite vein material (shown in b), and is cross-cut by a network of calcite hydrofracture veins (inset photograph), **b)** Photomicrograph in crossed polarised light showing a network of dolomite veins that are aligned broadly parallel to the macroscopic P-foliation within the foliated cataclasites. The Y-orientation, which parallels the margins of the fault core, is shown for reference. The dolomite veins contain elongate-blocky grain morphologies, that suggest a vein opening direction (VO) broadly normal to the P-foliation, **c)** Cathodoluminescence image of the calcite hydrofracture veins, that contain blocky-elongate grain morphologies characterised by fine-scale (10µm spacing) 'crack-seal' banding. Some post-tectonic calcite is also visible within the host rocks. Scale bars in b and c are 1mm.

The footwall and central core of the Zuccale fault are crosscut by an extensive network of late-stage calcite hydrofracture veins [Figure 4.11a, c; Chapter 6, *Collettini et al.*, 2006a]. The veins are broadly sub-vertical or sub-horizontal in orientation, and up to 20cm in width. Some of the veins appear to be synthetically rotated within the fault core, suggesting that they may, in part, be syn-tectonic. They contain closely-spaced (10μm) crack-seal banding visible in cathodoluminescence (Figure 4.11c). Individual calcite crystals are up to 1cm in length and have an elongate-blocky morphology. The crystals typically grew perpendicular to the vein margins, and may show a faceted shape indicative of growth into fluid-filled cavities. Optically resolvable twins are present only in a small number of crystals. The $\delta^{18}O_{V\text{-}SMOW}$ signature of the calcite hydrofracture veins is between 24.9‰ and 27.34‰, with a mean value of 26.34‰ (Figure 4.12, Table 4.1). $\delta^{13}C_{V\text{-}PDB}$ varies between -6.69‰ and -10.4‰, with a mean value of -8.88‰ (Figure 4.12). $^{87}Sr/^{86}Sr$ varies between 0.70904-0.70914 (Figure 4.13).

4.5. Discussion

4.5.1. Pluton emplacement and doming of low-angle normal faults

Kinematic relationships between the Zuccale fault and minor igneous intrusions associated with the Porto Azzurro pluton suggests that pluton emplacement and cooling occurred broadly contemporaneously with top-to-the-east movements across the Zuccale fault: 1) Tourmaline-bearing igneous sheets appear to have opened in a ~ESE-WNW orientation (Figure 4.4), similar to the mean azimuth (098°) of slickenline lineations within the Zuccale fault (Figure 4.2); 2) The Barbarossa stock contains solid-state lineations (mean azimuth 271°) and solid-state mylonitic shear zones (mean azimuth of lineations, 278°) that record approximately east-west oriented shearing (Figure 4.5), almost identical to that recorded by slickenline lineations within the Zuccale fault (Figure 4.2).

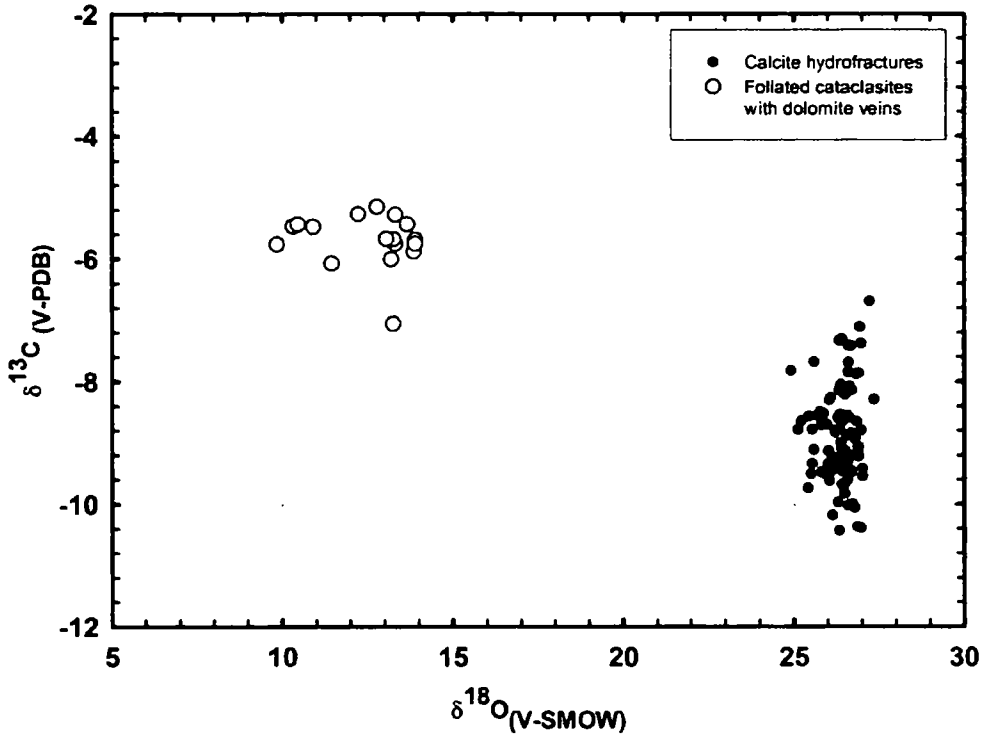

Figure 4.12) $\delta^{18}O_{V\text{-}SMOW}$ vs. $\delta^{13}C_{V\text{-}PDB}$ of the dolomite veins (n=17) and calcite hydrofracture veins (n=97) associated with the Zuccale fault.

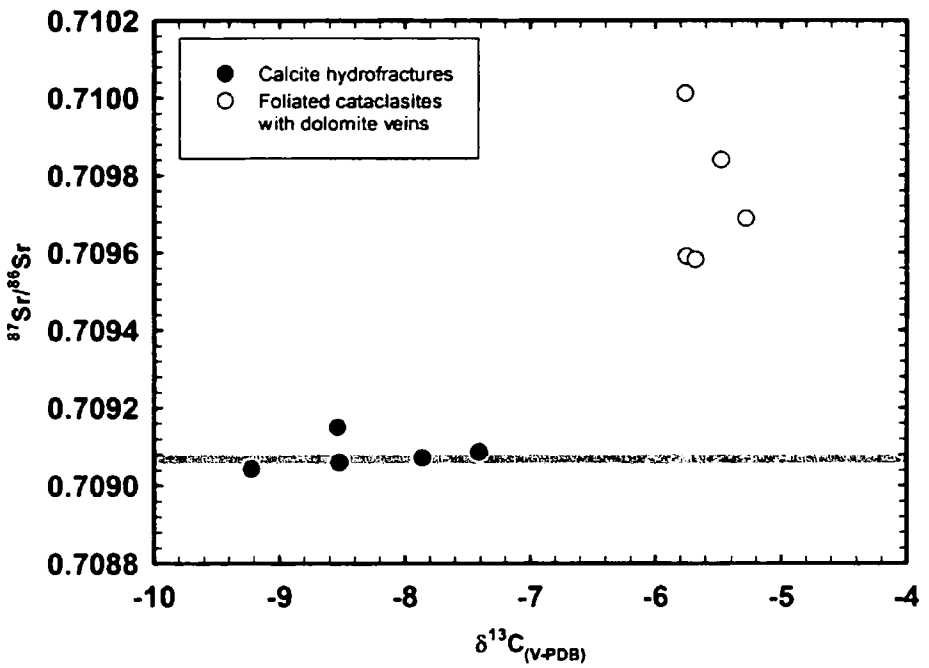

Figure 4.13) $^{87}Sr/^{86}Sr$ vs $\delta^{13}C_{V\text{-}PDB}$ of the dolomite and calcite veins. The light grey line represents the average $^{87}Sr/^{86}Sr$ composition of modern-day seawater [*Burke et al.*, 1982, *Smalley et al.*, 1994].

Table 4.1) Oxygen, carbon, and strontium isotopic compositions of carbonate material associated with the Zuccale fault. FC, Foliated cataclasites containing dolomite veins, H, calcite hydrofractures that cross-cut the fault core.

Sample no.	Fault zone component	$\delta^{13}C_{(V\text{-}PDB)}$	$\delta^{18}O_{(V\text{-}SMOW)}$	$^{87}Sr/^{86}Sr$
PZ1_1	FC	-5.76	9.84	0.710011
PZ1_2	FC	-5.47	10.31	
PZ1_3	FC	-5.44	10.45	
PZ2_1	FC	-5.69	13.89	
PZ2_2	FC	-5.75	13.31	0.709591
PZ2_3	FC	-5.88	13.85	
PZ7_4	FC	-6.01	13.19	
PZ7_5	FC	-5.75	13.89	0.709582
PZ7_6	FC	-5.68	13.29	
PZ5_7	FC	-6.07	11.45	
PZ5_8	FC	-5.48	10.90	0.709840
PZ6_1	FC	-5.27	12.23	
PZ6_2	FC	-7.06	13.24	
PZ6_3	FC	-5.67	13.04	
PZ6_4	FC	-5.44	13.66	
PZ18_6	FC	-5.28	13.31	0.709689
PZ18_7	FC	-5.15	12.77	
PZ32_1	H	-7.69	26.61	
PZ32_2	H	-8.08	26.63	0.709071
PZ32_3	H	-7.86	26.89	
PZ36_1	H	-9.61	26.56	
PZ36_2	H	-9.54	27.01	
PZ36_3	H	-9.41	26.16	
PZ37_1	H	-8.55	26.45	
PZ37_2	H	-8.93	26.80	
PZ37_3	H	-8.56	26.58	
PZ38_1	H	-9.83	26.49	
PZ38_2	H	-8.16	26.40	
PZ38_3	H	-10.00	26.73	
PZ38_4	H	-10.37	26.87	
PZ38_5	H	-10.39	26.97	
PZ38_6	H	-8.30	26.04	
PZ39_1	H	-9.13	26.02	
PZ39_2	H	-8.66	26.41	
PZ39_3	H	-8.79	26.34	
PZ40_1	H	-9.06	26.88	
PZ40_1	H	-8.14	26.69	
PZ3_1	H	-8.78	25.53	
PZ3_2	H	-9.11	25.58	
PZ3_3	H	-9.31	26.57	
PZ4_1	H	-8.64	25.21	
PZ4_2	H	-8.26	26.08	
PZ5_1	H	-8.62	25.80	
PZ5_2	H	-8.52	25.87	0.709058
PZ5_3	H	-9.48	25.80	
PZ5_4	H	-9.34	25.53	
PZ5_5	H	-8.78	25.12	
PZ5_6	H	-8.57	25.43	
PZ6_1	H	-8.54	26.36	0.709150

PZ6_2	H	-8.70	25.96	
PZ7_1	H	-9.44	26.09	
PZ7_2	H	-9.54	26.00	
PZ7_3	H	-9.13	26.50	
PZ8_1	H	-9.31	26.22	
PZ8_2	H	-9.22	26.45	
PZ8_3	H	-8.49	25.77	
PZ8_4	H	-8.55	25.68	
PZ9_1	H	-9.18	26.88	
PZ9_2	H	-8.86	26.70	
PZ9_3	H	-8.99	26.39	
PZ9_4	H	-8.05	26.39	
PZ10_1	H	-8.88	26.53	
PZ10_2	H	-9.20	26.78	
PZ11_1	H	-10.18	26.14	
PZ11_2	H	-9.23	26.13	
PZ11_3	H	-10.02	26.59	
PZ11_4	H	-9.37	26.44	
PZ11_5	H	-9.38	26.09	
PZ11_6	H	-9.46	26.11	
PZ11_7	H	-9.62	26.05	
PZ11_8	H	-7.88	26.83	
PZ12_1	H	-9.66	26.49	
PZ12_2	H	-9.68	26.42	
PZ12_3	H	-8.59	26.29	
PZ12_4	H	-9.38	26.16	
PZ12_5	H	-9.29	26.25	
PZ13_1	H	-9.22	26.90	0.709042
PZ13_2	H	-10.06	26.78	
PZ13_3	H	-9.97	26.30	
PZ13_4	H	-9.44	26.47	
PZ13_5	H	-9.42	27.01	
PZ14_1	H	-7.33	26.33	
PZ14_2	H	-8.83	26.23	
PZ14_3	H	-8.71	25.81	
PZ14_4	H	-8.80	26.21	
PZ15_1	H	-9.47	26.64	
PZ15_2	H	-9.08	26.40	
PZ15_3	H	-9.35	26.01	
PZ15_4	H	-10.43	26.34	
PZ16_1	H	-8.21	26.50	
PZ16_2	H	-8.10	26.38	
PZ17_1	H	-8.65	26.84	
PZ17_2	H	-8.65	26.83	
PZ17_3	H	-9.23	26.55	
PZ17_4	H	-8.29	27.34	
PZ17_5	H	-7.82	24.90	
PZ18_1	H	-7.68	25.59	
PZ18_2	H	-7.85	26.60	
PZ18_3	H	-8.14	26.33	
PZ18_4	H	-7.31	26.41	
PZ18_5	H	-7.38	26.96	
PZ18_6	H	-6.69	27.21	
PZ20_1	H	-9.26	26.24	
PZ20_2	H	-9.21	26.39	
PZ20_3	H	-9.46	26.42	
PZ21_1	H	-7.41	26.60	0.709086
PZ21_2	H	-7.42	26.68	

PZ21_3	H	-7.11	26.93	
PZ22_1	H	-8.84	26.68	
PZ22_2	H	-8.79	26.97	
PZ22_3	H	-8.58	26.61	
PZ23_1	H	-9.51	25.50	
PZ23_2	H	-9.42	26.06	
PZ23_3	H	-9.47	26.71	

Many low-angle normal faults that form part of metamorphic core complexes exhibit doubly-plunging domal (antiformal) and basinal (synformal) geometries, due to the interaction of folds whose axes are broadly parallel and broadly perpendicular to the regional extension direction [*Coney*, 1980, *Cann et al.*, 1997, *Cemen et al.*, 2005]. Folds with axes perpendicular to the extension direction are thought to form by arching of the footwall during isostatic rebound, or during the progression of a rolling hinge [*Wernicke*, 1981, *Buck*, 1988, *Wernicke and Axen*, 1988]. Folds with axes parallel to the extension direction are usually interpreted as primary mega-mullions [*John*, 1987, *Davis and Lister*, 1988, *Cann et al.*, 1997], or to result from sub-horizontal shortening perpendicular to extension during transcurrent or transtensional deformation [*Yin*, 1991, *Mancktelow and Pavlis*, 1994]. The latter form at all scales, but folds with a wavelength of several kilometres are expected to develop in the upper crustal portions of core complex systems [*Mancktelow and Pavlis*, 1994]. Well known examples of dome and basin low-angle normal fault geometries occur in the Death Valley region of the Basin and Range province, western USA, where they form the topographic surfaces known as 'turtlebacks', and separate strongly mylonitic footwall rocks from brittlely deformed hangingwall rocks. Such examples have typical wavelengths of 5-10km and amplitudes of several hundreds of metres to kilometres [e.g. Mormon Point, Copper Canyon, and Badwater turtlebacks; *Wright et al.*, 1974, *Davis and Lister*, 1988, *Miller*, 1992, *Cowan et al.*, 2003, *Miller and Pavlis*, 2005].

Structure contours constructed for the Zuccale fault (Figure 4.2) suggest that the fault has an overall domal shape, that exposes a nucleus of Complex I schists in the south-east of Elba, around Monte Calamita (Figures 4.1, 4.2). Outcrops of the Zuccale fault generally occur along coastal sections close to sea level, but the absence of any hangingwall units at the summit of Monte Calamita indicates that prior to erosion, the Zuccale fault must have attained an elevation in this area of at least 412m (Figure 4.2). The wavelength of the exposed dome measured normal to the easterly transport direction is 7-10km, and the amplitude is greater than 400m, values that are comparable to the turtleback structures in Death Valley. A lack of exposure to the east of Monte Calamita makes it difficult to assess the wavelength of the dome parallel to the transport direction, although offshore seismic data confirms a general shallow easterly dip for the Zuccale fault [*Keller and Coward*, 1996]. We emphasize that unlike the examples from the Basin and Range province and the Aegean Sea, and the example from Turkey presented by *Cemen et al.* [2005], there are no regional mylonitic fabrics associated with surface exposures of the Zuccale fault, and it may represent the first documented example of a long-wavelength, domal fault morphology that developed entirely within the upper crust.

Regional-scale variations in the shape of the Zuccale fault appear to correlate closely with the likely sub-surface position of the Porto Azzurro pluton. On the north, south and west sides of Monte Calamita, the margins of the pluton are associated with north-, south- and west-dipping portions of the Zuccale fault, respectively. Additionally, the coincidence between surface outcrops of the Porto Azzurro pluton around La Serra, and a clear increase in the elevation of the fault surface in the area, seems to indicate that the pluton was capable of directly influencing the geometry of the fault surface. We suggest that the Zuccale fault developed a domal morphology in the upper crust due to intrusion of the Porto Azzurro pluton at relatively shallow depths in the footwall of the fault. Although we

do not have absolute constraints on the ages of movement along the Zuccale fault, doming of the fault surface must have taken place after a significant amount of fault displacement had occurred. It seems likely that doming would have led to an abandonment of the Zuccale fault on the west side of Monte Calamita (e.g. Punta Di Zuccale), as this area would have been rotated out of an orientation favourable for top-to-the-east transport. However, the fault zone in this area is well developed and contains a 'mature' sequence of foliated fault rocks that record a protracted history of slip and exhumation [*Collettini and Holdsworth*, 2004, Chapter 6], suggesting that doming occurred after the development of the fault rock sequence at Punta di Zuccale. The available age data thus suggest that development of the Zuccale fault occurred after ~7.95Ma (intrusion of the Portoferraio porphyry) and prior to doming at around 5.9Ma (intrusion of the Porto Azzurro pluton), but this does not preclude the possibility that slip along the Zuccale fault continued after 5.9Ma in areas on the east side of Monte Calamita (that remained in an orientation favourable for top-to-the-east transport).

Other large, upper-crustal igneous bodies that have been studied on Elba include the Capo Bianco aplite [c.8.5 Ma; *Perugini and Poli*, 2007], the Portoferraio (c.8Ma) and San Martino (c.7.4Ma) granite porphyrys [*Dini et al.*, 2002, *Rocchi et al.*, 2002], and the Capanne monzogranite pluton [c. 6.9Ma; *Dini et al.*, 2002, *Gagnevin et al.*, 2004, *Dini et al.*, 2007, *Rossetti et al.*, 2007]. *Rossetti et al.* [2008] and *Acocella* [2000] also studied the plutonic bodies lying at shallow depths beneath the active Lardarello and Monte Amiata geothermal fields in mainland Tuscany. All of these plutons exhibit a composite or sheeted laccolithic form, and grew by horizontal expansion followed by vertical inflation resulting in roof uplift [e.g. *Corry*, 1988, *Cruden*, 1998, *Cruden and McCaffrey*, 2001]. The tectonostratigraphic architecture of Elba (and Tuscany in general) prior to, and during, post-collisional extension was apparently favourable for the exploitation of tectonic and

lithological discontinuities by sheeted magmatic intrusions. Little is known about the ascent or emplacement of the Porto Azzurro pluton, but if it grew by horizontal expansion followed by vertical inflation, this provides a mechanism for doming the overlying Zuccale fault.

Although we favour the idea that late-stage doming of the Zuccale fault was principally caused by igneous intrusion in the upper crust, we cannot rule out the possibility that other processes such as transcurrent or transtensional deformation amplified the doming effect [*Mancktelow and Pavlis*, 1994]. Clearly, where domal fault surfaces are produced in the absence of broadly synchronous magmatic activity, the doming process must be attributed to a mechanism other than igneous intrusion.

4.5.2. Transient thermal weakening and changes in footwall faulting style

Within the metamorphic carapace surrounding plutons, the intrusion of hypabyssal sills and dykes can result in transient thermal pulses and thermal softening in the adjacent country rocks [e.g. *Lister and Baldwin*, 1993, *Pavlis*, 1996]. Two distinct sets of footwall faults are recognised at Spiagge Nere, that we suggest are fundamentally influenced by emplacement and cooling of minor intrusions related to the Porto Azzurro pluton.

Sub-horizontal footwall faults (broadly parallel to the Zuccale fault where observed) preserve evidence suggesting that they may have been active during the intrusion of igneous sheets related to the Porto Azzurro pluton. Deformation along the sub-horizontal faults initially occurred by crystal-plasticity, but this was overprinted by brittle cataclasis that dominates the present-day fabric. We suggest that the early stages of movement along such faults occurred due to thermal softening associated with intrusion of individual igneous sheets during the incremental growth of the footwall dyke-sill complex (Figure

4.14a). As the transient temperature anomalies associated with small intrusions decreased, thermal softening of the wall rocks became less important, promoting a transition to cataclasis as the dominant mode of deformation. Once ambient wall rock temperatures were regained, extension out-with the weakened central core of the Zuccale fault was accommodated along high-angle, east-dipping footwall faults, like those documented at Punta di Zuccale (Figure 4.14b and Chapter 2). The mutual cross-cutting relationships observed between sub-horizontal and east-dipping faults suggests that transient pulses of ductile deformation in the footwall of the Zuccale fault alternated with periods of lower-temperature brittle deformation (Figure 4.14c).

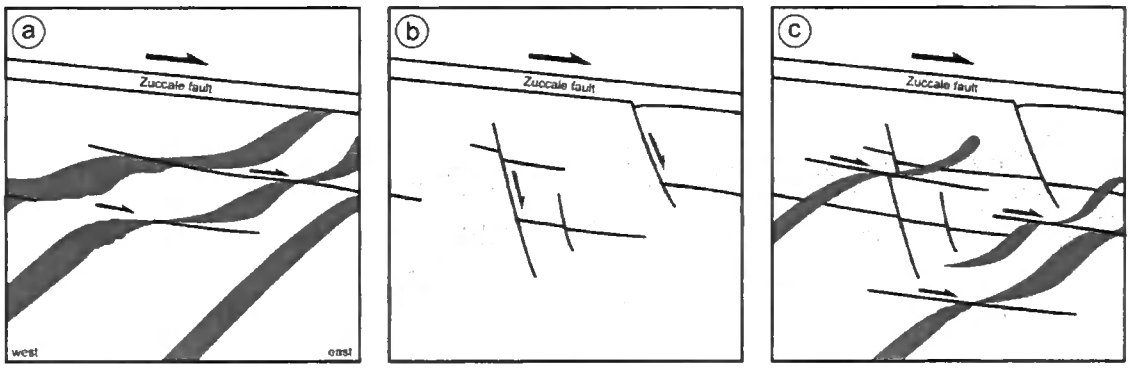

Figure 4.14) Schematic model to illustrate the sequence of faulting and intrusion events observed in the footwall of the Zuccale fault, **a)** Intrusion of igneous sheets parallel to the foliation within basement schists (moderately west-dipping, see Figure 4.3). This results in a transient thermal anomaly in a localized area within the footwall of the Zuccale fault, and promotes the formation of low-angle footwall faults, **b)** The thermal anomaly associated with minor igneous intrusions relaxes. Once ambient temperatures are regained, the footwall faulting sequence is dominated by high-angle east-dipping faults like those typically observed at Punta di Zuccale (Chapter 2), **c)** Further intrusion of minor igneous sheets results in renewed low-angle footwall faulting, accounting for the observed mutual cross-cutting relationships. The cycle repeats until final emplacement and cooling of the entire plutonic complex.

4.5.3. Fluid sources along the Zuccale fault

The dolomite veins within the central core of the Zuccale fault, and the calcite hydrofracture veins that cross cut the fault core, define clear and separate carbon, oxygen,

and strontium isotopic fields, strongly suggesting that the two carbonate materials were precipitated from fluids derived from different sources (Figures 4.12, 4.13, Table 4.1).

The interpretation of stable isotope data derived from vein and cement material requires that some constraints are placed on the temperatures at which mineral precipitation is believed to have taken place. Assuming that mineral and fluid were in equilibrium, this allows for the calculation of fluid isotopic ratios based on empirically- or theoretically-established mineral-fluid fractionation factors [e.g. *Valley and Cole*, 2001]. The temperatures at which the dolomite and calcite veins were precipitated along the Zuccale fault can be broadly estimated on the basis of the active deformation mechanisms in the host fault rocks, and from crosscutting relationships between different fault rock components within the fault core (see Chapter 6 for details).

The dolomite veins within the fault core are hosted by quartz- and dolomite-rich foliated cataclasites. There is no sign that crystal-plasticity was an active deformation mechanism in either of these minerals, limiting temperatures of deformation to <250°C [*Hirth and Tullis*, 1992, *Passchier and Trouw*, 2005]. The foliated cataclasites formed after a unit of phyllonites and calcite-mylonites that record deformation at temperatures of approximately 170°-250°C, but prior to a unit of foliated fault gouges that formed at <50°C (Chapter 6). The sequence of fault rocks within the core of the Zuccale fault appears to record progressive exhumation of the fault zone from depth, accompanied by a switch in the dominant deformation mechanisms (Chapter 6). In this case, we suggest that the relationships between the foliated cataclasites and the surrounding fault rocks, and the dominance of cataclastic deformation mechanisms, indicates precipitation of the dolomite veins at approximately 150°-200°C [Chapter 6; *Blenkinsop and Rutter*, 1986, *Passchier and Trouw*, 2005]. The analysis of fluid inclusions contained within the dolomite veins would provide much better constraints on temperatures of precipitation.

The calcite hydrofractures crosscut the fault core, and were precipitated after the formation of a unit of foliated fault gouges recording deformation at temperatures of <50°C (Chapter 6). This indicates that the calcite hydrofractures were among the latest structures to form along the Zuccale fault, and were likely precipitated at temperatures in the range of 20-50°C.

The dolomite veins have a wide range in oxygen isotope ratios (average $\delta^{18}O_{V\text{-}SMOW}$ = 12.5‰), and a much narrower range in carbon isotope ratios (average $\delta^{13}C_{V\text{-}PDB}$ = -5.7‰). Using the fractionation factors for dolomite-water of *Northrop and Clayton* [1966] and dolomite-CO_2 of *Ohmoto and Rye* [1979], the fluid in equilibrium with the dolomite veins at 150°-200°C would have $\delta^{18}O$ of around -6.5‰ to 1.1‰ and $\delta^{13}C$ of -5.9‰ to -8.7‰ (Figure 4.15). Adopting the alternative dolomite-water fractionations of *Matthews and Katz* [1977] extends the possible fluid-$\delta^{18}O$ range up to 3‰. Such values of $\delta^{18}O$ overlap with typical values for seawater (-2‰ to 2‰), and meteoric water that has exchanged with relatively high-$\delta^{18}O$ country rocks [Figure 4.15; *Sheppard*, 1986, *Hoefs*, 1987]. In this case, we suggest that the dolomite veins were precipitated from hot fluids of meteoric-hydrothermal origin, following exchange of oxygen isotopes with shallow-level igneous bodies, including the Porto Azzurro pluton. This is consistent with the findings of *Taylor and Turi* [1976], who reported low-$\delta^{18}O$ values (~5‰) in feldspar megacrysts from the Porto Azzurro pluton, but relatively high-$\delta^{18}O$ (~12‰) in coexisting quartz (Figure 4.15). As feldspar is more susceptible to O^{18} exchange than quartz, they interpreted the stable isotope data to indicate extensive interaction between the Porto Azzurro pluton and low-$\delta^{18}O$ meteoric-hydrothermal fluids subsequent to solidification. They concluded that the Porto Azzurro pluton was associated with an extensive meteoric-hydrothermal fluid system.

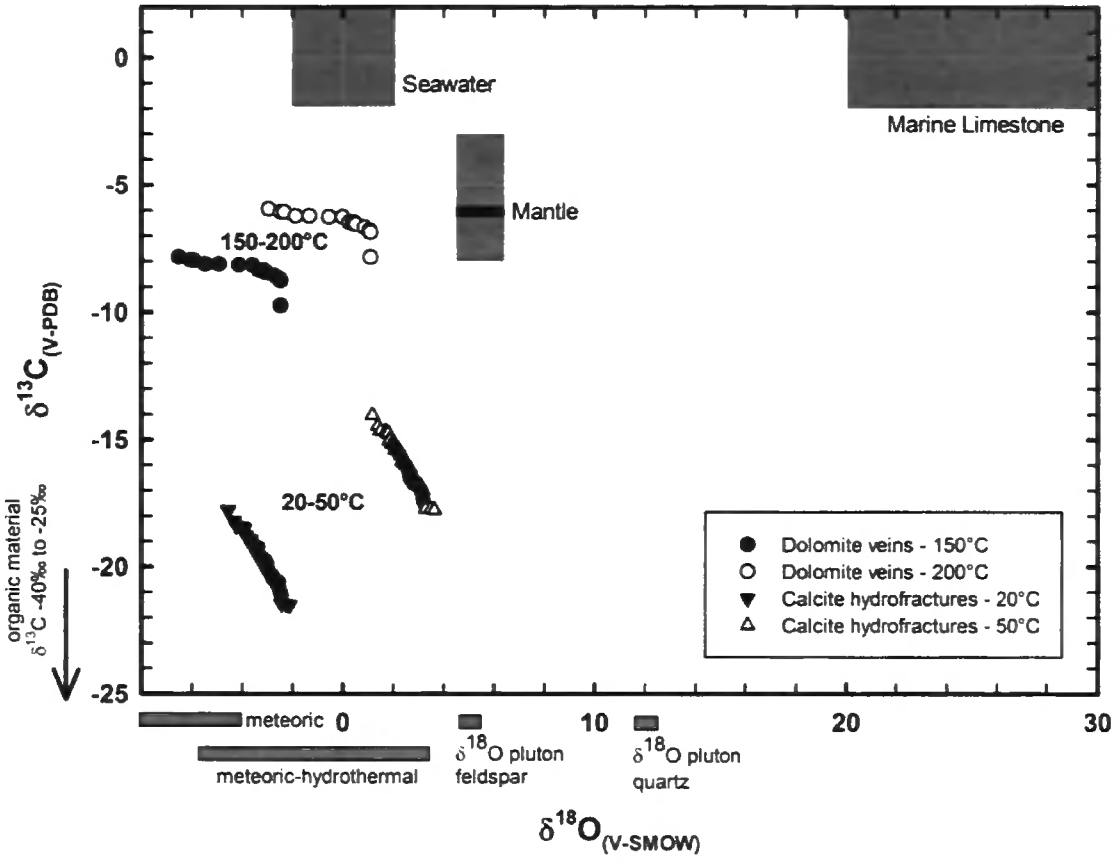

Figure 4.15) Calculated $\delta^{18}O$ and $\delta^{13}C$ of the fluids in equilibrium with the dolomite and calcite veins at 150°-200°C and 20°-50°C, respectively. Fractionation factors are discussed in the text. Typical compositions of seawater, unaltered marine limestone, and the mantle are added for comparison [*Sheppard*, 1986, *Mattey et al.*, 1994, *Deines*, 2002]. The black line in the mantle field represents an average mantle isotopic composition [*Deines*, 2002]. Also shown are typical $\delta^{18}O$ compositions of meteoric and meteoric-hydrothermal fluid, and $\delta^{13}C$ range of organic material [*Rollinson*, 1993]. The oxygen composition of minerals from the Porto Azzurro pluton is after *Taylor and Turi* [1976]

Interaction of meteoric fluids with upper-crustal igneous bodies can also adequately explain both the carbon and strontium isotopic ratios in the dolomite veins. Analysis of gas contents in groundwater springs along the present-day Tyrrhenian coast of Italy suggests that a significant flux of mantle-derived CO_2 is being released, that is mixed with CO_2 from shallow crustal sources [*Chiodini et al.*, 2000, *Chiodini et al.*, 2004]. Carbon with an average $\delta^{13}C$ of around -6‰ has been identified as a major isotopic signature for the

mantle, and has been recognised in mantle xenoliths, kimberlite and carbonatite magmas, and volcanic CO_2 gas [e.g. *Allard et al.*, 1997, *Chiodini et al.*, 1999, *Deines*, 2002]. Fluids in equilibrium with the dolomite veins possess a strongly clustered $\delta^{13}C_{V\text{-}PDB}$ signature between -6‰ and -8.5‰, suggesting that carbon may have been derived from the crystallisation and degassing of igneous bodies carrying mantle-derived CO_2.

Although most intrusive bodies in the Tuscan magmatic province appear to reflect large-scale melting and assimilation of high-$\delta^{18}O$ and high-$^{87}Sr/^{86}Sr$ metasediments [e.g. *Turi and Taylor*, 1976, *Hawkesworth and Vollmer*, 1979, *Taylor and Sheppard*, 1986], many of the larger plutons are thought to represent hybrid melts carrying both mantle and crustal components. For example, the $^{87}Sr/^{86}Sr$ values of the Capanne pluton (Figure 4.1), and related igneous products on Elba, range between ~0.711-0.719, reflecting mixing between a low-$^{87}Sr/^{86}Sr$ metasomatized 'mantle' end-member (0.706-0.708) and the highly radiogenic metasedimentary basement [>0.725; *Dini et al.*, 2002, *Gagnevin et al.*, 2004]. Interaction and exchange of meteoric fluids with igneous bodies can account for the elevated Sr isotopic signature of the dolomite veins, and the relatively wide range in Sr isotopic ratios, which is typically interpreted to indicate a mixing trend (Figure 4.13).

The calcite hydrofracture veins associated with the Zuccale fault are characterised by a relatively small range in oxygen isotope ratios, and a wider range in carbon isotope ratios [Figure 4.12; *Veizer and Hoefs*, 1976, *Rollinson*, 1993]. Applying the fractionation factors for calcite-water of *O'Neil et al.* [1969] and calcite-CO_2 of *Bottinga* [1968], the fluid in equilibrium with the calcite hydrofractures at temperatures of 20°-50°C would possess $\delta^{18}O$ in the range -4.5‰ to 3.5‰, and $\delta^{13}C$ in the range -14‰ to -21.5‰ (Figure 4.15). In this case, we favour precipitation from seawater, because the $^{87}Sr/^{86}Sr$ values of the calcite hydrofractures are constant and indistinguishable from those of modern-day seawater [$^{87}Sr/^{86}Sr \sim 0.70907$; Figure 4.13; *Burke et al.*, 1982, *Smalley et al.*, 1994]. The calculated

carbon isotopic ratio of the fluid suggests the involvement of an organic component heavily depleted in $\delta^{13}C$. The typical $\delta^{13}C$ range of sedimentary organic carbon extends from -25‰ to -40‰ [Figure 4.15; *Rollinson*, 1993]. The most abundant source of organic carbon in the area is the mudstones that form a large component of thrust complex V (Figures 4.1, 6.2). Complex V occurs extensively throughout central and eastern Elba, in both the hangingwall and footwall of the Zuccale fault. The complex is extensively faulted and fractured, and may have provided easy pathways for fluid flow from higher structural levels. The calculated carbon isotopic ratio of the fluid in equilibrium with the calcite hydrofractures is intermediate between that of seawater and sedimentary organic carbon. We suggest that it reflects mixing between these two components during the final stages of exhumation along the Zuccale fault. We also speculatively suggest that the switch from a meteoric-hydrothermal fluid to a seawater-derived fluid reflects a transition from sub-aerial to submarine conditions during regional extension.

4.6. Conclusions

Structural and geochemical data suggest that the development and emplacement of upper-crustal plutonic complexes on Elba, and in particular the Porto Azzurro pluton, fundamentally influenced the geometry and fluid flow history of the Zuccale low-angle normal fault.

On a regional scale, final emplacement of the Porto Azzurro pluton was associated with a broad doming of the Zuccale fault, suggesting that pluton emplacement occurred, at least in part, by vertical inflation and roof uplift. The domal nature of the Zuccale fault resembles the 'turtleback' structures reported from the Basin and Range province and elsewhere, but no regional mylonitic fabrics are associated with surface exposures of the

Zuccale fault. It seems to represent a domal fault morphology that developed during the latter stages of fault displacement, entirely within the upper crust, and as a direct consequence of pluton intrusion.

On a local scale, intrusion of minor igneous dykes and sills related to the Porto Azzurro pluton resulted in short-lived pulses of thermal softening in the footwall of the Zuccale fault, driving transient changes in the geometry of the footwall fault network. Mutual cross-cutting relationships between sets of high- and low-angle footwall faults suggests cyclic thermal softening followed by cooling and a return to ambient wall rock temperatures.

Two distinct fluid sources are recorded by the stable isotope signatures of fault vein material. During the relatively early stages of fault movement, meteoric fluids interacted with upper-crustal igneous bodies carrying a component of mantle-CO_2. This resulted in the development of a widespread meteoric-hydrothermal fluid system. During the late stages of fault movement, seawater-derived fluids were able to infiltrate the fault zone, probably by pervasive flow through faulted and fractured host rocks. Both sources of fluid were sufficient to generate supra-lithostatic fluid pressures within and surrounding the fault core, recorded by the presence of sub-horizontal and sub-vertical dolomite and calcite veins.

Chapter 5

Laboratory Measurements of the Frictional Properties of a Natural Low-Angle Normal Fault: The Zuccale Fault, Elba Island, Italy

A modified version of this chapter is to be submitted to the Journal of Geophysical Research in December 2008 as: S.A.F. Smith & Faulkner, D.R., Laboratory measurements of the frictional properties of a natural low-angle normal fault: The Zuccale Fault, Elba Island, Italy

Abstract

Using a case study from the Island of Elba, Italy, we seek to test the hypothesis that mineralogical weakening can explain prolonged slip on low-angle normal faults. The central core of the Zuccale low-angle normal fault contains a distinctive fault rock 'stratigraphy' that developed during progressive exhumation. Individual fault rock components within the fault core are mineralogically and texturally complex, but most components preserve microstructural evidence for having accommodated deformation entirely, or partly, by frictional mechanisms. 1mm-thick sample powders of all the major fault rock components were deformed in a triaxial deformation apparatus under water-saturated conditions, at room temperature, and at constant effective normal stresses of 25, 50, and 75MPa. Pore pressure was 50MPa in all the experiments. Overall, the coefficient of friction (μ) of the fault rocks varies between 0.25-0.8, emphasizing the marked strength heterogeneity that may exist within natural fault zones. μ is strongly dependent on fault rock mineralogy, and is <0.45 for fault rocks containing talc, chlorite, and kaolinite, and >0.6 for fault rocks dominated by quartz, dolomite, calcite and amphibole. Localization of frictional slip within talc-rich portions of the fault core can potentially explain movement along the Zuccale fault at all depths within the upper crust, without the need to appeal to other weakening mechanisms. Additionally, slip within kaolinite- and chlorite-bearing fault gouges with μ between 0.4-0.5 can explain movements in the upper 2km of the crust. For the other fault rock components, mineralogical weakening alone is insufficient to account for prolonged slip, and other weakening mechanisms such as the development of high fluid pressures, or dissolution-precipitation creep at low strain rates, must be inferred to have caused a dramatic reduction in fault strength.

5.1. Introduction

Low-angle normal faults that initiated and slipped at dip angles of <30° are recognized in many geological settings in both continental and oceanic lithosphere [e.g. *Anderson*, 1971, *Wernicke*, 1981, *Davis et al.*, 1986, *Lister and Davis*, 1989, *Cann et al.*, 1997, *Manatschal et al.*, 2000, *Hayman et al.*, 2003, *Axen*, 2004, *Karson et al.*, 2006]. They continue to draw widespread attention because their existence apparently contradicts Anderson-Byerlee frictional fault theory that assumes a vertical trajectory of the maximum principal stress, σ_1, and values of the coefficient of friction of 0.6-0.85 [*Anderson*, 1942, *Byerlee*, 1978]. Anderson-Byerlee theory suggests that normal faults should form at dip angles of ~60°, rotate to shallower angles and experience frictional 'lock-up' at angles >30° [e.g. *Collettini and Sibson*, 2001]. The existence of low-angle normal faults indicates that stress orientations must rotate on a regional or local scale [*Yin*, 1989, *Westaway*, 1999, *Faulkner et al.*, 2006], or that slip occurs within a weakened fault zone [e.g. *Collettini and Holdsworth*, 2004, *Holdsworth*, 2004].

Potential mechanisms of fault zone weakening in the mid- to upper-crust include the generation and maintenance of high fluid pressures [*Axen*, 1992, *Rice*, 1992, *Faulkner and Rutter*, 2001], the presence of fault rock materials with a coefficient of friction <0.6 [*Morrow et al.*, 2000, *Moore and Lockner*, 2004a], dynamic fault weakening during co-seismic rupture [*Di Toro et al.*, 2004, *Rice*, 2006, *Han et al.*, 2007a], or a combination of the above. The absence of unambiguously identified moderate-to-large earthquakes along low-angle normal faults [*Jackson and White*, 1989, *Collettini and Sibson*, 2001] suggests that dynamic weakening may be less important in this case, although *Wernicke* [1995] has argued that low-angle normal faults may be characterized by unusually long recurrence intervals, and rare examples of pseudotachylyte along low-angle normal faults have been

documented [e.g. *John*, 1987]. Tensile vein arrays [*Reynolds and Lister*, 1987, *Collettini et al.*, 2006a] and fluidized fault rock materials [Chapter 3; *Smith et al.*, 2008] associated with low-angle normal faults suggests that high fluid pressures can be generated over relatively small areas and for short periods of time. Additionally, laboratory experiments carried out on synthetic and, to a lesser extent, natural fault gouge materials indicate that many sheet structure minerals common within fault zones possess coefficients of friction <<0.6 [*Morrow et al.*, 1982, *Reinen et al.*, 1994, *Moore et al.*, 1997, *Morrow et al.*, 2000, *Saffer et al.*, 2001, *Moore and Lockner*, 2004b, 2008].

Numelin et al. [2007] investigated the frictional properties of natural fault gouge from the Panamint Valley low-angle normal fault located in eastern California, which accommodated slip within a 0.1-1m thick, clay-bearing fault core. They showed that most samples from the fault core have a friction coefficient between 0.6 and 0.7, consistent with standard Byerlee friction coefficents [*Byerlee*, 1978]. However, samples with a significant proportion of clay minerals possessed a friction coefficient of <0.4, and friction decreased with increasing total clay content. *Numelin et al.* [2007] suggested that localization of strain within the weaker portions of the clay-rich fault core could explain slip along the Panamint Valley fault zone within the upper 5km of the crust.

Natural fault zones often contain a complex internal structure [e.g. *Chester and Chester*, 1998, *Faulkner et al.*, 2003, *Wibberley and Shimamoto*, 2003, *Chester et al.*, 2004, *Jefferies et al.*, 2006b]. Natural fault rocks are also highly heterogeneous in terms of their composition, textural characteristics, and distribution, reflecting the heterogeneous nature of wall rock lithologies, a wide range of physical and chemical fault zone processes, and the kinematic history of the fault zone [e.g. *Wibberley et al.*, 2008]. The juxtaposition of different fault rock types within fault zones results in a complex mechanical structure that varies both spatially and temporally, with important implications for earthquake

nucleation, propagation, and arrest, and more generally for the behaviour of fault zones during the seismic cycle [e.g. *Scholz*, 2002, *Wibberley et al.*, 2008]. The most important advances in our understanding of fault zones are likely to arise by combining detailed observations of natural fault zones with tightly constrained laboratory studies, including an assessment of the mechanical properties of fault rock material under different pressure, temperature, fluid, and loading conditions.

In this paper, we investigate the relationships between frictional strength and stability, fault rock mineralogy, and fault zone structure, along the Zuccale low-angle normal fault, a well-studied fault zone exposed on the island of Elba, Italy [*Keller and Coward*, 1996, *Collettini and Holdsworth*, 2004, *Smith et al.*, 2007]. The Zuccale fault may represent a unique opportunity to study a 'passively' exhumed, large-displacement fault zone that appears to have been weak at the time of movement. We seek to test the hypothesis that mineralogical weakening alone could be responsible for prolonged slip along the Zuccale fault. Firstly, we document the textural and mineralogical properties of a series of natural fault rocks found along the Zuccale fault, before reporting the results of triaxial deformation experiments carried out under water-saturated conditions over a range of effective normal stresses. We then compare natural and experimental microstructures using optical and scanning-electron microscopy. Finally, we discuss the implications of our results for the mechanical behaviour of low-angle normal faults.

5.2. Geological Setting and Previous Work

The Zuccale fault is exposed on the island of Elba in the northern Tyrrhenian Sea, around 20km from the west coast of Tuscany (Figure 5.1). The northern Tyrrhenian Sea formed in response to post-orogenic extension, most likely driven by eastwards rollback of

the Ionian-Adriatic subduction zone [*Jolivet et al.*, 1998, *Doglioni et al.*, 1999, *Brunet et al.*, 2000, *Rosenbaum and Lister*, 2004]. Extension migrated progressively from west to east, and was accommodated along a crustal-scale system of shallowly east-dipping low-angle normal faults, in combination with synthetic and antithetic hangingwall structures [Figures 3.1, 6.1; *Barchi et al.*, 1998, *Jolivet et al.*, 1998, *Collettini*, 2002, *Collettini and Barchi*, 2002, *Hunstad et al.*, 2003, *Chiaraluce et al.*, 2004, *Collettini et al.*, 2005, *Collettini et al.*, 2006b, *Pauselli et al.*, 2006, *Chiaraluce et al.*, 2007]. Extension continues at the present-day beneath the Umbria-Marches Apennines in central Italy, where recent geological and geophysical campaigns have highlighted the presence of an active, shallowly east-dipping (~15°) normal fault termed the Altotiberina fault [*Barchi et al.*, 1998, *Collettini et al.*, 2000, *Pauselli et al.*, 2006, *Chiaraluce et al.*, 2007]. The Altotiberina fault creeps at a rate of ~1mm/yr^{-1}, in a stress field characterized by a sub-vertical σ_1 and a sub-horizontal, NE-SW trending σ_3 [*Montone et al.*, 2004]. The fault appears to produce microseismicity (M<2.3) at a nearly constant rate of ~3.5 events per day [*Chiaraluce et al.*, 2007]. It has recently been selected as a world-class target for a deep drilling project, and a full proposal is to be submitted to the International Continental Drilling Programme (ICDP) in the near future [*Cocco et al.*, 2007]. Extension to the west of the Umbria-Marche region has been active for a sufficiently long time to have affected the regional geophysical characteristics: the Tyrrhenian Moho is at a shallow depth of 20-25km, regional heat flow is high (80-120mW/m^2), and the area is characterized by a long-wavelength positive Bouger gravity anomaly [~30-40 mGals; Figure 3.1; *Collettini et al.*, 2006b, *Pauselli et al.*, 2006]. Additionally, regional uplift has exhumed older, inactive low-angle normal faults in the Tyrrhenian islands and in Tuscany, including the Zuccale fault on the island of Elba [*Carmignani and Kligfield*, 1990, *Daniel and Jolivet*, 1995, *Jolivet et al.*, 1998, *Rossetti et al.*, 1999, *Collettini and Holdsworth*, 2004].

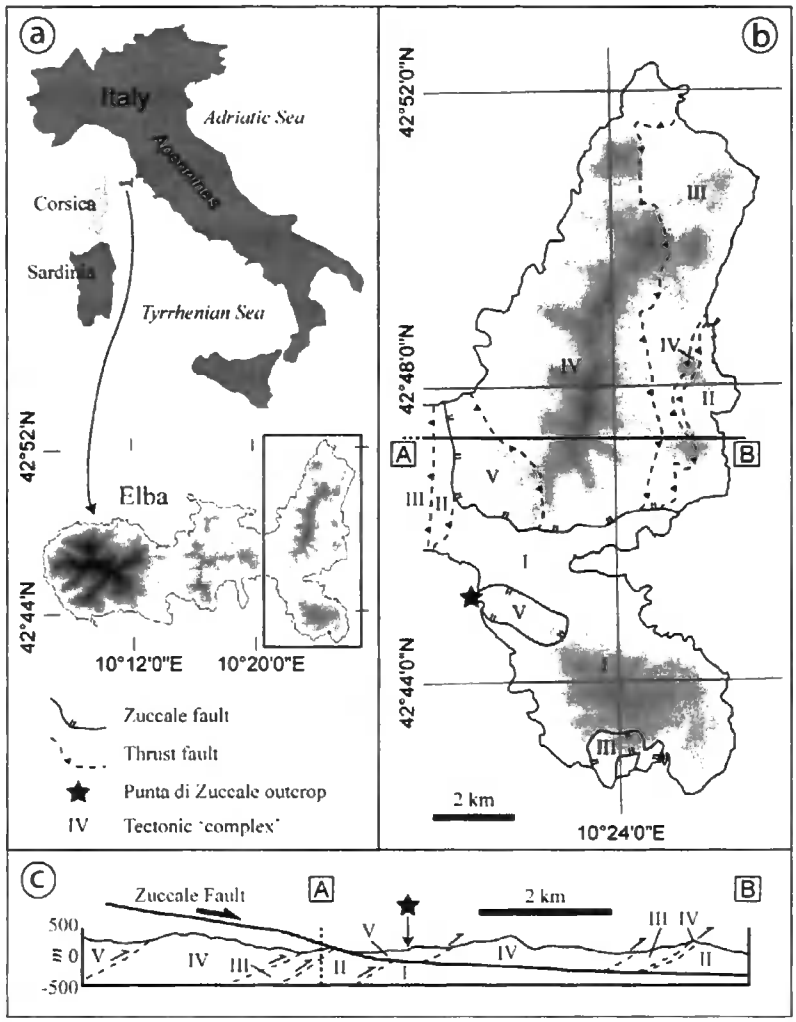

Figure 5.1) Geological setting of the Zuccale fault, **a)** Location of the Island of Elba in the northern Tyrrhenian Sea, **b)** Detail of the eastern side of Elba, where the Zuccale fault outcrops at the surface. I-V refers to the tectonic 'Complexes' of *Trevisan et al.* [1967], which are crosscut and displaced by the Zuccale fault, **c)** Cross-section through central and eastern Elba, highlighting the geometry of the Zuccale fault at depth, determined from structure contour analysis and borehole records [*Bortolotti et al.*, 2001a]. The star in b and c marks the location of the Punta di Zuccale outcrop, where samples were collected for mechanical tests.

The island of Elba consists of a sequence of continental and oceanic units juxtaposed within a thrust stack during Cretaceous-early Miocene collision between the Corsica-Sardinia microplate and the Adriatic plate [Figure 5.1; *Alvarez*, 1972]. *Trevisan et al.* [1967] recognized 5 thrust 'Complexes', composed of diverse lithological units that have continental (Complexes I-III) or oceanic (Complexes IV-V) affinities, all of which

currently dip to the west (Figure 5.1c). The entire thrust stack is crosscut and offset ~6km eastwards by the shallowly east-dipping Zuccale fault, so that on Elba there is a clear repetition of Complexes II-V in the centre and in the east of the island [Figure 5.1c; *Keller et al.*, 1994, *Keller and Coward*, 1996]. The geometry of the Zuccale fault has been affected by pluton intrusion and minor reorientation associated with subsidiary faulting, but there are several lines of evidence to suggest that the Zuccale fault slipped at a low-angle, and thus represents a weak fault (Figure 5.2). These are: 1) Pre-existing thrust faults in the hangingwall of the Zuccale fault have typical Andersonian dips [*Collettini and Holdsworth*, 2004]; 2) There are a suite of high-angle footwall faults that were active synchronously with slip along the main Zuccale fault. The orientation of such footwall faults has been used to place a ~5° limit on the amount of dip rotation experienced by the Zuccale fault [Chapter 2; *Smith et al.*, 2007]. Additionally, some of the footwall faults are part of conjugate sets that, together with the presence of sub-vertical tensile veins, suggest a sub-vertical maximum principal stress; 3) Steep normal faults in the hangingwall sole directly in to main Zuccale fault [*Collettini and Holdsworth*, 2004]; 4) The fault zone can be traced to depths of ~15km beneath the basins to the east of Elba, and appears to dip uniformly ~15° east [*Keller and Coward*, 1996]. There does not appear to be any reorientation of syn-extensional sedimentary strata within the basins, nor is there any noticeable offset of the Zuccale fault along later higher-angle normal faults [*Keller and Coward*, 1996].

The Zuccale fault is particularly well exposed in a series of large coastal outcrops at Punta di Zuccale, where it places a hangingwall of sandstones and siltstones (Complex V) against a footwall of phyllitic and quartzitic schists (Complex I, Figure 5.1). At Punta di Zuccale, a complete and representative section can be observed through the fault zone, and the collection of samples used in this study focussed exclusively on this outcrop. Similar

fault rocks and fault rock sequences are present in other sections of the Zuccale fault on Elba.

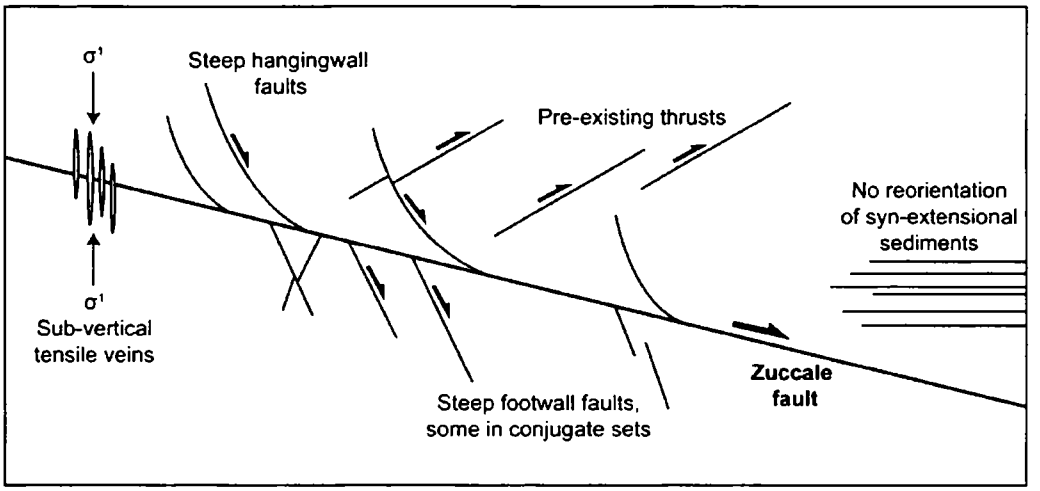

Figure 5.2) Schematic diagram to illustrate the lines of evidence that suggest the Zuccale fault slipped at a low-angle. See *Collettini and Holdsworth* [2004], *Collettini et al.* [2006a], *Keller and Coward* [1996], *Pascucci et al.* [1999] and *Smith et al.* [2007] for details.

The internal structure of the Zuccale fault has previously been described by *Collettini and Holdsworth* [2004] and *Smith et al.* [2007; Chapters 2, 6]. These authors recognized a distinctive fault rock 'stratigraphy' present within the central, 3-8m thick fault core. A representative profile through the fault core is shown in Figure 5.3, highlighting the distribution of different fault rock components, each of which has been labelled using the nomenclature of *Collettini and Holdsworth* [2004]. New mapping and textural analysis, combined with previous results, suggests that there are 5 main fault rock components within the fault core. From bottom to top they are: 1) Green amphibole schists [equivalent to 'L2' of *Collettini and Holdsworth*, 2004]; 2) Orange, white, and green, strongly foliated talc-chlorite-amphibole phyllonites, containing layers and lenses of plastically-deformed calcite-mylonite ['L3' of *Collettini and Holdsworth*, 2004]; 3) Yellow to brown carbonate-

rich foliated cataclasites ['L4' of *Collettini and Holdsworth*, 2004]; 4) Dark brown carbonate-rich fault breccias [part of 'L5' of *Collettini and Holdsworth*, 2004], and; 5) Light to dark brown carbonate-rich foliated fault gouges [part of 'L5' of *Collettini and Holdsworth*, 2004].

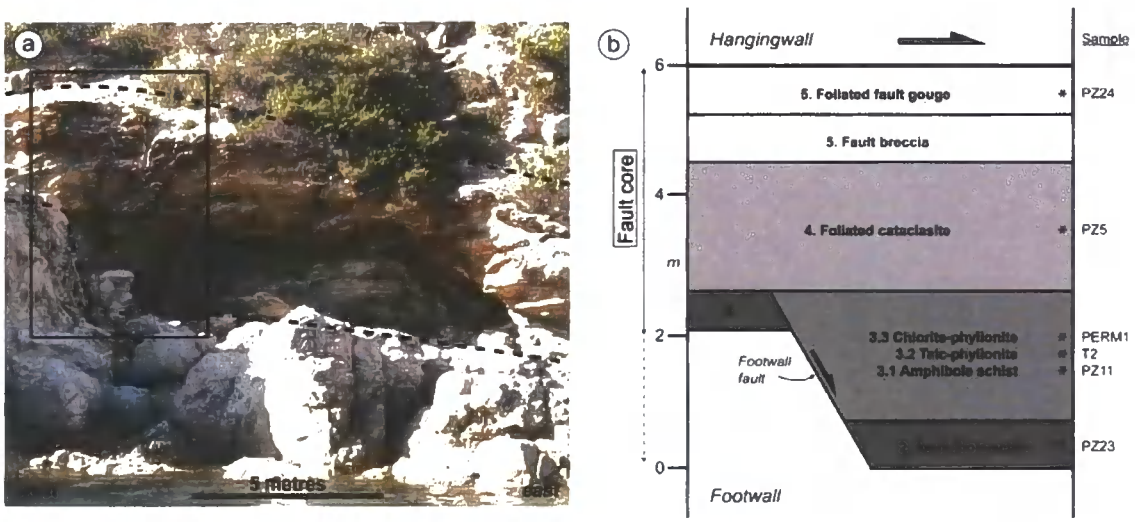

Figure 5.3a) Photograph of the Zuccale fault at Punta di Zuccale. The dashed lines mark the upper and lower margins of the fault core, and the rectangle marks the location of the schematic fault zone profile, **b)** Schematic profile through the Zuccale fault at Punta di Zuccale, after *Collettini & Holdsworth* [2004], *Smith et al.* [2007], and new microstructural analysis to be presented in a Chapter 6. Numbers 2-5 refer to the fault rock components discussed in the text, and are taken from the nomenclature of *Collettini and Holdsworth* [2004]. The original sample numbers are given on the right hand side, and correspond to the experiment numbers in Table 5.2. Note that the lower margin of the fault core is displaced by a series of high-angle footwall faults, resulting in fault core component 3 occurring as large isolated lenses that are not interconnected on a scale of tens to hundreds of metres [*Smith et al.*, 2007; Chapter 2].

We sampled 4 of the main fault rock components for mechanical tests (Figure 5.3), all of which exhibit grain-scale evidence for having deformed entirely, or partly, by frictional slip, cataclasis and/or particulate flow (Chapter 6). The fault breccias (part of component 5) are chaotic in nature and consist of large (up to 20cm), angular clasts predominantly derived from the underlying foliated cataclasites (component 4), set within a fine-grained carbonate- and quartz-rich matrix (Chapter 6). Due to the size of the clasts, they were not suitable for mechanical tests. The phyllonites (component 3) contain layers that are

dominated by varying proportions of talc, chlorite, amphibole and calcite. For this reason, we collected 3 samples from different parts of fault rock component 3 to assess its strength heterogeneity (Figure 5.3). We did not aim to reproduce crystal-plasticity in this set of experiments, and hence we did not sample the layers of calcite-mylonite within fault rock component 3, although it is interesting to note that they display evidence for cyclic frictional-viscous deformation.

5.3. Methodology

5.3.1. Sample characterization

Thin sections of each natural fault rock component were investigated using optical microscopy. Additionally, small chips of natural fault rock material were prepared and polished for scanning electron microscope (SEM) investigation, the primary purpose of which was to compare natural and experimental microstructures. Thin sections and rock chips were cut perpendicular to the macroscopic foliation and parallel to the sample lineation, or the mean lineation direction within the fault core. X-ray diffraction (XRD) analysis was performed on each sample, followed by Rietveld refinement using Siroquant software, allowing us to place important constraints on modal mineralogy (Table 5.1).

5.3.2. Experimental procedure

The experimental apparatus used in this study was a high-pressure high-temperature triaxial deformation apparatus with a servo-controlled axial loading system and fluid pressure pump [*Mitchell*, 2006, *Mitchell and Faulkner*, 2008]. The apparatus is located in

Sample	Component	Quartz %	K-feldspar %	Amphibole %	Calcite %	Dolomite %	Chlorite %	Talc %	Kaolinite %
Fault gouge	5	38	2		25	19	16		SEM
Foliated cataclasite	4	49			1	45			5
Chlorite-phyllonite	3.3			17	55		12	16	
Talc-phyllonite[†]	3.2			10	20			70	
Amphibole schist	3.1	1		39	60				
Amphibole schist	2	2		95	3				

[†]Estimated from thin section and SEM observations

Table 5.1) XRD results. Error is typically ±5%

the Rock Deformation Laboratory at Liverpool University, and can perform triaxial experiments up to 250MPa confining pressure. Silicone oil was used as a confining medium, and distilled water as a pore fluid. During the course of the experiments, the upstream pore pressure was servo-controlled to a resolution of 50Pa, and the axial load was measured using a calibrated internal force gauge with a resolution of 10Pa [*Mitchell*, 2006, *Mitchell and Faulkner*, 2008]. Axial displacement was measured externally using a displacement Linear Variable Differential Transformer (LVDT) that is in contact with the moving piston [*Mitchell*, 2006, *Mitchell and Faulkner*, 2008].

Triaxial experiments were conducted on powdered material of fault rock components 2, 3, 4, and the foliated fault gouges of component 5. Several duplicate tests were carried out to assess the reliability of our results (Table 5.2). Sample powders were prepared by passing thumb-sized pieces of material through a porcelain jaw crusher until they had disaggregated. Fault rock components 2, 3 and 5 were friable and disaggregated easily, whereas component 4 was more cohesive. Each disaggregated sample was passed through a series of sieves to produce the desired grain size fractions. In the experiments reported here we used the 63-125μm grain size fraction.

An initially 1mm-thick layer of sample powder was placed between 18.5mm-diameter forcing blocks containing a 30° sawcut surface. A schematic diagram of the sample assembly is shown in Figure 5.4. Both forcing blocks were made from a circular cylinder of hardened steel, and the elliptical sawcut surfaces were roughened prior to each

experiment using 400-grade abrasive grit sheets to reduce decoupling between the forcing blocks and the sample powders. The powder was initially applied to one of the sawcut surfaces as a thick slurry and allowed to dry in the open air for approximately 60 minutes. The forcing blocks containing the gouge layer were inserted in to a polyolefin jacket, a ~0.35mm thick annealed copper jacket, and an outer PVC jacket. This arrangement prevented any leakage of pore fluid between the forcing blocks and the copper jacket during the course of the experiments. The PVC jacket ensured that if the copper jacket ruptured during shear, confining fluid could not enter the sample. Inclusion of a Teflon spacer at the downstream end of the sample assembly allowed decoupling of the lower forcing block, preventing any rotation of the forcing blocks during the experiments.

Experiment	Sample	[1]Component	[2]σ_n^{eff} (MPa)	[3]Velocity steps (μm/s)	Behavior	[4]Thickness (mm)
PZ24_1	Fault gouge (wet)	5	25,50,75	-	Stable sliding	0.45
PZ24_2	Fault gouge (dry)	5	25,50,75	-	Stable sliding	-
PZ5_1	Foliated cataclasite	4	25,50,75	0.1, 1	Stable sliding	0.7
PZ5_2	Foliated cataclasite	4	25,50,75	-	Stable sliding	-
PERM1_1	Chlorite-phyllonite	3.3	25,50.75	0.1,1	Stable sliding	0.3
PERM1_2	Chlorite-phyllonite	3.3	50,75	-	Stable sliding	-
T2	Talc-phyllonite	3.2	25,50.75	0.1,1	Stable sliding	0.38
PZ11_1	Amphibole schist	3.1	50,75	0.1,1	Stable sliding	-
PZ23_1	Amphibole schist	2	25,50,75	-	Stick-slip	-
PZ23_2	Amphibole schist	2	25,50,75	-	Stick-slip	-
PZ23_3	Amphibole schist	2	60	0.1, 1	Stick-slip	0.5

[1]Corresponds to the fault rock component labelled in Figure 3
[2]Effective normal stresses
[3]Initial run-in performed at 0.3μm/s for ~250μm
[4]Initial thickness of sample powder = 1mm

Table 5.2) Summary of friction experiments

We designed our experiments to assess the frictional strength and stability of the fault rock material under water-saturated conditions at effective normal stresses of 25MPa, 50MPa, and 75MPa. All experiments were conducted at room temperature. Confining pressures were initially increased to 75MPa, and pore pressures to 50MPa, equivalent to an effective normal stress of 25MPa. Pore fluid was introduced through two small holes 1mm

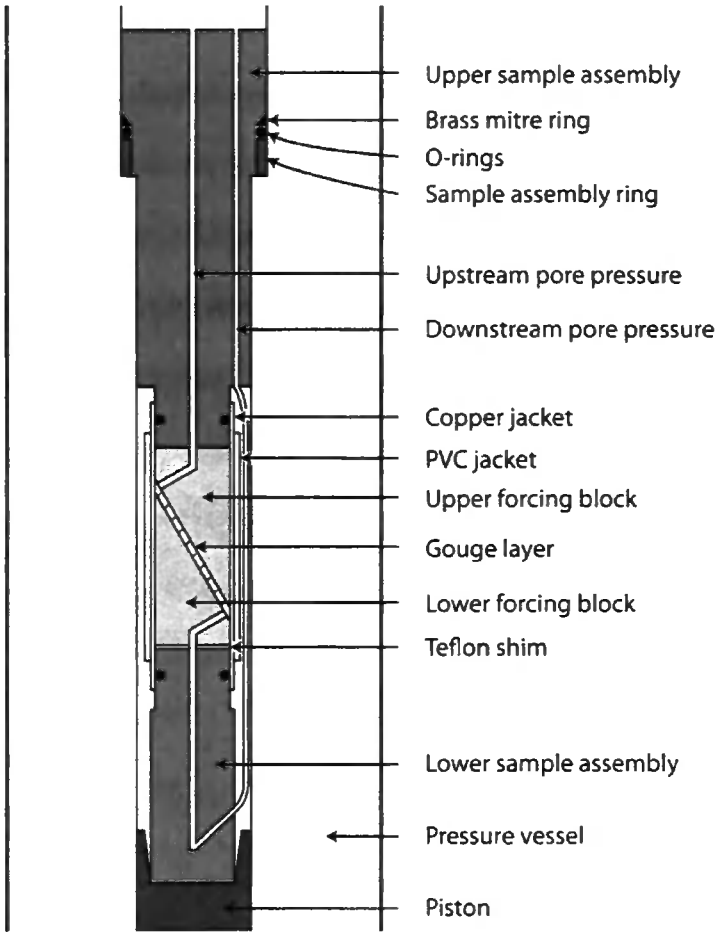

Figure 5.4) Schematic diagram of triaxial deformation apparatus.

in diameter that were drilled perpendicular to the sawcut surfaces in the steel forcing blocks. Pore fluid was allowed to equilibrate for approximately 60 minutes before commencing the experiments. In all the experiments we performed an initial run-in at an axial displacement rate of 0.3μm/s for ~250μm, or until the sample had clearly experienced yield. Typically, we sheared each sample at each effective normal stress for a total of ~1.4mm, producing a total axial displacement of ~4.2mm. This corresponds to a displacement along the sawcut surface of ~4.9mm. In some of the experiments (Table 5.2), we performed a series of velocity steps (0.1μm/s-1μm/s and 1μm/s-0.1μm/s) at each effective normal stress to characterise the velocity dependence of the fault rock material

(described in detail below). Throughout each experiment, the normal stress was maintained at a constant value using servo-controlled adjustments to the confining pressure. The mechanical data were corrected for the elastic axial distortion of the deformation apparatus. Following *Llana-Fúnez and Rutter* [2008], we chose not to correct the mechanical data for variations in the overlap area of the two elliptical forcing blocks during progressive displacement. In addition, we have chosen to report the raw mechanical data without applying a correction for the strength of the copper jacket. However, we did carry out friction experiments using thin sheets of Teflon instead of sample powder. The frictional properties of Teflon are well known, so we were able to calculate the approximate shear strength of the copper jacket, reported in Figure 5.6. The copper jackets appear to contribute ~0.04 to the friction coefficient at yield.

Following the experiments, fragments of the deformed powders were immersed under vacuum in low-viscosity resin and polished samples were prepared for SEM investigation. The experimental samples were cut perpendicular to the deformed sample powder and approximately parallel to the shearing direction.

5.4. Results

5.4.1. Composition and textural characteristics of natural fault rock samples

A more complete characterization of the fault rocks found along the Zuccale fault is presented in Chapter 6, but a brief description of the samples used for mechanical tests is provided below, accompanied by the results of XRD analyses in Table 5.1.

Amphibole schists (fault rock component 2) occur as a dark green to black, 5cm-1.5m thick layer at the base of the fault core (Figure 5.3). They are dominated by a matrix of platy, fine-grained (<50μm) amphibole crystals (Figure 5.5a). The matrix is crosscut by

numerous discrete cataclastic horizons that appear to have focussed Fe-bearing fluids (Figure 5.5b). The matrix wraps around fractured porphyroclasts of amphibole ranging in diameter from <50μm to several mms. The porphyroclasts contain intragranular fractures that accommodated progressive comminution and grain size reduction.

Talc- and chlorite-phyllonites (fault rock component 5.3) occur as large discontinuous lenses of material towards the base of the fault core. Their distribution is strongly controlled by the presence of subsidiary footwall faults, such that the thickness of this component varies locally between 0-5m [*Smith et al.*, 2007; Figure 5.3]. They are dominated by a strongly foliated matrix of fine-grained (<200μm) talc, chlorite, and minor amphibole grains, that surround polycrystalline ribbons and rounded porphyroclasts of calcite (Figures 5.5c, d). The phyllonites are also associated with layers containing only calcite and amphibole. We collected one sample containing 60% calcite and 39% amphibole (component 3.1, labelled as amphibole schists), one sample containing a total of 28% talc and chlorite (component 3.3, labelled as chlorite-phyllonites), and one sample containing ~70% talc (Component 3.2, labelled talc-phyllonites).

Foliated cataclasites (fault rock component 4) are the most volumetrically important fault rocks within the core of the Zuccale fault, and occur as a 3-4m thick unit in the centre of the fault core (Figure 5.3). They are dominated by quartz and dolomite, with subsidiary kaolinite and calcite (Figures 5e, f). The foliated cataclasites contain a strong mesoscopic P-foliation [Figure 5.5e; *Rutter et al.*, 1986], but a grain-scale foliation is typically not visible (e.g. Figure 5.5f) except in areas with a high concentration of clay phases. Grains of quartz and dolomite in the matrix are crosscut by intragranular fractures resulting in angular grain shapes and progressive grain size reduction (Figure 5.5f inset).

Foliated fault gouges (fault rock component 5) occupy the uppermost fault core (Figure 5.3), and are dominated by varying proportions of quartz, calcite, dolomite, and

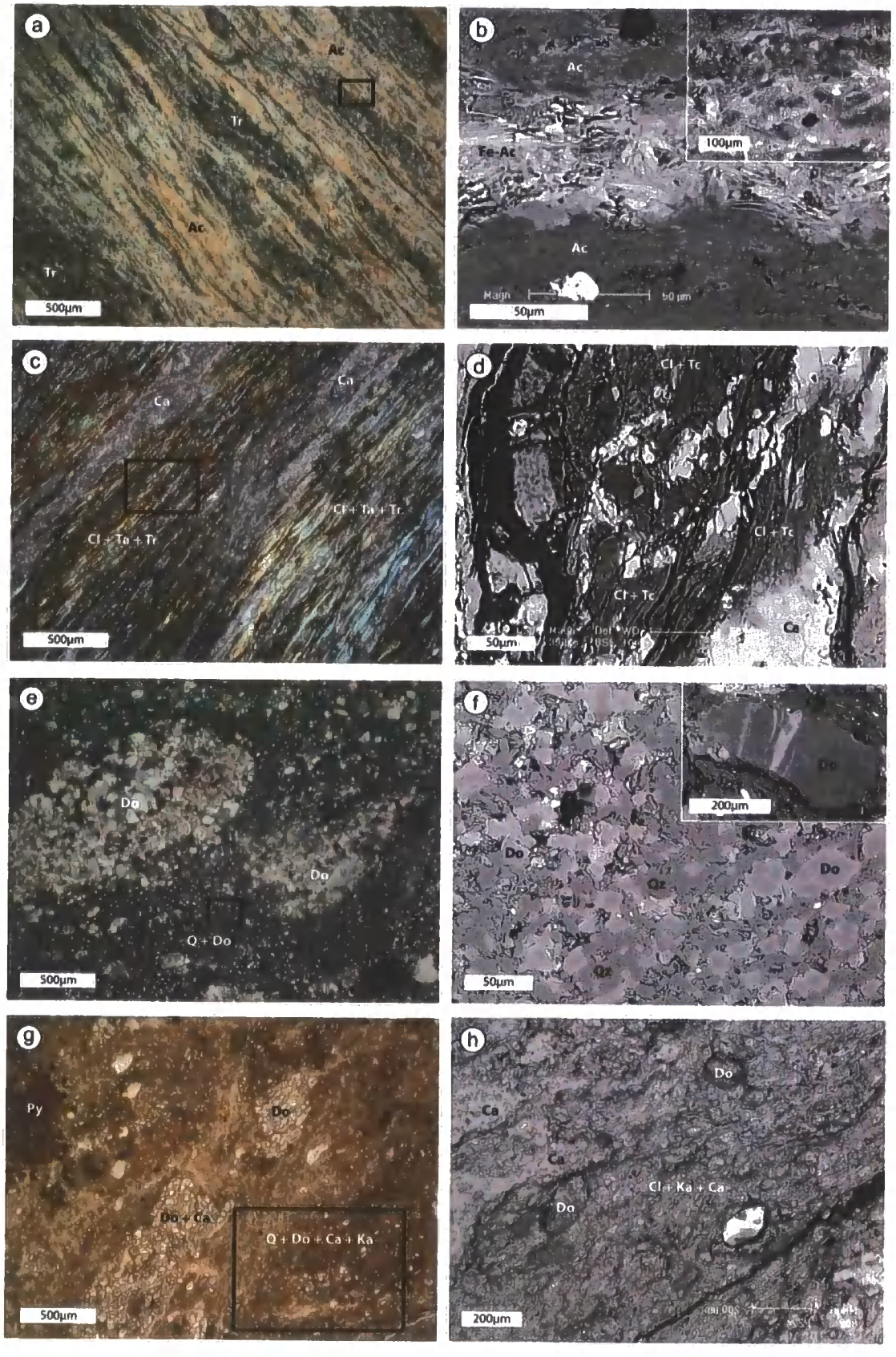
a
Ac
Tr
Ac
Tr
500µm
b
Ac
Fe-Ac
100µm
Ac
50µm
c
Ca
Ca
Cl + Ta + Tr
Cl + Ta + Tr
500µm
d
Cl + Tc
Cl + Tc
Cl + Tc
Ca
50µm
e
Do
Do
Q + Do
500µm
f
200µm
Do
Do
Qz
Do
Qz
50µm
g
Py
Do
Do + Ca
Q + Do + Ca + Ka
500µm
h
Do
Ca
Ca
Cl + Ka + Ca
Do
200µm

Figure 5.5) Optical photomicrographs and back-scattered SEM images illustrating the microstructural characteristics of natural fault rock samples. Left hand column are optical photomicrographs in crossed- (a, c, e) and plane- (g) polarised light. Right hand column are SEM images. The black boxes in the left hand column highlight the detail shown in the right hand column. The following abbreviations apply: Tr, tremolite; Ac, actinolite; Ca, calcite; Cl, chlorite; Tc, talc; Q, quartz; Do, dolomite; Ka, kaolinite; Py, pyrolusite, **a)** Amphibole schists containing a compositional banding of tremolite and actinolite layers up to several hundred microns thick. Porphyroclasts of tremolite are fractured and elongated within the actinolite matrix, **b)** Two images of cataclastic horizons within the actinolite matrix. The white grains are relatively Fe-rich actinolite, **c)** Phyllonites containing a compositional banding of chlorite-, talc- and tremolite-rich layers with calcite-rich layers, **d)** Detail of chlorite- and talc-rich layer enveloping rounded and fractured porphyroclasts of calcite. The chlorite and talc grains are typically strongly aligned and present as an interconnected network, **e)** Foliated cataclasites dominated by quartz and dolomite. Dolomite occurs as large polycrystalline porphyroclasts that are extensively fractured within a dolomite and quartz matrix. Note the alignment of the dolomite clasts that contributes towards a macroscopic P-foliation observed in the field, **f)** Detail of quartz and dolomite matrix. No alignment of grains is visible in this example. The inset image shows an intragranular fracture filled with relatively Fe-rich dolomite crosscutting a grain of relatively Fe-poor dolomite, **g)** Foliated fault gouges dominated by a fine-grained matrix of quartz, calcite, dolomite and kaolinite, surrounding survivor grains which include polycrystalline calcite and dolomite. Note post-tectonic growth of dendritic pyrolusite, **h)** Detail of fault gouge matrix, showing an alignment of small survivor grains of dolomite, within a foliated matrix of chlorite, kaolinite, and calcite.

clay phases such as chlorite and kaolinite (Figures 5.5g, h; the latter not revealed by bulk XRD analysis). SEM investigations suggest that the fine-grained matrix fraction is dominated by chlorite and kaolinite. The matrix contains a P-foliation defined by an alignment of platy chlorite and kaolinite, and by an alignment of elongate survivor grains of quartz and dolomite (Figure 5.5h). Overall, the fault gouges are noticeably finer-grained than the other fault rock components, with matrix phases typically being <20μm in diameter. There is little evidence in the fault gouges of grain fracturing and progressive grain size reduction, particularly within the fine-grained matrix. This suggests that deformation was achieved by rolling and sliding of grains past one another in the absence of grain fracturing, a deformation mechanism that has been termed 'particulate flow'. *Rawling and Goodwin* [2003] observed particulate flow in poorly lithified sediments deformed at low confining pressures (less than ~30MPa). *Cladouhos* [1999b], *Cowan et al.* [2003], and *Hayman* [2006] suggested that particulate flow was the dominant deformation mechanism at depths of less than 2km in the fault gouges that formed along the Black

Mountains detachments in Death Valley, California. The foliated fault gouges along the Zuccale fault contain survivor grains of dolomite and polycrystalline dolomite derived from the underlying fault rock components (Chapter 6), suggesting that they were the last fault rock component to form. Based on this, and on the dominance of particulate flow, we suggest that the fault gouges formed at depths of less than ~2km.

5.4.2. Triaxial friction experiments

5.4.2.1. Frictional strength

Figures 5.6 and 5.7 present a summary of triaxial friction experiments at 25MPa, 50MPa and 75MPa effective normal stress carried out on the six fault rock components shown in Figure 5.3, in addition to the strength of the copper jacket. For the samples for which we carried out duplicate tests (Table 5.2), only the experiment without velocity steps is shown for clarity in Figure 5.6. Reproducibility of duplicate tests was generally good. The largest difference in the friction coefficients (μ=0.07) between repeat experiments occurred for the chlorite phyllonites (component 3.3) at 75MPa (Figure 5.7). For all the other repeat experiments at each confining pressure, the differences in μ were $\leq$0.05, and are sufficiently small that they do not affect any comparisons of the relative strengths between the different fault rock components (Figure 5.7).

All of the samples experienced yield at <300μm axial displacement, and then followed similar strain hardening trends (Figure 5.6). Values of μ discussed herein, and shown in Figure 5.7, were measured after 500μm axial displacement (grey bar in Figure 5.6), and after 0.06 had been subtracted for the contribution to μ by the copper jackets (Figure 5.6).

Overall, μ ranges between 0.25-0.80, emphasizing the marked strength heterogeneity that can exist within natural fault zones. With the exception of the talc- and chlorite-

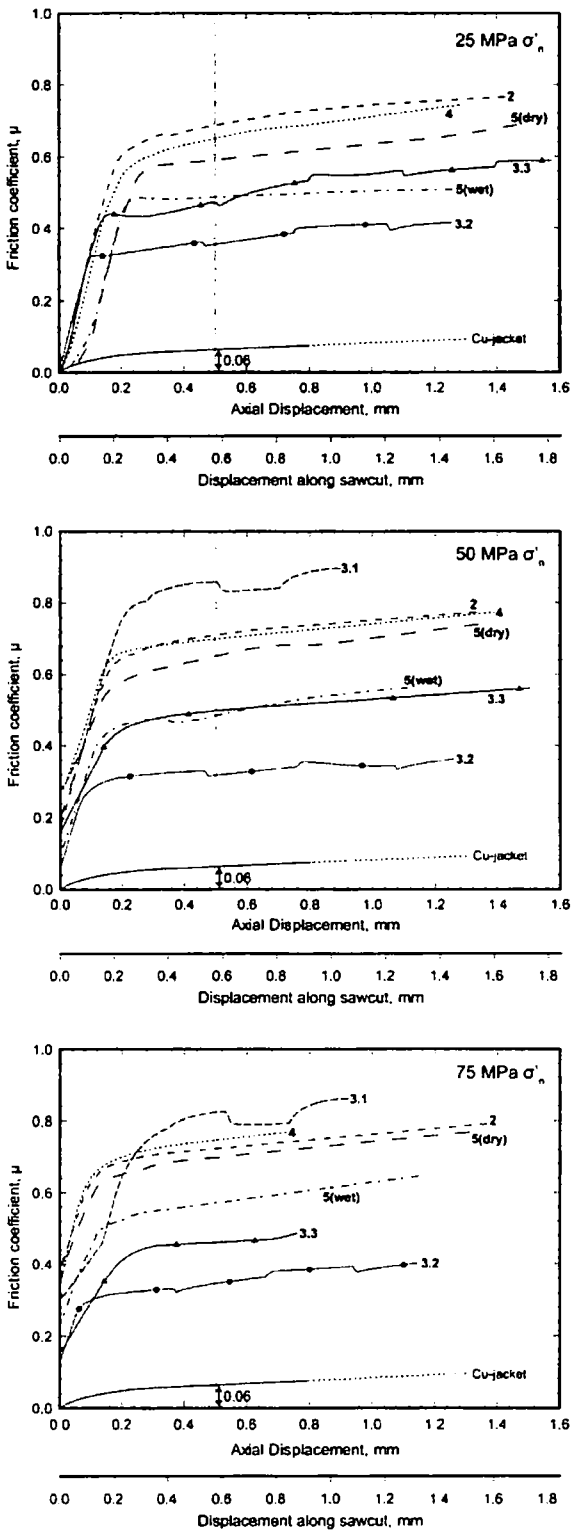

Figure 5.6) Summary of friction experiments carried out on the different fault rock components at 25, 50 and 75MPa effective normal stress. The strength of the copper jacket, determined from tests using teflon wafers, is also shown. Each of the curves is labelled with the number of the fault rock component shown in Figures 5.3 and 5.11. The grey bar at 500μm axial displacement is where the friction values in Figures 5.7 and 5.11, and discussed in the text, were taken from. At 500μm axial displacement, the copper jacket contributes ~0.06 to the friction coefficient.

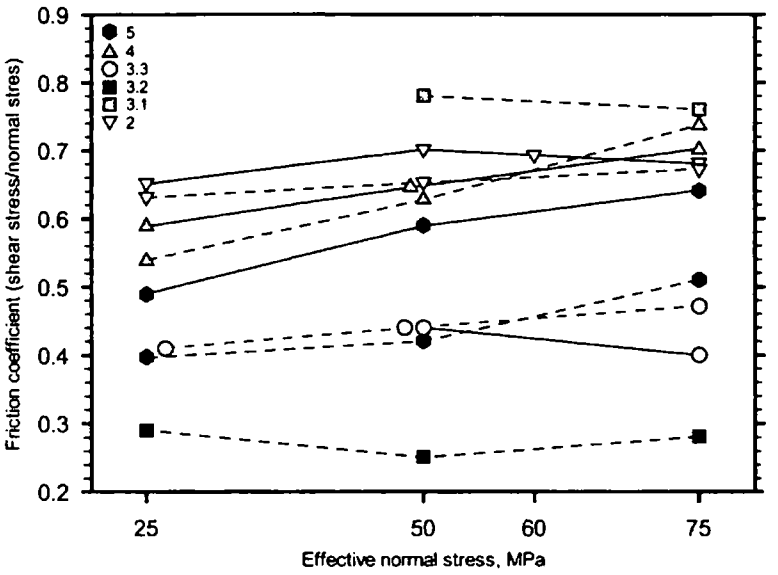

Figure 5.7) Friction coefficient versus effective normal stress for all of the fault rock components tested. Note the addition of one experiment carried out at 60MPa normal stress on component 2. For some of the samples, we carried out duplicate tests. Solid lines represent experiments without velocity steps, and dashed lines represent experiments with velocity steps. For samples that display identical friction coefficients, the symbols have been moved to one side for clarity.

phyllonites, μ increases with increasing effective normal stress (Figure 5.7). At 25MPa effective normal stress, μ varies between 0.29-0.65. The talc- and chlorite-phyllonites, and the water-saturated fault gouges, have μ ≤0.41. The talc phyllonites are the weakest samples with μ=0.29. The foliated cataclasites and the amphibole schists have μ ≥0.54. At 50MPa effective normal stress, μ varies between 0.25-0.80. The talc- and chlorite-phyllonites, and the water-saturated fault gouges have μ ≤0.44. The talc-phyllonites remain the weakest samples with μ=0.25. The foliated cataclasites and amphibole schists have μ ≥0.63. At 75MPa effective normal stress, μ varies between 0.28-0.76. The talc- and chlorite-phyllonites remain the weakest samples with μ ≤0.47, and the talc-phyllonites have μ=0.28. The water-saturated fault gouges have μ=0.51. The foliated cataclasites and amphibole schists have μ ≥0.64. The dry strength of the fault gouges is 0.1-0.18 greater than the water-saturated strength.

5.4.2.2. Velocity dependence of strength

The rate dependence of frictional strength can be characterized by the change in steady-state friction coefficient, $\Delta\mu_{ss}$, that occurs after imposing a logarithmic change in sliding velocity, $\Delta\mu_{ss}/\Delta\ln V$ (Figure 5.8). This is equivalent to the quantity *(a-b)*, where *a* represents the so-called 'direct effect' in the framework of rate-and-state friction, and *b* represents an evolution effect that occurs over a critical slip distance [*Dieterich*, 1979, *Ruina*, 1983, see *Marone*, 1998 for a comprehensive review]. When *(a-b)* is positive, the material is said to be velocity strengthening, leading to inherently stable behaviour. If *(a-b)* is negative, the material is velocity-weakening, and this can potentially lead to unstable behaviour [*Dieterich*, 1979, *Ruina*, 1983]. Due to the limited displacements that could be achieved during the experiments, only 2 or 3 velocity steps were carried out at each effective normal stress. In our experiments, we imposed velocity changes from 0.1μm/s to 1μm/s and from 1μm/s to 0.1μm/s. We observed that the 0.1μm/s to 1μm/s velocity steps were generally characterized by a poorly-defined and delayed direct effect (Figure 5.8). We believe that this resulted from using impermeable steel forcing blocks, which meant that pore fluids required a relatively long period of time to equilibrate with the low-permeability samples following an increase in sliding velocity. This delayed response is not observed following decreases in sliding velocity, because pore fluids had sufficient time to equilibrate with the samples (Figure 5.8). We have only used the 1μm/s to 0.1μm/s velocity steps to determine the values of *(a-b)*, but this means that, with the exception of the chlorite-phyllonites at 25MPa effective normal stress, only one velocity step was available to determine *(a-b)*. Further experiments carried out to higher displacements, and with a larger number of velocity steps, are required to confirm our preliminary measurements. The Windows-based software programme xlook was used to process the

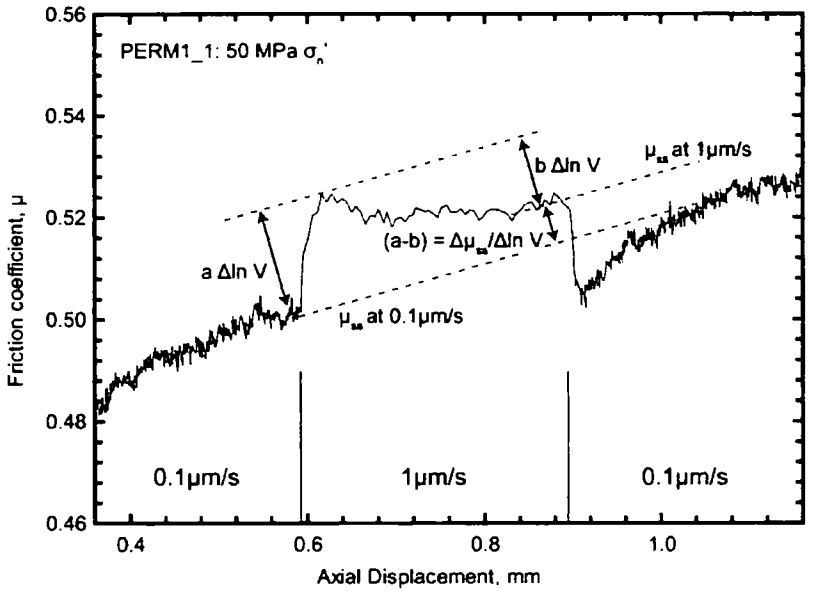

Figure 5.8) Diagram of a velocity step excerpted from experiment PERM1_1 at 50MPa effective normal stress (Table 5.2). Velocity steps from 0.1μm/s to 1μm/s are associated with a delayed and 'rounded' direct effect, that we believe reflects our use of steel forcing blocks (see text for discussion). Only the 1μm/s to 0.1μm/s velocity steps were used to determine the quantity *(a-b)*. If *(a-b)* is positive, the material is said to be *velocity-strengthening*. If *(a-b)* is negative, the material is said to be *velocity-weakening*.

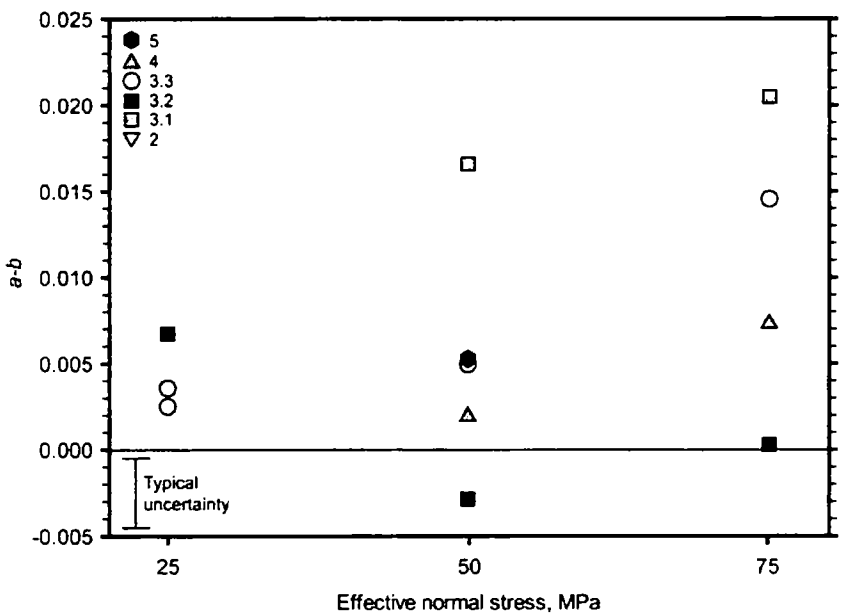

Figure 5.9) *(a-b)* versus effective normal stress.

velocity-stepping friction data [obtained from Chris Marone, Pennsylvania State University, personal communication]. This programme uses an iterative least-squares method to model rate-and-state friction parameters. The programme has the capability of removing the effects of strain hardening, and also takes in to account the stiffness of the apparatus loading column. *Blanpied et al.* [1995] have suggested that the contribution of the copper jacket to the quantity *(a-b)* is <0.0002.

All except one of the measured values of *(a-b)* are positive (Figure 5.9). The talc-phyllonites (component 3.2) displayed velocity-weakening behaviour at 50MPa effective normal stress. In other words, the steady-state frictional strength of most of the fault rocks increases following an increase in sliding velocity, and they can be defined as velocity-strengthening materials over the range of sliding velocities measured. After imposing a change in sliding velocity, most samples exhibited an instantaneous direct-effect, followed by an evolution effect of the opposite sign, before returning to a new steady-state frictional strength (Figure 5.8). However, the amphibole schists (component 3.1), and the chlorite-phyllonites at 75MPa effective normal stress (component 3.3), displayed a negative b value, resulting in relatively large values of *(a-b)* (Figure 5.9). The physical basis for this behaviour remains poorly understood, although similar behaviour has been observed in some wet clays, including talc [*Moore and Lockner*, 2008].

5.4.3. Textural characteristics of experimental gouge samples

All of the experimental samples accommodated slip by distributed deformation, and we observed no localization of slip along boundary shears at the margins between the sample powders and the steel forcing blocks. All the samples experienced significant compaction (Table 5.2). After loading and shearing at 75MPa effective normal stress, the

samples containing phyllosilicates were ≤0.4mm thick, whilst the samples dominated by amphibole, quartz, calcite, and dolomite compacted from 1mm to 0.5-0.7mm.

The samples of amphibole schist (components 2 and 3.1) and foliated cataclasite (4) accommodated slip by intensive fracturing and grain size reduction of constituent clasts (Figure 5.10a, b). Fracturing of clasts was most evident at the contacts between large grains (Figure 5.10a). Amphibole schists contain clasts of tremolite and actinolite that lie within a fine-grained matrix of comminuted tremolite, actinolite and Fe-rich actinolite (Figure 5.10a). None of the clasts exhibit a preferred orientation, and there is no localization of slip within cross-cutting Riedel shear bands. The sample of foliated cataclasite is characterized by clasts of quartz and dolomite that lie within a fine-grained comminuted matrix (Figure 5.10b). There is no alignment of grains, but the foliated cataclasites are crosscut by relatively fine-grained, incipient Riedel R_1-shears that lie at an angle of ~20° to the margins of the deformed sample.

The samples of chlorite and talc-phyllonite (components 3.2 and 3.3) both contain a strong foliation that parallels the margins of the deformed sample (Figure 5.10c). The foliation is defined by an alignment of platy chlorite and talc grains that wrap around angular, fractured clasts of calcite to form an interconnected network. The calcite grains show no preferential alignment, and there is no localization of slip within cross-cutting shear bands.

The fault gouges (component 5) are noticeably finer-grained than the other samples (Figure 5.10d). They contain clasts of calcite and dolomite not exceeding 100μm in size, although usually they are <<50μm. Relatively large clasts sit within a fine-grained (<10μm) matrix of comminuted dolomite and calcite, and a platy Al-silicate clay phase, most likely to be kaolinite (Figure 5.10d). Chlorite is also an important constituent of the

matrix. There is no alignment of grains in the matrix, and no localization of slip within shear bands.

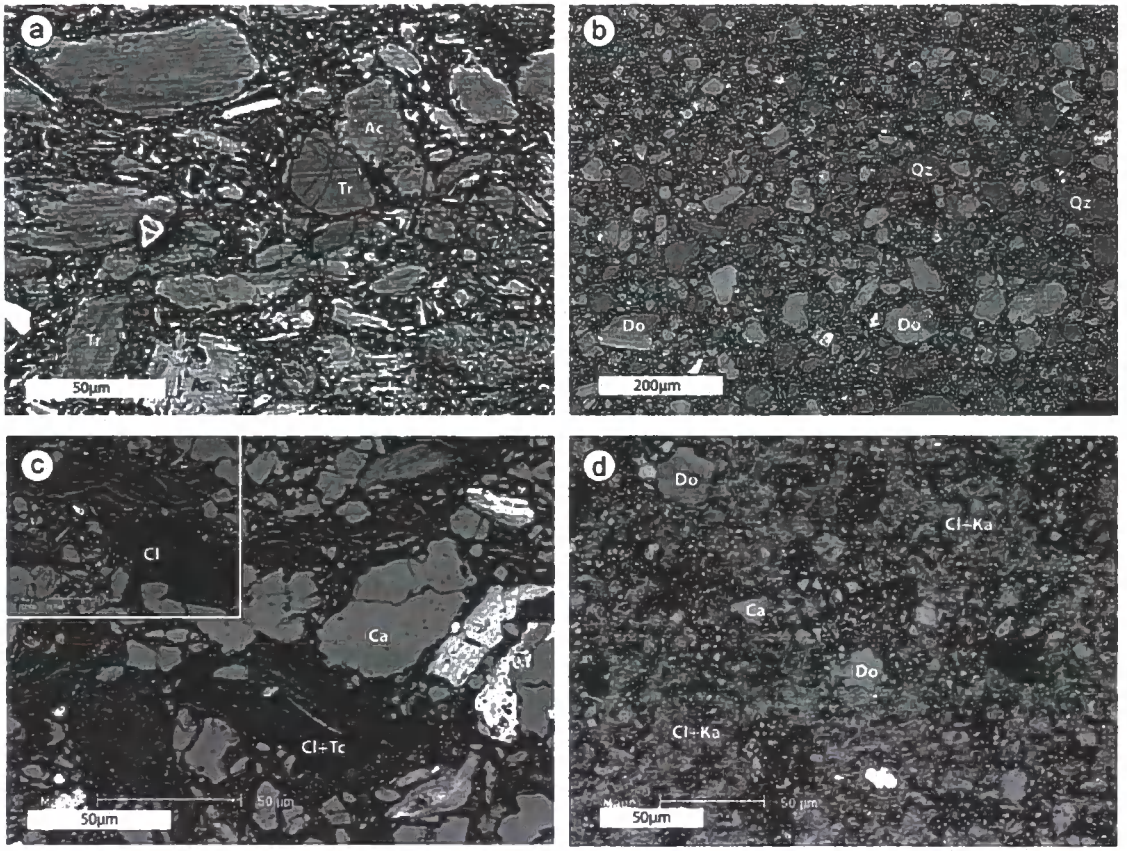

Figure 5.10) Back-scattered SEM images showing the microstructural characteristics of experimentally deformed fault rock powders. All samples were cut perpendicular to the deformed gouge layer and approximately parallel to the shearing direction. All of the samples are characterized by distributed deformation, and none show evidence for localization of slip along boundary shears, **a)** Amphibole schists (fault rock components 2 and 3.1) showing cataclastic grain size reduction and grain rotation. Note the presence of Hertzian fractures at the contact of the 2 grains which are labelled in the centre of the image, **b)** Foliated cataclasites (component 4) showing cataclastic grain size reduction and grain rotation. There is no evidence for grain alignment in this sample, although it is cross-cut by incipient Riedel R^1-shears that extend from the upper to lower boundary of the deformed sample, **c)** Phyllonites (components 3.2 and 3.3) showing a strong foliation defined by an alignment of platy, interconnected chlorite and talc grains. The chlorite and talc wrap around porphyroclasts of calcite, **d)** Foliated fault gouges (component 5) are characterized by small, rounded survivor grains of calcite and dolomite within a fine-grained matrix of chlorite and kaolinite.

5.5. Discussion

The interpretation of our experimental results must be made with some caution, because the imposed conditions are not equivalent to those that were likely operating along the Zuccale fault. Firstly, the displacement rates at which deformation occurred within the Zuccale fault (equivalent to average long-term slip rates of approximately 0.0001μm/s – 0.00001μm/s) are significantly lower than those imposed during the experiments. Secondly, the experiments cannot reproduce the high strains that were clearly accommodated by all of the fault rock components within the Zuccale fault, and hence they cannot provide information on the evolution of strength during the development of strong foliations, or the evolution of strength during the formation and destruction of localized shear planes. Thirdly, they cannot reproduce the effects of introducing a chemically active pore fluid, or the influence of elevated temperatures. Nevertheless, the experiments can provide important information on the relationships between frictional strength and mineralogy, and they serve to highlight any fault rock components that may have resulted in mineralogical weakening. Previous experiments carried out on a wide range of materials have demonstrated that decreases in sliding velocity, the development of foliations and Riedel fabrics (particularly when phyllosilicate-rich), and the introduction of chemically active pore fluids, all lead to marked reductions in frictional strength [e.g. *Cox and Paterson*, 1991, *Shea and Kronenberg*, 1993, *Marone*, 1998, *Mair and Marone*, 1999, *Giger et al.*, 2008]. For this reason, we consider our experimental results to represent an upper limit for the strength of fault rock materials within the Zuccale fault.

5.5.1. Relationship between frictional properties and fault rock mineralogy

Our results suggest that the frictional strength and stability of the different fault rock components within the Zuccale fault is strongly dependent on mineralogy and the presence or absence of well developed microstructural fabrics.

Amphibole schists at the base of the fault core (component 2), and mixed amphibole-calcite lithologies (component 3.1), are characterized by friction coefficients between 0.65 and 0.8. Experimental data on the frictional properties of amphibole are scarce, but it is not expected to be weak under the experimental conditions used in this study, and most likely possesses 'typical' Byerlee friction values in the range 0.6-0.85 [*Byerlee*, 1978]. *Morrow et al.* [2000] reported μ~0.7 for wet calcite gouge deformed at room temperature and 100MPa effective normal stress.

The weakest samples within the core of the Zuccale fault are the talc- and chlorite-phyllonites, that have frictional strengths of 0.25-0.3 and 0.4-0.47, respectively. The friction coefficients of the talc-phyllonites are similar to those reported by *Moore & Lockner* [2008] for pure talc gouge deformed under water-saturated conditions at room temperature and effective normal stresses up to 300MPa (μ in the range 0.16-0.23). They also found that the dependence of μ on effective normal stress was smaller for talc than for other sheet silicate minerals such as montmorillonite and muscovite. Although our experiments only extend from 25MPa to 75MPa effective normal stress, our results are broadly consistent with the observations of *Moore & Lockner* [2008], as we observe no obvious stress dependence of μ for the talc-phyllonites. The friction coefficients for the chlorite-phyllonites are similar to those reported by *Moore & Lockner* [2004b] and *Morrow et al.* [2000] for pure chlorite gouge deformed under water-saturated conditions at room temperature and an effective normal stress of 100MPa (μ~0.39). Petrographic

examination of the experimental samples suggests that our observed values of μ result from the development of an interconnected talc- and/or chlorite- network that was able to accommodate distributed deformation by frictional slip along (001) foliation planes. The experimentally deformed phyllonites closely resemble the natural phyllonites found within the core of the Zuccale fault (compare Figures 5.5d and 5.10c), so it seems likely that the strength of the natural samples may have been controlled by a network of interconnected talc and chlorite grains.

Interestingly, component 3.1 which possesses a friction coefficient of 0.4-0.47 only contains a total of 28% chlorite and talc (perhaps >30% if XRD uncertainty is taken into account), and more than 70% calcite and amphibole. The phyllosilicates appear to be influencing the strength of this sample despite their relatively low abundance. This suggests that phyllosilicate minerals may contribute towards the strength of an experimental sample if they are able to become interconnected during the early stages of slip. In other words, sheet silicates can effectively lubricate clasts of 'strong' minerals such as calcite and amphibole, preventing strong grain-to-grain contacts from developing. This result is in broad agreement with previous deformation experiments on mixtures of a 'strong' (e.g. quartz) and 'weak' (e.g. kaolinite) phase, that reported strength values intermediate between those of the two end-members [e.g. *Logan and Rauenzahn*, 1987, *Takahashi et al.*, 2007, *Crawford et al.*, 2008]. Such experiments also suggested that mechanical properties are strongly influenced by the weak phase if it accounts for >30% of the sample [*Logan and Rauenzahn*, 1987, *Crawford et al.*, 2008]. Both the talc- and chlorite- phyllonites are dominantly velocity-strengthening at the imposed slip rates, consistent with the documented velocity-strengthening behaviour of both chlorite [*Takahashi and Shimamoto*, 1998, *Mizoguchi et al.*, 2008] and talc [*Moore and Lockner*, 2008].

Samples of foliated cataclasite (component 4) are dominated by quartz and dolomite, in roughly equal proportions. They possess μ values between 0.54 and 0.72, and μ appears to increase significantly with increasing normal stress. These strength values are consistent with previously reported strengths of both quartz and dolomite gouge deformed at room temperature. *Morrow et al.* [2000] and *Crawford et al.* [2008] report μ of 0.65-0.7 for water-saturated quartz gouge at 100MPa and 50MPa effective normal stress, respectively. *Mair and Marone* [1999] report slightly lower μ values of ~0.55-0.6 for nominally dry quartz gouge deformed at normal stresses of 25MPa-70MPa, and relatively high sliding velocities of 1μm/s-10000μm/s. For dolomite gouge, *Weeks and Tullis* [1985] report μ ~0.56-0.58 for a dry sample deformed at 75MPa effective normal stress. The foliated cataclasites are characterized by velocity-strengthening behaviour at 50MPa and 75MPa effective normal stress. This result is consistent with our microstructural observations, which suggest that the experimental samples accommodated slip by distributed cataclasis, without any localization along boundary- or Riedel-shears. *Beeler et al.* [1996] and *Mair and Marone* [1999] found that velocity-strengthening behaviour dominated in quartz and granite gouges at slip displacements of <5-10mm, that correlated with a lack of microstructural fabrics indicating slip localization. At slip displacements >5-10mm, they observed a transition to velocity-weakening behaviour, that correlated with the development of boundary- and Riedel-shears. *Beeler et al.* [1996] observed a second transition back to velocity-strengthening at high displacements (>60mm), and used their observations to suggest that velocity-weakening may be directly associated with the development and maintenance of boundary-parallel Y-shears. Our experiments were performed up to displacements of ~5mm. At the highest displacements, incipient Riedel shears were observed within the foliated cataclasites, but they evidently did not develop early enough to promote a transition to velocity-weakening behaviour. *Weeks and Tullis*

[1985] observed velocity-strengthening behaviour in one experiment performed on dolomite gouge. The microstructural fabrics of the natural and experimental cataclasites are comparable (compare Figures 5.5f and 5.10b). Typically, the matrix of the natural cataclasites preserves evidence for distributed cataclasis (Figure 5.5f), suggesting that they may have been characterized by velocity-strengthening behaviour. However, the natural cataclasites are also cross-cut by R- and Y-shears, the latter being enriched in fine-grained quartz (Chapter 6). This potentially indicates a transition to velocity-weakening behaviour, perhaps driven by variations in slip magnitude, fluid pressure, strain rate, or by deformation at elevated temperatures.

Foliated fault gouges that occupy the uppermost fault core are noticeably finer-grained than the other fault rock components. XRD analysis suggests that quartz, calcite, dolomite, and chlorite are the dominant mineral phases, but SEM observations indicate that both chlorite and kaolinite are abundant matrix phases. Water-saturated fault gouges are characterized by μ between 0.4-0.5, whilst nominally dry fault gouges are typically 25-40% stronger, with μ between 0.5-0.65. μ increases significantly with increasing effective normal stress. Quartz, calcite, and dolomite have water-saturated frictional strengths that are too high to explain the strength of the fault gouges (see preceding paragraphs). On the other hand, chlorite and kaolinite have water-saturated frictional strengths of ~0.39 [*Moore and Lockner*, 2004b] and ~0.3-0.5 [*Moore and Lockner*, 2004b, *Crawford et al.*, 2008], that could explain the strength of the fault gouges. *Moore and Lockner* [2004b] reported that the strengths of oven-dried chlorite and kaolinite were ~0.65-0.7 and ~0.85, respectively. *Crawford et al.* [2008] report μ ~0.4 for kaolinite dried in the open air, and it also seems likely that chlorite dried in the open air (as oppose to oven dried) would possess $\mu<0.65$. Thus, both the wet and dry frictional strengths of the experimental fault gouges may be explained by small grains of chlorite and kaolinite in the matrix wrapping

around clasts of quartz, calcite, and dolomite. Additionally, the velocity-strengthening behaviour of the fault gouges at 50MPa and 75MPa effective normal stress is consistent with the velocity-strengthening behaviour of chlorite [*Takahashi and Shimamoto*, 1998, *Mizoguchi et al.*, 2008] and the non-expandable clays such as kaolinite [e.g. *Morrow et al.*, 1982, *Logan and Rauenzahn*, 1987, *Paterson and Wong*, 2005].

5.5.2. Mineralogical weakening along low-angle normal faults

The strength of crustal fault zones represents an outstanding debate in the earth sciences [e.g. *Scholz*, 2000, *Holdsworth et al.*, 2001]. Arguments focus on whether major fault zones support shear stresses consistent with 'typical' laboratory-derived friction coefficients of 0.6-0.85 [*Byerlee*, 1978, *Townend and Zoback*, 2000], or whether they are able to slip at much lower shear stresses [*Lachenbruch and Sass*, 1980, *Zoback*, 2000]. Several lines of evidence suggest that the Zuccale fault slipped at a low-angle and thus represents a weak fault (Figure 5.2), a characteristic that it, and other low-angle normal faults, may share with the San Andreas fault [*Zoback et al.*, 1987, *Scholz*, 2000].

Figure 5.11 presents a summary of the above results, highlighting the mineralogical and mechanical 'stratigraphy' observed within the fault core. Detailed microstructural and geochemical analyses (Chapter 6) suggest that strain within the fault core was initially accommodated within fault rock components 2 and 3, before being superseded by component 4, and ultimately by component 5 at depths of <2km. The overall fault rock stratigraphy records exhumation of the Zuccale fault from relatively deep to relatively shallow crustal levels. All of the fault rocks we tested preserve microstructural evidence of frictional deformation, such as cataclasis and/or particulate flow of constituent grains (Chapter 6). The principal aim of this investigation was to test whether frictional

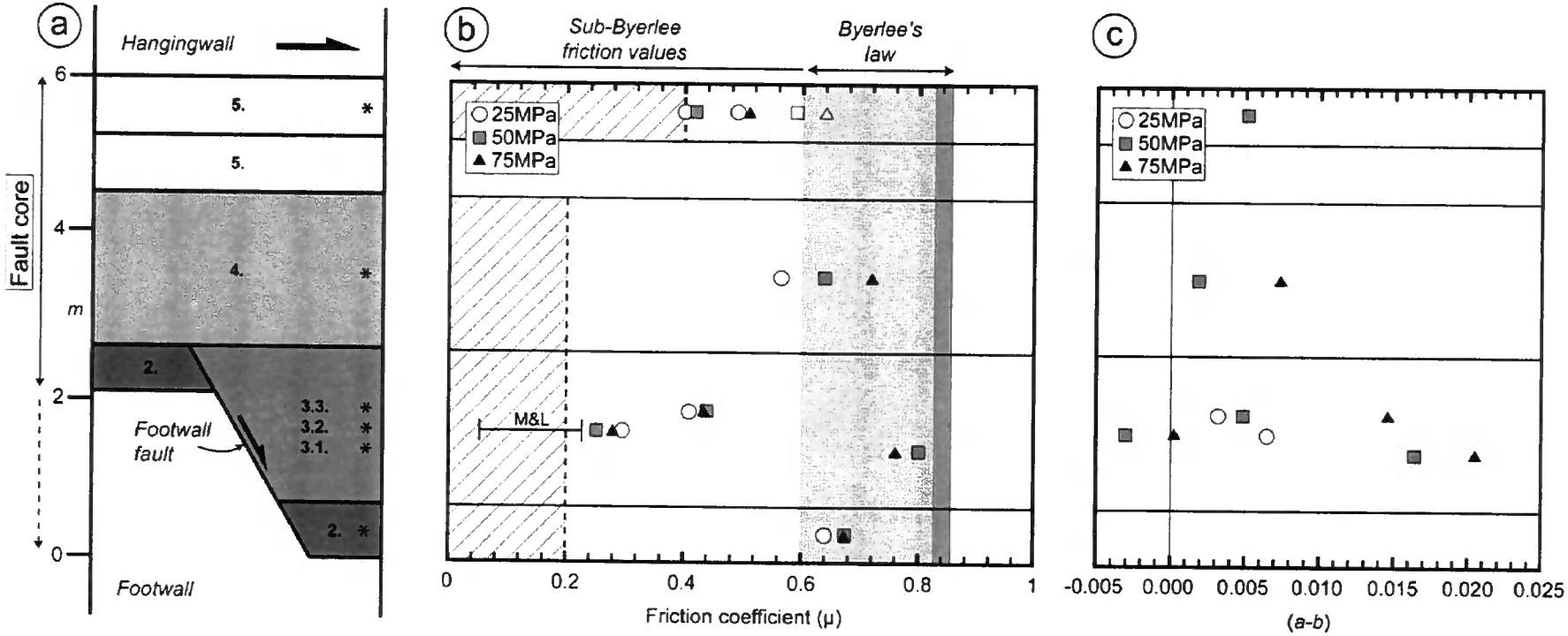
a
Hangingwall
6
5.
5.
4
4.
m
2.
2
3.3.
3.2.
3.1.
Footwall
fault
2.
0
Footwall
Fault core
b
Sub-Byerlee
friction values
Byerlee's
law
25MPa
50MPa
75MPa
M&L
0
0.2
0.4
0.6
0.8
1
Friction coefficient (μ)
c
25MPa
50MPa
75MPa
-0.005
0.000
0.005
0.010
0.015
0.020
0.025
(a-b)

Figure 5.11) Summary of the fault rock and mechanical stratigraphy present within the core of the Zuccale fault. **a)** Fault zone profile showing the various fault rock components, **b)** Friction coefficients of the different fault rock components. The range of 'typical' Byerlee friction coefficients (0.6-0.85) is also shown. The bar labelled 'M&L' shows the range in friction coefficients for pure talc measured by *Moore & Lockner* [2008]. The hatched areas represent the friction coefficients required to explain slip along a normal fault dipping at 15°. For the case of fault rock components 2, 3, and 4, depths of formation are poorly constrained, but a friction coefficient of <0.2 can explain slip at all depths in the upper crust. Fault rock component 5 likely formed at depths of <2km, where a friction coefficient of <0.4 can explain slip, **c)** The quantity (*a-b*) for the different fault rock components. The dominant velocity-strengthening behaviour of the fault materials at these experimental conditions suggests that the most likely mode of failure along the Zuccale fault was fault creep.

deformation accompanied by mineralogical weakening could explain slip along the Zuccale fault.

During periods of time when strain within the core of the Zuccale fault was accommodated by the foliated fault gouges, or localized in talc-rich areas within the talc-phyllonites, mineralogical weakening can explain slip along the Zuccale fault, without the need to appeal to other weakening mechanisms. Although the depths of formation of fault rock components 2-4 remains poorly constrained, talc has a coefficient of friction sufficiently low to account for slip along a normal fault dipping at 10°-15° at all depths in the upper crust [*Axen*, 2004, *Moore and Lockner*, 2008]. Similarly, the fault gouges (component 5) have a sufficiently low strength to account for slip during the late stages of exhumation in the upper ~2km of the crust [*Axen*, 2004]. An important field observation is that the talc-phyllonites presently occur as a series of large lenses of material that are not interconnected on a scale of tens to hundreds of metres (Figure 5.3). This geometry resulted from broadly synchronous movement on a network of subsidiary footwall faults, that locally displaced the lower margin of the fault core [*Smith et al.*, 2007; Chapter 2]. If the core of the Zuccale fault accommodated strain in its present configuration, then the talc-phyllonites would be unable to transmit grain-scale weakening effects up to the fault-zone- and crustal-scale. In such a situation, the strength of the Zuccale fault could not be

limited by the strength of the talc-phyllonites. *Smith et al.* [2007; Chapter 2] have presented evidence suggesting that the talc-phyllonites were interconnected on a fault-zone-scale during the early stages of movement along the Zuccale fault, and hence they may have played a key role in fault nucleation and initial growth.

During periods of time when strain was accommodated by the chlorite-phyllonites, amphibole schists and foliated cataclasites, mineralogical weakening alone is insufficient to account for movement along the Zuccale fault, although the friction coefficient of the chlorite phyllonites would permit slip if accompanied by only moderately-high fluid pressures. The foliated cataclasites are presently the most volumetrically important fault rocks in surface exposures of the Zuccale fault, and they also appear to be interconnected on scales of tens to hundreds of metres, suggesting that at some stage, they were probably controlling the mechanical behaviour of the overall fault zone. There is field and microstructural evidence that high fluid pressures [*Collettini et al.*, 2006a, *Smith et al.*, 2008] and fluid-driven 'dissolution-precipitation' creep [*Bos and Spiers*, 2002, *Collettini and Holdsworth*, 2004] were active processes along the Zuccale fault (Chapter 6). Both processes probably developed due to the widespread availability of fluids, and also the likely low-permeability of fault zone materials such as the foliated fault gouges and clay-bearing foliated cataclasites [e.g. *Faulkner and Rutter*, 2003]. In the absence of pure mineralogical weakening, such processes must be inferred to have caused a dramatic reduction in fault strength.

5.6. Conclusions

The Zuccale fault slipped at a low-angle within the upper crust, and appears to represent a weak fault. In this paper, we tested the hypothesis that mineralogical

weakening originating within the fault core could explain low-angle movements. The Zuccale fault possesses a distinctive and complex fault rock stratigraphy, primarily reflecting the lithological heterogeneity of the wall rocks, and prolonged interaction with fluids at a range of crustal levels. The fault core contains 5 main fault rock components, all of which preserve grain-scale evidence of frictional deformation. Triaxial deformation experiments conducted at room temperature and at a range of effective normal stresses indicate that the fault core as a whole has a frictional strength between 0.25-0.8. Frictional strength is strongly dependent on mineralogy. Deformation accommodated by talc-rich phyllonites and clay-bearing foliated fault gouges can explain slip along the Zuccale fault without the need to appeal to other weakening mechanisms. However, strain within the fault core was partly accommodated by amphibole schists and quartz-dolomite foliated cataclasites. The frictional strength of such components is broadly consistent with standard Byerlee friction coefficients, and too high to explain movement along the Zuccale fault. Prolonged slip must be explained by a combination of mineralogical weakening and other weakening mechanisms, such as the development of high fluid pressures or dissolution-precipitation creep at low strain rates.

Numerous studies have documented variations in frictional properties as a function of mineralogy, temperature, pressure, and water content. Our study reinforces the importance of understanding the spatial and temporal distribution of different fault rock components in detail, and how that distribution might affect fault zone mechanical properties over a wide range of scales.

Chapter 6

Fault Rock Development and Weakening Mechanisms During Exhumation of a Continental Low-Angle Normal Fault: The Zuccale Fault, Elba Island, Italy

A modified version of this chapter is to be submitted to Geochemistry, Geophysics, Geosystems in December 2008 as: S.A.F. Smith, C. Collettini, R.E. Holdsworth & M.A. Pearce, Fault Rock Development and Weakening Mechanisms During Exhumation of a Continental Low-Angle Normal Fault: The Zuccale Fault, Elba Island, Italy

Abstract

The Zuccale fault is an example of a continental low-angle normal fault preserving a complex fault rock sequence and a rich diversity of microstructures that record the interaction of multiple fluid-driven deformation mechanisms. The Zuccale fault crosscuts a lithologically heterogeneous sequence of wall rocks, and was active in the upper crust during intrusion of large plutonic complexes. Detailed microstructural and geochemical analyses reveal systematic changes in fault rock chemistry and texture related to progressive exhumation of the Zuccale fault. Cataclasis and dissolution-precipitation creep were the dominant deformation mechanisms during the early stages of fault activity. Cataclasis facilitated the influx of chemically active fluids, leading to widespread syn-tectonic growth of talc and chlorite. Crystal-plasticity was important within calcite-rich fault rocks that experienced pervasive dynamic recrystallisation by dislocation creep. Such calcite-mylonites were crosscut by vein material that was progressively sheared and recrystallised, indicating cyclic brittle-ductile deformation driven by changes in fluid pressure. During the later stages of fault activity, cataclasis was superseded by particulate flow as the dominant deformation mechanism. Rolling and sliding of grains past one another was accommodated along clay-lined grain boundaries. Exhumation was associated with a switch from dolomite to calcite as the principal syn-tectonic fault cement, reflecting a change in fluid source. Abundant sub-horizontal, tensile dolomite veins within the fault core indicate supra-lithostatic fluid pressures. Potential fault zone weakening mechanisms along the Zuccale fault include: (i) frictional slip and the operation of dissolution-precipitation creep within phyllosilicate-rich fault rocks; (ii) strain softening and a switch to grain-size sensitive deformation mechanisms within calcite-mylonites; (iii) transiently high fluid pressures, and; (iv) particulate flow accommodated by clay-lined grain boundaries. These weakening mechanisms were not mutually exclusive, and their relative importance varied as a function of temperature, fault zone structure, grainsize and composition, and the availability of fluid associated with regional igneous intrusion episodes.

6.1. Introduction

Most tectonic fault zones are lined by deformed fault rock materials produced by the relative movement of opposing wall rocks [e.g. *Evans*, 1990]. The diversity of fault rocks produced during deformation reflects the interaction between a large number of structural and metamorphic processes, all of which are dependent on a variety of intrinsic and extrinsic parameters [e.g. *Sibson*, 1977, *Knipe*, 1989]. Fault rocks can control the permeability structure [*Caine et al.*, 1996, *Agosta et al.*, 2007], strength [*Holdsworth*, 2004, *Moore and Lockner*, 2004b], and stability [*Marone*, 1998, *Saffer et al.*, 2001, *Faulkner et al.*, 2003] of fault zones, with important implications for seismicity and fluid-flow-related mineralization [e.g. *Scholz*, 2002, *Hammond and Evans*, 2003, *Wibberley and Shimamoto*, 2005, *Sheldon and Micklethwaite*, 2007, *Tullis et al.*, 2007]. It is increasingly recognized that many fault zones contain a number of distinctive types of fault rock that are juxtaposed against one another during progressive displacement, resulting in a complex and continuously evolving mechanical structure [e.g. *Childs et al.*, 1996, *Chester and Chester*, 1998, *Wibberley et al.*, 2008], whilst also providing valuable information on aspects of the exhumation history [e.g. *Davis*, 1987, *Cladouhos*, 1999a, *Pennacchioni et al.*, 2006, *Watts et al.*, 2007].

Normal faults that initiate and slip at low-angles (<30°) are particularly important places to study fault mechanics, because they probably represent weak faults compared to the surrounding crust and to laboratory-determined values of rock friction [*Byerlee*, 1978, *Collettini and Sibson*, 2001]. Andersonian faulting theory [*Anderson*, 1942] predicts that normal faults should be active in the upper crust at angles of around 60°, yet there is a growing body of evidence to suggest that low-angle normal faults have accommodated a significant amount of crustal extension in a wide variety of tectonic settings [*Coney*, 1980,

Wernicke, 1981, *Lister*, 1984, *Wernicke*, 1995, *Cann et al.*, 1997, *Smith et al.*, 2006, *Axen*, 2007, *Cottle et al.*, 2007]. *Axen* [2004, p85] stated that "The difficulty of explaining low-angle normal fault formation and slip suggests that our understanding of crustal mechanics is lacking some key ingredient(s), possibly related to spatial, temporal, and/or chemical changes that are not addressed in standard rock mechanical theory." One possibility that deserves attention is that weakening processes are related to the presence and evolution of the fault rock material that is ubiquitously found along, and surrounding, low-angle normal fault surfaces.

Despite the potential importance of fault rocks in contributing towards the rheological and mechanical behaviour of low-angle normal faults, there are surprisingly few studies that document in detail the mineralogical, textural, and chemical changes that accompanied faulting, particularly in the brittle upper crust. With the exception of those mentioned in the following paragraph, many previous authors have concentrated on the regional tectonic settings, mesoscopic structural relationships, and the kinematic histories of low-angle normal faults [*Axen*, 1988, *Lister and Davis*, 1989, *Mancktelow and Pavlis*, 1994, *Axen and Bartley*, 1997, *Cichanski*, 2000, *Hayman et al.*, 2003, *Axen*, 2004 and references within, *Kapp et al.*, 2008].

Continental low-angle normal faults with displacements of more than ~10-15km typically expose ductile, mylonitic footwalls characterized by pervasive foliations and stretching lineations, that commonly define broad, antiformal domes [*Wright et al.*, 1974, *Axen and Bartley*, 1997, *Cemen et al.*, 2005, *Miller and Pavlis*, 2005]. Early ductile fabrics are often overprinted by a continuum of ductile, semi-brittle, and brittle fault rocks that record a localisation of deformation under steadily decreasing pressure and temperature conditions [e.g. *Davis*, 1987, *Miller*, 1992]. These relationships were originally recognised along low-angle normal faults associated with 'Cordilleran' metamorphic core complexes

in western north America [e.g. *Coney*, 1980, *Davis*, 1980, 1987], but they have subsequently been documented in other metamorphic core complexes in areas such as the Aegean Sea [*Lister*, 1984, *Buick*, 1991, *Kumerics et al.*, 2005, *Mehl et al.*, 2005] and the Woodlark rift [*Little et al.*, 2007]. Recent studies in the Black Mountains region of Death Valley [*Cladouhos*, 1999b, *Cowan et al.*, 2003, *Hayman et al.*, 2004, *Hayman*, 2006], and in the eastern Swiss Alps [*Manatschal*, 1999], have shown that upper crustal brittle deformation was focussed initially into breccias and cataclasites, and later within relatively thin horizons (<2-3m) of fine-grained, foliated fault gouge, sometimes accompanied by pervasive fluid flow and authigenic mineral growth [*Manatschal et al.*, 2000, *Hayman*, 2006]. Similar structural relationships and overprinting fault rock sequences are starting to be recognised along low-angle normal faults associated with oceanic core complexes, most notably along the Mid-Atlantic Ridge [e.g. *Escartin et al.*, 2003, *Boschi et al.*, 2006a, *Karson et al.*, 2006].

In this paper, we present detailed mineralogical and textural descriptions of upper crustal fault rocks found along the Zuccale fault, a continental low-angle normal fault exposed on the Island of Elba, Italy. The Zuccale fault possesses a complex and distinctive fault rock 'stratigraphy', and a rich diversity of microstructures that record the operation of multiple fluid-driven deformation mechanisms. The evolution of the Zuccale fault, on a regional- to microscopic-scale, was strongly influenced by the intrusion of upper-crustal plutonic complexes. Our results provide important constraints on deformation conditions along low-angle normal faults, the interaction between fault rock development and fluid flow, and potential mechanisms of fault zone weakening.

6.2. Geological setting and previous work

The northern Tyrrhenian-Apennine region of Italy has experienced two main phases of post-Cretaceous deformation, both of which migrated progressively from west to east [*Elter et al.*, 1975, *Pauselli et al.*, 2006]. Cretaceous to Quaternary collision between the Adria microplate and the Corsica-Sardinia block of the European plate was followed by Miocene-recent post-collisional extension, resulting in opening of the Tyrrhenian basins [e.g. *Alvarez*, 1972, *Keller et al.*, 1994, *Keller and Coward*, 1996, *Jolivet et al.*, 1998]. Eastwards migration of post-collisional extension was most likely to have been driven by rollback of the Ionian-Adriatic subduction zone [*Malinverno and Ryan*, 1986, *Doglioni et al.*, 1999, *Brunet et al.*, 2000, *Rosenbaum and Lister*, 2004], and it was principally accommodated along a crustal-scale system of shallowly east-dipping low-angle normal faults, in combination with numerous synthetic and antithetic hangingwall structures [Figure 6.1; *Barchi et al.*, 1998, *Collettini and Barchi*, 2002, *Collettini et al.*, 2006b, *Pauselli et al.*, 2006]. One of the low-angle normal faults, the Altotiberina fault, is currently active beneath the Umbria-Marche Apennines, and creeps at a rate of ~1mm/yr^{-1}, producing microseismicity (M<2.3) between depths of ~4-14km [*Chiaraluce et al.*, 2007]. Prolonged regional uplift to the west of the Umbria-Marche Apennines has exhumed older, inactive low-angle normal faults in western Tuscany [*Carmignani and Kligfield*, 1990] and in the Tyrrhenian islands, that includes the late-Miocene to early-Pliocene Zuccale fault on the island of Elba [Figure 6.1; *Daniel and Jolivet*, 1995, *Keller and Coward*, 1996, *Rossetti et al.*, 1999, *Collettini and Holdsworth*, 2004].

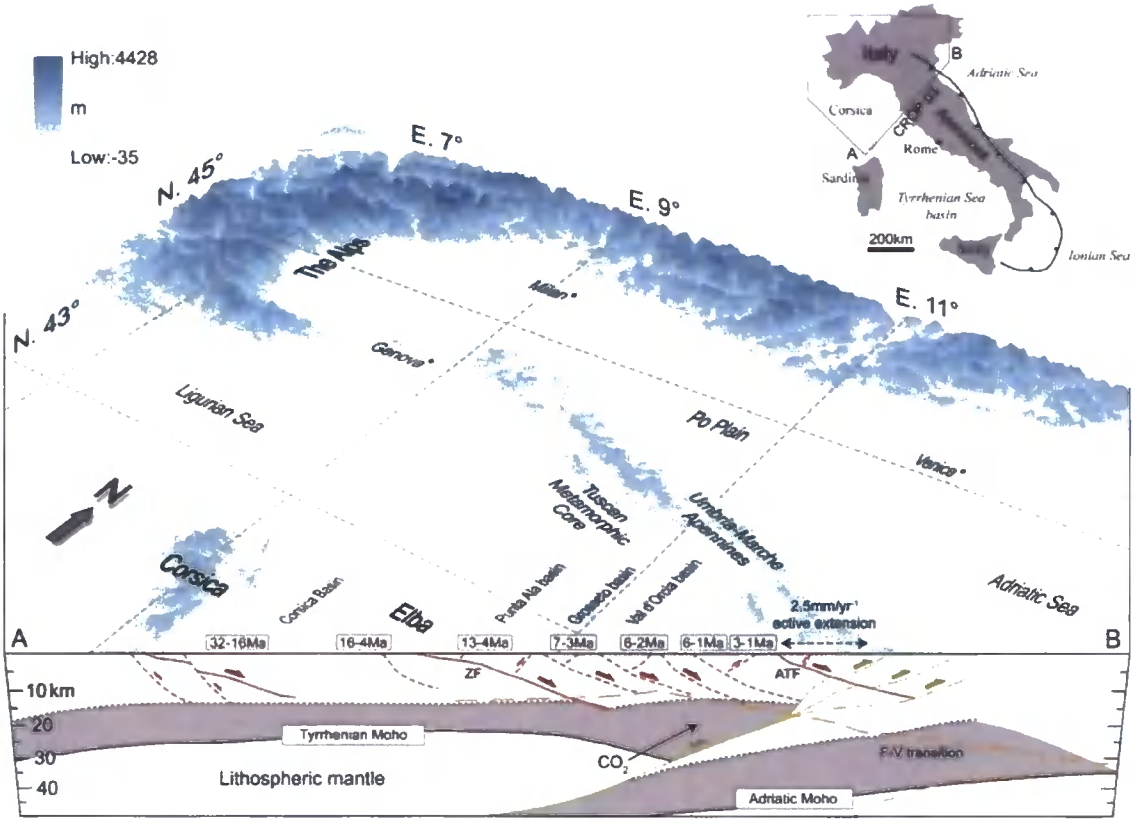

Figure 6.1) Crustal-scale block diagram and cross section of the northern Tyrrhenian Sea [*Jolivet et al.*, 1998] and the northern Apennines, based on the CROP03 seismic reflection profile [*Barchi et al.*, 1998, *Pauselli et al.*, 2006]. The inset shows the location of the CROP03 profile in Italy, and the location of the Ionian-Adriatic subduction zone. The cross section shows the location and approximate geometry of major thrust faults (green lines) and later normal faults (red lines) formed during post-collisional extension. The ages of syn-tectonic basins in the white boxes document an eastwards migration of extension [*Jolivet et al.*, 1998, *Brunet et al.*, 2000, *Rosenbaum et al.*, 2005]. The suggested location of the frictional-viscous (F-V) transition is after *Pauselli and Federico* [2002]. Extension was partly accommodated by shallowly east-dipping low-angle normal faults, including the Zuccale fault (ZF) exposed on the Island of Elba. Extension is active in the Umbria-Marche Apennines at a rate of ~2.5mm/yr^{-1} [*Hunstad et al.*, 2003], some of which is accommodated along the Altotiberina fault [ATF; *Chiaraluce et al.*, 2007]. The area to the west of the Umbria-Marche Apennines is characterised by high regional heat flow, a relatively shallow Tyrrhenian Moho, and high fluxes of CO_2 discharge [e.g. *Chiodini et al.*, 1999, *Collettini et al.*, 2006b].

Elba is composed of a series of stacked thrust slices that formed during late-Cretaceous-early Miocene compression (Figure 6.2). *Trevisan et al.* [1967] recognized five thrust 'Complexes' composed of diverse oceanic and continental units, all of which currently dip to the west. From bottom to top, the five thrust Complexes are as follows: 1) Complex I, Palaeozoic basement schists and metamorphosed Triassic cover; 2) Complex

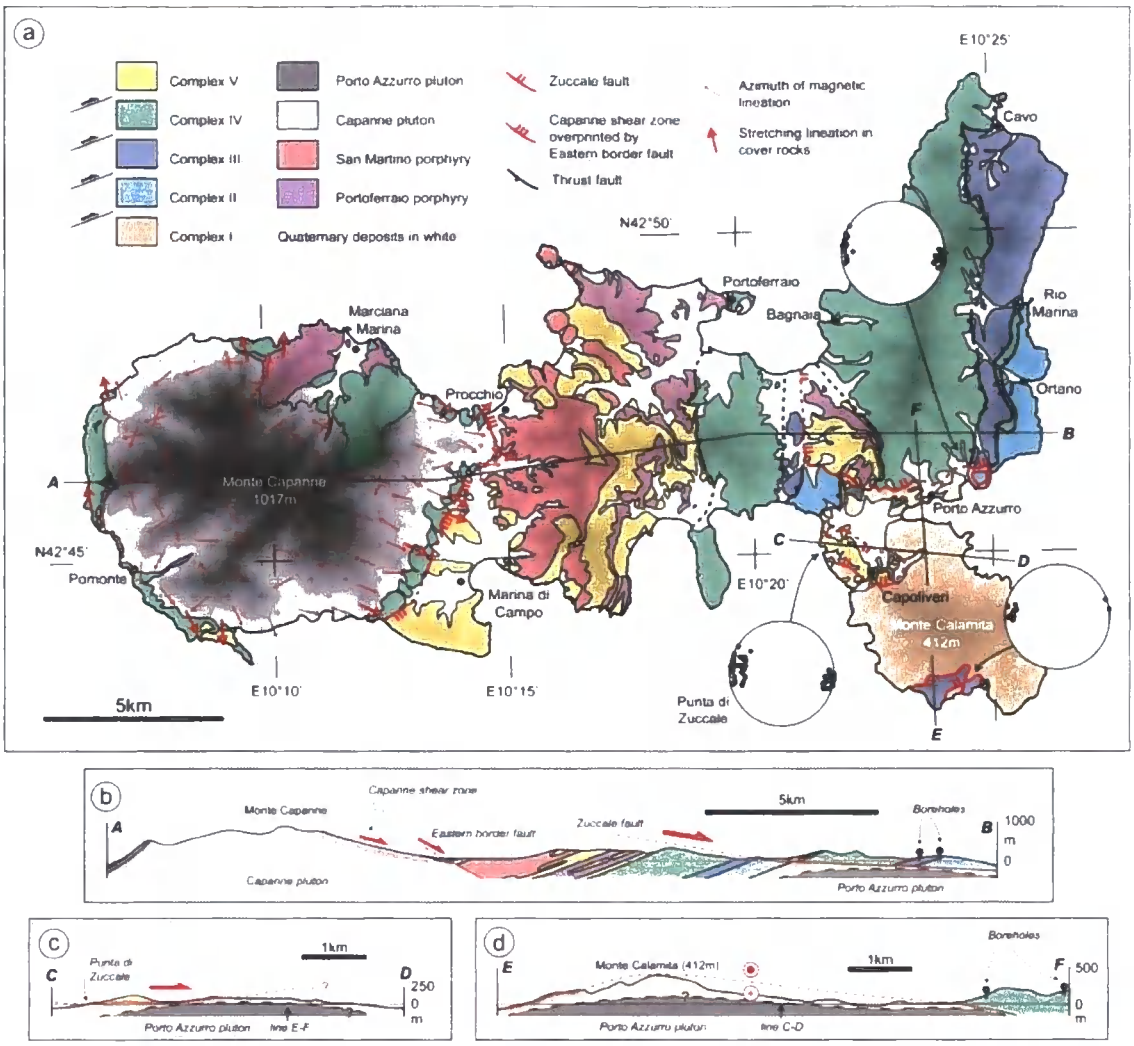

Figure 6.2a) Simplified geological map of Elba superimposed on a digital elevation model of the island, after *Trevisan et al.* [1967], highlighting the 5 tectonic 'Complexes' which are cross-cut and displaced by the Zuccale fault. Complex I, Palaeozoic basement schists; Complex II, Tuscan metamorphic sequence; Complex III, Tuscan limestone sequence; Complex IV, Ligurian ophiolite sequence; Complex V, Cretaceous and Eocene flysch sequence. The distribution of igneous units is after *Dini et al.* [2002]. Azimuth of magnetic lineations within the Capanne pluton, and stretching lineations in the cover rocks are from *Bouillin et al.* [1993]. Stereonets show lineations measured within the core of the Zuccale fault in 3 different areas, including Punta di Zuccale, **b-d)** Simplified cross sections highlighting the geometry of the Zuccale fault at depth, determined by structural mapping, structure contour analysis, and borehole data taken from *Bortolotti et al.* [2001a]. Note the broadly domal morphology of the Zuccale fault in SE Elba, most likely to have been influenced by intrusion and inflation of the Porto Azzurro pluton which lies at depths of <400m throughout this area.

II, Tuscan metavolcanic and metacarbonate sequences; 3) Complex III, Tuscan limestone sequences; 4) Complex IV, Ligurian ophiolite sequences, and; 5) Complex V, Cretaceous

and Eocene deep-water flysch sequences. These five Complexes were entirely cross-cut and displaced ~6km eastwards by the shallowly east-dipping (~15°) Zuccale fault [Figure 6.2; *Keller and Pialli*, 1990, *Keller et al.*, 1994], that can be traced on seismic reflection profiles to depths of ~15km beneath the basins to the east of Elba [*Keller and Coward*, 1996]. During regional extension, the thrust complexes on Elba were intruded by a series of upper crustal igneous bodies between ~8.5-5.9Ma, including nested laccoliths [*Rocchi et al.*, 2002, *Perugini and Poli*, 2007], and at least 2 major plutons [*Dini et al.*, 2002, *Maineri et al.*, 2003]. The igneous intrusions were associated with significant hydrothermal fluid-flow systems [*Taylor and Turi*, 1976, *Maineri et al.*, 2003, *Rossetti et al.*, 2007, *Dini et al.*, 2008], and they are thought to have caused remobilisation of sedimentary iron resulting in the formation of economically important Fe-ore deposits in eastern Elba [*Bortolotti et al.*, 2001b, *Tanelli et al.*, 2001, *Duenkel et al.*, 2003]. *Daniel and Jolivet* [1995] used detailed structural analysis to suggest that intrusion of the Capanne pluton [~6.9Ma; *Dini et al.*, 2002], the older of the two main plutons, was accommodated by high-temperature, top-to-the-east movements along the low-angle Capanne shear zone, an inference that is consistent with the presence of a strong WNW-ESE oriented magnetic lineation along the eastern border of the pluton [Figure 6.2; *Bouillin et al.*, 1993].

The Zuccale fault is exposed in eastern Elba beneath a series of erosionally-isolated hangingwall blocks. Top-to-the-east movement across the Zuccale fault resulted in a clear repetition of Complexes II-V in the centre and in the east of Elba, and exhumation of a nucleus of Complex I basement schists in the south-east of Elba [Figure 6.2; *Trevisan et al.*, 1967]. The Porto Azzurro pluton is a poorly understood igneous body that was intruded beneath south-east Elba at *c.*5.9Ma [*Saupe et al.*, 1982, *Maineri et al.*, 2003, *Dini et al.*, 2008]. Geometric and kinematic relationships between the Porto Azzurro pluton and the Zuccale fault (Chapter 4) suggest that: 1) intrusion occurred contemporaneously with

top-to-the-east movement across the Zuccale fault, and; 2) final emplacement and vertical inflation of the pluton resulted in a broad doming of the Zuccale fault (Figure 6.2). In previous papers, we focussed primarily on the structural geology and kinematic history of the Zuccale fault [*Collettini and Holdsworth*, 2004, *Collettini et al.*, 2006a, *Smith et al.*, 2007, *Smith et al.*, 2008]. *Collettini and Holdsworth* [2004] presented preliminary microstructural observations of fault rocks collected from the Zuccale fault, and recognised at least five distinctive fault rock units that developed during prolonged fluid-assisted deformation (their L1-L5 in Figure 6.3b). They showed that one of the principal characteristics of the Zuccale fault is the presence of early cataclastic fault rocks that were overprinted by foliated, macroscopically ductile fault rocks following the onset of stress-induced dissolution-precipitation creep. The data and interpretations presented here build on this earlier work, and are used to provide a more complete description of the fault rock assemblages found along the Zuccale fault. Throughout this paper, we use the term 'fault core' to refer to the area within the overall fault zone that contains well developed, in this case predominantly foliated fault rocks, and which accommodated a large majority of displacement during slip (Figure 6.3b). All of the fault rocks exposed within the fault core, with the exception of the chaotic fault breccias described in section 6.4.6, display 'macroscopic' ductility [c.f. *Rutter*, 1986], but we do not imply the operation of any specific deformation mechanisms when using this term.

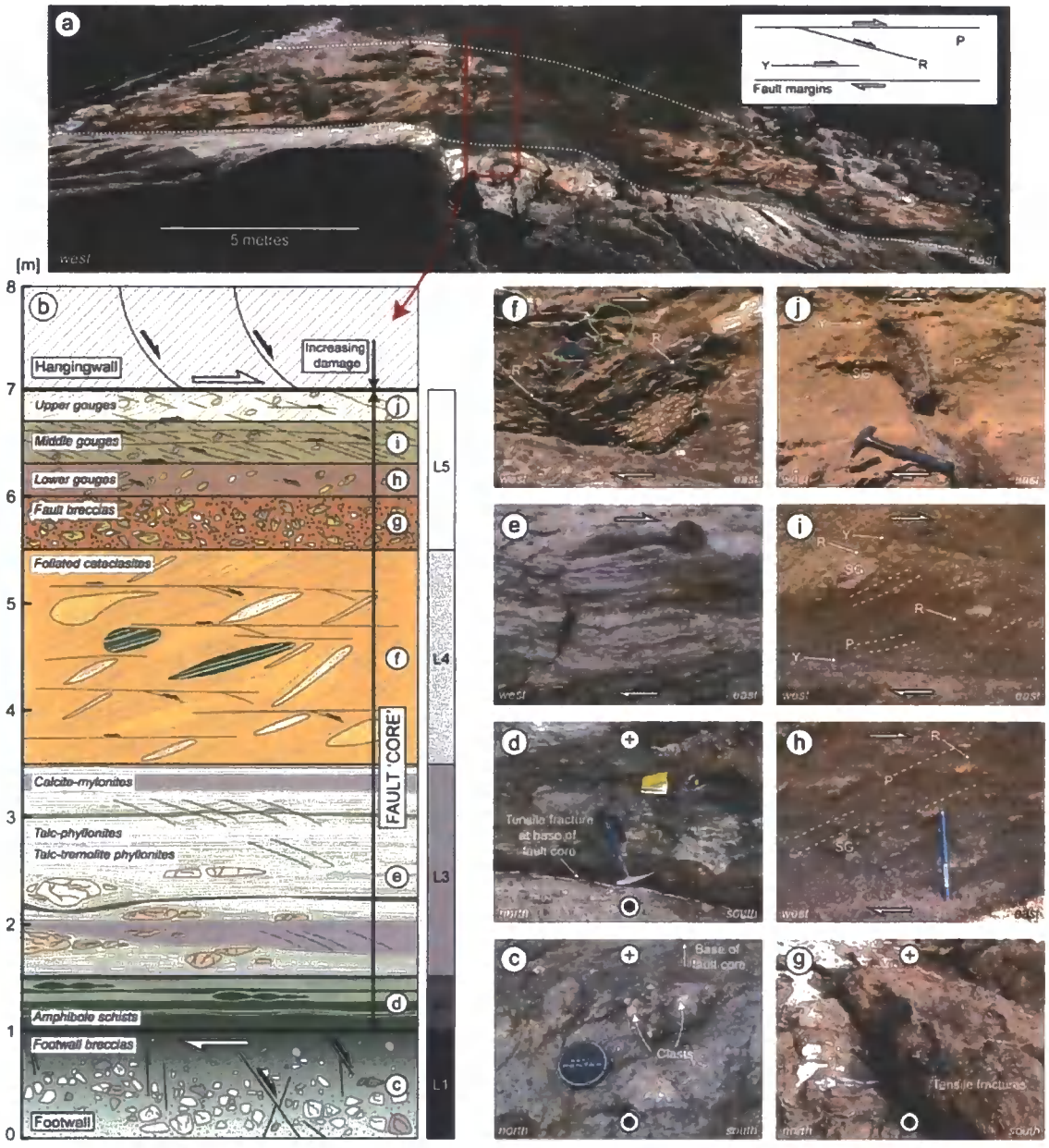

Figure 6.3) Schematic representation of the fault rock 'stratigraphy' found at Punta di Zuccale, **a)** Model of the Zuccale fault constructed using a Riegl Z420i terrestrial laser scanner. The dashed white lines mark the upper and lower margins of the fault 'core' (see text for discussion). Note the stepped lower margin of the fault core, reflecting interaction of the fault core with subsidiary normal faults in the immediate footwall [*Smith et al.*, 2007]. The inset white box shows the geometry of typical fabric elements found within the fault core, and discussed in the text, **b)** Schematic structural log illustrating the fault rock stratigraphy discussed from bottom to top in the text, corresponding to the photographs shown in Figures 6.3c-j. The wall rocks to the fault core are also discussed separately in the text. The structural log highlights the relative thickness of each fault rock type, and the typical fabric elements found within each. L1-L5 refers to the fault rock subdivisions used by *Collettini and Holdsworth* [2004], **c)** Breccias at the top of the footwall, **d)** Amphibole schists, **e)** Lens of calcite-ultramylonite contained within talc- and tremolite-phyllonites, **f)** Dolomite vein-rich foliated cataclasites, **g)** Fault breccias, **h)** Lower fault gouges, **i)** Middle fault gouges, **j)** Upper fault gouges.

6.3. Methodology

The internal structure of the Zuccale fault is spectacularly exposed in a series of coastal outcrops at Punta di Zuccale, on the west side of Monte Calamita, where we collected more than 50 hand specimens (Figures 6.2, 6.3). We focussed our attention exclusively on this series of outcrops, as they contain the most diverse array of fault rock assemblages. Furthermore, 100% exposure means that the spatial and temporal relationships between the different fault rocks can be analysed in detail. All of the fault rock descriptions below refer to samples collected from Punta di Zuccale, although during the course of our work on Elba we have recognised similar fault rocks and fault rock sequences in other areas. We prepared thin sections for optical microscopy, and polished rock chips for scanning electron microscope (SEM) analysis. Scanning electron microscopy was carried out on a Phillips XL30 SEM at the University of Liverpool, and was supplemented by energy-dispersive x-ray (EDX) analysis, and by electron-backscatter diffraction (EBSD) analysis of selected samples [e.g. *Prior et al.*, 1999]. Unless indicated, all the SEM images presented here were taken in back-scattered electron mode. A representative suite of 18 sample powders were used for X-ray diffraction (XRD) and X-ray fluorescence (XRF) analyses (Tables 6.1, 6.2).

6.4. Results

In the following sections, we present detailed observations of individual fault rock types that have been recognized at Punta di Zuccale. The fault rocks are arranged in to a distinct 'stratigraphy', and we describe this stratigraphy from bottom to top. Figure 6.3 shows a schematic profile through the Zuccale fault at Punta di Zuccale, and Tables 6.1

and 6.2 present the results of quantitative XRD and XRF analyses, respectively, which will be discussed further below. Most of the fault rocks we have studied lie within the central fault core, but we initially provide a description of the local wall rocks, and of a series of tectonic breccias developed in the footwall immediately beneath the fault core. Many of the fault rock types are lithologically and texturally heterogeneous, and are further subdivided into different components based on dominant mineralogy and fabric. It should be noted that not all of the fault rock types are present everywhere within the fault zone, partly reflecting the influence of subsidiary footwall faults that locally disrupt the fault rock stratigraphy [*Smith et al.*, 2007]. Many of the fault rocks are characterized by a pervasive P-foliation, which is typically inclined at an angle of ~20-30° from the margins of the fault core [Figure 6.3; *Logan et al.*, 1979, *Rutter et al.*, 1986, *Cladouhos*, 1999b]. Other fabric elements that are referred to below include Y-shears that parallel the margins of the fault core, and synthetic Riedel(R^1)-shears that crosscut and deflect the P-foliation [Figure 6.3; *Chester et al.*, 1985, *Rutter et al.*, 1986, *Chester and Logan*, 1987].

6.4.1. Fault wall rocks

The footwall of the Zuccale fault at Punta di Zuccale is composed of phyllites, quartzites, and quartz-mica schists belonging to a Palaeozoic age metamorphic basement, found extensively throughout the Tyrrhenian Islands and central Italy [*Bortolotti et al.*, 2001a, *Garfagnoli et al.*, 2005]. The rocks are part of Complex I of *Trevisan et al.* [1967] and the Monte Calamita Formation of *Bortolotti et al.* [2001a]. The basement fabric is primarily defined by an alignment of platy muscovite, biotite, and chlorite grains, and a compositional banding of quartz- and phyllosilicate-rich layers several hundred microns (μm) in thickness. The original basement fabric was widely overprinted by post-tectonic

Table 6.1) XRF results

Sample	Description	Na_2O %	MgO %	Al_2O_3 %	SiO_2 %	P_2O_5 %	SO_3 %	K_2O %	CaO %	TiO_2 %	MnO %	Fe_2O_3 %	BaO %	LOI %	TOTALS %
PZ3-2903	Mudstone Complex V	0.09	0.66	3.13	27.15	0.04	0.08	0.81	35.32	0.19	0.02	1.33	0.16	31.0	99.96
PZ4-2903	Sandstone Complex V	0.20	0.99	10.39	64.82	0.05	0.04	2.79	8.38	0.29	0.03	1.72	0.04	10.2	99.96
PZ29	Fault gouge 3	0.11	1.30	5.32	28.26	0.02	0.04	0.48	29.98	0.31	0.19	4.65	0.03	29.1	99.74
PZ24	Fault gouge 2	0.13	7.03	4.49	41.62	0.04	0.03	0.60	17.54	0.28	0.30	5.00	0.01	22.6	99.65
PZ4	Fault gouge 1	0.04	10.46	4.08	35.17	0.01	0.77	0.11	15.76	0.30	0.18	4.60	0.10	28.1	99.72
PZ27	Fault breccia	0.08	6.66	2.65	50.95	0.01	0.05	0.15	15.54	0.18	0.21	3.87	0.07	19.5	99.93
PZ7	Foliated cataclasite	0.04	12.63	3.17	39.05	0.01	0.04	0.06	15.15	0.22	0.22	3.23	0.08	26.1	99.97
PZ5	Foliated cataclasite	0.07	7.69	2.66	51.39	0.01	0.21	0.26	12.30	0.27	0.20	3.48	0.03	21.3	99.83
PZ13	Tremolite schists	1.25	7.70	14.95	50.44	0.08	0.02	0.17	13.78	0.88	0.24	7.86	0.02	2.6	99.96
PZ11	Calc-mylonites	0.03	9.16	0.90	27.66	0.01	0.02	0.18	33.28	0.05	0.32	3.95	0.05	24.4	100.00
PERM 1	Calc-mylonites	0.06	10.03	1.06	23.07	0.01	0.03	0.02	31.16	0.06	0.20	6.58	0.06	27.6	99.96
PZ21	Calc-mylonites	0.30	3.78	0.87	11.13	0.01	0.01	0.12	41.57	0.05	0.31	3.50	0.06	38.0	99.70
PZ2-0508	Tremolite schists	0.32	14.18	5.82	50.32	0.04	0.02	0.56	11.12	0.30	0.36	11.83	0.02	4.8	99.63
PZ23	Trenolite schists	0.12	16.28	1.05	54.02	0.01	0.06	0.29	11.50	0.03	0.51	11.67	0.01	4.0	99.57
FWBREC	Footwall breccia	1.46	1.94	16.80	58.13	0.09	0.02	1.49	8.25	0.86	0.19	6.41	0.04	4.3	99.94
PZ20	Footwall breccia	0.16	0.66	2.68	92.10	0.01	0.02	1.19	0.08	0.15	0.03	1.83	0.03	1.0	99.95
PZ19	Footwall breccia	0.15	0.93	3.39	90.25	0.00	0.04	1.48	0.35	0.18	0.04	1.85	0.08	1.3	99.98
PZ2-2903	Basement schist	0.77	0.42	8.44	83.62	0.06	0.01	2.10	0.66	0.74	0.02	1.33	0.05	1.8	99.98

Table 6.2) XRD results

Sample	Description	Actinolite %	Biotite %	Calcite %	Chlorite %	Dolomite %	Epidote %	Kaolinite %	K-feldspar %	Muscovite %	Plagioclase %	Quartz %	Talc %
PZ3-2903	Mudstone Complex V			64.00	2.00					11.00		23.00	
PZ4-2903	Sandstone Complex V			19.00	3.00					23.00		55.00	
PZ29	Fault gouge 3			58.00		3.00		15.00				24.00	
PZ24	Fault gouge 2			25.00	16.00	19.00			2.00			38.00	
PZ4	Fault gouge 1				6.00	58.00				4.00		32.00	
PZ27	Fault breccia			19.00	12.00	20.00			1.00			48.00	
PZ7	Foliated cataclasite			1.00	10.00	51.00						38.00	
PZ5	Foliated cataclasite			1.00		45.00		5.00				49.00	
PZ13	Tremolite schist	41.00					31.00				28.00		
PZ11	Calc-mylonites	39.00		60.00								1.00	
PERM 1	Calc-mylonites	17.00		55.00	10.00								16.00
PZ21	Calc-mylonites	5.00		80.00	10.00							5.00	
PZ2-0508	Tremolite schists	65.00	9.00		12.00		12.00						2.00
PZ23	Tremolite schists	95.00		3.00								2.00	
FW BREC	Footwall breccia			3.00	11.00		20.00			9.00	25.00	31.00	1.00
PZ20	Footwall breccia				6.00				5.00			89.00	
PZ19	Footwall breccia			1.00	6.00				7.00			86.00	
PZ2-2903	Basement schist			2.00	3.00					20.00	2.00	73.00	

growth of muscovite, biotite, K-feldspar, andalusite, and cordierite porphyroblasts during intrusion of the Porto Azzurro pluton [*Bortolotti et al.*, 2001a]. Complex I is locally capped by a thin sequence (<20m) of quartzite, crystalline dolostone and dolomitic limestone, thought to represent the metamorphosed Triassic cover [*Bortolotti et al.*, 2001a, *Garfagnoli et al.*, 2005]. No widespread mylonitic deformation has been found associated with movements on the Zuccale fault, but fault breccias are developed at the top of the footwall (section 6.4.2).

The hangingwall of the Zuccale fault at Punta di Zuccale is composed of interbedded sandstones, marls, and mudstones belonging to a Cretaceous deep-water turbidite sequence. The rocks are part of Complex V of *Trevisan et al.* [1967] and the Marina Di Campo Formation of *Bortolotti et al.* [2001a]. The sandstones are fine-to medium-grained and are dominated by quartz, feldspar, and muscovite within a carbonate cement [*Bortolotti et al.*, 2001a]. Calcaranetic marls and carbonaceous sandstones can contain upwards of 30 wt% CaO. The dark grey mudstones contain varying amounts of illite, smectite, illite-smectite, chlorite-vermiculite, chlorite-kaolinite, and vermiculite [*Bortolotti et al.*, 2001a]. In general, the hangingwall appears relatively undeformed compared to the footwall. Pervasive fracture damage is restricted to a few metres at most at the base of the hangingwall, but the fractured rocks have not accommodated significant shear strains. The hangingwall is cross-cut by discrete listric or planar normal faults with observed displacements ranging between several centimetres to a few metres [*Collettini and Holdsworth*, 2004].

6.4.2. Footwall breccias derived from Complex I

The distribution of fault breccias towards the top of the footwall is heterogeneous, and in places they are entirely absent. The maximum observed thickness of the footwall breccias is ~5 metres, although it is important to note that mesoscopic fracturing and damage related to the Zuccale fault extends for at least several tens of metres down into the footwall (possibly hundreds of metres), most commonly in the form of discrete fault surfaces that are themselves associated with small amounts of fault rock material. *Smith et al.* [2008] have previously described the occurrence of fluidized footwall breccias, that occur over areas of 10^{-2}-10^{-3} km^2, and deform the overlying fault core in to a series of metre-scale open folds. We differentiate such fluidized breccias from those described below [the 'frictional breccias' of *Smith et al.*, 2008], which do not contain any textural evidence suggesting fluidization processes.

The breccias can be classified as mosaic or chaotic breccias after *Mort and Woodcock* [2008], with the degree of clast separation and misorientation increasing with increasing strain (Figures 6.4a, b, 6.5c). Clasts within the breccias are generally angular to sub-angular, do not show any preferential alignment, and can be up to several tens of centimetres in diameter [Figures 6.4b, 6.5c; *Smith et al.*, 2008]. The breccias are clearly polygenetic in nature, and display clast-in-clast textures suggesting multiple episodes of brecciation followed by cementation. The clasts sit within an extremely cohesive, fine-grained matrix of comminuted material, the mineralogy of which depends on the protolith to the breccias and proximity to the overlying fault core. Footwall breccias at Punta di Zuccale are derived either from the quartzites that locally cap Complex I (Figure 6.4), or from the quartz-mica schists that dominate Complex I (Figure 6.5), and these are described separately below.

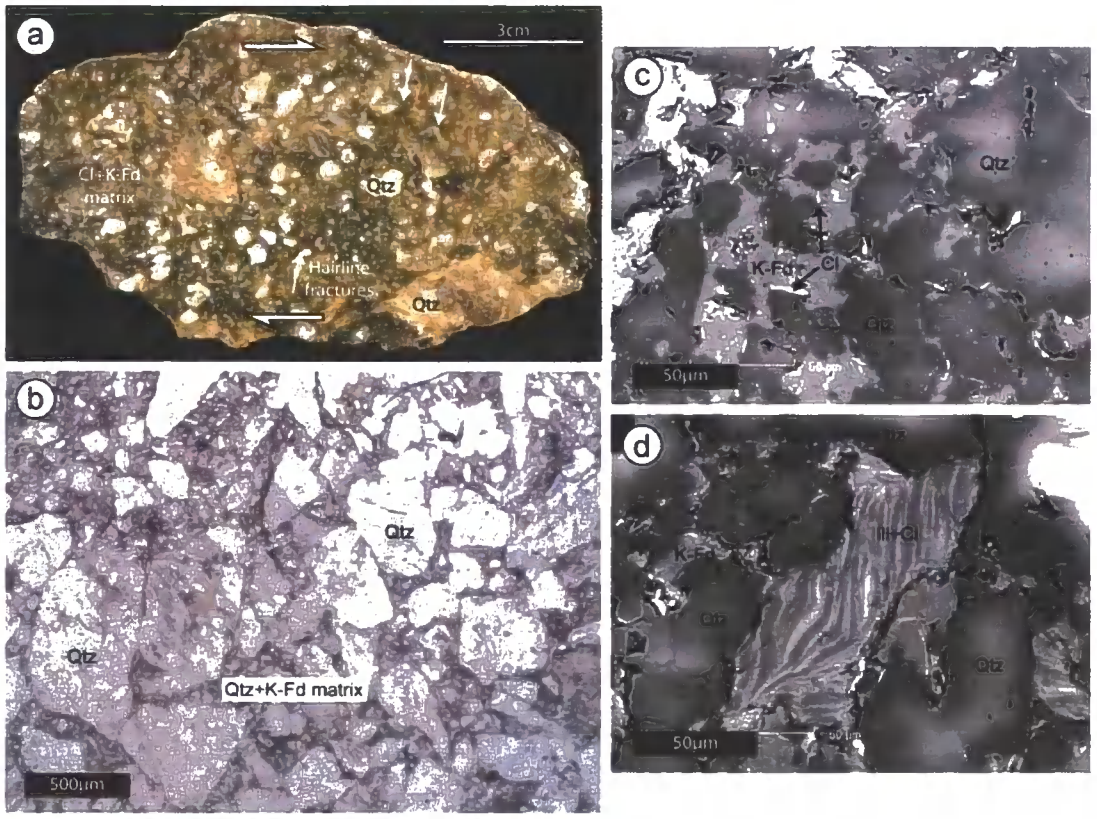

Figure 6.4) Footwall breccias derived from quartzites, **a)** Polished slab showing the chaotic fabric of the footwall breccias in this area. The light green matrix is composed of comminuted quartz, K-feldspar, chlorite, and illite, **b)** Photomicrograph in plane polarised light of angular quartz and feldspar clasts within a surrounding fine-grained matrix. Note the presence of clasts in the upper right which are experiencing progressive fracturing and grain size reduction, **c)** SEM image showing clasts of quartz and K-feldspar associated with small, platy grains of chlorite, **d)** SEM image of closely associated chlorite and illite, possibly derived from the syn-tectonic breakdown of biotite during brecciation. The light colouration at the centre of the quartz grains in c) and d) is an artefact of the SEM imaging. **The following abbreviations are used in all the Figures in Chapter 6: Qtz, Quartz; Cl, Chlorite; K-fd, K-feldspar; Plag, Plagioclase feldspar; ill, illite; Ep, Epidote; Ca, Calcite; Tr, Tremolite; Ac, Actinolite; Fe-Ac, Fe-rich actinolite; Do, Dolomite; Tc, Talc; Ka, Kaolinite; Fe-O, Fe-oxide.**

6.4.2.1. Footwall breccias derived from quartzites

Angular to sub-angular clasts are dominated by quartzite or individual grains of quartz (Figures 6.4a, b). Quartzite clasts retain their pre-existing metamorphic fabrics, defined by a quartz grain-shape preferred orientation, and an alignment of platy muscovite and biotite grains distributed along quartz grain boundaries. Intra- and inter-granular fractures cross-

cut quartzite clasts, and often follow pre-existing grain or clast boundaries. Most clasts show clear evidence for progressive brittle fragmentation and grain size reduction, and also contain planar arrays of healed microcracks containing decrepitated fluid inclusions. The matrix is light grey to light green in colour and consists of fine-grained (<30μm) comminuted quartz and K-feldspar fragments, and closely associated platy grains of chlorite and a K-Al-silicate phase, most likely illite (Figures 6.4c, d). The chlorite and illite grains are typically <20μm in length and show no preferential alignment. Chlorite replaces biotite along the pre-existing metamorphic foliation, suggesting that chlorite and illite in the matrix may be derived from the syn-tectonic breakdown of biotite during brecciation.

6.4.2.2. Footwall breccias derived from quartz-mica schists

Angular to sub-angular clasts are dominated by quartz-mica schist, and individual grains of quartz, plagioclase-feldspar and K-feldspar (Figure 6.5). Quartz-mica schist clasts are characterized by a strong metamorphic foliation, defined by a quartz shape-preferred orientation, an alignment of platy grains of chlorite and prehnite (after biotite), and a compositional banding of quartz- and mica-rich layers up to several hundred microns in thickness (Figure 6.5f). Most clasts show clear evidence for brittle fragmentation and grain size reduction (Figure 6.5c). At distances of more than a few tens of centimetres from the overlying fault core, the matrix of the breccias is light- to dark-green, and consists of fine-grained (<50μm) epidote, chlorite, and comminuted fragments of quartz and feldspar (Figures 6.5a, f).

A transition in breccia texture occurs in the upper few tens of centimetres of the footwall, marked by an increasing modal abundance of epidote, and the development of a foliation defined by an alignment of plagioclase and K-feldspar clasts (Figure 6.5a, b).

a
Ep+Cl+Ca
Incipient foliation
Breakdown of breccia fabric
Qtz+Plag
Qtz+Plag+Ep matrix
R
R
3cm
b
1500µm
Qtz-schist
c
Qtz+Plag
Qtz+Plag
500µm
d
Cl
Ep
20µm
e
Ep
Ca
A
B
50µm
f
Qtz-schist
500µm
g
800
700
600
500
400
100
0
Al
Fe
A
B
Counts per second
Distance

Figure 6.5) Footwall breccias derived from quartz-mica schists, **a)** Polished slab showing the typical chaotic fabric of the breccias which undergoes a pronounced textural transition at distances of less than a few tens of centimetres from the overlying fault core, **b)** Photomicrograph showing the progressive breakdown of the breccia fabric to one consisting of elongate, aligned plagioclase grains sitting in a matrix of almost pure epidote. The plagioclase is widely replaced by fine-grained sericite (and possibly zeolite). Dashed white lines highlight the alignment of the plagioclase long axes, **c)** Photomicrograph highlighting the typical breccia fabric away from the fault core, consisting of angular quartz, feldspar, and quartz-mica schist clasts in a fine-grained matrix of quartz, feldspar, epidote, and chlorite, **d)** SEM image showing the cataclastic nature of matrix epidote. Chlorite is also present but does not show any preferential alignment, **e)** SEM image showing an aggregate of zoned epidote. Note the calcite filling void space which appears undeformed, **f)** SEM image of typical breccia fabric away from the fault core. Note the pre-existing metamorphic foliation within clasts of quartz-mica schist (outlined by yellow dashed lines), defined by an alignment of chlorite grains (after biotite), **g)** EDX line traverse in the SEM, highlighting the chemical zoning present within many matrix epidote grains. In this case, 3 distinct chemical zones are present, defined by variations in Fe and Al content. The epidote becomes more Fe-rich towards grain margins.

This textural transition is noticeable in the field as a thin horizon of dark green material developed at the top of the footwall. Typically, the transition occurs over distances of only a few centimetres. Moving upwards towards the fault core, the initial signs of a change in breccia texture and composition are a discolouration of feldspar clasts, which turn from light grey or milky white to light- or dark-brown, and are replaced by fine-grained sericite (Figure 6.5b). The clasts become progressively elongated and aligned to define an asymmetric foliation, the obliquity of which is consistent with top-to-the-east transport. The long axes of the altered feldspar clasts are commonly aligned parallel to the P-foliation observed in many of the fault rocks within the overlying fault core (see below). The matrix is composed of >90% epidote, with chlorite, Ca-Al-Ti-silicates, and calcite as minor accessory phases (Figures 6.5d, e). The calcite is completely undeformed and appears to fill void spaces between epidote grains, suggesting that it may have been precipitated post-tectonically (Figure 6.5e). Epidote grains are typically euhedral and 10-50μm in length, but are extensively fractured and have locally experienced progressive grain size reduction (Figure 6.5d). Epidotisation appears to have been a continual syn-tectonic process, because aggregates of fractured epidote are themselves reworked and

incorporated in to a younger, and texturally distinct, epidote-rich matrix. Most of the larger epidote grains are zoned, and possess cores that are relatively poor in Fe, and rims that become progressively enriched in Fe (Figure 6.5e, g).

6.4.3. Amphibole schists

Amphibole schists occur as a dark green to black, 5cm-1.5m thick layer at the base of the fault core (Figure 6.3d). They are locally associated with thin horizons (<5cm) and lenses of chlorite- and talc-rich phyllonite. In the field, the schistose foliation parallels the margins of the fault core (Y-orientation) and is infrequently cross-cut by R^1-shears (Figure 6.3d). Fragments of heavily fractured amphibole schist are locally tectonically dismembered and incorporated into the overlying calcite-mylonites and foliated cataclasites (described below), and also into the underlying epidote-rich breccias (section 6.4.2).

Figure 6.6) Amphibole schists, **a)** Photomicrograph in crossed-polarised light highlighting the strong Y-foliation within the amphibole schists, defined by an alignment of actinolite grains, and a compositional banding, **b)** SEM image showing 2 large, fractured tremolite porphyroclasts with asymmetric tails of actinolite and Fe-rich actinolite, **c)** Enlargement of a fractured tremolite porphyroclast, showing fracture networks filled by actinolite. Note the presence of thin horizons of Fe-rich actinolite within the matrix, one of which is enlarged in e). The Fe-rich actinolite horizons are deflected around the large porphyroclast, **d)** SEM image of individual fractured amphibole grain, showing thin fractures in-filled by Fe-rich actinolite. Note the fine-grained, aligned nature of the matrix grains, **e)** SEM image showing a discrete cataclastic horizon within the matrix, containing fractured and rotated grains of zoned tremolite and actinolite. The box highlights an amphibole grain showing 3 distinct chemical zones. Dashed lines mark the edge of the cataclastic horizon, **f, g)** SEM images of a fibrous amphibole and epidote vein which cross-cuts the Y-foliation at high angles. Note the presence of epidote along the margins of the veins. The wall rocks in this case are tremolite schist containing fractures filled by actinolite, or fractured and fine-grained epidote.

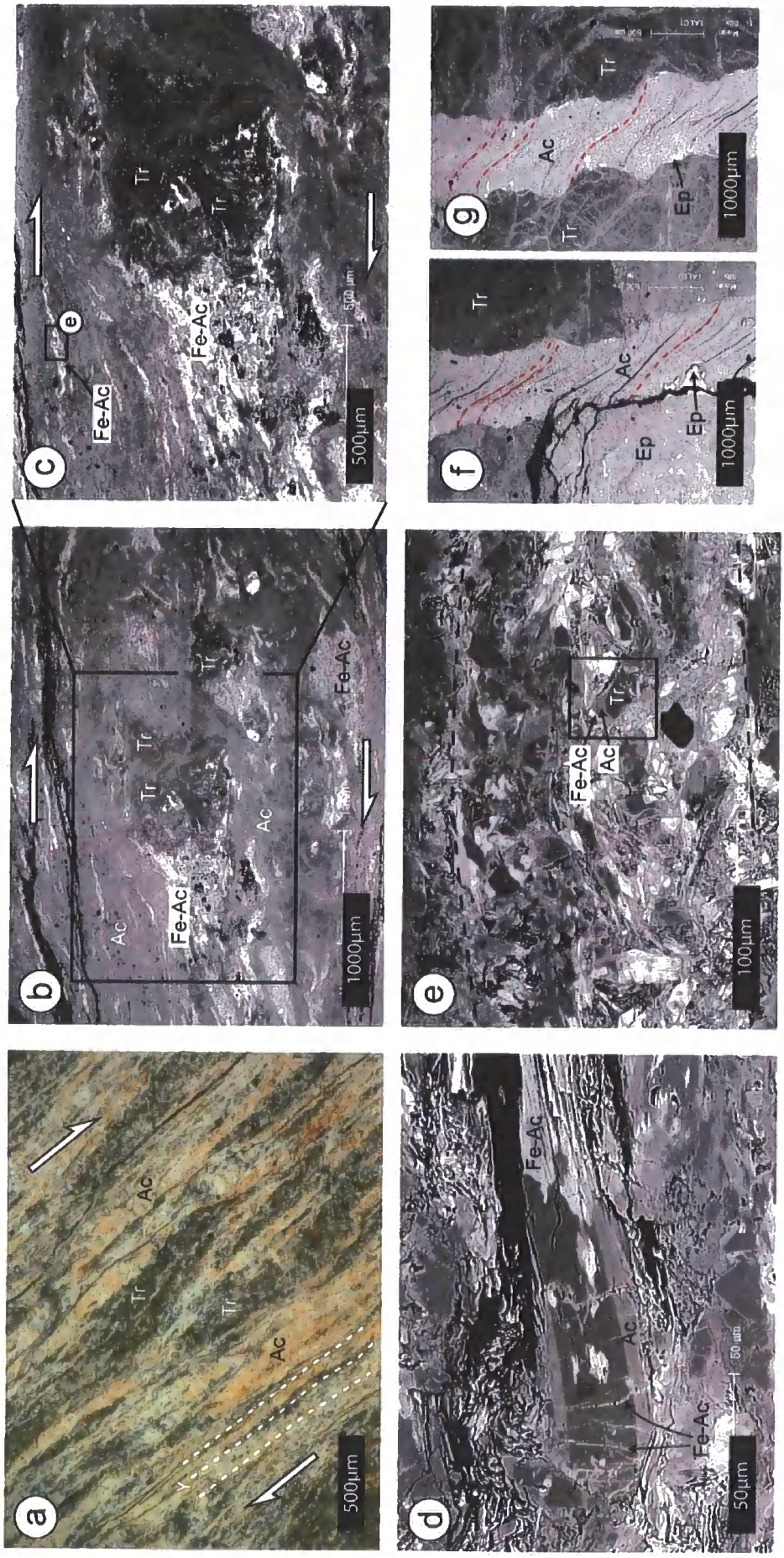
a
Ac
Tr
Tr
Ac
Y
500µm
b
Ac
Fe-Ac
Tr
Tr
Tr
Ac
Fe-Ac
1000µm
c
Fe-Ac
e
Tr
Tr
Fe-Ac
500µm
d
Fe-Ac
Ac
Fe-Ac
50µm
e
Fe-Ac
Ac
Tr
100µm
f
Tr
Ac
Ep
Ep
1000µm
g
Tr
Ac
Tr
Ep
1000µm

SEM investigations reveal that variations in the Fe and Mg content of the amphibole grains represents the primary compositional variation within these fault rocks (Figure 6.6). Based on our observations, we have classified the amphibole as tremolite (relatively Fe-poor), actinolite, or Fe-rich actinolite (towards ferroactinolite), but it is important to note that we have not carried out quantitative microprobe analysis. Large (up to 1000μm) fractured porphyroclasts of tremolite lie within a strongly foliated matrix of fine-grained actinolite and Fe-rich actinolite (Figures 6.6b, c). Porphyroclasts show clear evidence for brittle deformation accompanied by progressive grain size reduction. The matrix is characterised by elongate actinolite grains 10-20μm in length that are strongly aligned parallel to the schistose foliation. The matrix foliation wraps around porphyroclasts of tremolite. Apatite, chlorite, biotite, and a platy K-Al-silicate phase are minor constituents of the matrix. There are several lines of evidence to suggest that amphibole compositions became progressively more Fe-rich over time, and that the development of Fe-rich compositions was syn-tectonic. These are: 1) Actinolite lines fracture networks cross-cutting porphyroclasts of tremolite (Figure 6.6c); 2) actinolite and Fe-rich actinolite occur in the strain shadow regions surrounding large porphyroclasts of tremolite, and the asymmetry of the strain shadows is consistent with top-to-the-east transport within the Zuccale fault (Figures 6.6b, c); 3) large single crystals of amphibole are zoned, and contain cores of tremolite or actinolite, and rims of actinolite or Fe-rich actinolite (Figures 6.6d, e). Additionally, where single crystals of tremolite or actinolite in the matrix are fractured, the fractures are typically lined with Fe-rich actinolite (Figures 6.6d); 4) the matrix is cross-cut by numerous discrete fractured horizons up to 100μm in thickness that are dominated by Fe-rich actinolite. These horizons are deflected around large porphyroclasts of tremolite (Figures 6.6c, e), and contain a high concentration of Fe-rich actinolite that experienced fracturing, grain rotation and progressive grain size reduction (Figure 6.6e).

Amphibole schists (and the underlying epidote-rich breccias) are cross-cut by a network of epidote- and amphibole-bearing fibrous veins (Figures 6.6f, g). The veins lie at a high angle to the main schistosity, and contain crystals with extremely high (>100:1) aspect ratios that grew broadly perpendicular to the vein margins. Epidote was precipitated within narrow (<20μm) veinlets and along the margins of larger veins (<500μm). Epidote and amphibole (actinolite and/or Fe-rich actinolite) grew synchronously towards the centre of the veins, and occasionally incorporated planar bands of wall rock inclusions.

6.4.4. Phyllonites and calcite-ultramylonites

These two distinctive fault rock components occur within an intensely foliated orange, white and green unit that occurs towards the base of the fault core (Figure 6.3e). There is a strong structural control on the distribution of this unit, and its thickness varies between 0 and 5 metres [*Smith et al.*, 2007]. The mesoscopic foliation parallels the margins of the fault core, and it is principally defined by a compositional banding of calcite-, tremolite- and phyllosilicate-rich layers centimetres to tens of centimetres in thickness (Figure 6.3e). These layers are crosscut by numerous, discontinuous R^1-shears. Two dominant fault rock lithologies can be distinguished, which may be derived from a lithologically banded and heterogeneous protolith. They are described separately below: 1) Phyllonites dominated by varying amounts of dolomite, calcite, talc, chlorite, and tremolite, and; 2) Calcite-ultramylonites containing variable amounts of chlorite and tremolite. The calcite-ultramylonites typically occur as elongate lenses of material within the phyllonites.

6.4.4.1. Phyllonites

The phyllonites occur in close association with large (tens of centimetres in diameter) pods of heavily fractured dolostone, that probably represents one protolith component (Figures 6.3e, 7a). The dolostone consists of equigranular dolomite grains ~100μm in diameter (Figure 6.7b). In low strain areas, the dolostone is cross-cut by low-displacement shear fractures, which are often filled by calcite and fibrous talc grains up to several hundred microns in length [Figure 6.7b, *Collettini et al*, submitted manuscript, included in Appendix IV]. Calcite appears to replace dolomite along grain boundaries within the protolith (Figure 6.7c, d). The replacement boundaries between dolomite and calcite are sharp and well defined, although they typically have a lobate morphology [Figure 6.7d, *Collettini et al.*, submitted manuscript, Appendix IV]. Talc also occurs as randomly oriented grains 100-200μm long dispersed throughout the dolostone protolith, where it is clearly associated with small intergranular fractures [*Collettini et al.*, submitted manuscript, Appendix IV].

In high strain areas adjacent to the fractured pods of dolostone, the phyllonites contain a strong foliation, defined by an alignment of elongate talc grains up to 200μm in length, and a compositional banding of talc- and calcite-rich layers up to several hundred μm wide (Figure 6.7e-g). Dolomite appears to have experienced complete replacement by calcite. Calcite occurs in elongate polycrystalline ribbons, and as rounded porphyroclasts [Figure 6.7h, *Collettini et al.*, submitted manuscript, Appendix IV]. Individual calcite grains are typically 10-20μm in diameter and resemble those found within the calcite-ultramylonites. Talc dominates the matrix, and also occurs at calcite grain boundaries, as irregular intra-clast aggregates, and in fibrous strain shadows surrounding calcite porphyroclasts [Figure 6.7h; *Collettini et al.*, submitted manuscript, Appendix IV]. Tremolite is a relatively minor

constituent of the matrix, and may have formed by secondary metamorphic reactions between calcite and talc. The talc-rich matrix frequently contains thin (<1000μm) calcite veins that appear to have formed parallel to the main foliation (Figure 6.7g). Such calcite veins possess a clear median line and blocky-elongate grain morphologies, with calcite grains growing perpendicular to vein margins (Figure 6.7g).

6.4.4.2. Calcite-ultramylonites

The microscopic foliation in the ultramylonites is defined by a compositional banding of calcite-, chlorite- and tremolite-rich layers up to 1000μm in thickness, and by small variations in the grain size of matrix calcite (see below; Figures 6.8a, b). This main foliation is aligned parallel to the margins of the fault core.

Figure 6.7). Phyllonites, **a)** Polished slab of fractured dolostone protolith. The white layers are calcite beginning to develop along through-going fracture surfaces. Note the widespread growth of dendritic pyrolusite, **b)** Photomicrograph in plane polarised light showing a wide fracture cross-cutting dolostone protolith. The fracture contains calcite and fibrous talc, **c)** SEM image of dolostone aggregates being replaced by calcite along grain boundaries and within cross-cutting fracture networks, **d)** Detailed SEM image showing replacement of individual dolomite grains by calcite along grain boundaries, **e)** Polished slab of a high strain area within the phyllonites, showing widespread growth of light green talc and chlorite, **f)** Photomicrograph in plane polarised light showing layers of calcite-mylonite interbanded with layers of fibrous talc and tremolite, **g)** Photomicrograph in plane polarised light showing fibrous talc and tremolite layers which are cross-cut by thin carbonate veins which parallel the main foliation. The carbonate veins are characterized by blocky-elongate grain morphologies, and most contain a distinct median line (black arrows), **h)** Detailed SEM image of talc-rich foliation planes, and elongate porphyroclasts of calcite. The inset SEM image is in secondary-electron mode, and shows a rounded calcite porphyroclast with talc-rich strain shadows on either side.

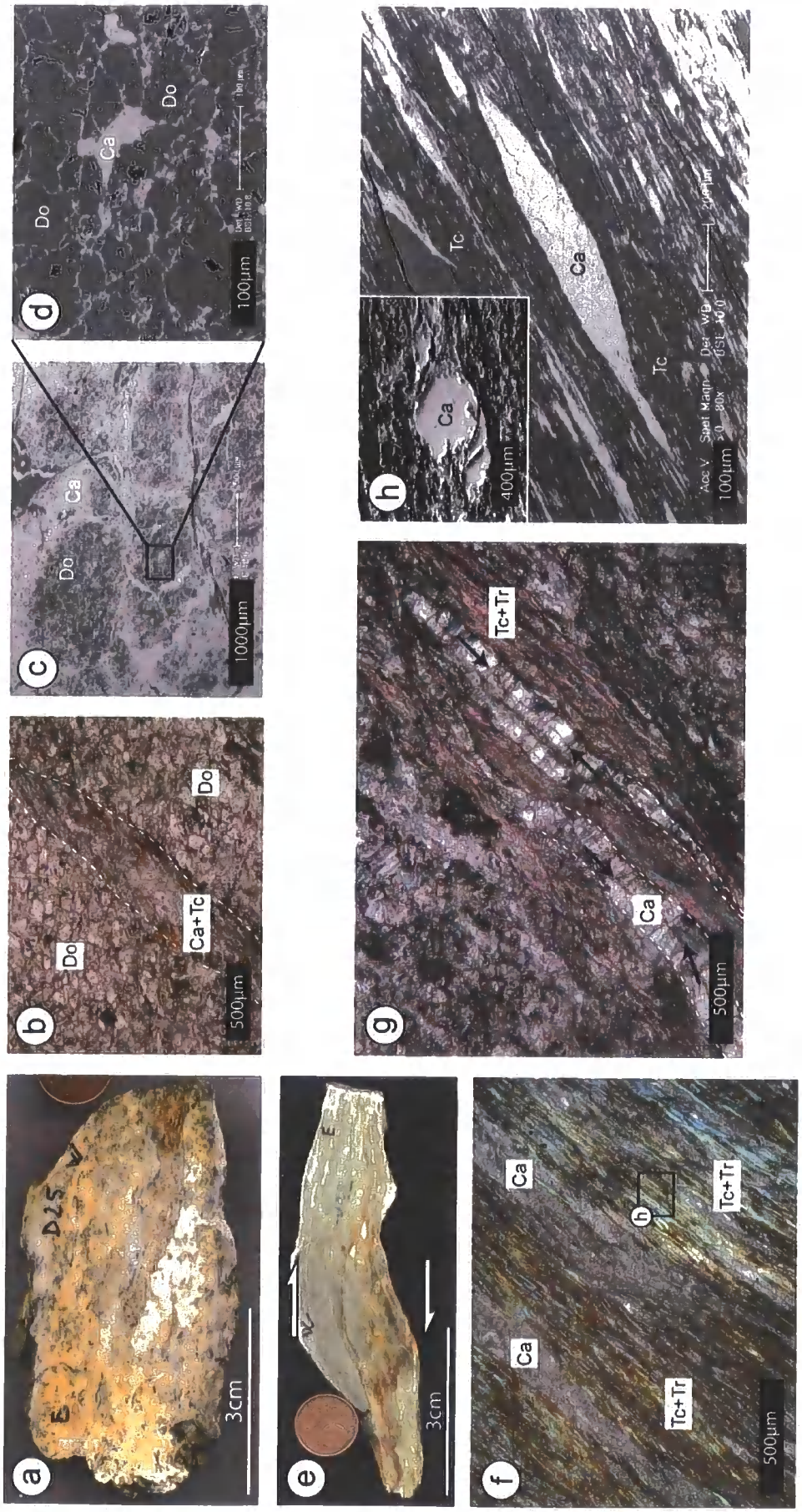
a
3cm
b
Do
Ca+Tc
Do
500µm
c
Do
Ca
Do
1000µm
d
Do
Ca
Do
100µm
e
3cm
f
Ca
Ca
Tc+Tr
Tc+Tr
500µm
g
Tc+Tr
Ca
500µm
h
Ca
400µm
Tc
Ca
Tc
100µm

Calcite occurs as: 1) relatively coarse-grained (up to 1000μm) vein material that typically cross-cuts the main foliation at high angles (Figures 6.8c, 6.9) and; 2) fine-grained (5-10 μm), homogenous aggregates that dominate the surrounding matrix (Figures 6.8d, 6.9). Vein calcite contains 'Type II' and 'Type III' twins, characterised by thick (>1μm) twin widths and slightly curved, bent, or tapered shapes [Figure 6.8c; *Burkhard*, 1993, *Ferrill et al.*, 2004]. Vein calcite also commonly displays sweeping or patchy undulose extinction (Figure 6.8c). The veins are between 100-1000μm in width but are progressively sheared in to the surrounding fine-grained matrix, accompanied by an overall synthetic rotation of the veins, and an intense reduction in grain size (Figure 6.9). Electron backscatter diffraction (EBSD) analysis in the SEM [*Prior et al.*, 1999] reveals that grains of vein calcite contain numerous subgrain boundaries, across which there is 2°-5° of crystallographic misorientation (Figure 6.9a, b). Subgrains within the vein calcite are often of a similar size to grains in the surrounding matrix. Matrix calcite grains do not contain any twins or undulose extinction, and appear internally strain free. The matrix contains layering up to several hundred microns thick, defined by small variations in calcite grain size and by variations in cathodoluminescence intensity. The mean grain size of matrix calcite, measured as the diameter of an area-equivalent circle, is between ~8-10μm. Cathodoluminescence imaging also reveals that individual grains of matrix calcite are zoned, perhaps reflecting minor chemical variations formed during deformation. EBSD analysis indicates that the texture of matrix calcite is characterised by a single c-axis (0001) maxima that is broadly perpendicular to the main foliation, although there is some rotation (~15°) of the c-axes in a synthetic direction with respect to a top-to-the-east shear sense (Figure 6.9c). No partial girdle of the c-axes is detected perpendicular to the main foliation. Both the a-axes show distinct girdle distributions approximately parallel to the main foliation and approximately normal to the c-axis maxima. Grains of matrix calcite

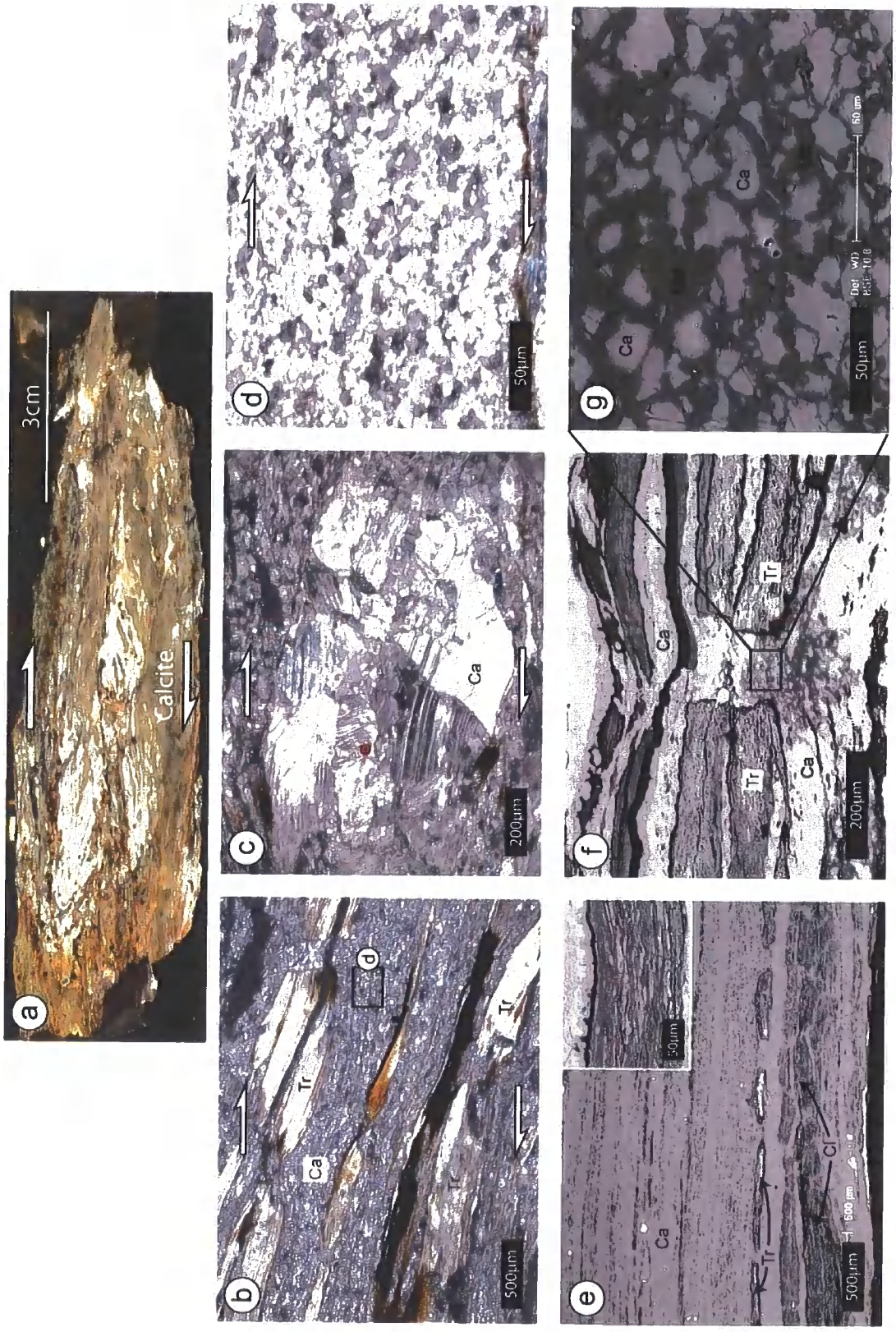
a
3cm
Calcite
b
Tr
Ca
d
Tr
500µm
c
Ca
200µm
d
50µm
e
Ca
Tr
Cl
500µm
50µm
f
Ca
Tr
Tr
Ca
200µm
g
Ca
Ca
50µm
50 nm

Figure 6.8) Calcite ultramylonites, **a)** Polished slab showing pure calcite horizons interlayed with light green chlorite and tremolite horizons. Note the presence of dispersed Fe-oxides, **b)** Photomicrograph in crossed polarised light highlighting the compositional banding of calcite, tremolite, and chlorite layers. The calcite-rich matrix is enlarged in d), **c)** Photomicrograph in crossed polarised light of coarse calcite which is part of a sheared calcite vein cross-cutting the dominant foliation at high angles. The red dot marks a calcite grain containing thick (>1μm), slightly curved and tapered 'Type III' twins [compare to Figure 7c in *Burkhard*, 1993], **d)** Photomicrograph in crossed polarised light of fine-grained, recrystallised calcite matrix, showing an approximately equigranular grain size distribution. The mean calcite grain size is around 10μm, **e)** SEM image showing boudinaged chlorite and tremolite layers in a recrystallised calcite matrix. The inset SEM image shows a chlorite-rich layer containing a strong 001 foliation, along which small, elongate calcite grains are present, **f)** SEM image of a boudin neck in tremolite. Calcite and quartz are precipitated in the boudin neck. Quartz is present as spherical, irregular clots up to 500μm in diameter, **g)** Detailed SEM image showing quartz precipitated along calcite grain boundaries in a boudin neck.

are separated by grain boundaries across which there is >25° of crystallographic misorientation, suggesting that the matrix has experienced pervasive dynamic recrystallisation (Figure 6.9b). Matrix calcite contains a strong grain shape-preferred orientation. The mean long-axis orientation of matrix grains is parallel to the main foliation (Figure 6.9d).

Chlorite and tremolite occur in 100-500μm thick layers within the calcite-ultramylonites (Figure 6.8e). Chlorite grains up to 50μm long are also dispersed along calcite grain boundaries within the fine-grained matrix. The presence of platy chlorite along grain boundaries may influence grain growth during dynamic recrystallisation, accounting for the small variations in grain size observed within the recrystallised calcite aggregates [e.g. *Herwegh and Kunze*, 2002, *Krabbendam et al.*, 2003]. Chlorite possesses a strong (001) cleavage, along which small (<20μm in length, <5μm in thickness) tabular grains of calcite are present (Figure 6.8e inset). Both chlorite and tremolite are boudinaged within the surrounding matrix (Figure 6.8e, f). Within boudin necks, blocky-elongate calcite grains have been precipitated, that track the boudin opening direction. Additionally, quartz is precipitated in boudin necks along calcite grain boundaries, to form irregular spherical clots up to 500μm in diameter (Figure 6.8f, g).

Hematite and/or magnetite grains up to 1000μm in diameter are found throughout the matrix (Figure 6.8a), often surrounded by fibrous strain fringes of calcite. EDX spot analysis reveals that the Fe-oxides are surrounded by reaction rims that are relatively enriched in silica.

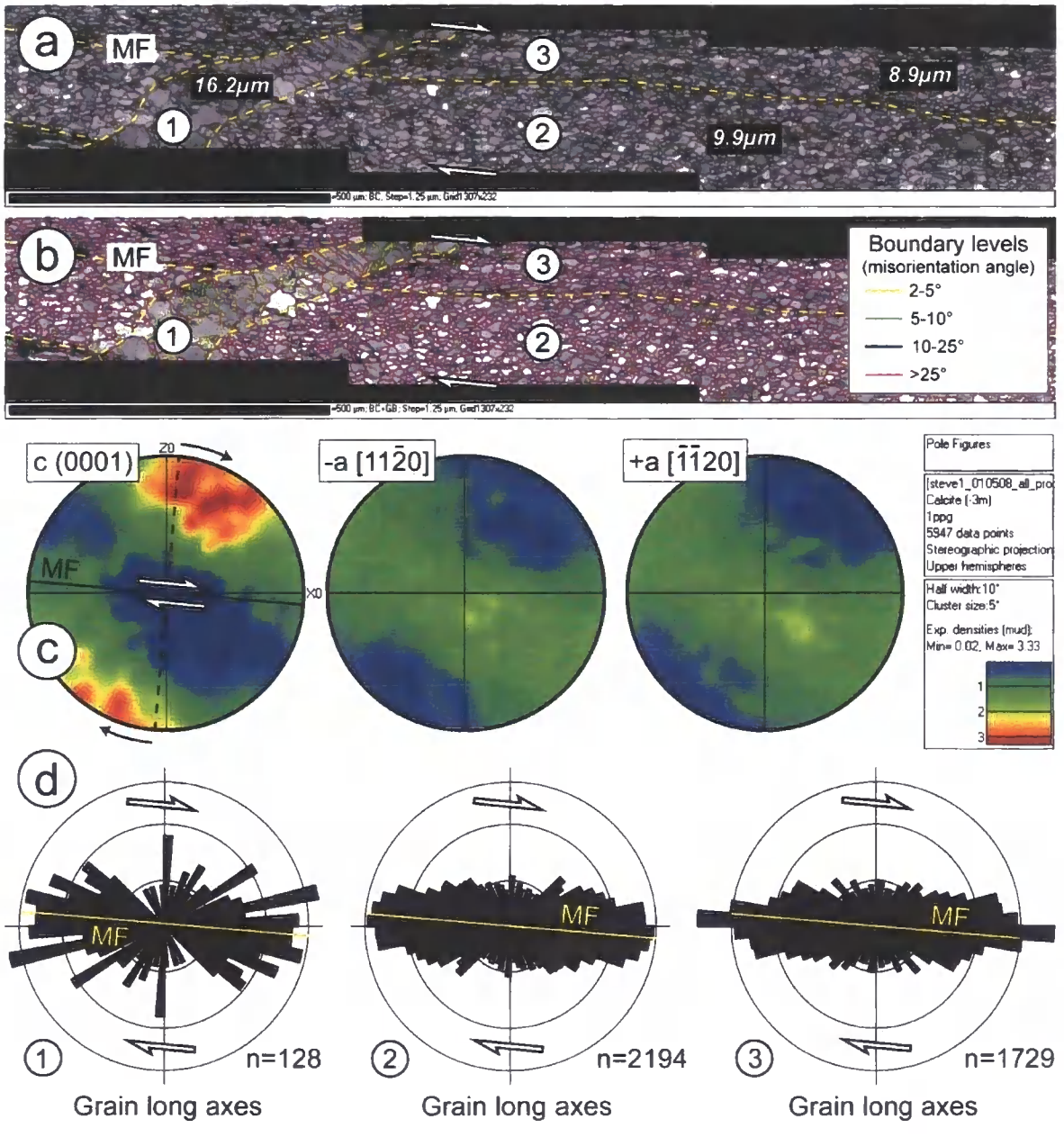

Figure 6.9) Electron backscatter diffraction analysis (EBSD) of the calcite-ultramylonites, **a)** EBSD band contrast map highlighting the general microstructure of the ultramylonites. Two distinct matrix domains (labelled 2, 3) are cross-cut by a calcite vein (labelled 1). The matrix domains are characterised by small variations in mean calcite grain size (given in the black boxes), whilst the vein calcite is noticeably coarser grained. MF, Main foliation, which broadly parallels the margins of the fault core. Step size used for EBSD analysis is 1.25μm, **b)** EBSD band contrast map overprinted with subgrain and grain boundary misorientation levels. Boundary levels are detected by analysing the crystallographic misorientation of pairs of grains. Note the presence of numerous low-angle subgrain boundaries in the calcite vein, whilst the matrix grains are generally separated by high-angle boundaries, **c)** Bulk crystallographic preferred orientation data of the ultramylonites determined by EBSD analysis. The data are presented as pole figures (equal area, upper hemisphere stereo plots), which were constructed by using one point per grain (n=5947). Dashed line represents a plane lying orthogonal to the main foliation, **d)** Calcite grain shape preferred orientations within the 3 separate areas labelled in a and b. In all 3 areas, the orientation of the calcite long axes is approximately parallel to the main foliation observed within the ultramylonites.

6.4.5. Foliated cataclasites

Foliated cataclasites occur as a 3-4 metre thick, yellow to light brown unit towards the centre of the fault core (Figure 6.3f). Foliated cataclasites are the most volumetrically significant fault rock found at Punta di Zuccale and in other exposures of the Zuccale fault. A strong P-foliation dominates the macroscopic and microscopic fabric. The macroscopic P-foliation is principally defined by an alignment of elongate inclusions of amphibole schist, calcite-ultramylonite, and phyllonite (Figure 6.3f), whilst the microscopic P-foliation is defined by a compositional banding of calcite-, dolomite, and quartz-rich layers up to several centimetres thick (Figures 6.10a, b). In many areas, the foliated cataclasites are dominated by thin dolomite veins (described separately below). Where present, the dolomite veins are aligned parallel to, and enhance, the P-foliation. The foliated cataclasites are cross-cut by discrete Y-shears that are enriched in fine grained (<50μm) quartz, and by discontinuous R^1-shears (Figures 6.10a, b).

Sub-rounded to sub-angular clasts of reworked dolomite and polycrystalline dolomite sit within a matrix of fine-grained (<50μm) quartz, dolomite, apatite, and a K-Al-silicate clay phase (possibly illite; Figures 6.10c-f). Small grains of Fe-oxide are also

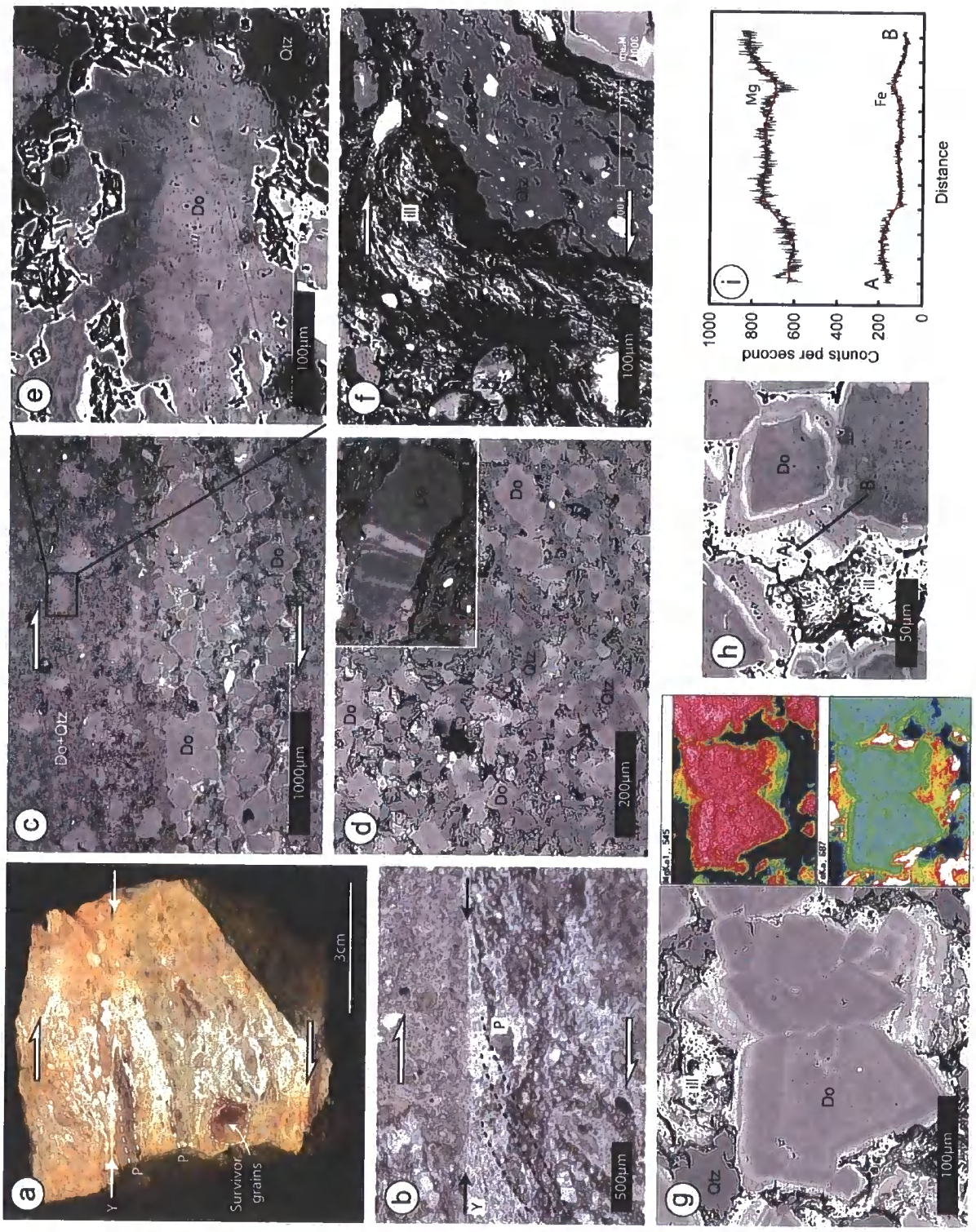
a
Y
P
P
Survivor grains
3cm
b
Y
P
500µm
c
Do+Qtz
Do
Do
1000µm
d
Do
Qtz
Do
Qtz
200µm
e
Qtz
Do
100µm
f
III
100µm
g
Qtz
Do
III
100µm
h
A
B
Do
III
50µm
i
Mg
Fe
A
B
Counts per second
1000
800
600
400
200
0
Distance

Figure 6.10) Foliated cataclasites, **a, b)** Polished slab and photomicrograph in plane polarised light showing the dominant P-foliation defined by a compositional banding of quartz- and dolomite-rich layers, and an alignment of large survivor grains. The P-foliation is cross-cut by discrete Y-shears which are relatively enriched in fine-grained quartz, **c)** SEM image showing the fractured dolomite and quartz-bearing matrix (upper half) and a layer rich in post-tectonic dolomite (lower half), **d)** Detailed SEM image showing the dolomite and quartz rich matrix. Note the lack of fabric. The inset SEM image shows a grain of matrix dolomite cross-cut by a fracture filled by Fe-rich dolomite, **e)** Detailed SEM image showing angular matrix dolomite containing diffuse chemical zoning, perhaps inherited from pre-existing dolomite veins or cements, **f)** SEM image showing an alignment of quartz, Fe-oxides, and illite in the matrix of the foliated cataclasites, **g)** SEM image of large, post-tectonic dolomite grain containing clear chemical zoning. The inset image shows chemical maps produced by EDX in the SEM. The upper map shows variations in Mg content of the dolomite, whilst the lower map shows variations in the Fe content of the dolomite, **h, i)** SEM image and EDX line traverse highlighting chemical variations in post-tectonic dolomite. Note the presence of a platy clay phase (probably illite) filling void space in h).

dispersed throughout the matrix. Many of the polycrystalline dolomite clasts contain aggregates of dolomite grains that have a blocky-elongate morphology and contain diffuse chemical zoning, suggesting derivation from pre-existing dolomite veins or from dolomite cements (see below; Figures 6.10e). Matrix phases show clear evidence for fracturing and progressive grain size reduction by brittle processes. Fractures that cross-cut clasts of relatively Fe-poor dolomite are filled by relatively Fe-rich dolomite (Figures 6.10d inset). Quartz, clay, apatite, and Fe-oxides grains in the matrix are aligned parallel to the microscopic P-foliation (Figures 6.10f).

Dolomite additionally occurs as post-tectonic cement. Post-tectonic dolomite is coarse-grained (up to 500μm), euhedral, clearly zoned, and grows at the expense of matrix phases or in to pore spaces filled by clay phases (Figures 6.10c, g, h). The post-tectonic dolomite shows systematic chemical zoning from relatively Fe-poor grain centres to relatively Fe-rich grain rims (Figures 6.10g, i).

6.4.5.1. Foliated cataclasites containing dolomite veins

In places, the foliated cataclasites are composed of >90% dolomite vein material (Figure 6.3f). Veins are typically 200-1000μm wide and are closely spaced. Thus, as many as ~20 individual veins can be stacked adjacent to one another over a distance of less than 1cm (Figures 6.11a, b). Individual veins are laterally discontinuous, and they tend to branch and merge with adjacent veins to form vein networks that, overall, parallel the macroscopic P-foliation (Figures 6.11b, d). Veins are deflected in to cross-cutting R^1-shears, indicating that they are syn-tectonic in origin (Figure 6.11c).

Most dolomite veins display a central core that contains blocky or elongate-blocky grain morphologies (Figure 6.11e). It is unusual to find evidence for multiple growth episodes, such as crack-seal banding or planar wall-rock inclusion bands. Elongate-blocky grains are typically 100-200μm long and up to 100μm wide, and their long axes are perpendicular to vein margins (Figure 6.10e). The central core is relatively poor in Fe, but it frequently contains a thin (~20μm) median line that is slightly enriched in Fe (Figure 6.11e). Most dolomite grains display sweeping or patchy undulose extinction, but only a small percentage contain optically resolvable Type I twins [*Burkhard*, 1993, *Ferrill et al.*, 2004]. The central core of the veins is flanked by wide rims of coarse-grained (up to 500μm), euhedral dolomite that is relatively enriched in Fe (Figures 6.11d, e). These dolomite grains have a faceted morphology and contain clear primary growth zones, but they do not show any evidence for growth within discrete vein networks (Figure 6.11e). It is likely that they grew post-tectonically along the margins of the pre-existing dolomite veins.

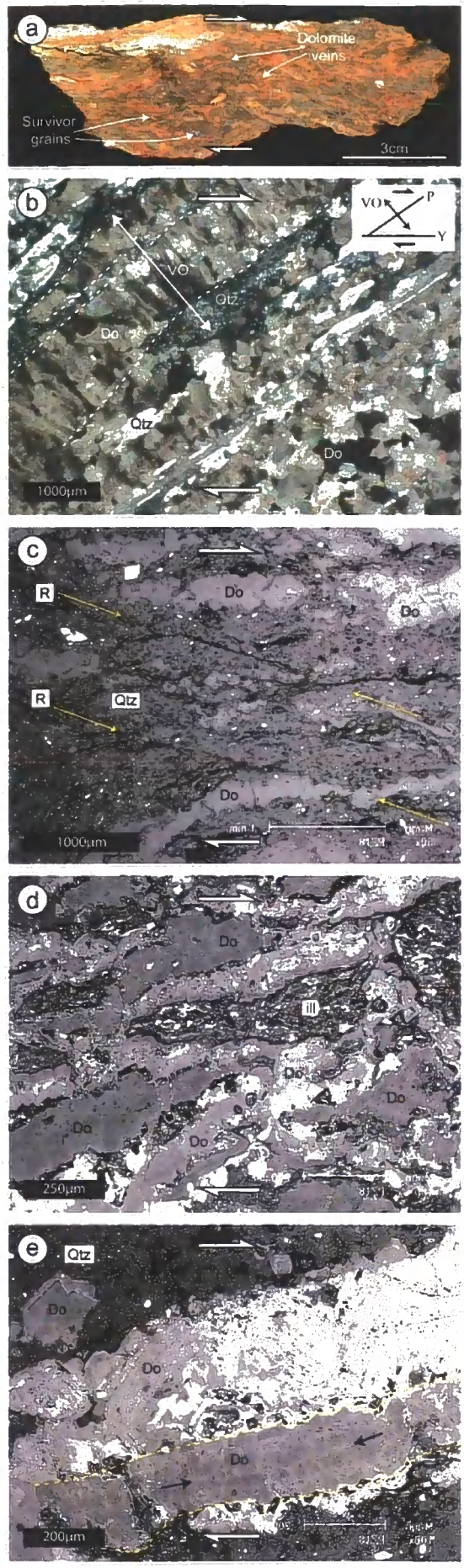
a
Dolomite veins
Survivor grains
3cm
b
VO
P
Y
VO
Qtz
Do
Qtz
Do
1000µm
c
R
Do
Do
R
Qtz
Do
1000µm
d
Do
Ill
Do
Do
Do
Do
250µm
e
Qtz
Do
Do
Do
200µm

Figure 6.11) Foliated cataclasites rich in dolomite veins, **a)** Polished slab showing the high abundance of dolomite veins, which locally parallel the macroscopic P-foliation. Elongate survivor grains are dispersed throughout the matrix, **b)** Photomicrograph in crossed polarised light highlighting the geometry of dolomite vein networks. Overall, the veins parallel the macroscopic P-foliation. Each vein contains dolomite grains with blocky-elongate morphologies. The long-axes of these grains is perpendicular to vein margins, suggesting that the vein opening direction (VO) was broadly perpendicular to the P-foliation. There is no evidence that the dolomite is strained, or that the veins contain multiple crack-seal bands, **c)** SEM image showing a pair of R-shears which deflect a thin dolomite vein. Note that the matrix foliation is also deflected into these shear bands, **d)** SEM image highlighting the branched, anastomosing nature of the vein networks, **e)** SEM image showing a dolomite vein with a central core which is relatively poor in Fe, flanked by wide rims of Fe-rich dolomite. The central cores of the veins (highlighted by yellow dashed lines) contain a thin median line (between black arrows) which is relatively enriched in Fe. The Fe-rich dolomite around the outside is coarse grained, clearly zoned, but does not contain grain morphologies consistent with growth in vein networks.

6.4.6. Fault breccias

Chaotic fault breccias within the core of the Zuccale fault can be up to 1.5m thick (Figure 6.3g), but they are also entirely absent in many places. The fault breccias are yellow to light brown in colour and contain no internal fabric. They are extremely cohesive and are dominated by angular clasts up to 20 cm in size, predominantly derived from the underlying foliated cataclasites (>80% of clasts; Figure 6.12a), but also containing smaller fractured clasts of chloritic material (<10% of clasts; Figure 6.12b). The clasts are set within a fine-grained matrix of quartz and chlorite, and subsidiary calcite and dolomite (Figures 6.12b, c).

Figure 6.12) Fault breccias, **a)** Polished slab showing the chaotic nature of the fault breccias. Clasts in this example are dominated by angular fragments of foliated cataclasite derived from the immediately underlying fault rocks, **b)** Photomicrograph between crossed-polars showing angular clasts of chloritic material sitting within a fine-grained matrix of quartz, chlorite, and dolomite. The inset image shows a relatively coarse-grained aggregate of post-tectonic dolomite, **c)** SEM image of large chlorite clasts. The chlorite clast is fractured, and the fractures are filled by relatively Fe-rich chlorite, **d)** SEM image showing an aggregate of euhedral, post-tectonic dolomite in the process of being replaced by calcite. Calcite replaces dolomite from the grain boundaries inwards, and exploits primary growth zones, **e)** SEM image showing the near-complete replacement of dolomite aggregates by calcite. Only one patch of dolomite remains in the lower right, **f)** Enlargement of e) showing replacement calcite grains which contain diffuse chemical zoning. The zoning reflects small variations in the Mg content of the calcite, and was probably inherited from pre-existing dolomite.

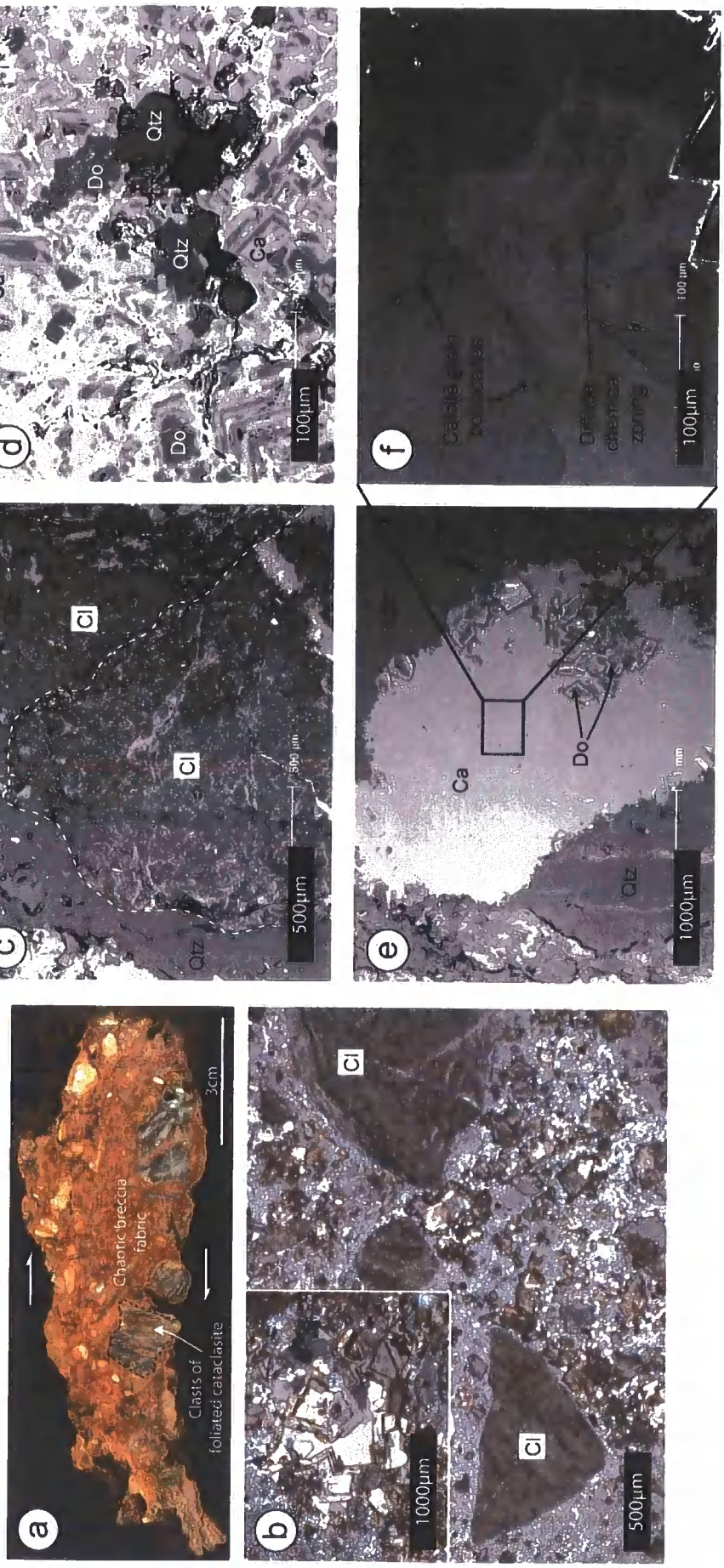
a
Chaotic breccia fabric
Clasts of foliated cataclasite
3cm
b
Cl
1000µm
Cl
500µm
c
Cl
Cl
Qtz
500µm
d
Ca
Do
Qtz
Qtz
Do
Ca
100µm
e
Ca
Do
Qtz
1000µm
f
Calcite grain boundaries
Diffuse chemical zoning
100µm

Dolomite cement was precipitated syn-tectonically within irregular inter- and intra-granular fractures 500-2000μm thick, and also within irregular vein networks surrounding large clasts. Dolomite also appears to have grown as a post-tectonic cement phase, and occurs in unstrained aggregates of large (up to 500μm), euhedral grains that show primary growth zoning, reflecting variations in the Mg content (Figure 6.12b inset). The last stage of cementation was the widespread replacement of both syn- and post-tectonic dolomite by calcite (Figure 6.12d). Calcite initially replaced dolomite along grain boundaries and along specific growth zones (Figure 6.12d), eventually leading to the complete replacement of dolomite aggregates (Figure 6.12e). Calcite crystals are unstrained, subhedral in shape, and contain relict zoning inherited from the pre-existing dolomite (Figure 6.12f). A thin coat (<50μm) of Fe-oxide is occasionally present along the boundaries of dolomite crystals that have been partially or completely replaced by calcite (Figure 6.12d).

6.4.7. Fault gouges

Light to dark brown foliated fault gouges occupy the upper 50cm to 2m of the Zuccale fault core (Figures 6.3h-j). 3 distinctive variations of fault gouge have been recognised based on colour, structural position, clast composition, and clast/matrix ratios. In well-exposed sections, the 3 distinctive fault gouges are separated by laterally continuous Y-shears that are lined by a thin layer (<0.5cm) of dark grey scaly clay material. Each of the fault gouges is characterised by a pervasive P-foliation. The middle and upper fault gouges are crosscut by numerous, closely spaced R-shears and, less frequently, by Y-shears. The R- and Y-shears are laterally discontinuous, anastomosing, and tend to be lined by <2mm of dark grey scaly clay material. The geometry of all of the Riedel shears is consistent with top-to-the-east transport.

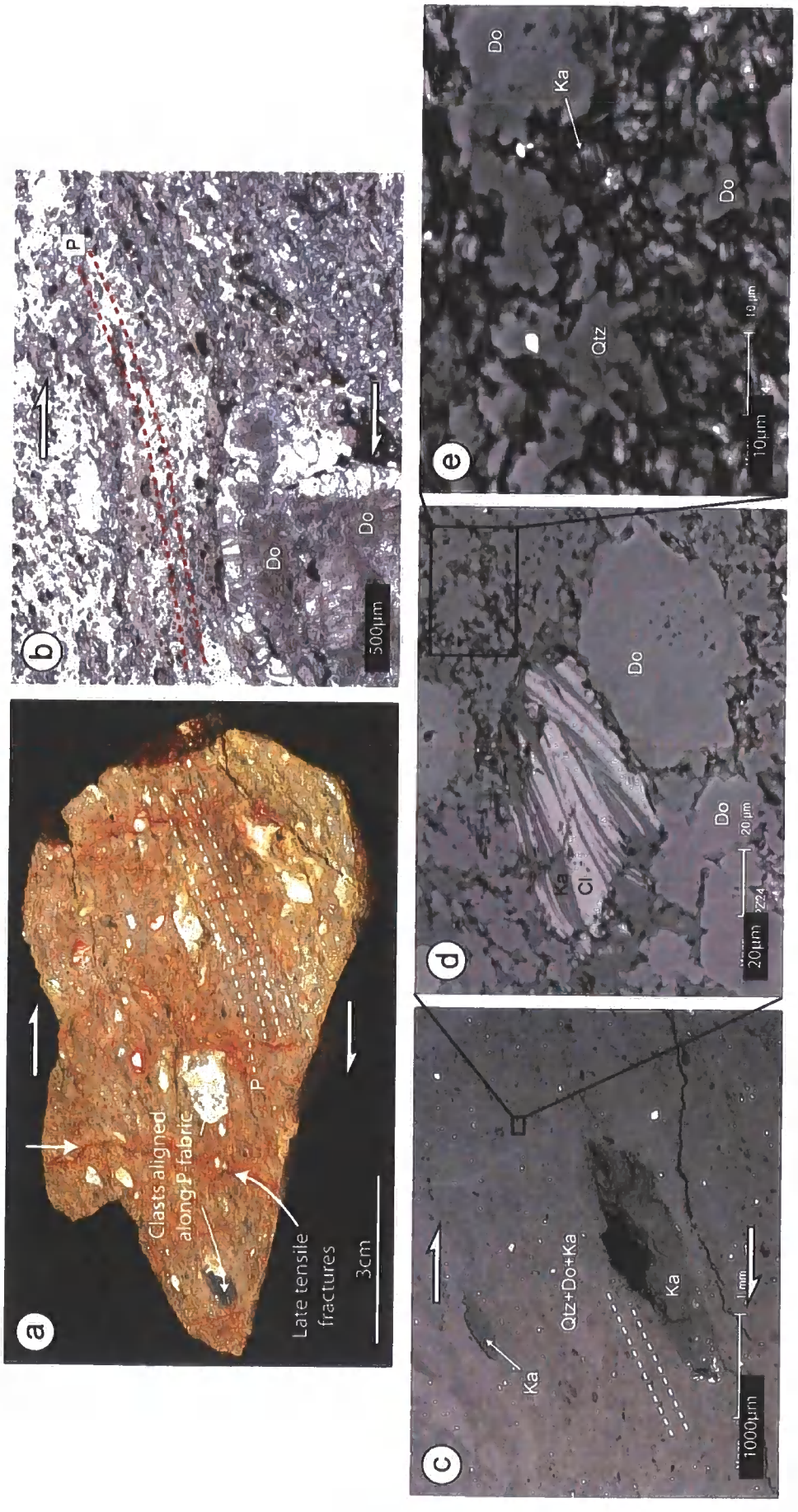
a
Clasts aligned along P fabric
P
Late tensile fractures
3cm
b
P
Do
Do
Do
500µm
c
Ka
Qtz+Do+Ka
Ka
1000µm
1 mm
d
Ka
Cl
Do
Do
20µm
20 µm
e
Do
Ka
Qtz
Do
10µm
10 µm

Figure 6.13) Lower fault gouges, **a)** Polished slab showing large dolomite survivor grains in a fine-grained, Fe-stained matrix. The survivor grains are aligned parallel to the P-foliation (white dashed lines). Note the presence of late tensile fractures filled with calcite, **b)** Photomicrograph in plane polarised light showing a large, polycrystalline dolomite grain within a fine-grained quartz and dolomite matrix, **c)** SEM image showing 2 large grains of kaolinite aligned parallel to the P-foliation, **d)** SEM image of chlorite-kaolinite grain within a fine-grained matrix of quartz and dolomite. Note the small matrix dolomite grains are typically rounded and many are aligned parallel to the P-foliation. The large dolomite grains may be post-tectonic, **e)** Detailed SEM image of the matrix, showing stacked pseudo-hexagonal plates of kaolinite filling pore space between quartz and dolomite grains.

6.4.7.1. Lower fault gouges

The lower fault gouges are between 0-1m thick (Figure 6.3h). In the field, they are characterised by 10-15% large survivor grains, which are well rounded and aligned parallel to the dominant P-foliation (Figures 6.13a, b). The P-foliation is enhanced by variations in the degree of cementation, by compositional variations between quartz-and dolomite rich layers, and by clay-rich seams that anastomose around survivor grains. The matrix is light to dark brown in colour, and is often stained red due to the presence of Fe-sulphides in the matrix, and by Fe-oxides in cross-cutting vein networks (Figure 6.13a).

At least 2 dominant types of survivor grain can be recognised in the lower fault gouges. The most frequent survivor grains consist of polycrystalline dolomite or individual grains of dolomite (Figure 6.13b). The dolomite often has a blocky-elongate morphology, and appears to represent reworked vein material. Large grains of kaolinite up to several mm long are also found dispersed throughout the fault gouges, and probably represent replacement of feldspar grains derived from the hangingwall sandstones (Figure 6.13c). Kaolinite occurs as a single phase, or in close association with chlorite (Figure 6.13d).

The matrix of the lower fault gouges is dominated by dolomite, quartz, and kaolinite (Figure 6.13e). Dolomite occurs as fine-grained (<10μm), rounded to sub-rounded grains that are often elongate and aligned parallel to the P-foliation (Figure 6.13d). Fine-grained

(<10μm) quartz and kaolinite are intimately mixed. Kaolinite occurs as stacked, pseudo-hexagonal plates that occupy pore spaces between quartz grains. Fe-sulphides are dispersed throughout the matrix.

Dolomite also occurs as syn-tectonic and post-tectonic cements. Syn-tectonic dolomite is precipitated in thin tensile veins (<1mm) that line the margins of large survivor grains, and also in rare intragranular fractures cross-cutting survivor grains. Grains of syn-tectonic dolomite show sweeping undulose extinction and rare Type I twins [*Burkhard*, 1993, *Ferrill et al.*, 2004]. Post-tectonic dolomite occurs as coarse (>100μm), euhedral to subhedral grains containing cores that are relatively poor in Fe, and rims that are relatively enriched in Fe.

With the exception of large survivor grains that are crosscut by intragranular fractures, there is little evidence for progressive grain size reduction due to grain fracturing, particularly within the fine grained matrix (Figure 6.13e).

6.4.7.2. Middle fault gouges

The middle fault gouges are ~50cm thick, although poor exposure prevents a complete assessment of their lateral continuity (Figure 6.3i). In the field, they are characterized by <5% large survivor grains, that are well rounded and aligned parallel to the P-foliation (Figure 6.14a). The P-foliation is enhanced by anastomosing, scaly layers of dark grey clay material. The matrix is light to dark brown in colour, resulting in part from pervasive post-tectonic growth of dendritic pyrolusite (Figures 6.14a, b).

At least 3 types of survivor grain can be recognised in the middle fault gouges. The most frequent survivor grains are polycrystalline dolomite or individual grains of dolomite (Figure 6.14b). Mixed quartz/calcite grains, and sandstone grains derived from

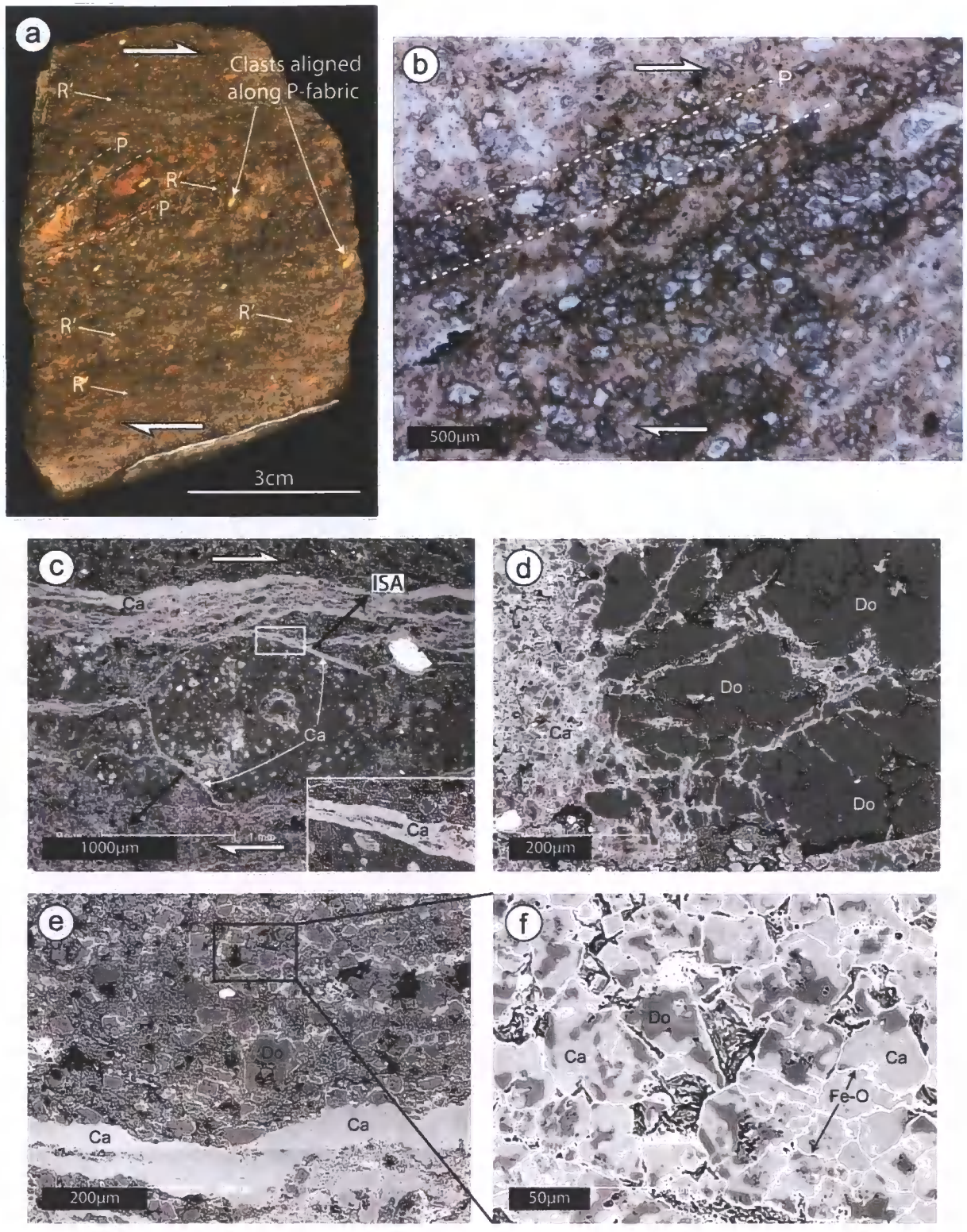

Figure 6.14) Middle fault gouges, **a)** Polished slab showing small, rounded survivor grains which are aligned parallel to the dominant P-foliation. The dark brown matrix contains post-tectonic pyrolusite, and is cross-cut by numerous thin, anastomosing R-shears, **b)** Photomicrograph in plane polarised light highlighting the P-foliation defined by a compositional banding of dolomite/calcite- and quartz-rich horizons. The colourless grains are dolomite/calcite, **c)** SEM image of a rounded calcite and quartz survivor grain. The matrix contains calcite-bearing shear veins which are in a Y-shear orientation (upper half of the SEM image). Thin tensile calcite veins are present along the

upper right and lower left edges of the survivor grain, in a position which would be consistent with their opening during top-to-the-east transport. The inset image shows a close-up of the white box, highlighting the presence of a thin planar wall-rock inclusion in the centre of one of the tensile veins. ISA, Instantaneous Stretching Axes, **d)** SEM image of a large, fractured dolomite grain being replaced by calcite, **e)** SEM image of quartz and dolomite matrix. Note the fractured nature of the dolomite grains, and the calcite-bearing shear vein in the lower half of the image, **f)** Detailed SEM image showing the replacement of dolomite grains by calcite. Replacement occurs along grain boundaries, and along specific growth zones in the dolomite. A thin layer of Fe-oxide is present along grain boundaries.

hangingwall lithologies, are also present (Figure 6.14c). Dolomite is widely replaced by calcite along grain boundaries, along the margins of fractures, and along specific growth zones (Figure 6.14d-f). Calcite exploits fracture networks cross-cutting polycrystalline survivor grains (Figure 6.14d). Visual inspection of optical- and scanning-electron images, coupled with the results of XRD analyses, suggests that >50% of the dolomite has been replaced by calcite. Within individual grains, the transition from relict dolomite cores to calcite rims is sharp, but the boundary is typically highly irregular and lobate in nature (Figure 6.14f). A thin coating (<5μm) of Fe-oxide is present around grains of dolomite that are partly or completely replaced by calcite (Figure 6.14f).

Calcite is clearly a syn-tectonic cement phase, because it is freshly precipitated in thin (<100μm) shear veins that parallel the margins of the fault core (Y-orientation), and also within thin (<50μm) tensile veins around the margins of large survivor grains (Figure 6.14c). The position and internal morphology of the tensile veins is consistent with their opening parallel to the instantaneous stretching axes during top-to-the east transport (Figure 6.14c).

The matrix of the middle fault gouges contains fine grained quartz, calcite and dolomite, as well as chlorite and a platy K-Al-silicate phase (possibly illite). The <10μm size fraction is dominated by quartz, but there is little evidence for any fracturing and grain size reduction within the matrix.

6.4.7.3. Upper fault gouges

The yellow to dark brown upper fault gouges are ~30cm thick (Figure 6.3j). In the field, they are characterized by <5% large survivor grains, that are well rounded and aligned parallel to the P-foliation (Figures 6.15a, b). The boundary between the upper fault gouges and the overlying hangingwall is marked by a thin (2-3mm) calcite extension vein that contains blocky-elongate calcite crystals whose long axes are perpendicular to the fault and vein margins. Although discrete slip surfaces occur at various structural levels within the fault core, we did not find any evidence for a discrete 'principal slip plane' at the lower boundary of the hangingwall, equivalent to those reported by *Cowan et al.* [2003] from other low-angle normal faults in the Basin and Range province.

Common types of survivor grain in the upper fault gouges include sandstone derived from hangingwall lithologies, polycrystalline dolomite, and mixed quartz/calcite. Large survivor grains of dolomite are cut by extensive calcite-filled fracture networks (Figure 6.15c). The calcite that fills the fracture networks does not show any evidence for being a replacement phase, and appears to be freshly precipitated.

The matrix of the upper fault gouges is dominated by quartz, calcite and kaolinite (Figures 6.15d, e). More than 95% of the matrix dolomite has been replaced by calcite. On a grain-scale, the P-foliation is enhanced by an alignment of all of the matrix phases, and a compositional banding of calcite- and quartz-rich horizons (Figures 6.15d, e). Kaolinite is dispersed intimately within the matrix and wraps around small (<10μm) rounded grains of calcite and quartz. It also occurs within larger (<100μm) aggregates of stacked pseudo-hexagonal plates. There is little evidence for any fracturing or progressive grain size reduction of the matrix phases (Figure 6.15e).

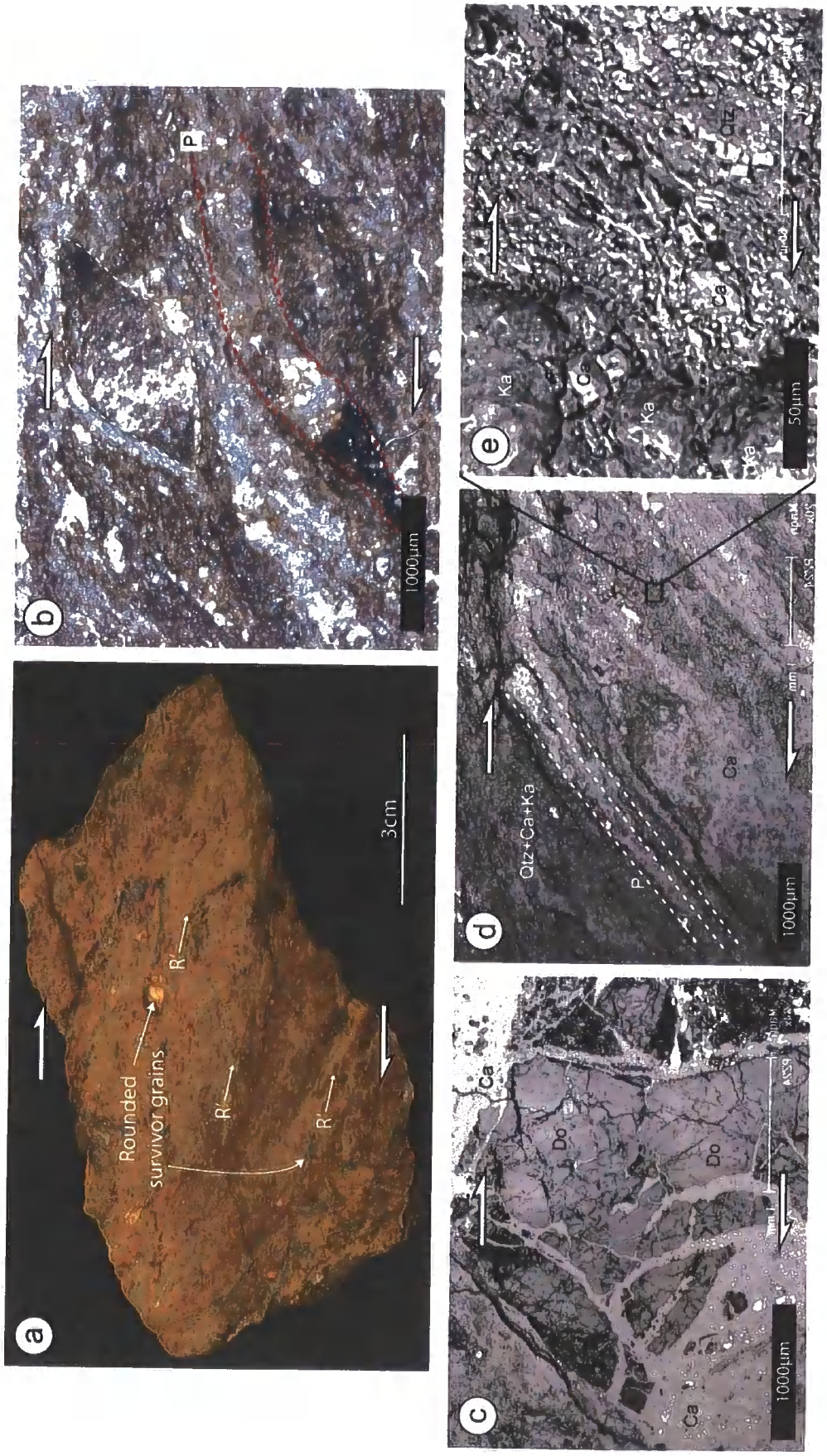
a
Rounded survivor grains
R'
R'
R'
3cm
b
P
1000µm
c
Ca
Do
Do
Ca
1000µm
d
Qtz+Ca+Ka
P
Ca
1000µm
e
Ka
Ca
Ka
Ka
Qtz
50µm

Figure 6.15) Upper fault gouges, **a)** Polished slab showing small, rounded survivor grains within a dark brown matrix which is cross-cut by thin, anastomosing R-shears, **b)** Photomicrograph in plane polarised light showing an elongate survivor grain which is parallel to the P-foliation, **c)** SEM image of a large, fractured dolomite grain. Freshly precipitated calcite fills fracture networks, **d)** SEM image of the characteristic matrix texture, consisting of fine-grained quartz, calcite and kaolinite. The P-foliation is defined by a compositional banding, **e)** Detailed SEM image showing small quartz and calcite grains within a foliated, kaolinite-rich matrix. Note the two larger aggregates of stacked chlorite in the left hand side of the image.

6.5. Discussion

The discussion initially focuses on the nature of the deformation mechanisms that were active in each of the fault rock types within the Zuccale fault. The interactions between fault rock deformation and fluid flow are then considered, followed by the implications for the mechanical behaviour of low-angle normal faults. Table 6.3 summarises the fault rock stratigraphy within the Zuccale fault (also see Figures 6.3 and 6.16), including the principal deformation mechanisms, syn- and post-tectonic authigenic minerals and cement phases, and potential mechanisms of fault zone weakening.

6.5.1. Deformation mechanisms and deformation conditions

Footwall breccias that lie immediately beneath the core of the Zuccale fault are characterised by intense fracturing and progressive grain-size reduction. There is abundant microstructural evidence for distributed cataclastic deformation. Cataclasis can be defined as deformation involving continuous brittle fracturing of grains, accompanied by grain rotation and frictional sliding of particles past one another [e.g. *Sibson*, 1977, *Twiss and Moores*, 1992, *Passchier and Trouw*, 2005]. It is a dominant deformation process at relatively shallow crustal levels (<10km), relatively low-temperatures and/or high strain rates [e.g. *Sibson*, 1977, *Hadizadeh and Rutter*, 1983, *Blenkinsop and Rutter*, 1986, *Evans*,

1988]. The breakdown of the breccia fabric in the upper few centimetres of the footwall, coupled with syn-tectonic growth of abundant epidote and transformation of feldspars to aligned aggregates of fine-grained white mica, all suggest channelized fluid flow, probably facilitated by the development of a pervasive footwall fracture network [*Jefferies et al.*, 2006a]. This general sequence of deformation within the footwall breccias was recognised by *Collettini and Holdsworth* [2004], who suggested that it may have initiated strain localisation and subsequent fault zone weakening (see section 5.3).

Amphibole schists within the Zuccale fault are characterized by a strongly foliated matrix that contains discrete fractured horizons, wrapping large fractured porphyroclasts of tremolite. This suggests that deformation was accommodated partly by cataclastic processes. Much of the fine-grained matrix appears to have grown syn-tectonically within fracture networks and strain shadow regions surrounding the porphyroclasts, emphasizing the important role of fluid-assisted mass transfer during deformation [*Rutter*, 1976, *Imber et al.*, 1997]. Although the exact nature of the deformation mechanisms operating in the matrix remains uncertain, the fine grain sizes (typically <100μm) and the availability of fluid suggests that some plasticity and grain boundary sliding may have operated. The amphibole schists record a complex history of coeval macroscopically-ductile and brittle processes, and are comparable to the amphibole schists documented by *Escartin et al.* [2003] from the 15°45'N oceanic core complex on the mid-Atlantic ridge. They suggested that strain localisation and deformation may have proceeded at temperatures of <300°C [but certainly <500°C; after *Miyashiro*, 1973], consistent with the presence of co-existing amphibole, chlorite, and minor talc.

The phyllonites and associated dolostones preserve evidence for the interaction of multiple deformation mechanisms. In low strain zones within the phyllonites, pods of dolostone protolith are highly fractured, suggesting deformation by cataclasis and grain

Table 6.3) Summary of microstructural observations, deformation mechanisms, and fault zone weakening mechanisms

Fault rock type	Approximate temperature/depth of formation	Dominant deformation mechanisms	Syn-tectonic cement/ authigenic minerals	Post-tectonic cement	Fault zone weakening mechanisms
Upper fault gouges	<2km <50°C	Particulate flow Cataclasis of large survivor grains	Calcite (>90% of reworked dolomite replaced by calcite)		Particulate flow accommodated along clay-rich grain boundaries, and along clay-lined Riedel shears
Middle fault gouges	<2km <50°C	Particulate flow Cataclasis of large survivor grains	Calcite (>50% of reworked dolomite replaced by calcite)		Particulate flow accommodated along clay-rich grain boundaries, and along clay-lined Riedel shears
Lower fault gouges	<2km <50°C	Particulate flow	Dolomite	Dolomite	Particulate flow accommodated along clay-rich grain boundaries, and along clay-lined Riedel shears
Fault breccias	<200°C	Cataclasis	Dolomite	Dolomite Calcite	Fluid overpressure.
Foliated cataclasites	<200°C	Cataclasis	Dolomite	Dolomite	Fluid overpressure.
Foliated cataclasites containing dolomite veins	<200°C	Cataclasis	Dolomite	Dolomite	Fluid overpressure.
Calcite Ultramylonites	170-250°C	Crystal plasticity (dislocation creep accomplished by subgrain-rotation recrystallisation, possibly accompanied by diffusion creep at ultra-fine grain sizes)	Calcite Quartz		Strain weakening by dynamic recrystallisation and grain size reduction. Onset of grain-size sensitive deformation mechanisms. Fluid overpressure.
Talc-phyllonites	>170-250°C	Fracturing and diffusive mass transfer to produce phyllonites Frictional slip in phyllonites Crystal-plasticity in calcite	Talc Tremolite Replacement of dolomite by calcite Minor quartz		Frictional-viscous creep at low strain rates. Frictional slip along 001 foliation planes. Fluid overpressure.
Amphibole schists	<300°C	Cataclasis Plasticity and grain boundary sliding in fine-grained matrix?	Actinolite and Fe-rich actinolite		None identified – possible frictional-viscous creep in fine-grained matrix.
Footwall breccias adjacent to the fault core	300°C?	Cataclasis Plasticity associated with breakdown of plagioclase to sericite?	Epidote	Calcite	
Footwall breccias away from fault core	300°C?	Cataclasis	Chlorite Illite Minor epidote		

size reduction. Fractures are lined by fibrous calcite (and minor quartz), that also appears to have replaced dolomite along grain boundaries throughout the dolostone protolith, suggesting that mineral replacement proceeded by a dissolution-reprecipitation mechanism [Collettini et al., submitted manuscript, *Putnis*, 2002, *Putnis and Putnis*, 2007]. Dolomite and calcite grains are closely associated with fibrous talc, that commonly grew in strain shadows surrounding calcite porphyroclasts, indicating fluid-assisted diffusive mass transfer ('pressure-solution') processes [*Rutter*, 1976, *Andreani et al.*, 2005]. Collectively, these microstructural observations suggest that talc may have formed from the interaction of dolomite with silica-bearing fluids by the reaction [e.g. *Gordon and Greenwood*, 1970]:

$$3\ CaMg(CO_3)_2 + 4\ SiO_2 + H_2O = Mg_3Si_4O_{10}(OH)_2 + 3\ CaCO_3 + 3\ CO_2$$
dolomite quartz talc calcite

Secondary reactions between talc and calcite resulted in the formation of tremolite, that may have been facilitated by further grain size reduction of calcite due to dynamic recrystallisation following the replacement of dolomite. The talc-forming reaction is widely documented in the metamorphic aureoles surrounding igneous intrusions [*Tracy and Frost*, 1991], and within faults and shear zones [e.g. *Hecht et al.*, 1999]. Determining the temperature of this reaction is problematic, but it can occur at temperatures as low as 170°C in aqueous-dominated systems characterized by low CO_2 contents [*Holness*, 1997]. The close association between the phyllonites and calcite-ultramylonites, which occur together within the same fault rock unit, suggests that formation of talc most likely proceeded in the temperature range 170-250°C (see below). Once talc formed, microstructural fabrics suggest that it deformed by frictional slip along (001) foliation planes [*Collettini et al.*, submitted manuscript; Appendix IV], a mechanism that can persist to near-surface temperatures and pressures [*Moore and Lockner*, 2008].

The calcite ultramylonites are dominated by fine-grained, dynamically recrystallised aggregates of calcite that possess C-axis maxima approximately perpendicular to the main foliation. This texture is relatively common in calcite mylonites, and has been observed for both coaxial and non-coaxial strains in natural shear zones [e.g. *Bestmann et al.*, 2000, *Trullenque et al.*, 2006, *Oesterling et al.*, 2007, *Rutter et al.*, 2007] and in deformation experiments on calcite [e.g. *Barnhoorn et al.*, 2004]. The presence of a preferred c-axis orientation is usually taken to indicate that dislocation creep was an operative crystal-plastic deformation mechanism [e.g. *De Meer et al.*, 2002]. In this case, the observation that matrix grains are of a broadly similar size to subgrains within the cross-cutting calcite veins perhaps suggests that rotation-recrystallisation was the dominant mechanism resulting in grain size reduction [*Bestmann and Prior*, 2003, *Passchier and Trouw*, 2005], although further work is necessary to establish this. The observation that the calcite-ultramylonites contain progressively sheared vein material is significant, because it strongly suggests that plastic deformation alternated with brittle fracture, driven by variations in strain rate or fluid pressure [e.g. *Famin et al.*, 2005, *Viola et al.*, 2006]. Indeed, the calcite-ultramylonites are cross-cut by rare cataclastic horizons that appear to have focussed Fe-bearing fluids. Such cataclastic horizons were then progressively deformed and folded during renewed crystal-plasticity. The relatively coarse-grained vein calcite accommodated a small amount of strain by mechanical twinning prior to recrystallisation. Twin morphology has been proposed as a reliable indicator of deformation temperatures at low metamorphic grade in calcite [*Burkhard*, 1993, *Ferrill et al.*, 2004, *Passchier and Trouw*, 2005]. The vein calcite within the ultramylonites contains Type II and Type III twin morphologies, bracketing the temperature of deformation between ~170-250°C [*Burkhard*, 1993, *Ferrill et al.*, 2004]. Pervasive dynamic recrystallisation of calcite is possible at these temperatures and geological strain rates.

Interestingly, *Kennedy and White* [2001] have suggested that the cyclic introduction of coarse-grained vein material may be a pre-requisite for dynamic recrystallisation to occur at low temperatures (150-250°C).

Both the foliated cataclasites and the fault breccias contain clear evidence for fracturing and progressive fragmentation of constituent clasts. Typically, large angular to sub-angular clasts sit within a finer-grained matrix of comminuted material, some of which appears to represent reworked veins or fault zone cements. Both are suggested to have accommodated a majority of strain by distributed cataclastic flow, with some localisation of deformation along Riedel shears within the cataclasites. Cataclastic foliations can be produced by brittle processes alone [*Chester et al.*, 1985], but given the apparent abundance of fluids within the Zuccale fault (see below), and the presence of clay phases that can increase rates of diffusion [*Hickman and Evans*, 1995], it seems likely that cataclasis was accompanied by pressure solution processes and diffusive mass transfer [e.g. *Evans and Chester*, 1995, *Jefferies et al.*, 2006a]. An absence of crystal-plasticity in quartz and dolomite within the foliated cataclasites limits the temperatures during deformation to <250°C, but we suggest that it is more likely that deformation occurred at <200°C. This is supported by the observation that fragments of the underlying calcite-ultramylonites and phyllonites are present within the foliated cataclasites.

Fault gouge is a relatively common product of low-temperature deformation within fault zones [e.g. *Sibson*, 1977, *Vrolijk and Van der Pluijm*, 1999]. Several characteristics are common to all of the identified fault gouges within the Zuccale fault. Rounded survivor grains are aligned parallel to a dominant P-foliation [*Cladouhos*, 1999b], and lie within a fine-grained matrix containing clay phases such as kaolinite and chlorite. The clays within the fault gouges are most likely to have been derived from alteration and mechanical incorporation of clasts of wall rock material, although we cannot rule out authigenic

growth of clays facilitated by fluid influx [e.g. *Vrolijk and Van der Pluijm*, 1999]. With the exception of the largest survivor grains, there is little evidence in optical- or SEM-images for inter- or intra-granular fracturing of grains. The gouges appear to have accommodated distributed, macroscopically-ductile deformation, accompanied by localization of deformation along clay-bearing Riedel shears. The above microstructural features are inconsistent with cataclastic deformation by pervasive fracturing and grain size reduction. Rather, they suggest that deformation was accommodated by particulate flow, that we define here as the rolling and sliding of grains past one another in the absence of grain fracturing [following *Twiss and Moores*, 1992]. Particulate flow has been observed in faulted, poorly lithified sediments deformed at low confining pressures [less than around 30MPa; *Rawling and Goodwin*, 2003]. *Cowan et al.* [2003] and *Hayman* [2006] observed that particulate flow was the dominant deformation mechanism at depths of <2km in the fault gouges that formed along the Black Mountains detachments in Death Valley, a similar conclusion to that reached by *Manatschal* [1999] who studied the detachment fault exposed in the Err nappe in Switzerland. Thus, we conclude that the fault gouges within the Zuccale fault were formed at temperatures of less than 50°C and depths of less than 2km.

6.5.2. Relationship between deformation and fluid flow

Focussed fluid flow during movement along the Zuccale fault is required to explain the presence of abundant fault cements and vein material, and the syn-tectonic mineral reactions observed at the top of the footwall and within the fault core. It seems likely that most, if not all of the deformation mechanisms described above were intimately linked to the presence of fluids, a conclusion that applies to many detachment fault systems

worldwide [e.g. *Coney*, 1980, *Morrison and Anderson*, 1998, *Floyd et al.*, 2001, *Douglas et al.*, 2003, *Famin et al.*, 2005, *Famin and Nakashima*, 2005].

Syn-tectonic vein and cement materials within the Zuccale fault are dominated by dolomite and calcite. Dolomite was precipitated as a syn-tectonic cement within the foliated cataclasites, fault breccias, and the lower fault gouges, and was superseded by calcite in the middle and upper fault gouges. Late-stage calcite hydrofracture veins also cross-cut the fault core at Punta di Zuccale [*Collettini et al.*, 2006a]. The observation that calcite represents the last cement phase is supported by its occurrence as a post-tectonic cement in both the footwall breccias and the fault breccias, both of which are likely to have possessed relatively high post-tectonic permeability. Preliminary carbon, oxygen, and strontium isotope analyses (Chapter 4) indicate that the dolomite veins within the foliated cataclasites were precipitated from a meteoric-hydrothermal fluid that may have interacted with igneous bodies carrying a mantle carbon signature. All of the syn- and post-tectonic dolomite within the Zuccale fault, together with cataclastic epidote at the top of the footwall, and amphibole grains within the amphibole schists, display systematic enrichment in Fe from grain centres to grain margins. Hematite and/or magnetite grains are also dispersed within the calcite-ultramylonites and the foliated cataclasites. Elba is famous for the Fe-ore deposits that are located mainly along the south and south-east coasts, in close proximity to the Zuccale fault. Fe mineralization is thought to have resulted from remobilisation of sedimentary Fe within the metamorphosed Palaeozoic/Triassic basement of Complex I. Most authors agree that remobilisation was caused by fluid flow associated with intrusion of the Porto Azzurro plutonic complex [*Bortolotti et al.*, 2001a, *Duenkel et al.*, 2003 and references therein]. The progressive enrichment in Fe observed within the Zuccale fault suggests that fluids carrying Fe became increasingly important during deformation. This represents further evidence for the

development of a meteoric-hydrothermal fluid system, and an increasingly important contribution from the Porto Azzurro pluton. The calcite from the fault gouges and from the late-stage hydrofracture veins has an isotopic signature pointing towards a seawater fluid source, which penetrated downwards through the fractured hangingwall and footwall of the Zuccale fault.

6.5.3. A conceptual model of fault rock development

Collectively, the microstructural and fluid flow histories summarized above suggest a model in which the fault rock 'stratigraphy' developed during progressive exhumation of the Zuccale fault from deep to relatively shallow levels within the upper crust. We have no quantitative constraints on the depths of formation of the various fault rock assemblages, although it is likely that the fault gouges formed at depths of <2km. We can envisage two scenarios to explain the observed fault rock sequence:

1) The sequence developed during progressive exhumation under a relatively 'normal' geotherm (25°C/km), in which case there may be up to 8km of vertical difference between the depths of formation of the fault gouges and the amphibole schists, calcite-ultramylonites, and phyllonites. Approximately 6km of displacement across the Zuccale fault can only account for ~1.5km of vertical exhumation, assuming the fault dips uniformly 15° to the east. Additional syn- and post-tectonic exhumation may have been achieved by the combined effects of flexural isostatic rebound [e.g. *Buck*, 1988], regional uplift and erosion at rates of ~0.1-0.8mm/yr^{-1} [*Branca and Voltaggio*, 1993, *Fellin et al.*, 2007], and late-stage inflation of the Porto Azzurro pluton [*Cruden and McCaffrey*, 2001, *Acocella and Rossetti*, 2002, *Rocchi et al.*, 2002].

2) The sequence developed during progressive exhumation, but the geotherm was elevated at depth due to the presence of the developing Porto Azzurro pluton and other plutonic complex in Elba [see *Rossetti et al.*, 2008 for a possible present-day analogue from southern Tuscany]. If this is the case, then all of the fault rocks potentially formed at much shallower depths than would be inferred for a normal geotherm. Transient periods of relatively high-temperature deformation are known to occur during pluton/sill/dyke emplacement [e.g. *Lister and Baldwin*, 1993], although it is important to reiterate that no regional mylonitic fabrics are found in the footwall of the Zuccale fault at the current erosion level. An alternative explanation for elevated temperatures along the Zuccale fault is channelized flow of 'hot' fluids that interacted with the developing plutonic complex [e.g. *Kopf et al.*, 2003, *Famin and Nakashima*, 2005]. The absolute depths at which the various fault rocks formed does not affect our interpretations regarding their mechanical significance, which is the focus of this paper.

During the initial stages of deformation along the Zuccale fault, cataclasis (at relatively deep crustal levels) and particulate flow (at relatively shallow levels) were the dominant deformation mechanisms in most of the pre-existing tectonic Complexes. In Complexes dominated by carbonate (mainly Complexes II and III), phyllosilicate-bearing assemblages formed by metasomatic reactions between dolostones and Si-bearing fluids, most likely to have been derived from the developing plutonic bodies. Additionally, low-temperature crystal-plastic shear zones formed by dynamic recrystallisation, grain size reduction, and strain localization. The fault rock stratigraphy at Punta di Zuccale records deformation at progressively shallower crustal levels and lower temperatures, and a switch in the dominant deformation mechanisms from cataclasis to dissolution-precipitation creep and/or crystal-plasticity (depending on lithology), and finally to particulate flow (Figure 6.16, Table 6.3). As displacement on the Zuccale fault accumulated, the lithologically

heterogeneous hangingwall of the Zuccale fault moved past a fixed reference point in the footwall, in this case the Punta di Zuccale outcrop (Figures 6.16b-e). Eventually, Complex V was juxtaposed against Complex I (Figure 6.16e). Movement of all 5 Complexes past a fixed reference point resulted in a series of lithologically distinct fault rocks, derived from different Complexes, being 'stacked' one on top of another. This may have occurred for 3 reasons, some or all of which may apply: 1) Overall, the fault zone experienced thinning and a localization of strain towards the upper fault core at progressively lower temperatures [*Means*, 1995, *Cowan et al.*, 2003]; 2) certain fault rocks were isolated from the evolving fault zone due to movements on subsidiary normal faults in the footwall [*Smith et al.*, 2007] and; 3) fault rocks experienced post- and/or syn-tectonic hardening due to vein and cement precipitation, and thus were 'abandoned' at the expense of younger, weaker, and structurally-higher fault rock assemblages [*Wintsch*, 1975, *Wibberley*, 1999, *Steffen et al.*, 2001]. In contrast to most of the evolutionary models proposed for the exhumation of ductile-to-brittle core complexes and detachment faults in the western US [e.g. *Coney*, 1980, *Davis*, 1980, *Davis*, 1983a, *Davis et al.*, 1986, *Davis*, 1987, *Lister and Davis*, 1989, *Miller*, 1992, *Cowan et al.*, 2003], there is little evidence that finite shear strains increased systematically towards the core of the Zuccale fault, or towards a principal slip plane within the fault core. High strains appear to have been accommodated by all of the foliated fault rocks within the core of the Zuccale fault, regardless of their relative structural positions, suggesting that the first reason outlined above may not be applicable. The second reason is applicable to the amphibole schists, phyllonites, and calcite-ultramylonites, which are only present along the Zuccale fault as a series of isolated

west
east
Complex V
Fault gouges
Foliated cataclasites
Fault breccias
Foliated cataclasites
Phylonites and
calcite-mylonites
Footwall breccias
Amphibole schists
Complex I
5 metres
a
b
Complex I
Cataclasis
Focused
fluid flow
Complex I
c
DMT, frictional slip,
crystal-plasticity
Cataclasis
I
d
Cataclasis
DMT, frictional slip,
crystal-plasticity
Cataclasis
I
e
V
Particulate flow
Cataclasis
DMT, frictional slip,
crystal-plasticity
Cataclasis
I

Figure 6.16) Summary of the deformation mechanisms and fault rock evolution within the Zuccale fault, **a)** Model of the Zuccale fault at Punta di Zuccale shown in Figure 6.3a, overlain by a map of the dominant deformation mechanisms derived from microscopic analysis. The colours correspond to those shown in parts b-e. The margins of the fault core are marked by red lines, **b-e)** Schematic diagrams showing the proposed evolution of the fault rock stratigraphy at Punta di Zuccale. Active deformation mechanisms are labelled in red, inactive deformation mechanisms in blue. DMT, diffusive mass transfer. Cataclasis dominated in basement lithologies during the early stages of slip (b). This was superseded by DMT, frictional slip, and crystal plasticity as carbonate-dominated wall rock lithologies were translated past the footwall (c). These deformation mechanisms were in turn superseded by cataclasis during exhumation and cooling (d), and ultimately by particulate flow at shallow crustal levels (e). Between parts c and d, the phyllonites and calcite-ultramylonites were isolated from the evolving fault zone by broadly synchronous movements on high-angle, subsidiary footwall faults [see *Smith et al.*, 2007 for details]. The transition from cataclasis to particulate flow in part e may have been facilitated by widespread post-tectonic growth of dolomite within the foliated cataclasites and fault breccias, resulting in precipitation-hardening and a transfer of deformation upwards within the fault core. Deformation of the fault gouges was accompanied by fluid flow derived from shallow reservoirs.

lenses that escaped later deformation [Figure 6.3, 6.16c, d; see *Smith et al.*, 2007 for details]. The third reason may be applicable to the foliated cataclasites and fault breccias, both of which experienced widespread post-tectonic precipitation of dolomite, followed by deformation within the fault gouges at structurally-higher levels within the fault core (Figure 6.16e).

6.5.4. Implications for the mechanics of low-angle normal faults

In the absence of stress rotation around low-angle normal faults, for which there is currently little geological evidence, low-angle normal faults must be anomalously weak, in that they appear to slip under low resolved shear stresses compared to those determined by 'typical' Byerlee friction coefficients (μ=0.6-0.85) and hydrostatic fluid pressures [*Byerlee*, 1978, *Axen*, 2004]. Fault weakness most likely originates due to the mechanical and fluid flow properties of the fault zone and its constituent fault rocks. Our microstructural observations suggest that multiple fault zone weakening mechanisms may have operated along the Zuccale fault, and they demonstrate how the complex mechanical

behaviour of fault zones may change as a function of wall rock/fault rock lithology, fluid availability, and ambient environmental conditions.

Fractured pods of dolostone embedded within the phyllonites reacted with silica-bearing hydrothermal fluids to form calcite and talc. The calcite may have deformed by continued crystal-plasticity, but the talc horizons appear to have deformed by a combination of frictional slip and fluid-assisted diffusive mass transfer. This multi-mechanism behaviour may be an example of 'frictional-viscous' creep, whereby the mechanical behaviour is dependent on both normal stress (confining pressure) and strain rate/temperature [*Bos and Spiers*, 2000, 2001, *Imber et al.*, 2008]. Fracturing and cataclasis followed by fluid influx and the development of phyllonites has been documented along several large-displacement strike-slip, normal, and reverse faults, although the mineralogical details in each case differ [e.g. *Bruhn et al.*, 1994, *Wintsch et al.*, 1995, *Stewart et al.*, 2000, *Imber et al.*, 2001, *Gueydan et al.*, 2003, *Jefferies et al.*, 2006b]. *Collettini and Holdsworth* [2004] recognised the general importance of the cataclasite-phyllonite transition along the Zuccale fault, but did not elaborate on the evolution of the fault rock stratigraphy in detail. Weakening of the talc-rich phyllonites may have arisen in one of two ways, although they are likely to be interrelated. Firstly, talc horizons derived from dolostone pods are continuous and interconnected. If slip had localized within any one of these talc horizons, then the frictional strength of the Zuccale fault may have been limited for the duration of localization by the frictional strength of talc, that is <0.2 over a wide range of pressures and temperatures [*Moore and Lockner*, 2008]. Secondly, the operation of fluid-assisted 'frictional-viscous' processes at geological strain rates can lead to profound weakening (as much as a 50-70% reduction in strength) compared to conventional brittle-ductile strength envelopes [e.g. *Chester and Higgs*, 1992, *Bos and Spiers*, 2002, *Holdsworth*, 2004, *Niemeijer and Spiers*, 2005].

Based on studies of natural calcite shear zones, it is commonly observed that dynamic recrystallisation and grain size reduction leads to progressive strain localization and consequent rheological weakening [e.g. *Bestmann et al.*, 2000, *Ebert et al.*, 2007, *Oesterling et al.*, 2007]. Deformation experiments on calcite designed to simulate dislocation creep suggest that strain softening following the onset of dynamic recrystallisation typically does not exceed ~25% of the peak stress [*ter Heege et al.*, 2002, *Barnhoorn et al.*, 2004], but it could be significantly more pronounced at the higher strains and lower strain rates typical of natural shear zones [*De Meer et al.*, 2002]. Perhaps more importantly, grain size reduction may lead to an increasing contribution from grain-size sensitive deformation mechanisms such as diffusion creep, leading to deformation at lower flow stresses than required for grain-size insensitive dislocation creep. There is a general lack of high-strain experiments on calcite that demonstrate a recrystallisation-induced transition to grain-size sensitive creep. However, extrapolation of calcite flow laws to geological strain rates, temperatures appropriate for deformation of the calcite-ultramylonites within the Zuccale fault (170°-250°C), and grain sizes around 10μm, suggests that grain-size sensitive creep may have dominated following pervasive recrystallisation, leading to a significant strength reduction [*Rutter*, 1995]. Recently, *de Bresser et al.*, [2001] have suggested that drastic weakening due to the onset of diffusion creep is unlikely, because grain size reduction will be balanced by grain growth, leading to steady-state deformation close to the boundary between the dislocation and diffusion creep fields. They suggested that significant weakening by grain size reduction and diffusion creep is only possible if grain growth is inhibited. We infer a contribution to strain from grain-size sensitive diffusion creep following dynamic recrystallisation, but also speculate that it may have been particularly important because of the presence of fine-grained chlorite (and possibly other phases) along calcite grain boundaries, that can potentially

lead to grain boundary 'pinning' and grain growth inhibition, and also enhanced diffusion rates [*Jessell*, 1987, *Hickman and Evans*, 1995, *Passchier and Trouw*, 2005].

Evidence for the development of transiently high fluid pressures along the Zuccale fault is widespread. Late-stage hydrofracture systems [*Collettini et al.*, 2006a] and fluidized footwall breccias [*Smith et al.*, 2008] have been described previously, and suggest that high fluid pressures were able to develop immediately *beneath* the core of the Zuccale fault, that likely represents a relatively low-permeability seal in comparison to the fractured footwall and hangingwall [*Faulkner and Rutter*, 2000, 2003]. The foliated cataclasites, talc-phyllonites, and calcite-ultramylonites described here all contain syn-tectonic vein material indicating that high fluid pressures were able to develop *within* the core of the Zuccale fault. The dolomite veins within the foliated cataclasites exploited the dominant P-foliation planes (i.e broadly sub-horizontal planes), that may have permeability up to 2 orders of magnitude larger than in a direction normal to the P-foliation [*Faulkner and Rutter*, 2000, 2003]. All of the dolomite veins appear to have opened normal to the P-foliation, suggesting that fluid pressures locally exceeded the lithostatic load. Few veins display a second or third phase of opening, perhaps indicating that precipitation of dolomite led to local *hardening* of the foliated cataclasites. Weakening of low-angle normal faults due to elevated fluid pressures is a well-described phenomenon, and is favoured during periods of high fluid flux from depth [e.g. *Reynolds and Lister*, 1987, *Axen*, 1992, *Floyd et al.*, 2001, *Little et al.*, 2007]. The stable isotope signature of the dolomite veins suggests that high fluid pressure weakening may have been particularly important during the growth and emplacement of plutonic complexes. We suggest that fluids were channelled up the Zuccale fault, mainly within the fractured and faulted footwall, where they were able to infiltrate the fault core along relatively high-permeability layers such as the P-foliation planes. The presence of fine-grained phyllosilicates and clays

promoted the development of high fluid pressures, leading to transient fluid pressure weakening of the Zuccale fault.

The significance of particulate flow within the fault gouges is that the frictional strength of such granular aggregates is potentially controlled by grain boundary processes and grain boundary mineralogy, as opposed to the inherent tensile strength of the constituent clasts (which would be the main control during cataclasis). SEM observations suggest that all 3 fault gouges within the Zuccale fault contain a significant amount of kaolinite and/or chlorite, which typically occur as platy, fine-grained matrix phases. The XRD analysis seems to underestimate, or entirely miss, the presence of some phyllosilicate phases, a common consequence of the crystallographic properties of phyllosilicates. The frictional strength of water-saturated kaolinite measured in a triaxial deformation apparatus ranges between ~0.3 [*Crawford et al.*, 2008, at 50MPa effective normal stress] and ~0.5 [*Moore and Lockner*, 2004b, at 100MPa effective normal stress], whilst the strength of chlorite is ~0.4 [*Moore and Lockner*, 2004b; where friction is shear stress/normal stress]. If distributed particulate flow was accommodated by water-saturated kaolinite and/or chlorite along grain boundaries, then this can potentially explain low-angle slip within the fault gouges in the upper ~2km of the brittle crust [*Axen*, 2004].

An important unresolved question, highlighted by *Cowan et al.* [2003] amongst others, is how much deformation was accommodated by distributed particulate or cataclastic flow in each of the fault rocks, versus more localized, potentially seismogenic deformation along Riedel-shears? The core of the Zuccale fault contains abundant Y- and R-shears, particularly within the fault gouges where they are commonly lined by dark grey, scaly clay material. Clearly, the localized shears within the fault gouges accommodated slip at some stage during the late exhumation history of the Zuccale fault, at which point its strength may feasibly have been limited by the frictional strength of the clay minerals.

6.6. Conclusions

The diversity of fault rock materials found along the Zuccale low-angle normal fault primarily reflects the inherited structural and lithological complexity of the local wall rocks, the availability of fluids, and the ambient pressure and temperature conditions. Multiple deformation mechanisms, including cataclasis, diffusive mass transfer, crystal-plasticity, and particulate flow, were operative within the fault zone, and many were probably active broadly contemporaneously. The fault rock stratigraphy records progressive exhumation of the Zuccale fault associated with a change in dominant fluid reservoir. Potential fault zone weakening mechanisms include frictional slip and frictional-viscous flow in phyllosilicate-rich fault rocks, plastic grain size reduction and the onset of grain-size sensitive creep in calcite mylonites, high fluid pressures, and particulate flow accommodated by clay minerals. As the evolution of the Zuccale fault is so closely linked with intrusion of plutonic complexes, most notably the Porto Azzurro pluton, the relative importance of such weakening mechanisms must have varied over time. An interesting area for future research is to determine the mechanical significance of different fault zone fabrics, and to assess how granular mechanical behaviour might be influenced by changes in particle size, shape, and alignment that are so commonly observed within natural fault zones.

Chapter 7

Future Work

7.1 Regional geophysics

Crustal-scale seismic reflection surveys such as the CROP03 profile [*Barchi et al.*, 1998] have been pivotal in the identification of a series of major low-angle normal faults that cut the upper crust in central Italy [*Pauselli et al.*, 2006]. The Zuccale fault has been proposed as an analogue for currently active low-angle normal faults beneath central Italy, but seismic data around Elba are scarce, and the geometry and location of the Zuccale fault in the subsurface are still poorly constrained. Only a small number of 2-dimensional seismic profiles exist for the basins to the east of Elba, and there is little subsurface data on the island of Elba itself [*Keller and Coward*, 1996, *Pascucci et al.*, 1999, *Bortolotti et al.*, 2001a]. Acquisition of higher-resolution (possibly 3-dimensional) seismic data around Elba, coupled with a gravity survey on Elba itself, would help to address the following questions:

1) What is the location of the Porto Azzurro pluton in the subsurface?
2) Are there any other large, unexposed plutonic bodies that are currently not documented?
3) What is the subsurface geometry of the Zuccale fault, and is it influenced in any way by the emplacement of unexposed plutons, passive rotation, or later high-angle faulting?

The extent of the metamorphic aureole surrounding the Porto Azzurro pluton, and the distribution of small surface outcrops on Elba, suggests that the Porto Azzurro pluton has a substantial size, and probably contributed towards doming of the Zuccale fault (Chapter 4). In detail, the location of the pluton margins, the depth to the top and base of the pluton, and the thickness of the pluton, are all virtually unknown. Addressing the above questions could significantly contribute towards our understanding of: 1) shallow-level igneous emplacement mechanisms; 2) the relationships between plutonic bodies and major fault systems, and; 3) whether it is reasonable to consider the Zuccale fault and the island of Elba as an exhumed analogue for the active Altotiberina low-angle normal fault [*Chiaraluce et al.*, 2007], and/or the presently active Lardarello and Monte Amiata geothermal fields. Both geothermal fields are associated with active plutonic systems, and contain sub-horizontal to shallowly-dipping crustal reflectors that may represent fault systems [*Rossetti et al.*, 2008].

7.2 Fieldwork

Many large-displacement low-angle normal faults in north America and elsewhere are exposed in structural domes a few kilometres to a few tens of kilometres in diameter [*Coney*, 1980, *Lister*, 1984]. In many cases, the footwalls contain pervasive crystal-plastic fabrics and have clearly been exhumed from mid-crustal depths [*Davis et al.*, 1986]. Typical models for the evolution of these 'metamorphic core complexes' involve extension and removal of the hangingwall followed by isostatic rebound of the footwall driven by buoyancy forces [*Wernicke and Axen*, 1988, *Axen and Bartley*, 1997]. At some stage, the evolving domal footwall approaches the surface or breaches the surface and is known as a 'breakaway' [*Axen*, 2004]. Such a breaching process typically leads to an abandonment of

parts of the fault system that are back-rotated out of an orientation favourable for continued slip. Chapter 4 of this thesis presented evidence that the Zuccale fault has an overall domal shape (see Figure 4.2). However, in this case, doming was primarily attributed to late-stage intrusion and inflation of the Porto Azzurro pluton, rather than to isostatic rebound of the footwall and the formation of a 'rolling hinge'. If such a model is correct, it also predicts that parts of the Zuccale fault exposed on the west side of Monte Calamita (e.g. the Punta di Zuccale outcrop) would have been progressively back-rotated and abandoned during incremental growth of the pluton. It further predicts that low-angle slip may have continued in areas to the north and east of Monte Calamita (e.g. the Spiagge Nere outcrop). Indeed, preliminary structural analysis suggests that the magnitudes of extension in the footwall of the Zuccale fault are greater on the east side of Monte Calamita than on the west. Further detailed structural mapping, perhaps combined with dating of fault rock materials [e.g. K-Ar dating of illite in fault gouges; *Vrolijk and Van der Pluijm*, 1999], may allow for the documentation of different stages of low-angle slip, or for the recognition of a series of low-angle normal faults that progressively cut up section in to the hangingwall. Unfortunately, inland exposure on Elba is generally poor, which may hinder any continuous detailed mapping.

7.3 Fluid inclusion analysis

The study of fluid inclusions hosted principally in the minerals quartz and calcite provides an opportunity to determine fluid compositions, densities, temperatures, and pressures at the time of fluid entrapment [e.g. *Touret*, 2001]. Fluid inclusion analysis has the potential to provide a range of important data related to the evolution of the Zuccale fault, particularly if it were coupled with high-resolution geochemistry (e.g. stable isotope analysis on coexisting calcite and dolomite, or quartz and calcite). Chapter 3 describes a

suite of fluidized footwall breccias that are suggested to have formed during transient increases in fluid pressure beneath the core of the Zuccale fault. At least three variants of fluidized breccia have been recognized in the field. Optical microscopy suggests that the breccias, which are hosted predominantly in quartzites, contain abundant fluid inclusions that are typically a few tens of microns in diameter. Fluid inclusion analysis raises the possibility of quantifying changes in fluid properties during formation of the breccias, which has important implications for high fluid pressure weakening of low-angle normal faults. In this case, fluid inclusion analysis would have to be preceded by a detailed study of inclusion textures and overprinting relationships, because there are likely to be multiple sets of inclusions related to initial cataclastic deformation along the Zuccale fault, and later fluidization of the breccias.

7.4 Experimental rock deformation

The triaxial friction experiments described in Chapter 5 were carried out at room temperature, effective normal stresses of 25-75MPa, and axial loading rates of 0.1μm/s and 1μm/s. The experiments provided important insights in to the mechanical behaviour of the Zuccale fault over a restricted range of conditions, but deformation along the Zuccale fault probably occurred at temperatures of up to 250°C (Chapter 6), and at strain rates equivalent to 0.0001μm/s – 0.00001μm/s. Carrying out deformation experiments at very slow strain rates presents serious technical problems [*Paterson and Wong*, 2005], and would require that samples are deformed for anything between a few days and a few months. If technical limitations could be overcome, a more comprehensive experimental programme could be designed to test the frictional properties and permeability of the fault rocks at elevated temperatures and more realistic strain rates. Potentially, this would open up the possibility of using chemically active pore fluids [e.g. *Le Guen et al.*, 2007], and

simulating the effects of dissolution-precipitation creep, that are likely to be of major importance within large fault cores accommodating distributed deformation [*Gratier and Gueydan*, 2007].

7.5 Fault rocks and the mechanics of low-angle normal faults

The Zuccale fault appears to cross-cut pre-existing structural anisotropies in the upper crust. There are many other examples of low-angle normal faults that cross-cut homogenous, isotropic plutonic rocks. No current theoretical models satisfactorily explain the initiation of such faults, and this remains the biggest problem in low-angle normal fault mechanics. Initiation may occur within an inclined regional stress field [e.g. *Westaway*, 1999], but there is no compelling evidence for this, and there are many examples of focal mechanisms, borehole breakouts, and macroscopic structures that suggest that a large angle between the maximum principal stress and low-angle normal faults existed during continued slip. Low-angle normal faults may nucleate within shallowly-dipping mylonitic shear zones in the mid- to lower-crust and propagate in to the upper crust [*Axen*, 1992]. Alternatively, they may nucleate within pre-existing fracture zones in the upper crust, in which case the local stress field may readily deviate from that expected in a typical 'Andersonian' regime [*Chester and Chester*, 2000, *Faulkner et al.*, 2006]. Recent numerical models are able to reproduce the spontaneous nucleation of low-angle normal faults at the frictional-viscous transition [e.g. *Regenauer-Lieb et al.*, 2006], but they fail to account for many key geological observations, such as the marked asymmetry of crustal extension in the northern Apennines [*Pauselli et al.*, 2006].

Once formed, low-angle normal faults are able to slip for prolonged periods of time. This thesis has described several mechanisms that may promote low-angle slip, but there is a general paucity of studies worldwide that focus on the nature, evolution, and significance

of the fault rock material associated with low-angle normal faults. Physical and chemical interactions that take place during the seismic cycle within fault cores and fault damage zones probably hold the key to understanding the mechanics of low-angle normal faults, and fault zones in general. Low-angle normal faults are particularly suited to the study of fault zones and fault rocks since they typically preserve materials exhumed from a wide range of crustal depths. Future studies should focus on using high-resolution microscopy and microsampling to document the internal structure of low-angle normal faults, grain-scale fabrics and geochemistry, and fluid compositions. Such studies can be used as inputs for a new generation of numerical models incorporating complex rheologies, and can be compared with the results of laboratory experiments carried out under a wide range of realistic boundary conditions.

Appendix I

Journal of the Geological Society, London, Vol. **164**, 2007, pp. 1187–1191. Printed in Great Britain.

Using footwall structures to constrain the evolution of low-angle normal faults

S. A. F. SMITH[1], R. E. HOLDSWORTH[1], C. COLLETTINI[2] & J. IMBER[1]

[1]*Reactivation Research Group, Department of Earth Sciences, University of Durham, Durham DH1 3LE, UK (e-mail: steven.smith@durham.ac.uk)*

[2]*Dipartimento di Scienze della Terra, Universita di Perugia, 06123 Perugia, Italy*

Abstract: Controversy exists over the presence of normal faults that initiate and slip at low angles (<30°). Evidence from the Zuccale Fault, which dips *c.* 15° east on the island of Elba, Italy, indicates that the early stages of low-angle faulting were synchronous with development of subsidiary high-angle footwall faults. These footwall structures controlled fault rock distribution and caused the development of flow folds similar to those produced in analogue studies of synchronous high- and low-angle faulting. The current configuration of footwall structures indicates that the Zuccale Fault cannot have originally dipped greater than *c.* 20° east, and represents a primary low-angle normal fault.

Normal faults that currently dip at low angles (<30°, often <15°) are recognized worldwide in both continental and oceanic settings, and have frequently played an important role in accommodating large-magnitude extension in zones of rifting (e.g. Wernicke 1981, 1995; Davis & Lister 1988; Axen 2004; Smith *et al.* 2006). Despite this, unambiguous recognition in the geological record of primary low-angle normal faults, which initiated and slipped at a low angle, remains problematic. Axen (2004) summarized several compelling examples of large-displacement (5–50 km) primary low-angle normal faults, but because of the apparent mechanical paradox of these structures (Sibson 1985; Jackson & White 1989; Collettini & Sibson 2001) many geoscientists still strongly favour the idea that such faults are formed by passive rotation of high-angle structures, during either footwall isostatic rebound (Buck 1988) or rotation within 'domino' or listric fault sets (Proffett 1977; Davis 1983*a*, *b*). One commonly encountered problem is that it can be difficult to discern the temporal relationships between low-angle normal faults and subsidiary high-angle structures, which commonly cross-cut hanging-wall rocks (e.g. Cichanski 2000). This leads to ambiguity regarding the dip history of the main low-angle structure, and whether or not high-angle subsidiary structures formed early or late in the faulting sequence. Part of the problem results from the fact that hanging-wall faults rarely interfere with the well-defined fault rock 'stratigraphy' common to many Cordilleran-type metamorphic core complexes (Davis & Lister 1988), typically consisting of (from bottom to top): mylonites with gently inclined fabrics, foliated cataclasites and gouges, and chlorite breccias or microbreccias (Coney 1980; Cowan *et al.* 2003). In contrast, high-angle footwall faults that lie immediately below low-angle normal faults have received little attention, and in this paper we investigate the interactions between such high-angle structures and fault rocks found along the shallowly dipping Zuccale Fault on the island of Elba, Italy. Our findings demonstrate that the Zuccale Fault must have been active as a low-angle structure throughout its slip history and that it has not experienced a decrease in dip value on a regional scale of more than *c.* 5°. This suggests that, whenever they are present, such footwall faults can be used as indicators of low-angle extensional slip along detachment faults worldwide, and that they can also be used to place constraints on the amount of post-slip rotation experienced by low-angle normal faults.

Geological setting

The northern Tyrrhenian–Apennine region of Italy has experienced two phases of eastward-migrating deformation since the Cretaceous (Elter *et al.* 1975; Jolivet *et al.* 1998; Pauselli *et al.* 2006). An early stage of Cretaceous to Pliocene shortening and thrusting was closely followed by a later stage of Miocene–Recent post-collisional extension, which continues in the Umbria–Marche region of Italy. The current stress field in central Italy is characterized by subvertical σ_1 and east–west- to NE–SW-trending, subhorizontal σ_3 (Montone *et al.* 2004). Extension is largely accommodated along shallowly east-dipping normal faults, including the currently microseismically active Altotiberina Fault, and the older exhumed Zuccale Fault on Elba, which dips regionally *c.* 15° east (e.g. Collettini *et al.* 2006).

The geology of Elba comprises five thrust sheets stacked towards the NE during the Late Cretaceous to Early Miocene (Complexes I–V, Fig. 1; Trevisan 1950; Keller & Pialli 1990; Bortolotti *et al.* 2001). The Zuccale Fault does not appear to reactivate any of the earlier thrust faults, but instead cross-cuts the entire pre-existing thrust stack. Collettini & Holdsworth (2004) defined a distinct sequence of fault rocks produced during prolonged slip along the Zuccale Fault. An initial phase of cataclasis and fluid influx was followed by profound weakening as a result of the onset of pressure-solution accommodated deformation within the fault core, and the development of macroscopically ductile phyllonites and foliated cataclasites. Further brittle deformation led to the formation of coarse fault breccias and fault gouges. Shear sense along the Zuccale Fault is consistently top-to-the-east, and overall extensional offsets are *c.* 7–8 km. The relationship between movements along the low-angle Zuccale Fault and subsidiary high-angle footwall faults is best displayed in 100% exposed coastal sections at the type locality for the fault zone, Punta Di Zuccale (Figs 1–3).

Footwall faulting patterns, Punta Di Zuccale

At Punta Di Zuccale, Complex V Cretaceous flysch in the hanging wall of the Zuccale Fault is juxtaposed against Complex I basement schists in the footwall (Fig. 1). Extension-related deformation in the footwall and hanging wall is exclusively brittle and the footwall of the Zuccale Fault is everywhere pervasively faulted. Footwall faults located in Complex I schists

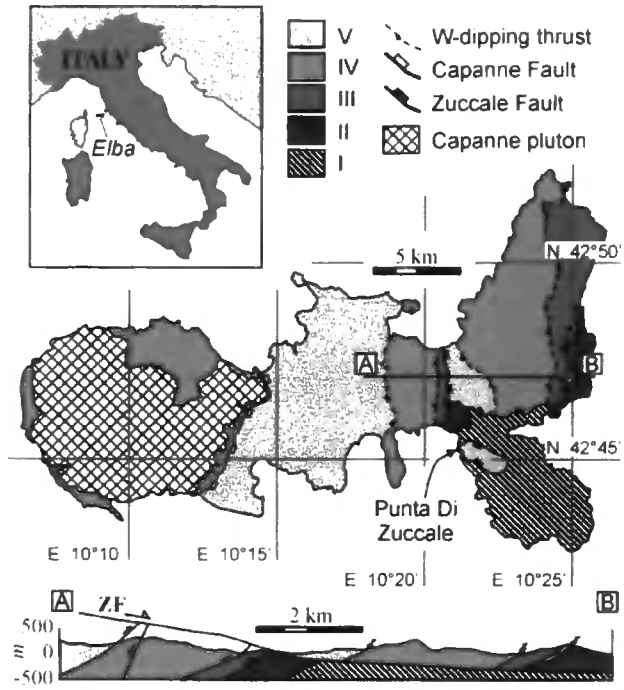

Fig. 1. Simplified geological map of Elba, and cross-section through central and eastern Elba showing the geometry of the Zuccale low-angle normal fault. I, Complex I basement schists; II, Complex II Tuscan metamorphic sequence; III, Complex III Tuscan limestone sequence; IV, Complex IV Ligurian ophiolite sequence; V, Complex V Cretaceous and Eocene flysch (Trevisan 1950).

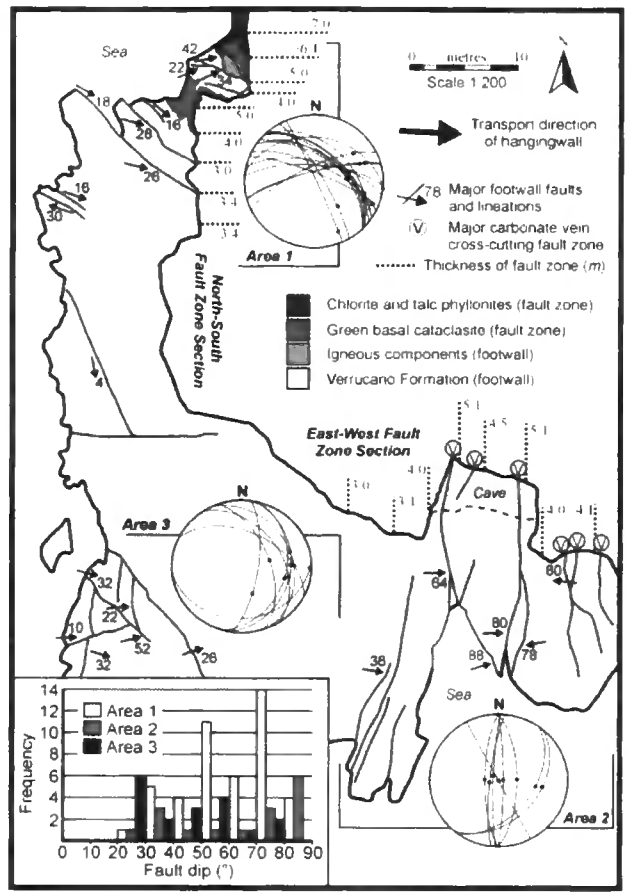

Fig. 2. Detailed geological map of faulting in the footwall of the Zuccale low-angle normal fault at Punta Di Zuccale. Stereonets show fault-plane orientations and slickenline lineations. Only major faults are shown on the map and stereonets. All measured faults are included in the dip histograms (inset).

are widely spaced, but occur in geometrically distinct sets (Fig. 2). Kinematic patterns appear to be relatively simple, with a large majority of faults accommodating east–west-directed extension. Faults that trend east–west or NW–SE (e.g. Area 1 in Fig. 2) contain shallowly to moderately east-plunging slickenline lineations, accommodate east-directed extension, and represent oblique or strike-slip faults. Faults that trend north–south (e.g. Area 2 in Fig. 2) contain steeply plunging slickenline lineations and represent dip-slip normal faults. Fault dip values in Area 2 vary widely between 22 and 88°, but major faults that link upwards into the fault core commonly dip *c.* 70–90° east (Fig. 2 inset, Fig. 3). Displacements on footwall structures are typically tens of centimetres to several metres. Overall, this fault pattern divides the upper surface of the footwall into a 3D block-and-basin topography. Large footwall structures cut upwards into the lower part of the main low-angle fault zone (e.g. Fig. 3), and frequently host, or are linked to, major steeply dipping to subvertical hydrofracture veins filled with carbonate (labelled 'V' in Fig. 2), suggesting that footwall structures are able to periodically tap and release fluids stored beneath the low-permeability fault core.

Fault zone architecture, Punta Di Zuccale

New mapping (Figs 2 and 3) demonstrates that the distribution of fault rocks within the Zuccale Fault is controlled significantly by footwall faulting, and that a complete fault rock sequence is not preserved everywhere at Punta Di Zuccale. Major footwall structures cut directly up into the base of the Zuccale Fault and cause the fault core to increase in thickness from *c.* 3 to *c.* 8 m (Figs 2 and 3). This occurs along both east–west (parallel to transport direction) and north–south (orthogonal to transport direction) sections. Figure 3(b and d) shows that chlorite- and talc-rich phyllonites, which formed early during the evolution of the Zuccale Fault, are found only as elongate lenses in areas where the fault core is unusually thick. In other words, these phyllonites are found only where they lie in the hanging wall (or 'lee' side) of footwall faults where they locally thicken the fault core. Along the east–west section at Punta Di Zuccale, the phyllonites are found as an isolated lens *c.* 8 m long by 3 m high (Fig. 3b). Along the north–south section the phyllonites are interlayered with green schists, and occur in a lens at least 20 m long by 5 m high (Fig. 3d). In areas where the footwall is not down-faulted, the fault rock sequence is dominated by carbonate-rich foliated cataclasites, with a notable absence of phyllonite. In the field, the base of the carbonate-rich foliated cataclasite is marked by a discrete brittle fault surface, which either cross-cuts and terminates all high-angle footwall faults, or causes a rapid decrease in their offsets across it (e.g. Fig. 3a). This suggests that during the development of the extensional fault zone, large-offset low-angle and smaller-offset high-angle fault movements have alternated. As we explain below, the alternating low-angle and high-angle scenario provides a compelling explanation for the current preservation or excision of the early formed phyllonites in the core of the Zuccale Fault.

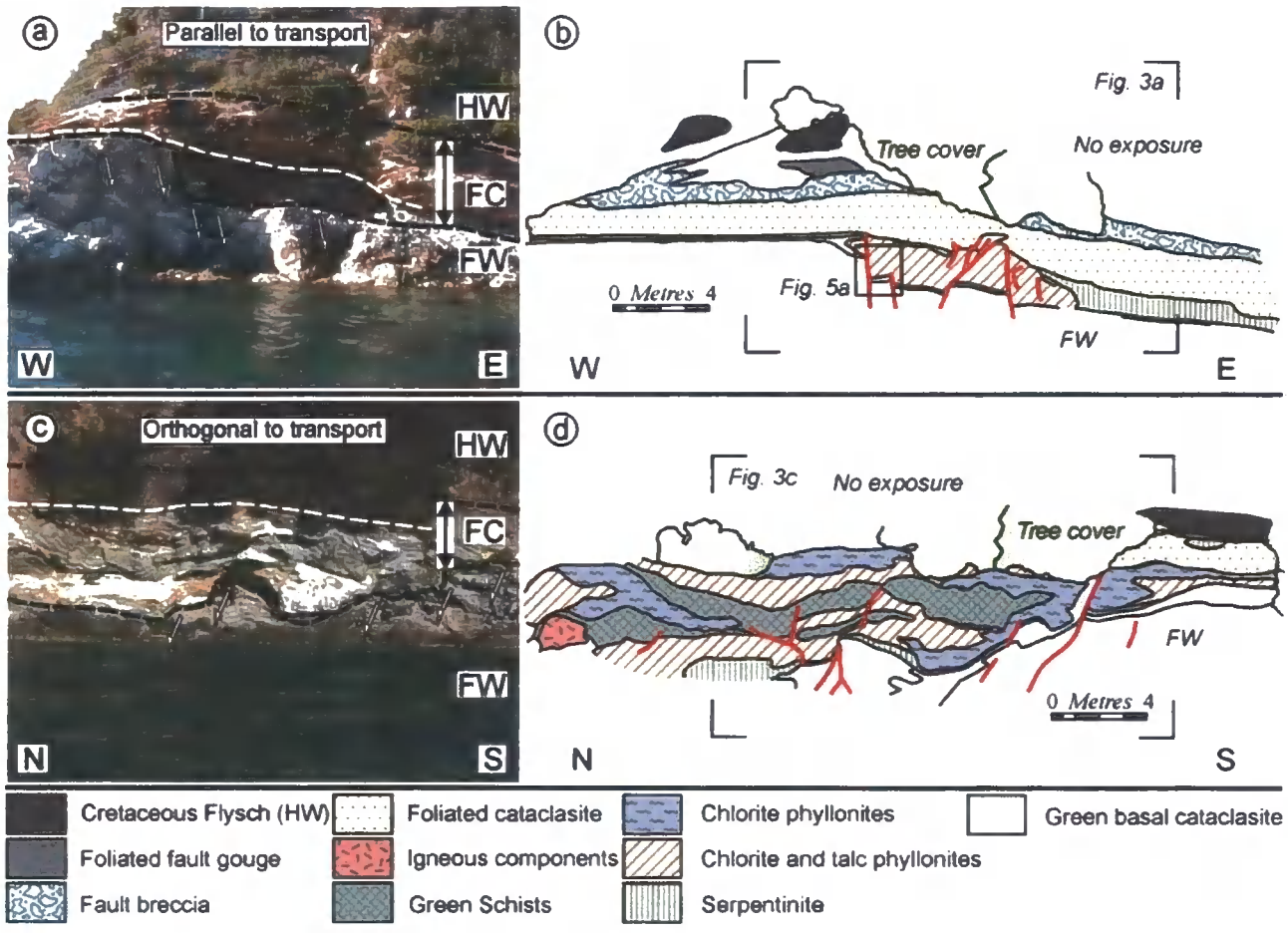

Fig. 3. (**a**, **b**) Photograph and detailed sketch illustrating the internal architecture of the Zuccale low-angle normal fault (top-to-the-east), and the position of footwall faults, along an east–west coastal section (Area 2 in Fig. 2). Double-headed arrows in (**a**) indicate 4.0 m thickness. (**c**, **d**) North–south coastal section (including Area 1 in Fig. 2). Double-headed arrows in (**c**) indicate 3 m thickness. HW, hanging wall of Zuccale Fault; FC, fault core; FW, footwall of Zuccale Fault. White dashed lines mark the location of a late brittle detachment.

Fault zone evolution

The sequence of structures and distribution of fault rocks preserved within the core of the Zuccale Fault suggests the following deformation history (Fig. 4). Early fault rocks including phyllonites developed along the low-angle Zuccale Fault. It is unclear whether low-angle faulting then ceased for some period during which high-angle footwall (and hanging-wall) structures initiated, or whether this occurred synchronously with low-angle displacements (as shown in Fig. 4a). The footwall faults grew and eventually cut up into the base of the fault zone, causing thickening of the phyllonitic fault core in directions parallel and perpendicular to transport (Fig. 4b). Significantly, in three areas at Punta Di Zuccale, the phyllonites contain east-verging asymmetric folds, all of which are located directly above footwall structures (Figs 4b and 5). These folds have amplitudes of *c.* 1–3 m, exhibit moderately west-dipping axial planes and subhorizontal or shallowly plunging fold axes, and possess geometries that closely resemble those produced in analogue experiments of synchronous low-angle detachment-slip and high-angle oblique-slip (Fig. 5c; Fossen & Rykkelid 1992). All of the observed folds have overturned western limbs, suggesting that they are not simply extensional forced folds produced by 'draping' of phyllonitic material above a footwall ramp (Fig. 5; Maurin & Niviere 2000; Withjack & Callaway 2000). Further low-angle faulting resulted in the formation of carbonate-rich foliated cataclasites and a sequence of brittle fault breccias and gouges (Fig. 4c), which probably represent progressive exhumation of the fault zone. Infrequent reworked clasts of phyllonitic material are found within the overlying foliated cataclasites, indicating that the phyllonites predate the formation of foliated cataclasites at Punta Di Zuccale. The phyllonites were excised from many parts of the main fault zone by a late brittle detachment in the Punta Di Zuccale and other areas, but remain preserved in isolated lenses down-faulted in the hanging wall 'lee regions' of high-angle footwall faults (Fig. 4c).

Discussion

The footwall extension recognized during the present study could conceivably originate in several ways, including flexural forces associated with isostatic rebound (Buck 1988), the progression of a 'rolling hinge' (Axen & Bartley 1997), or stress concentration at the margins of a larger, curviplanar ('wavy') fault zone (Chester & Chester 2000). Alternatively, footwall faulting may simply be the natural consequence of overall regional extension in areas outside the weakened low-angle fault core.

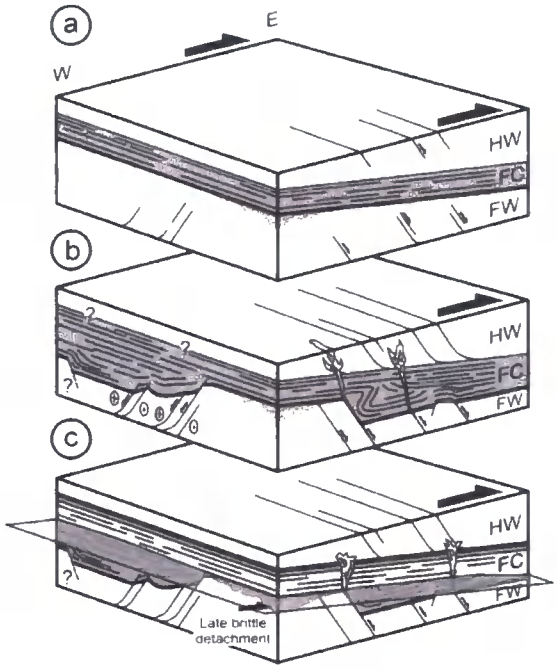

Fig. 4. Synoptic 3D diagram of fault slip history. (**a**) Development of early fault rocks and incipient growth of high-angle subsidiary structures. (**b**) Footwall faulting causes thickening of the main fault zone, and folding of early formed phyllonitic fault rocks. Fluids are periodically released by footwall structures to form carbonate hydrofracture veins. (**c**) Present-day geometry. A late brittle detachment excises the early phyllonitic sequence, which is 'protected' in thickened areas of the fault core.

Many of the large footwall structures that formed contemporaneously with early displacements on the Zuccale Fault have dips greater than 80° (e.g. Area 2, Figs 2 and 3). This makes it unlikely that the Zuccale Fault has experienced a post-slip decrease in dip of more than *c.* 5° in this area, because this would require that the steep footwall structures were originally reverse faults. Synchronous movement along a major extensional fault and a suite of reverse faults in the footwall would represent a highly unusual situation, and one that would introduce major compatibility problems within both the fault core and the adjacent wallrocks. In other localities, successive footwall faulting has caused the Zuccale Fault to rotate more than 5°, so that locally the fault zone dips westward. However, the key relationships preserved at Punta Di Zuccale indicate that on a regional scale the Zuccale Fault cannot originally have dipped more than *c.* 20° east.

Footwall faults played a key role in the preservation of early formed fault rock assemblages, materials that carry vital evidence concerning the initial weakening mechanisms that may facilitate movements along high-displacement low-angle normal faults, and the early kinematic history of the fault zone. In addition, many footwall faults lying immediately beneath the main fault core of the Zuccale Fault are filled with vein carbonate or act as the origin for subvertical hydrofracture veins, some of which currently cross-cut the complete fault zone stratigraphy. This relationship strongly suggests that overpressured fluids that accumulated in the footwall region below the foliated fault core seal were periodically released and that, once formed, footwall faults acted as long-lived preferential conduits for fluid flow.

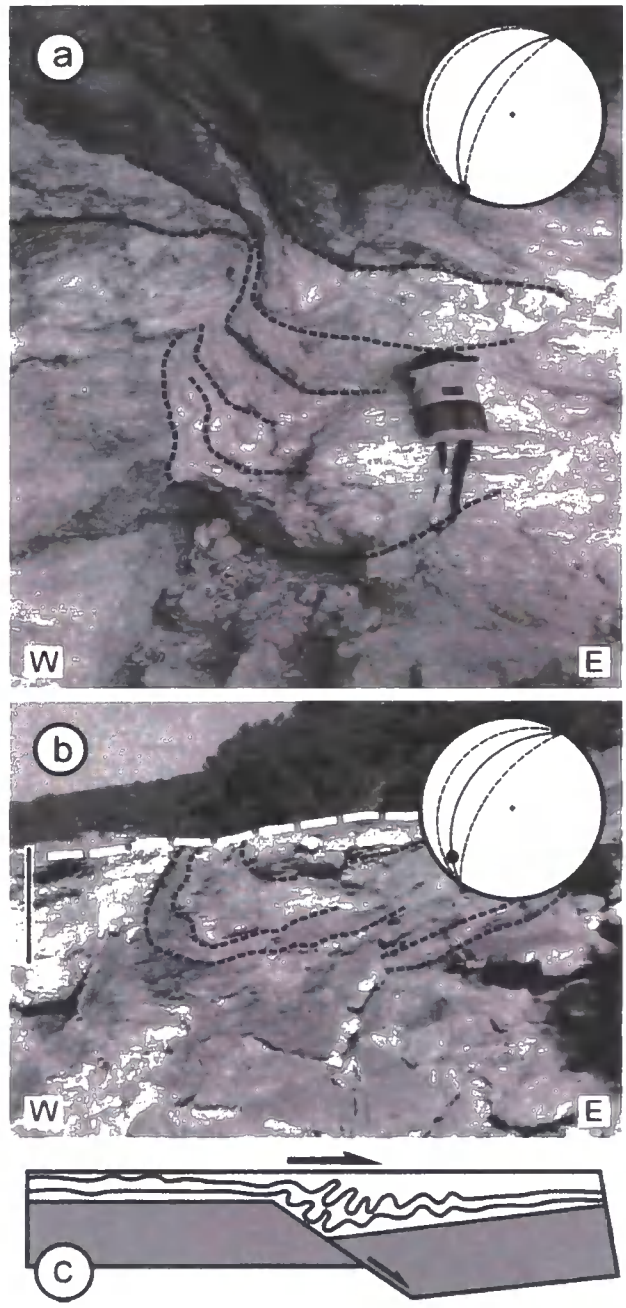

Fig. 5. (**a**) Photograph of asymmetric east-verging fold developed in phyllonites within the east–west section of thickened fault core. Location is shown in Figure 3b. (**b**) East-verging asymmetric fold within phyllonites to the north of the mapped area. White dashed line marks the location of a late brittle detachment. Scale bar represents *c.* 2 m. (**c**) Sketch of analogue model of synchronous layer-parallel and oblique shear after Fossen & Rykkelid (1992). Stereonets show orientations of fold axial planes (continuous lines) and fold axes. Mean orientations of fold limbs are shown as dashed lines.

It seems likely that movements along high-angle footwall faults have acted as a first-order control on fault rock distribution and fluid circulation in other areas where low-angle normal faults are known to be important. For example, there is a noticeable

similarity between the geometry and distribution of fault rocks presented in this paper and the example given by Hayman (2006, fig. 3), from the Black Mountain detachments in Death Valley. The orientation of footwall structures found along other detachment faults may help in placing constraints on the amount of post-slip rotation caused by mechanisms such as isostatic rebound.

Subsidiary faulting patterns over a range of scales are likely to affect the distribution of fault rocks in a wide range of extensional, compressional and strike-slip regimes, and we believe that understanding these patterns has important implications for reconstructing fault zone histories and fault zone permeability properties, and for transmitting the effects of grain-scale weakening mechanisms up to the fault and crustal scales.

Conclusions

The Zuccale Fault on the island of Elba slipped as a low-angle (*c.* 15°) extensional structure throughout its history. Subsidiary high-angle footwall faults strongly controlled the distribution of phyllonites that formed early within the fault core, indicating that the footwall structures themselves must have formed early. The phyllonites also contain a series of inclined asymmetric folds that resemble those produced in analogue experiments, suggesting that low-angle and high-angle faulting were synchronous, or alternated with one another. On a regional scale the Zuccale Fault has not experienced a decrease in dip of more than *c.* 5° and its current geometry cannot be explained by significant passive reorientation. The outcrop-scale field relationships described in this paper can be applied to detachment faults worldwide to infer that the early stages of movement occurred at low angles.

S.A.F.S. is supported by a Durham University postgraduate fellowship. Fieldwork was generously funded by grants from the Geological Society of London, The American Association of Petroleum Geologists, the Geologists' Association, the Mineralogical Society of Great Britain and Ireland, the John Ray Trust, and the Edinburgh Geological Society. We thank G. Axen for comments on a previous version of the manuscript, and P. T. Osmundsen and U. Ring for insightful reviews.

References

Axen, G.J. 2004. Mechanics of low-angle normal faults. *In:* Karner, G.D., Morris, J.D., Driscoll, N.W. & Silver, E.A. (eds) *Rheology and Deformation of the Lithosphere at Continental Margins*. MARGINS Theoretical and Experimental Earth Science Series, 46–91.

Axen, G.J. & Bartley, J.M. 1997. Field tests of rolling hinges: existence, mechanical types, and implications for extensional tectonics. *Journal of Geophysical Research*, **102**, 20515–20537.

Bortolotti, V., Fazzuoli, M., Pandeli, E., Principi, G., Babbini, A. & Corti, S. 2001. Geology of Central and Eastern Elba Island, Italy. *Ofioliti*, **26**, 97–150.

Buck, W.R. 1988. Flexural rotation of normal faults. *Tectonics*, **7**, 959–973.

Chester, F.M. & Chester, J.S. 2000. Stress and deformation along wavy frictional faults. *Journal of Geophysical Research*, **105**, 23421–23430.

Cichanski, M. 2000. Low-angle, range-flank faults in the Panamint, Inyo, and Slate ranges, California: implications for recent tectonics of the Death Valley Region. *Geological Society of America Bulletin*, **112**, 871–883.

Collettini, C. & Sibson, R.H. 2001. Normal faults, normal friction? *Geology*, **29**, 927–930.

Collettini, C., De Poala, N., Holdsworth, R.E. & Barchi, M.R. 2006. The development and behaviour of low-angle normal faults during Cenozoic asymmetric extension in the Northern Apennines, Italy. *Journal of Structural Geology*, **28**, 333–352.

Coney, P.J. 1980. Cordilleran metamorphic core complexes: an overview. *In:* Crittenden, M.D. Jr., Coney, P.J. & Davis, G.H. (eds) *Cordilleran Metamorphic Core Complexes*. Geological Society of America, Memoirs, **153**, 7–31.

Cowan, D.S., Cladouhos, T.T. & Morgan, J.K. 2003. Structural geology and kinematic history of rocks formed along low-angle normal faults. *Geological Society of America Bulletin*, **115**, 1230–1248.

Davis, G.H. 1983a. Shear zone model for the origin of metamorphic core complexes. *Geology*, **11**, 342–347.

Davis, G.H. 1983b. A shear zone model for the structural evolution of metamorphic core complexes in southeastern Arizona. *In:* Coward, M.P., Dewey, J.F. & Hancock, P.L. (eds) *Continental Extensional Tectonics*. Geological Society, London, Special Publications, **28**, 247–266.

Davis, G.H. & Lister, G.S. 1988. Detachment faulting in continental extension: perspectives from the southwestern U.S. Cordillera. *In:* Clark, S.P. Jr., Burchfiel, B.C. & Suppe, J. (eds) *Processes in Continental Lithospheric Deformation*. Geological Society of America, Special Papers, **218**, 133–159.

Elter, P., Giglia, G., Tongiorgi, M. & Trevisan, L. 1975. Tensional and compressional areas in recent (Tortonian to present) evolution of the northern Apennines. *Bollettino di Geofisica Teorica ed Applicata*, **17**, 3–18.

Fossen, H. & Rykkelid, E. 1992. The interaction between oblique and layer-parallel shear in high-strain zones: observations and experiments. *Tectonophysics*, **207**, 331–343.

Hayman, N.W. 2006. Shallow crustal fault rocks from the Black Mountain detachments, Death Valley, CA. *Journal of Structural Geology*, **28**, 1767–1784.

Jackson, J.A. & White, N.J. 1989. Normal faulting in the upper continental crust: observations from regions of active extension. *Journal of Structural Geology*, **11**, 15–36.

Jolivet, L., Faccenna, C. & Goffe, B. *et al.* 1998. Midcrustal shear zones in postorogenic extension: example from the northern Tyrrhenian Sea. *Journal of Geophysical Research*, **103**, 12123–12160.

Keller, J.V.A. & Pialli, G. 1990. Tectonics of the Island of Elba: a reappraisal. *Bollettino della Società Geologica Italiana*, **109**, 413–425.

Maurin, J.C. & Niviere, B. 2000. Extensional forced folding and décollement of the pre-rift series along the Rhine graben and their influence on the geometry of the syn-rift sequences. *In:* Cosgrove, J.W. & Ameen, M.S. (eds) *Forced Folds and Fractures*. Geological Society, London, Special Publications, **169**, 73–86.

Montone, P., Mariucci, M.T., Pondrelli, S. & Amato, A. 2004. An improved stress map for Italy and surrounding regions (central Mediterranean). *Journal of Geophysical Research*, **109**, B10410, doi:10.1029/2003JB002703.

Pauselli, C., Barchi, M.R., Federico, C., Magnani, M.B. & Minelli, G. 2006. The crustal structure of the northern Apennines (Central Italy): an insight by the CROP03 seismic line. *American Journal of Science*, **306**, 428–450.

Proffett, J.M. Jr 1977. Cenozoic geology of the Yerington district, Nevada, and implications for the nature and origin of Basin and Range faulting. *Geological Society of America Bulletin*, **88**, 247–266.

Sibson, R.H. 1985. A note on fault reactivation. *Journal of Structural Geology*, **7**, 751–754.

Smith, D.K., Cann, J.R. & Escartin, J. 2006. Widespread active detachment faulting and core complex formation near 13N on the Mid-Atlantic Ridge. *Nature*, **442**, 440–443.

Trevisan, L. 1950. L'Elba orientale e la sua tettonica di scivolamento per gravità. *Memorie dell'Istituto Geologico dell'Università di Padova*, **16**, 1–30.

Wernicke, B. 1981. Low-angle normal faults in the Basin and Range province: nappe tectonics in an extending orogen. *Nature*, **291**, 645–648.

Wernicke, B. 1995. Low-angle normal faults and seismicity: a review. *Journal of Geophysical Research*, **100**, 20159–20174.

Withjack, M.O. & Callaway, S. 2000. Active normal faulting beneath a salt layer: an experimental study of deformation patterns in the cover sequence. *AAPG Bulletin*, **84**, 627–651.

Received 12 January 2007; revised typescript accepted 23 April 2007.
Scientific editing by Rob Strachan

Appendix II

Journal of Structural Geology 30 (2008) 1034–1046

Contents lists available at ScienceDirect

Journal of Structural Geology

journal homepage: www.elsevier.com/locate/jsg

Recognizing the seismic cycle along ancient faults: CO_2-induced fluidization of breccias in the footwall of a sealing low-angle normal fault

S.A.F. Smith [a,*], C. Collettini [b], R.E. Holdsworth [a]

[a] Reactivation Research Group, Department of Earth Sciences, University of Durham, Durham, DH1 3LE, UK
[b] Geologia Strutturale e Geofisica, Dipartimento Di Scienze della Terra, Universita degli studi di Perugia, Perugia, 06123, Italy

ARTICLE INFO

Article history:
Received 26 September 2007
Received in revised form 10 April 2008
Accepted 28 April 2008
Available online 10 May 2008

Keywords:
Breccia
Fluidization
Interseismic
Fault-valve
Low-angle normal fault

ABSTRACT

The Zuccale low-angle normal fault exposed on the island of Elba, Italy, is a crustal-scale structure which contains a strongly foliated fault core. In the immediate footwall of the Zuccale fault, cohesive fault-related breccias which were initially deformed by typical frictional deformation mechanisms experienced fluidization over areas of at least 10^{-2}–10^{-3} km^2.

Three internal variants of fluidized breccia are recognized, with each related to a separate fluidization event. Characteristics of the fluidized breccias include: (1) a highly irregular 'intrusive' boundary with the overlying fault core; (2) no grain-scale evidence for typical frictional deformation mechanisms; (3) an association with carbonate cements indicating that fluids contained CO_2; and (4) a clast-preferred orientation suggesting that fluids were moving vertically and spreading laterally as they encountered the foliated fault core.

Our observations suggest that the fluidized breccias are representative of the interseismic period along the Zuccale low-angle fault, and developed across small fault patches during build-ups in fluid overpressure. Attainment of a critical fluid overpressure triggered embrittlement and the formation of low-angle slip surfaces and sub-vertical tensile veins within the overlying fault core, which may account for the presence and the dimensions (10^{-1}–10^{-3} km^2) of rupture surfaces which produce microseismicity along active low-angle normal faults in central Italy.

1. Introduction

Fluids exert a fundamental control on the mechanical and chemical behaviour of all types of fault and shear zone. There is a voluminous literature detailing field, laboratory and theoretical work carried out in an attempt to understand the role of fluids in earthquake rupture, the formation of hydrothermal ore deposits, and the long-term evolution of faulted regions of the crust and lithosphere at all depths and scales (e.g. reviews by Hickman et al., 1995; Oliver, 1996; Sibson, 2000; Person et al., 2007). Increasingly it is recognized that cycling of fluid pressure, e.g. 'fault-valve' models (Sibson, 1990), within faults and shear zones strongly affects their mechanical behaviour, and can be intimately linked to the earthquake cycle (e.g. Parry and Bruhn, 1990; Sibson, 1992, 2007; Cox, 1995; Henderson and McCaig, 1996; Nguyen et al., 1998; Famin et al., 2005).

Low-angle normal faults, which dip less than 30°, have received considerable attention since standard 'Andersonian' frictional fault theory does not predict such orientations and because large earthquakes on low-angle normal faults are rare or absent (Anderson, 1942; Jackson and White, 1989; Wernicke, 1995; Collettini and Sibson, 2001; Axen, 2004, 2007). Low-angle normal faults may slip over prolonged periods of time if fault rock materials lining the fault surface possess a low friction coefficient (e.g. Numelin et al., 2007), or if high fluid pressures are generated within, or adjacent to, the fault zone (e.g. Axen, 1992). Attainment of tensile fluid overpressure ($P_f > \sigma_3$) is critical for reactivation and slip along low-angle normal faults, particularly in the upper 10 km of the brittle crust. For example, Collettini and Barchi (2002) applied frictional reactivation theory to study the conditions necessary for reactivation of the Altotiberina fault, an active low-angle normal fault in central Italy. They found that the Altotiberina fault can be reactivated for low values of differential stress ($\sigma_1 - \sigma_3 < 28$ MPa), relatively high values of tensile strength of the surrounding rocks (~ 10 MPa), and tensile fluid overpressure $P_f > \sigma_3$ (e.g. $\lambda_v > 0.93$). There is strong evidence from the footwalls of metamorphic core complexes and their associated low-angle normal faults, where vein and fracture networks are commonly observed, that tensile fluid overpressure is locally obtained (e.g. Reynolds and Lister, 1987). However, the factors leading to focused

* Corresponding author: Tel. +44 (0)798 8777642; fax: +44 0191 3342301.
E-mail addresses: steven.smith@durham.ac.uk (S.A.F. Smith), colle@unipg.it (C. Collettini), r.e.holdsworth@durham.ac.uk (R.E. Holdsworth).

0191-8141/$ – see front matter © 2008 Elsevier Ltd. All rights reserved.
doi:10.1016/j.jsg.2008.04.010

fluid flow and to the development of fluid overpressure at specific sites are unknown, and there is still a paucity of direct geological evidence for any form of fluid cycling along low-angle normal faults.

The aim of this paper is to describe in detail the geological setting, microstructural characteristics, and evolution of a suite of frictional fault rocks (breccias) which we believe to have experienced widespread fluidization beneath the Zuccale fault, a low-angle normal fault exposed on the Island of Elba. We focus our attention on a single coastal outcrop which contains 100% exposure in the immediate footwall of the Zuccale fault, and use our observations to develop a conceptual model for fluidization. We discuss our observations in the context of fluid cycling, the development of fluid overpressure associated with low-angle normal faults, and the recognition of fault rocks which represent particular phases of the seismic cycle.

2. Geological context

2.1. The northern Apennines

Elba lies ~20 km to the west of Tuscany in the northern Tyrrhenian Sea. This area has experienced two contrasting phases of deformation, both of which migrated progressively from west to east (Fig. 1a; Elter et al., 1975; Pauselli et al., 2006). An earlier phase of Cretaceous to Quaternary collision was followed by a later phase of Miocene to currently active post-collisional extension. Geological and geophysical studies have highlighted that a majority of post-collisional extension has been accommodated along shallowly east-dipping low-angle normal faults (Fig. 1a; Barchi et al., 1998; Jolivet et al., 1998; Pauselli et al., 2006; Collettini et al., 2006b; Chiaraluce et al., 2007). Active extension presently occurs along the Altotiberina low-angle normal fault, which produces abundant microseismicity ($M < 2.3$) at a rate of ~8.1 events day^{-1} km^{-2} (Chiaraluce et al., 2007) over a depth range of 4–14 km (Fig. 1a; Boncio et al., 1998, 2000). Microseismic activity occurs on rupture surfaces in the size range of 10^{-1}–10^{-3} km^2 (Sibson, 1989; Collettini and Barchi, 2002; Chiaraluce et al., 2007). The active regional stress field in central Italy is characterized by a sub-vertical σ_1 and an east–west to NE–SW trending, sub-horizontal σ_3 (Montone et al., 2004). Older, inactive low-angle normal faults are exhumed in western Tuscany and the Tyrrhenian islands, which includes the Zuccale fault exposed on Elba.

Central Italy is characterized by an anomalously high flux of non-volcanic CO_2, focused specifically within the area which has experienced widespread post-collisional extension (Fig. 1a; Chiodini et al., 2004). The flux of CO_2 reaches ~0.8 tonnes day^{-1} km^{-2}, whereas to the east of the active extensional front, the flux of CO_2 decreases rapidly. Based mainly on $^3He/^4He$ and $\delta^{13}C$ isotopic analysis, it appears that around 40% of the CO_2 gas discharged in central Italy is derived from the upper mantle, which acts as an important source of CO_2-bearing fluid to the base of the brittle crust (Chiodini et al., 2004; Minissale et al., 2000; Minissale, 2004). Two deep boreholes (Santo Donato at 4750 m below sea level and Santo Stefano at 3700 m below sea level) which penetrated the active Altotiberina fault encountered fluid overpressures which were ~85% of the lithostatic load ($\lambda_v = 0.85$), induced by trapped CO_2-bearing hydrous fluids in the footwall of the fault (Chiodini and Cioni, 1989). Several authors have suggested that deeply derived CO_2-bearing fluids play a critical role in the nucleation of crustal earthquakes and the time–space evolution of aftershocks in central Italy (e.g. Collettini and Barchi, 2002; Miller et al., 2004; Chiaraluce et al., 2007).

2.2. The Zuccale fault on the island of Elba

Elba consists of a series of 5 stacked thrust sheets (Complexes I–V) which formed during late Cretaceous–early Miocene shortening (Fig. 1b). All of the thrust sheets currently dip moderately to the west and are crosscut and displaced by the shallowly east-dipping Zuccale fault (Fig. 1b; Trevisan et al., 1967; Keller and Pialli, 1990; Bortolotti et al., 2001). Shear sense along the Zuccale fault is

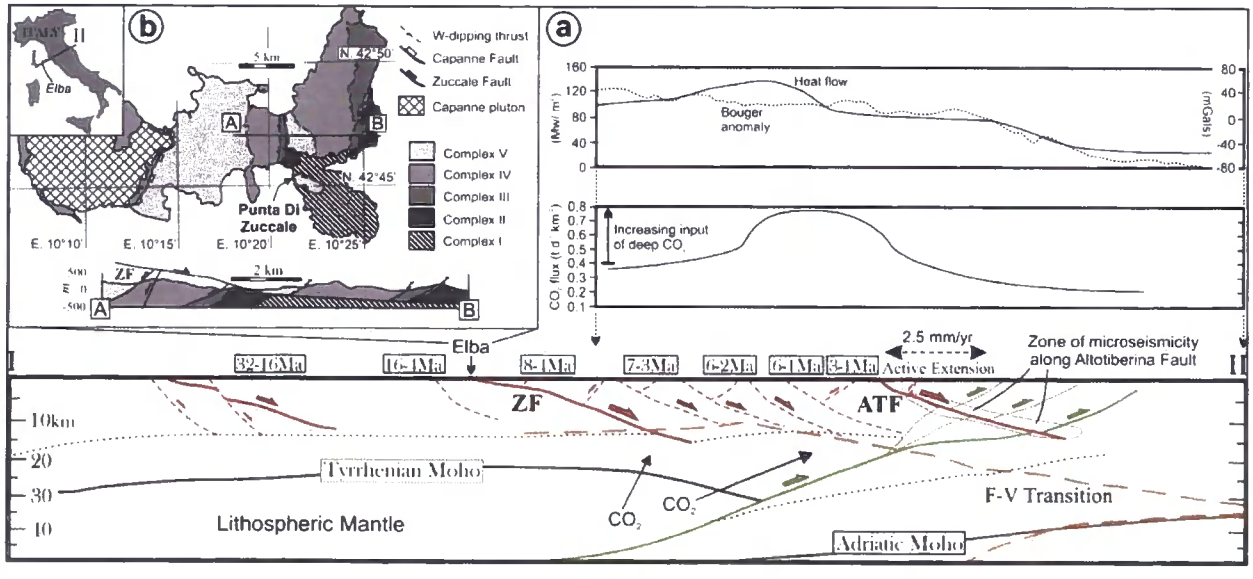

Fig. 1. (a) Crustal-scale cross section from Corsica to the Adriatic coast based partly on the CROP03 deep seismic reflection profile (Barchi et al., 1998). Location of the cross section is shown in part (b). The age ranges of syn-tectonic extensional basins are shown in white boxes. Extensional processes in the Tyrrhenian Sea and Tuscany have caused high average heat flows, a regional positive Bouger gravity anomaly, and a shallow Moho (after Collettini et al., 2006b). Additionally, the area is associated with high fluxes of deeply-derived CO_2. Location of the frictional–viscous (F–V) transition after Pauselli and Federico (2002). Zone of microseismicity along the Altotiberina Fault (ATF) after Chiaraluce et al. (2007). ZF, Zuccale fault. (b) Simplified geological map of Elba (after Trevisan et al., 1967) and cross section through central and eastern Elba highlighting the geometry of the Zuccale fault. Complex I, Paleozoic basement schists; Complex II, Tuscan metamorphic sequence; Complex III, Tuscan limestone sequence; Complex IV, Ligurian ophiolite sequence; Complex V, Cretaceous flysch.

uniformly top-to-the-east, and overall extensional offsets are c. 6–8 km (Keller and Coward, 1996). The movement history of the Zuccale fault is poorly constrained, but a majority of displacement is likely to have occurred between ~8 Ma and ~4 Ma based on ages obtained for displaced granitic intrusions (Dini et al., 2002), and for sediments deposited in extensional basins to the east (Pascucci et al., 1999). Extension on Elba was accompanied by intrusion of the Capanne (c. 6.9 Ma) and Porto Azzurro (c. 5.9 Ma) plutons, both of which were associated with significant hydrothermal fluid flow systems (Taylor and Turi, 1979; Dini et al., 2002; Maineri et al., 2003; Gagnevin et al., 2004; Rossetti et al., 2007).

The Zuccale fault is exposed particularly well at its type locality at Punta Di Zuccale (Fig. 1b), where it juxtaposes a hangingwall of Cretaceous sandstone and siltstone flysch deposits (Complex V) against a footwall of Palaeozoic quartzites and quartz–mica schists (Complex I; Fig. 2). Collettini and Holdsworth (2004) and Smith et al. (2007) studied the fault rock sequence and internal structure of the Zuccale fault, and only a brief summary of necessary details is provided below.

From bottom to top, the sequence of fault rocks found along the Zuccale fault consists of five units: (1) breccias and cataclasites derived exclusively from the Palaeozoic footwall rocks and containing clasts of quartzite and quartz–mica schist surrounded by a carbonate–chlorite–quartz matrix. These were deformed by frictional deformation mechanisms including fracture, grain fragmentation and grain rolling. Although their distribution is heterogeneous, they typically have a minimum thickness of ~3 m. Below, we refer to them as *frictional breccias*; (2) calc-mylonites and chlorite–talc–phyllonites; (3) foliated serpentinite with inclusions of tremolite–talc–chlorite schist; (4) carbonate-rich foliated cataclasites containing lenses of serpentinite, phyllonite, and calc-mylonite; (5) coarse fault breccias and foliated fault gouges derived predominantly from the hangingwall Cretaceous sandstones and siltstones. Throughout this paper we refer to fault rock units 2–5 as the 'fault core'. The footwall and fault core are crosscut by abundant carbonate veins, often possessing crack-seal textures, and interpreted to represent hydrofractures formed due to periodic build-ups in fluid overpressure (Collettini et al., 2006a). The largest hydrofracture veins link directly downwards into subsidiary, steeply-dipping extensional faults present in the footwall of the Zuccale fault (Fig. 2), strongly suggesting that these footwall faults focused and channelled fluid flow (Smith et al., 2007). Along part of the north south (transport-perpendicular) coastal section at Punta Di Zuccale, frictional breccias (fault rock unit 1) locally adopt a different, and unusual, appearance. Typically, these unusual breccias are grey to milky-white in colour and below we refer to them collectively as *grey breccias*.

3. Grey breccias

3.1. Field relationships

Grey breccias occur in the immediate footwall of the Zuccale fault where they occupy a minimum area in plan view of ~70 × 40 m, and occur over large areas of continuous outcrop and as a series of isolated windows which are eroded through the overlying fault rocks (Figs. 3–5). The total vertical extent of the grey breccias is unknown, but they are present to a depth of at least 3 m in the footwall of the Zuccale fault. Three internal variants of grey breccia are recognized and we refer to these as breccias A, B, and C

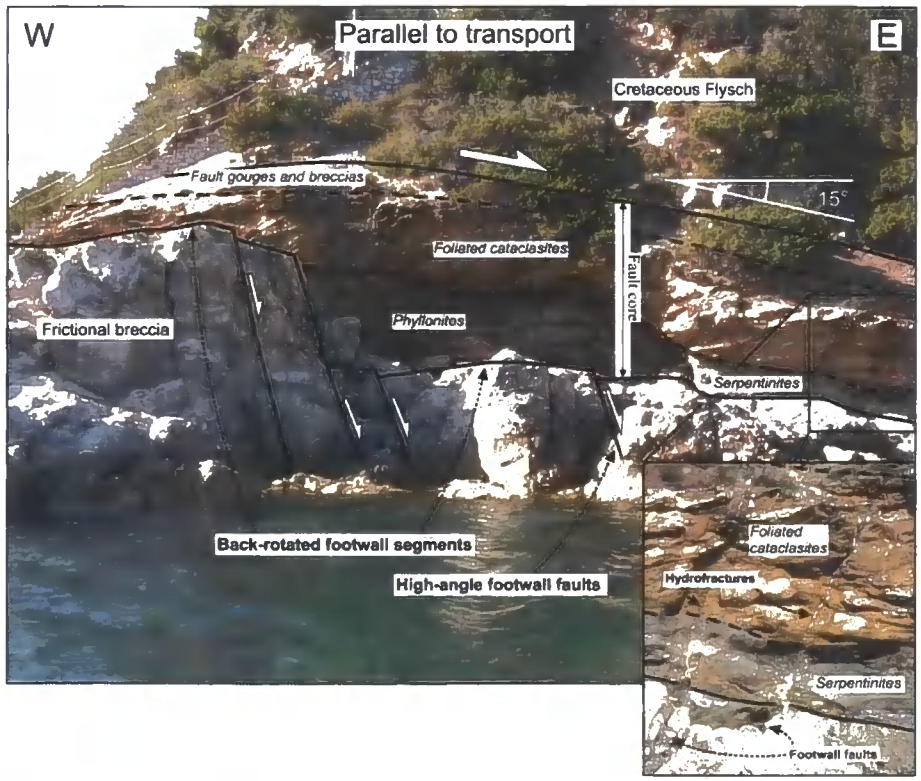

Fig. 2. Characteristic geometry of the Zuccale fault observed along an east–west coastal section at Punta Di Zuccale, where it places Cretaceous flysch in the hangingwall against Paleozoic schists in the footwall. Double headed arrow labelled 'Fault Core' is 5 m in thickness. Overall, the Zuccale fault dips ~15°E, but locally the base of the fault core has been back-rotated by a series of high-angle footwall faults, which also strongly control the distribution of individual fault rock units. Hydrofracture veins cross-cut the footwall and fault core, and are always directly linked to high-angle footwall faults (see inset photograph).

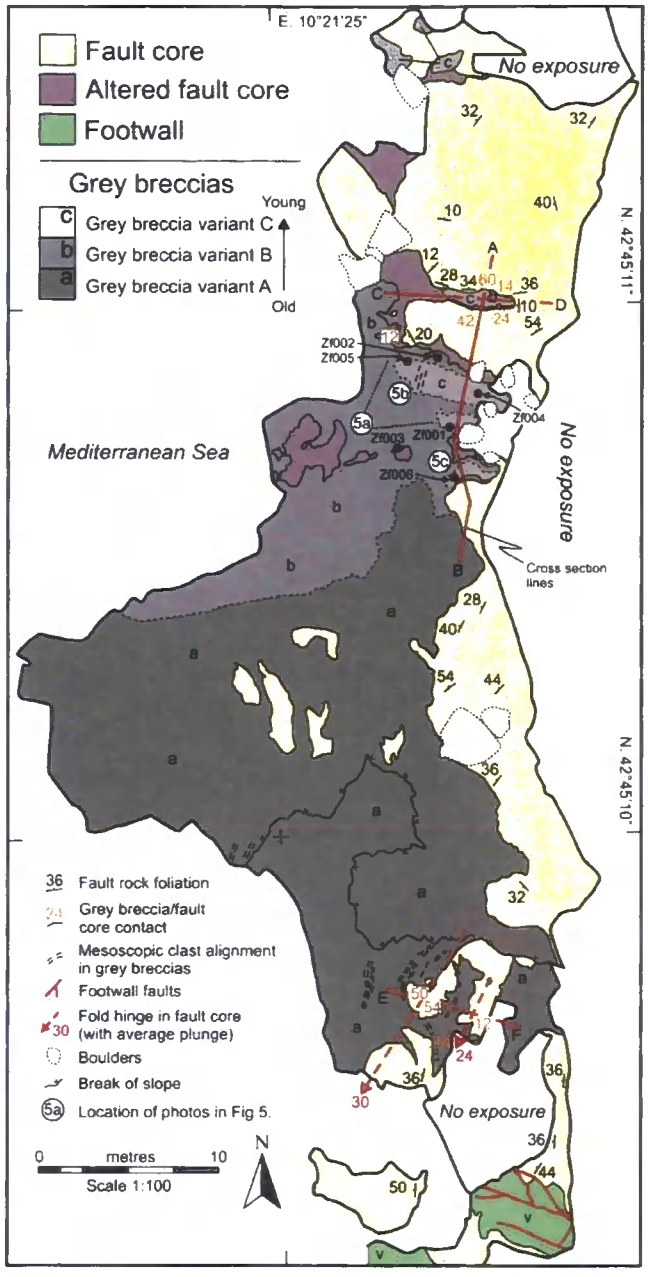

Fig. 3. Detailed geological map of the north–south coastal section at Punta Di Zuccale where grey breccias are present. Also shown are the cross section lines in Fig. 4, the locations of photographs in Fig. 5, and the locations of samples Zf001–Zf006 discussed in Section 4.2.

(Figs. 3, 4). They are differentiated in the field on the basis of colour, structural position beneath the Zuccale fault, textural features, and maximum clast size.

Grey breccia A is the most voluminous variant and occupies an area of ~40 × 40 m in the southern half of the mapped outcrop (Fig. 3). Compositionally and texturally it is highly heterogeneous, and is dominated by large blocks of basement quartzite and quartz–mica schist which can be up to several meters in diameter. The lithologies of clasts within this variant, and those in variants B and C, are indistinguishable from the local wallrock.

Variants B and C are texturally much more homogenous. Both are grey to milky-white in colour, and contain clasts of basement quartzite and quartz–mica schist not exceeding several tens of centimetres in diameter. Breccia C is differentiated from B on the basis of two specific mesoscopic characteristics. First, it occurs solely as discrete pods of material which sit at topographically and structurally higher levels than B (Figs. 4, 5a). Second, breccia C possesses a distinct honeycomb weathering texture, particularly noticeable towards its base, which appears to reflect erosion and removal of large clasts (Fig. 5b).

The three variants of grey breccia appear to have formed at different times based on their structural relationship to extensional slip surfaces within the overlying foliated core of the Zuccale fault. Slip surfaces are commonly highly polished and associated with a thin (<1 mm) veneer of ultra-fine grained cataclastic material. Breccia A appears to be the oldest variant, because in places the upper surface of this breccia is defined by a cross-cutting extensional slip surface which contains well-developed east–west slickenlines. In turn, breccias B and C cross-cut the same slip surface and so, by definition, must be younger than A. Breccia C is interpreted to be younger than B because of its occurrence as isolated pods of material which sit on top of and appear to originate from within B (Figs. 4, 5a).

Importantly, there is strong evidence that the coastal section containing the grey breccias is underlain by a major north–south trending high-angle extensional fault like those described in Section 2.2 and shown in Fig. 2. Smith et al. (2007) showed that well-exposed footwall faults are directly associated with (Fig. 2): (1) the preservation of phyllonitic fault rocks as isolated lenses of material; (2) inclined flow folds within the fault core; and (3) back-rotation of footwall blocks so that locally they are sub-horizontal or dip westward. All of these structural relations are found in the area containing the grey breccias (Fig. 3). Large flow folds are present within the fault core in the southern half of the mapped outcrop, and all fault core rocks dip moderately to the west or north-west, indicating that the fault core has experienced local back-rotation.

3.2. *The boundary between the grey breccias and the overlying fault core*

All three variants of grey breccia appear to preserve 'intrusive' relationships with overlying foliated fault rocks within the core of the Zuccale fault (Figs. 4, 5, 7b). The boundary between the grey breccias and the overlying fault core is well defined and typically has a highly irregular nature, preserving undulations with wavelengths between 10 cm and 5 m, both parallel and perpendicular to the easterly transport direction within the Zuccale fault. These undulations are directly associated with warping and folding of the overlying fault core, so that the foliation within the overlying fault rocks closely follows the shape of the underlying boundary (Fig. 4). In detail, the boundary has a cuspate-lobate nature (Fig. 5c). Additionally, small fragments (<30 cm in diameter) of heavily altered fault core material are commonly found 'floating' within the underlying grey breccias (Fig. 5c). Within breccia variants A and C a mesoscopic north–south alignment of elongate clasts of quartzite and quartz–mica schist can be observed on sub-horizontal (plan view) surfaces (Fig. 6).

3.3. *Microstructural observations*

Frictional breccias are typically characterized by a mosaic texture (following the terminology of Mort and Woodcock, 2008), so that at any scale of observation, the textural framework appears to be 'clast-supported' (Fig. 7a). The frictional breccias contain abundant cataclastic fractures which are commonly lined with fibrous chlorite. The matrix of the frictional breccias typically consists of fine-grained quartz, chlorite and sericite, derived from

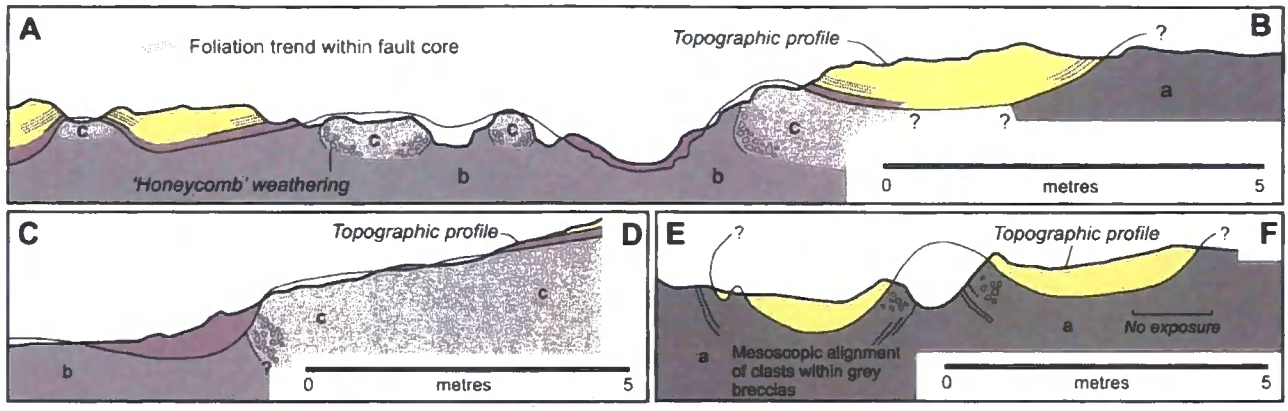

Fig. 4. Cross sections through the grey breccias and overlying fault rocks within the core of the Zuccale fault. Key is the same as Fig. 3. Note the presence of a mesoscopic clast alignment within the grey breccias, and a layer of altered fault core overlying the grey breccias.

comminution of larger clasts. Qualitatively, clasts within the frictional breccias at any scale of observation have an angular to sub-angular appearance, and contain no visible shape-preferred orientation (Fig. 7a). They appear relatively fresh and have not been overgrown by any late alteration or replacement products.

Grey breccias appear remarkably different on a grain-scale, and their overall texture does not readily fit into one of the breccia classes proposed by Mort and Woodcock (2008); (Fig. 7b). At any scale of observation, the breccia framework appears to be 'matrix-supported'. Relatively large clasts of quartzite and quartz–mica schist (up to ~1000 μm) are isolated within an ultra-fine grained matrix. There is a complete lack of any localized deformation features such as cataclastic fractures or shear bands. Qualitatively, clasts within the grey breccias have a sub-rounded to rounded appearance and are commonly overgrown by euhedral crystals of colourless dolomite (Fig. 8a). In thin section, the boundary between the grey breccias and the overlying fault core preserves a well-defined, irregular nature (Fig. 8b). Immediately above the boundary, in a layer 30 cm to 1 m thick, the fault core is highly altered and is dominated by fine-grained Fe-oxide phases and inter-grown calcite and dolomite crystals (Figs. 3, 4, 5, 8b). These carbonate crystals are fresh and undeformed, and often preserve primary growth zoning (Fig. 8c). In places, a relict breccia texture is overgrown by undeformed, subhedral–anhedral calcite crystals (Fig. 8d). Table 1 provides a summary of microstructural observations of frictional breccias and grey breccias.

4. Quantifying grain-scale deformation in the grey breccias

4.1. Analysis of fragmented counterparts

Monzawa and Otsuki (2003) and Otsuki et al. (2003) proposed a quantitative method to determine whether a particular granular fault rock has experienced fluidization. The key parameter analyzed using their method is the 'detection probability of fragmented counterparts' in thin sections of fault rock. A clast in thin section is considered a fragmented counterpart when it can be recognized that it was originally part of a larger clast. In other words, if two clast fragments are found adjacent to one another, and they evidently fit together like a jigsaw puzzle, they can be considered fragmented counterparts.

During frictional deformation, granular fault rocks such as breccias and cataclasites, which consist of packed and interlocking clasts, experience continuous fracturing due to high stresses at grain–grain contacts. Consequently, the probability that clasts will be fractured during frictional deformation is high.

Once a granular fault rock becomes fluidized, the only mechanism capable of generating new clast fragments is head-on collision between clasts, or between clasts and the wall rocks. However, Monzawa and Otsuki (2003) showed that in most circumstances the probability of fragmenting clasts smaller than a few millimetres during fluidization is virtually zero, because the collision velocities required are extremely high (e.g. 10 m s^{-1} for clasts of quartzite 1 mm in diameter). Although only currently developed for 2-dimensional analysis, their simple theoretical treatment indicates that an assessment of the number of fragmented counterparts can yield important insights into whether a granular fault rock has experienced fluidization or not.

The analysis of fragmented counterparts involves scanning thin sections under the optical microscope and searching for fragmented counterparts with radius $r < r < r + \Delta r$ within a given area for a given magnification. During fault slip, fragmented counterparts will move away from one another. The total number of identifiable fragmented counterparts with radius r, $\Delta N_f(r)$, can be expressed as a percentage probability, $P(r)$, relative to the total number of clasts with radius r, $\Delta N_t(r)$. At this stage we define the parameter $R_f(r)$ as the fragmentation rate per clast per unit incremental fault slip, Δs. Therefore, the total number of fragmented counterparts produced during incremental fault slip is $N_t(r)R_f(r)\Delta s$. For a fragmented counterpart to remain identifiable, it must stay within a critical distance, d_c. The probability at which a pair of counterparts can be identified after fragmentation is proportional to $(d_c/v_r)/\Delta s$, where v_r is the mean residence 'time' for counterparts to stay within d_c. In summary, Monzawa and Otsuki (2003) show that the total number of identifiable fragmented counterparts is proportional to $N_t(r)R_f(r)\Delta s \times d_c/v_r\Delta s$, and the detection probability of fragmented counterparts is:

$$P(r) \equiv \frac{N_f(r)}{N_t(r)} \propto \frac{R_f(r)d_c}{v_r} \tag{1}$$

As noted above, $R_f(r)$ during fluidization is likely to be low, whereas in the frictional regime, it can be high due to grain–grain contact stresses. Additionally, v_r is likely to be considerably higher for the fluidization regime compared to the frictional regime because clasts are able to move more freely in a fluid phase. Consequently, $P(r)$ is expected to be small for fluidized fault rocks, but much larger for fault rocks produced during typical frictional deformation.

We measured $P(r)$ in 8 thin sections of breccia from the immediate footwall of the Zuccale fault (Fig. 9). Four thin sections were cut from 2 samples of breccia deformed by typical frictional mechanisms (PZ019, PZ020), and 4 thin sections were cut from 2

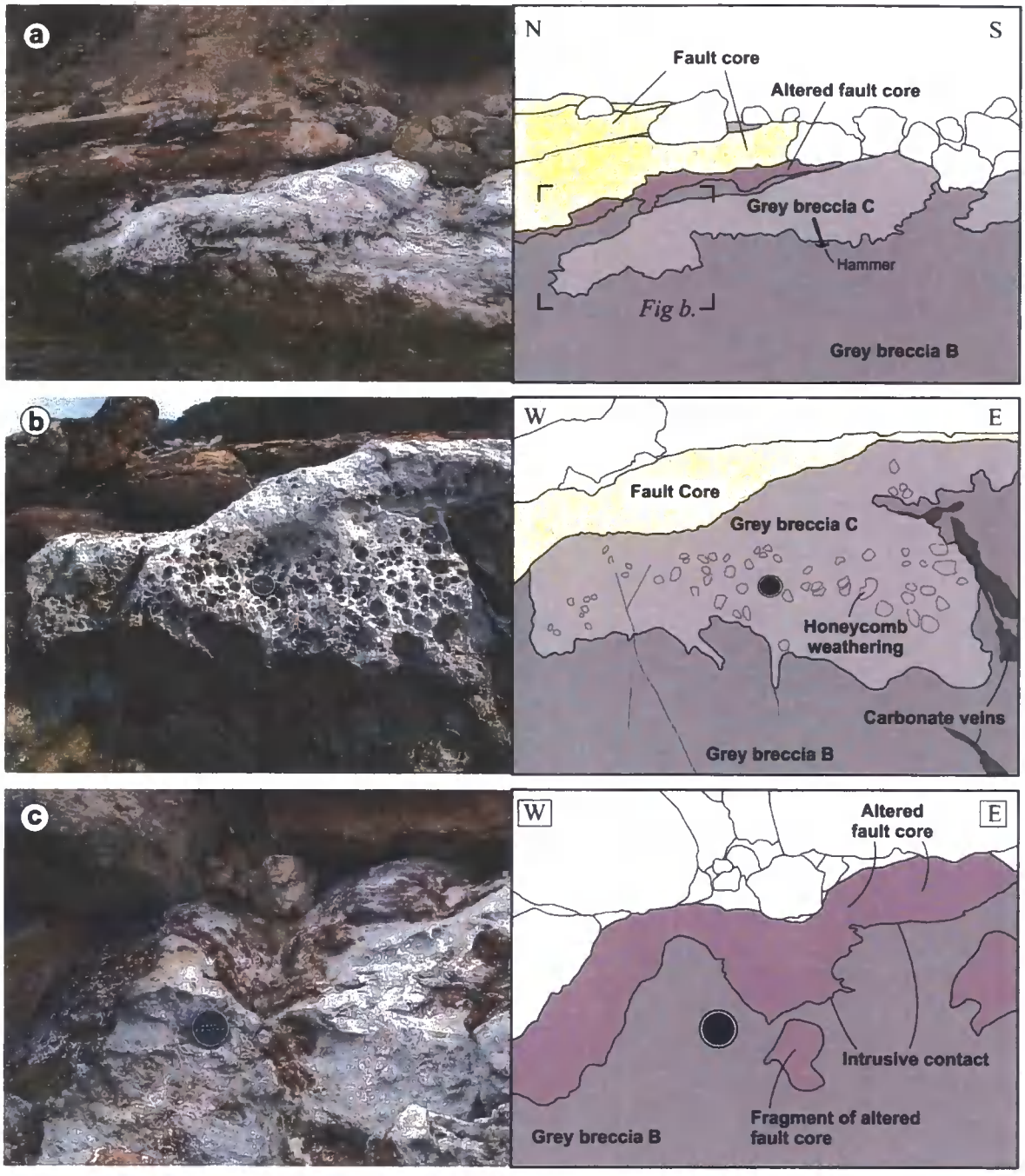

Fig. 5. Photographs and detailed sketches of the grey breccias and overlying fault core. Locations of photographs are shown in Fig. 3.

samples of grey breccia (PZ001 from variant C, PZ003 from variant B). Fragmented counterparts were analyzed over the size range 10–4000 μm, and 200–600 measurements were carried out on each thin section.

The P values of sample PZ020 are the highest, and reach 60–70% for clast diameters of ~1000 μm, decreasing to <50% at clast diameters of <100 μm. The average P value for this sample is 61%. Sample PZ019 also shows high values, with an average of 44.5%. Again, P values reach 50–70% for clast diameters of ~1000 μm, decreasing to <40% for clast diameters of <100 μm. In both cases, P clearly shows a strong clast size dependency. This is related to the fact that the tensile strength of clasts is strongly size dependent, and consequently the fragmentation rate $R_f(r)$ is also size dependent (Monzawa and Otsuki, 2003; Otsuki et al., 2003). This highlights the fact that when carrying out fragmented counterpart analysis it is necessary to consider clast sizes over as wide a size range as possible.

In marked contrast, samples PZ001 and PZ003 show uniformly low P values and no obvious size dependency. The average values of P are 8% for PZ001 and 7.6% for PZ003. There are clearly 2 separate groups identifiable in our results, the first group consisting of PZ019 and PZ020, the second group consisting of PZ001 and PZ003.

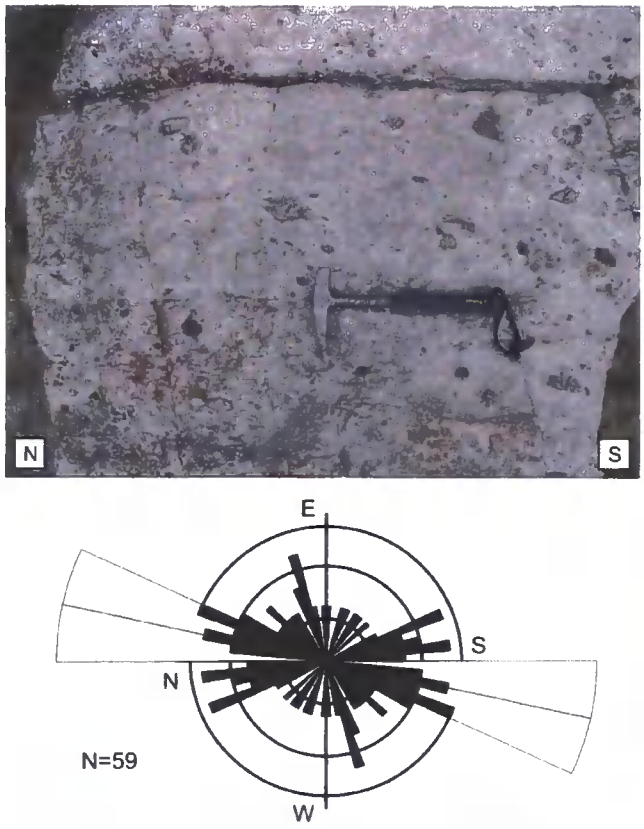

Fig. 6. Photograph of horizontal surface showing an alignment of elongate clasts of quartzite and quartz–mica schist within grey breccia variant C. The clasts are aligned broadly north–south. See Section 4.2 and the caption for Fig. 11 for a description of the construction and labelling of the rose diagram. Orientation statistics were calculated for this example by tracing all visible clasts in the photograph. Mean vector orientation, 12° clockwise from north; mean vector strength, 0.4; mean aspect ratio of visible clasts, 2.17.

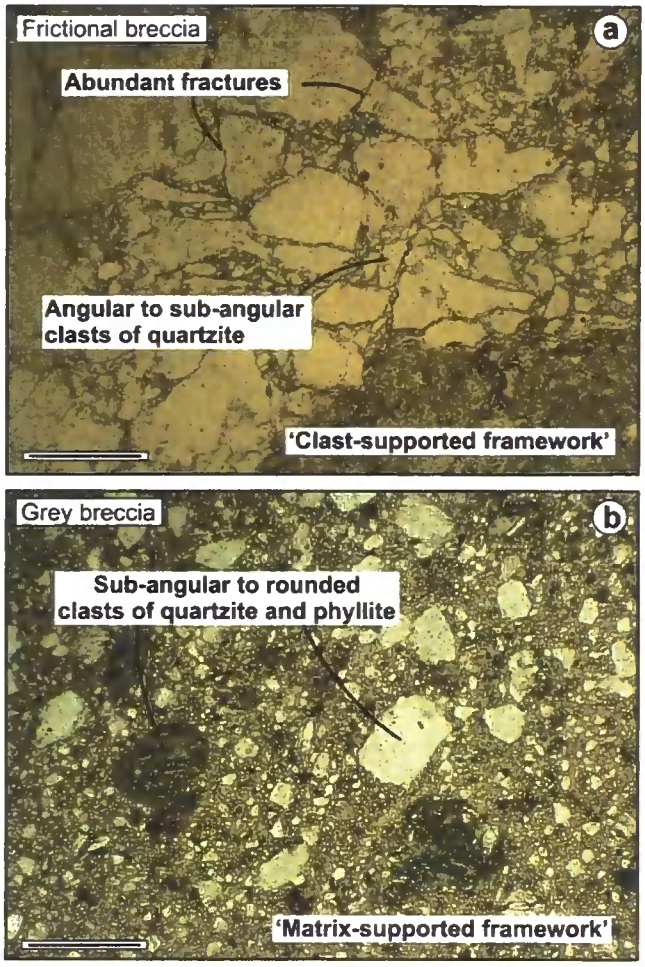

Fig. 7. Photomicrographs showing grain-scale textures within typical frictional breccias (a) and grey breccias (b). Note the 'matrix-supported' framework, and the lack of cataclastic fractures within the grey breccias. Scale bars are 1 mm, and both images are taken in plane polarized light.

4.2. Analysis of clast shape-preferred orientation

Field observations suggest that a mesoscopic shape-preferred orientation (SPO) of quartzite and quartz–mica schist clasts is visible in places within grey breccia variants A and C (Fig. 6). This SPO is aligned roughly north–south on sub-horizontal (plan view) surfaces, but these surfaces only provide a 2-dimensional view of an inherently 3-dimensional SPO vector. To partly overcome this problem, we measured the SPO of clasts within thin sections of grey breccia cut in 3 orthogonal planes through oriented samples collected at the outcrop. Six oriented samples of grey breccia were collected from variants B and C (Fig. 3). Three orthogonal thin sections were cut from each sample, and each thin section is given reference indices to help with identification and analysis. We have followed the labelling convention of Hayman et al. (2004) and provide a description of this convention in the caption for Fig. 11b. Using a BATY® Shadowmaster, thin sections were projected in plane polarized light at ×1 magnification on to a large tracing table. All of the visible clasts within the breccias were traced at ×1 scale. At least 300 clasts were traced in each thin section, although in most cases significantly more than 400 clasts were traced. The resulting images were scanned, processed and imported into ImageTool® textural analysis software (Fig. 10). By tracing all the visible clasts, we eliminate clast selection bias which is usually implicit in manual measurements of SPO at the outcrop or on a grain-scale. Only clasts with an aspect ratio (L/S) greater than 1.5 were included in the final statistical analysis. Although this methodology forces us to restrict our analysis to ×1 magnification, Cladouhos (1999) found that the orientation of the SPO mean vector remains roughly constant at all magnifications.

The results of grain-scale SPO analyses are shown qualitatively as equal-area rose diagrams in Fig. 11b. Quantitatively, the orientation of the mean vector, M, can be calculated using the semi-circular vector mean (Agterberg, 1974; Davis, 2002):

$$M = 0.5\tan^{-1}\left(\frac{\sum \sin 2\theta_i}{\sum \cos 2\theta_i}\right) \tag{2}$$

while the mean vector strength, R, is:

$$R = \frac{1}{N}\left\{\left(\sum \sin 2\theta_i\right)^2 + \left(\sum \cos 2\theta_i\right)^2\right\}^{1/2} \tag{3}$$

for N measurements with clast long axes oriented θ_i. Statistical results for all 6 samples of grey breccia are provided in Table 2.

The results indicate that there is a statistically significant SPO (at a 95% confidence level) of clasts present within the grey breccias. The SPO is strongest in the X1/X2 (horizontal) and X2/X3 (vertical, east–west) sections (Fig. 11b). In the X1/X2 sections, 4 out of 6 samples show a vector strength varying between 0.17 and 0.36. In one sample (Zf002) there is no SPO in the X1/X2 section, and

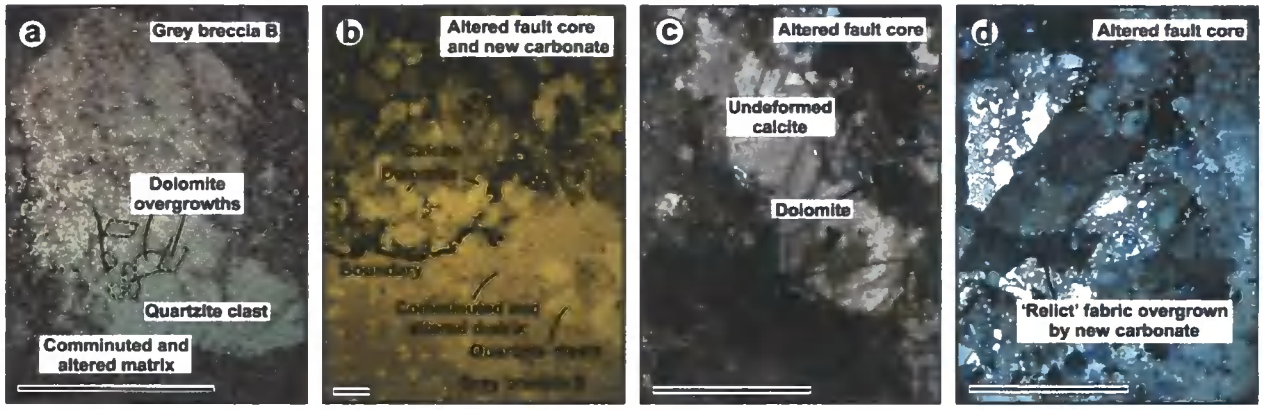

Fig. 8. Photomicrographs showing details of grain-scale textures within grey breccias and overlying fault core. Scale bars are 1 mm. Images (a) and (b) were taken in plane polarized light, (c) and (d) in crossed polarized light. (a) Detail of quartzite clast within grey breccia B which is overgrown by abundant euhedral dolomite crystals. (b) Irregular, well-defined boundary between grey breccia variant B and overlying altered fault rocks within the core of the Zuccale fault. The overlying fault rocks are dominated by fine-grained Fe-oxide phases and fresh growths of calcite and dolomite. (c) Detail of calcite and dolomite intergrowths within altered fault core overlying the boundary. Note the primary growth zoning in both minerals. (d) Relict breccia fabric overgrown by new subhedral–anhedral calcite crystals within the altered fault core.

in another the vector strength is weak (Zf001). For those 4 samples which show a stronger SPO, the orientation of the mean vector is approximately north–south. Significantly, this vector orientation is similar to that observed in horizontal surfaces in the field, suggesting that the grain-scale measurements are reliable. In the X2/X3 sections, all 5 analyses show a vector strength varying between 0.16 and 0.34. One thin section was unsuitable for analysis because the entire slide was occupied by one large clast. All of the mean vector orientations are at a high angle (84–127°) to horizontal. Three out of 6 samples show a significant SPO in the X1/X3 sections (vertical, north–south). However, the vector strengths are generally weak (0.12–0.19) and subordinate to the SPO observed in the other 2 sections. In summary, the dominant shape-preferred orientations of clasts within the grey breccias are approximately north–south in horizontal surfaces, and sub-vertical in east–west trending vertical surfaces.

5. Discussion and conclusions

5.1. Generation of grey breccias

Several outcrop-scale observations suggest that the grey breccias have experienced fluidization. We define fluidization after Monzawa and Otsuki (2003) as "the state in which grains fly around with a mean free path like gaseous molecules". More precisely, we consider fluidization of grey breccias at Punta Di Zuccale to result in the constituent clasts experiencing particle transport in the presence of a fluid phase. First, grey breccias preserve 'intrusive' relationships with foliated fault rocks lying within the core of the Zuccale fault. Second, the boundary between the grey breccias and the fault core is highly irregular and undulose in nature. Third, fragments of altered fault core material are found floating within the underlying grey breccias. Finally, a shape-preferred orientation of clasts is present within all variants of grey breccia. The grey breccias contain low values of fragmented counterparts, providing complementary grain-scale evidence that they experienced fluidization. In addition, the rounded to sub-rounded nature of clasts within the grey breccias has previously been suggested as indicating particle transport in the presence of a fluid (e.g. Clark and James, 2003).

Clasts of quartzite within the grey breccias are commonly overgrown by crystals of dolomite, and the red oxidized layer overlying the grey breccias is dominated by intergrowths of calcite

Table 1
Summary of microstructural observations of typical frictional breccias and grey breccias at Punta Di Zuccale

Frictional breccia	'Clast' supported mosaic texture Abundant cataclastic fractures Matrix is fine grained quartz and fibrous chlorite Upper boundary of breccias is commonly a fault contact Sub-angular to angular clasts
Grey breccia	'Matrix' supported fabric No cataclastic fractures Matrix is ultra-fine grained quartz, sericite, and infrequent chlorite Abundant growth of undeformed calcite and dolomite Quartzite clasts frequently overgrown by dolomite Upper boundary of breccias is intrusive in nature Sub-rounded to rounded clasts

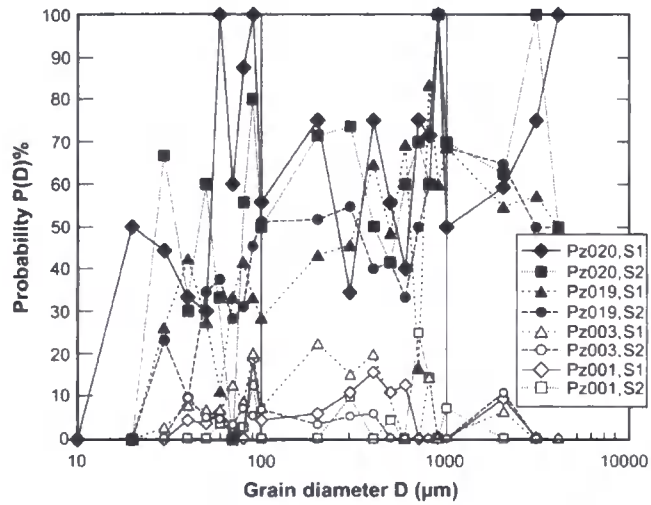

Fig. 9. Detection probability of fragmented counterparts as a function of grain diameter (D) for 4 thin sections of frictional breccia (PZ019, PZ020) and 4 thin sections of grey breccia (PZ001, PZ003). Note the separation in the probability values between the frictional and grey breccias. See text for discussion.

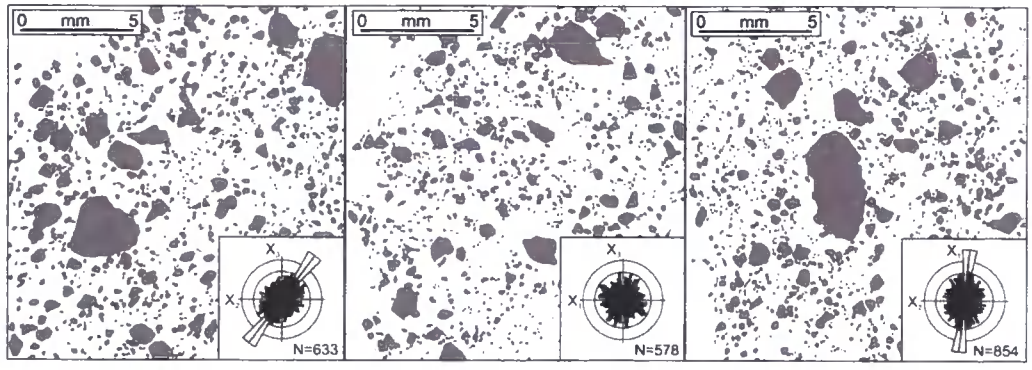

Fig. 10. Examples of images which were used as input to ImageTool® textural analysis software, and the resulting rose diagrams calculated using EZ-ROSE (Baas, 2000). The images represent tracings of 3 thin sections cut along orthogonal planes through one oriented sample. See text for discussion.

and dolomite (Fig. 7). Additionally, there are abundant carbonate hydrofracture veins which cross-cut the footwall and the core of the Zuccale fault. These observations indicate that the fluids which were circulating adjacent to the Zuccale fault contained CO_2. Sources of fluid and CO_2 may include mantle degassing, hydrothermal fluid flow associated with intrusion of the Porto Azzurro pluton, metamorphic fluid, or deeply-circulating meteoric fluid. Regardless of the source(s) of the fluids, recent experimental data (e.g. Le Guen et al., 2007) has shown that CO_2-bearing fluids can cause rapid dissolution of carbonate and silicate minerals, particularly if the fluids are under high partial pressures.

5.1.1. Precursors to fluidization

Grey breccias are developed in the footwall of the Zuccale fault in an area which contains: (a) pre-existing frictional breccias; (b) a north–south trending high-angle footwall fault (Section 3.1); and (c) a strongly foliated fault core dominated by calc-mylonites, phyllonites and foliated cataclasites (Fig. 12a; Section 2.2). Prior to fluidization, the migration of fluids containing CO_2 occurred, which was controlled, at least in part, by fault and fracture networks located in the footwall of the Zuccale fault (Fig. 12a). We suggest that the fluids were forced to pond in structural traps or migrate laterally at the base of the Zuccale fault because of the likely impermeable nature of the foliated fault core (cf. Faulkner and Rutter, 1998, 2000). At this stage, fluids were able to percolate along fracture networks within the pre-existing frictional breccias, causing dissolution of constituent quartzite and quartz–mica schist clasts, and eventually leading to a partial loss of cohesion within the frictional breccias.

5.1.2. Fluidization and the development of fluid overpressures

We interpret the clast-preferred orientations within the grey breccias as representative of a flow fabric generated by fluids moving through the breccias and causing transport and realignment of the constituent clasts. The SPO data are consistent with fluids moving upwards within the footwall from depth and spreading laterally in a north–south direction once they encountered the relatively impermeable fault core. This scenario would account for the sub-vertical SPO observed on vertical planes and the approximately north–south SPO observed on horizontal planes.

All major hydrofracture veins which cross-cut the fault core link directly downwards into high-angle footwall faults, strongly suggesting that footwall structures act to focus and channel fluid flow (Section 2.2, Fig. 2). We believe that the SPO of clasts within the grey breccias can be explained by invoking fluidization during periodic slip events along high-angle footwall faults (Fig. 12b). During such slip events, fault planes can experience dilation allowing short-term focused fluid flow at rates of up to several 10s of centimetres per second (Sibson, 2000; Eichhubl and Boles, 2000; Sheldon and Ord, 2005). The overlying fault core in this case maintained its integrity, and its low permeability, by continuing to experience macroscopically ductile deformation, meaning that the footwall-hosted fluid pulse was forced to spread laterally beneath the core, explaining the development of an SPO on horizontal (plan view) surfaces (Fig. 12b). This scenario also satisfies a condition of Bagnold's (1954) experimental investigation into the generation of fluidized granular materials. He showed that the transition from frictional deformation to fluidization occurs when the Bagnold number decreases from infinity to a finite value (larger than 450), and that the most likely reason for this is a small decrease in the volume fraction of clasts. To explain this small decrease, Monzawa and Otsuki (2003) and Otsuki et al. (2003) invoked normal interface vibration (Brune et al., 1993) and a resulting increase in the distance between fault wall rocks. In our model, a small decrease in the volume fraction of breccia clasts beneath the Zuccale fault could result directly from slip along high-angle footwall faults in one of two ways: (1) fault plane dilation; or (2) the hangingwall of such faults would experience negative (tensional) static stress changes

Table 2
Shape-preferred orientation statistics for 6 samples (18 thin sections) of grey breccia (see Fig. 11 for corresponding rose diagrams and orientation conventions)

Sample	X2X3				X1X3				X1X2			
	M	*R*	*L/S*	*N*	*M*	*R*	*L/S*	*N*	*M*	*R*	*L/S*	*N*
Zf001 (C)	97.08	0.19	2.04	622	17.73	0.16	1.92	684	30.6	0.08	1.89	836
Zf002 (B)	126	0.34	1.8	422			1.67	531			1.7	531
Zf003 (B)	84.35	0.16	1.84	469			1.89	476	107.6	0.19	1.84	620
Zf004 (C)	126.61	0.2	1.85	633			1.86	578	95.91	0.17	1.85	854
Zf005 (C)	89.392	0.181	1.82	555	34.64	0.12	1.70	324	80.48	0.358	1.84	396
Zf006 (C)					40.1	0.19	1.78	516	102.39	0.239	2.02	400

M, mean vector orientation (α°); *R*, mean vector strength; *L/S*, mean aspect ratio; *N*, number of clasts used in each thin section. Boxes are left blank where results were not statistically significant at 95% confidence.

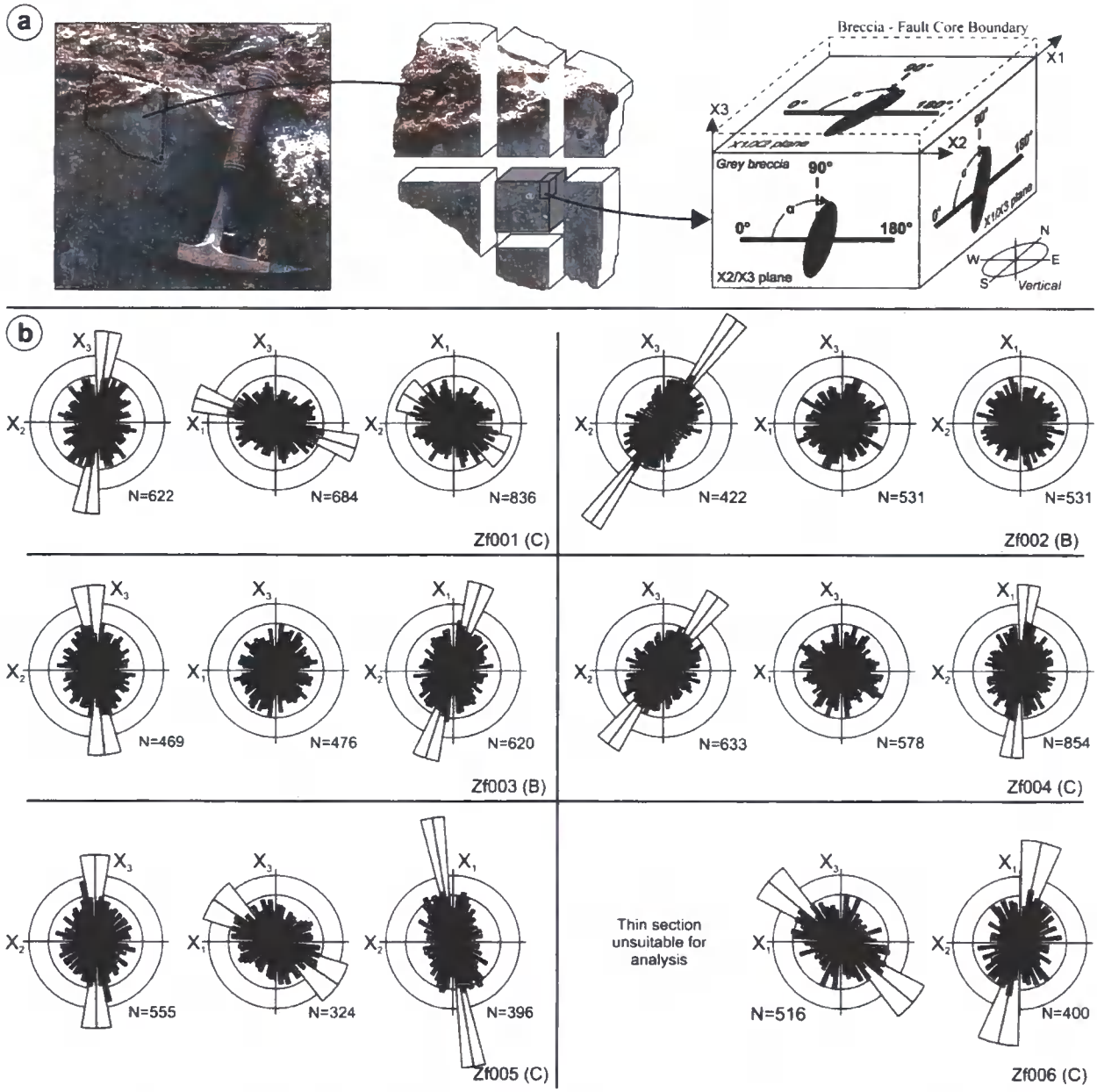

Fig. 11. (a) Orientation conventions used for calculating grain-scale shape-preferred orientation (SPO). Three orthogonal thin sections were cut from samples collected in the field. The X1/X2 thin section is sub-horizontal, and the edges of the thin section aligned with X1 (north–south) and X2 (east–west). The X2/X3 thin section is vertical, and the edges of the thin section aligned with X2 and X3. The X1/X3 thin section is vertical, and the edges of the thin section aligned with X1 and X3. α is the angle (0–180° measured clockwise) between the reference line indicated and the long-axis of the measured clast. (b) Equal-area rose diagrams of the shape-preferred orientation of clasts within 6 samples of grey breccia (Zf001–Zf006; letters in brackets refer to the grey breccia variant from which the sample was taken). The rose diagrams were constructed using EZ-ROSE (Baas, 2000) and the data are plotted in 5° bin intervals. The outer circle represents 10% of the data. The grey sector in each rose diagram shows the mean vector orientation (black bisector line) and mean vector strength (length of grey sector). The angular confidence interval (95% confidence) is indicated by the width of the grey sector. *N* is the total number of clasts measured in each thin section. In all cases $N > 300$, usually $N \gg 400$. Where no grey sector is present, the data has a uniform distribution and there is no statistically significant preferred orientation at 95% confidence. Measurements of all angles presented in Table 2 are clockwise from the reference line indicated in part (a). One thin section from sample Zf006 was unsuitable for microscopic analysis.

(Nostro et al., 1997). The most likely reason for approximately north–south directed lateral flow beneath the fault core is enhanced permeability parallel to the σ_2 direction and the strike of the footwall fault (e.g. Sibson, 2000).

The ponding of fluids at the base of the Zuccale fault as a consequence of a waning in flow could result in the slow growth of fresh and undeformed carbonate within a thin alteration horizon overlying the grey breccias (Figs. 4, 12b). This may also explain the fact that large clasts of quartzite and quartz–mica schist, now eroded to form a honeycomb texture, appear to have settled downwards towards the base of breccia variant C (Fig. 5b). During successive slip events along the high-angle footwall fault, continued input of fluids would lead to a gradual increase in the concentration of CO_2, eventually leading to gas bubble formation. This would increase fluid overpressure, inducing deformation (warping and folding) of the boundary between the grey breccias and the

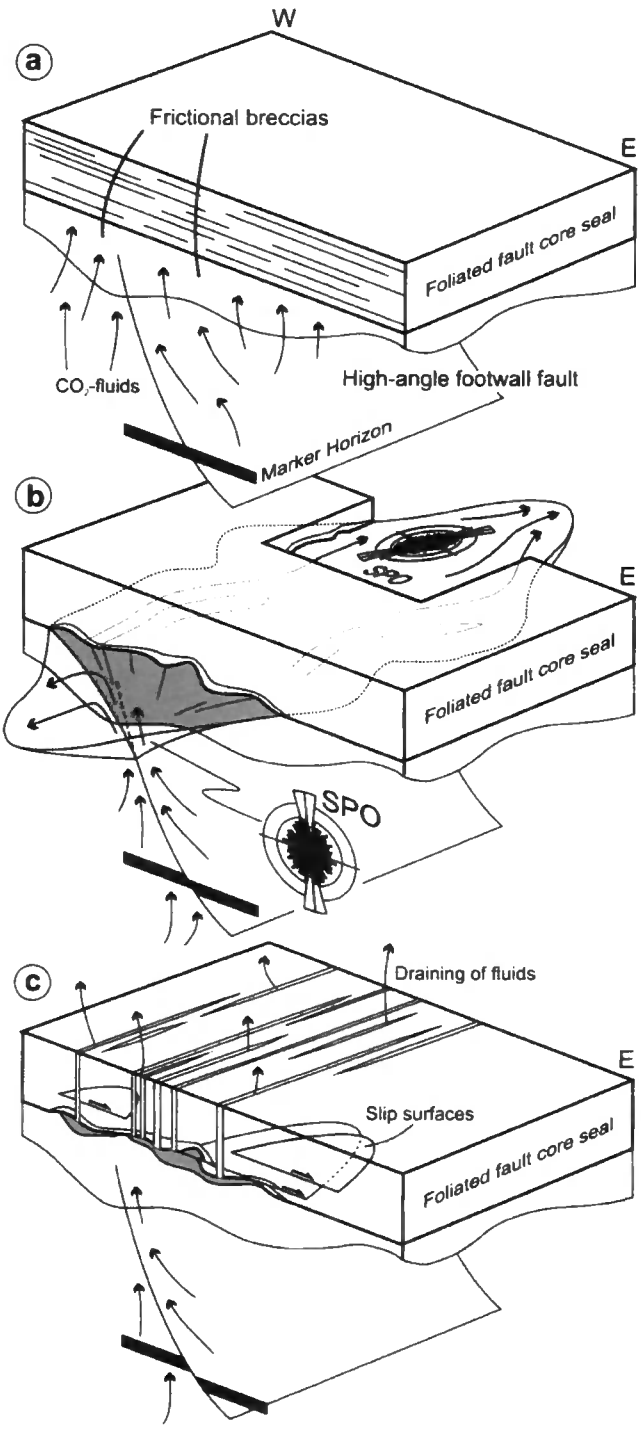

Fig. 12. Generation of grey breccias. (a) Precursors to fluidization: the Zuccale fault possesses a strongly foliated fault core which acts as a low-permeability seal to CO_2-bearing fluids migrating within the footwall. The fault core is underlain by a high-angle footwall fault. Fluids infiltrate pre-existing frictional breccias, leading to dissolution and a loss of cohesion. (b) Fluidization: periodic slip along high-angle footwall faults leads to focused and rapid fluid flow, causing fluidization of clasts within the frictional breccias. The fluid pulse spreads laterally as it encounters the fault core. Ponding of fluids, and deformation of the boundary, may occur during continued input of fluids. (c) Hydrofracturing: critical fluid overpressure leads to embrittlement within the core of the Zuccale fault, allowing fluids to drain from footwall to hangingwall. The fractures undergo healing processes returning to a low-permeability nature, allowing the fault-valve cycle to repeat.

fault core, and promoting the incorporation of fault core material into the breccias (Figs. 4, 5). Deformation of the boundary may also have been enhanced by reaction-weakening processes within the fault core, triggered by the presence of chemically active CO_2-bearing fluids.

5.1.3. Hydrofracturing and fault-valve behaviour

Once fluid overpressure in the footwall of the Zuccale fault reached a critical value (e.g. $P_f = \sigma_3 + T$), this triggered hydrofracturing of the fault core and a significant increase in permeability, allowing fluids to drain from the footwall into the hangingwall (Fig. 12c). We speculate that an increase in fluid overpressure also promoted movement along extensional slip surfaces within the fault core, because at Punta Di Zuccale, the concentration of these slip surfaces is greatest within the fault core immediately overlying the grey breccias. As described in Section 3.1, grey breccia variant A is cross-cut along its upper margin by a low-angle slip surface. Draining of fluids from the footwall to the hangingwall resulted in a decrease in fluid overpressure. Hydrofractures and slip surfaces were mineralized, and the fault core underwent sealing processes returning to a low-permeability state (e.g. Tenthorey and Cox, 2006; Gratier and Gueydan, 2007). The presence of multiple variants of grey breccia attests to the fact that fluid flow along the Zuccale fault was cyclic. The combined grey breccia–hydrofracture–slip surface association therefore represents an integrated example of fault-valve behaviour along low-angle normal faults.

5.2. Fluidized fault rocks and the seismic cycle

Fluidized fault rocks have been described on several occasions in the literature from a variety of tectonic settings. These include, but are not restricted to: decimetre-thick lenses of fluidized cataclasite found in association with pseudotachylytes within ancient accretionary complexes (Rowe et al., 2005; Ujiie et al., 2007); centimetre-thick fluidized cataclasites and fault gouges from major intracontinental strike-slip faults in Japan (Monzawa and Otsuki, 2003; Otsuki et al., 2003); fluidized breccias found as meter-scale dyke- and pipe-like bodies around intrusions, faults and near ore deposits in eastern Australia (Oliver et al., 2006) and South Africa (Boorman et al., 2003); and variably-sized fluidized breccias controlled by dilational fault jogs (e.g. Clark and James, 2003). In each of these cases, the fluidized fault rocks are found as bodies which cross-cut wall rocks with sharp angular contacts, and are interpreted as forming due to single rapid events related to a sudden release, or increase, of fluid overpressure. The close link between fluidized cataclasites and pseudotachylytes found along exhumed subduction thrust faults prompted Rowe et al. (2005) and Ujiie et al. (2007) to suggest that this type of fluidized cataclasite may be used as an indicator of co-seismic slip.

We believe that fluidization of the grey breccias found at Punta Di Zuccale is related to the interactions between slip along the low-angle Zuccale fault (which accommodates 6–8 km of displacement), and slip along high-angle footwall faults (individually accommodating, at most, 5 m of displacement). With respect to the Zuccale fault, we suggest that fluidization of the grey breccias is related to gradual build-ups of fluid overpressure in the footwall of the Zuccale fault during the interseismic stage of the earthquake cycle. It is important to note that build-ups of fluid overpressure were punctuated by co-seismic slip events along high-angle footwall faults, but not by slip events within the low-angle core of the Zuccale fault itself. In other words, the fault-valve and seismic-cycle along the Zuccale fault were intimately related to, and dependent upon, the fault-valve and seismic cycle along the high-angle footwall faults.

During the interseismic stage along the Zuccale fault, the fault core likely possessed a low permeability and was deforming by mechanisms such as pressure-solution ('frictional-viscous') creep (Bos and Spiers, 2002; Collettini and Holdsworth, 2004). Migration of CO_2-bearing fluids at this stage acted to corrode frictional breccias in the footwall. Both migration of fluids and corrosion of frictional breccias were essential precursors to fluidization. Build-ups of fluid overpressure in the footwall of the Zuccale fault, perhaps combined with reaction weakening within the fault core, led to deformation and folding of the boundary between the grey breccias and the fault core. Only when fluid overpressure in the footwall obtained a critical value could hydrofracturing and brittle slip occur along the Zuccale fault. In our opinion, the size of the grey breccias, characteristics of the boundary with the overlying Zuccale fault core, and structural position *beneath* the fault core, are most compatible with fluidization having occurred during the interseismic period along the Zuccale fault. Comparison with the studies of fluidized fault rocks mentioned above suggests that fluidization of grey breccias during co-seismic slip along the Zuccale fault would have resulted in angular and sharp cross-cutting relationships with the fault core and local wall rocks, and/or formation of fluidized material formed by slip *within*, and emanating from, the core of the Zuccale fault.

The fluidization of grey breccias at Punta Di Zuccale occurred over areas of 10^{-3}–10^{-2} km^2. We suggested in Section 5.1.3, based on field evidence, that attainment of critical fluid overpressures in the footwall of the Zuccale fault triggered the formation of low-angle extensional slip surfaces within the overlying fault core, and therefore it seems likely that the slip surfaces would possess dimensions roughly equal to those of the grey breccias. We speculate that hydrofracturing and brittle slip processes, triggered by fluid overpressure, may represent co-seismic events along the low-angle Zuccale fault. Interestingly, microseismicity produced along the active Altotiberina low-angle normal fault occurs on rupture surfaces on the order of 10^{-3}–10^{-1} km^2.

Cowan (1999) concluded that, based on our current understanding, the only fault rocks which are unambiguous indicators of co-seismic slip are pseudotachylytes. More recently, Han et al. (2007a,b) conducted high-velocity friction experiments and reported that at seismic slip velocities (up to 2 m s^{-1}) calcite and siderite experienced thermal decomposition resulting in formation of CO_2 + lime and CO_2 + magnetite, respectively. Ujiie et al. (2008) also suggested that stretching of fluid inclusions in calcite might indicate frictional heating associated with co-seismic slip. The present study shows that it is possible to identify distinctive fault rocks and fault structures which are characteristic of different parts of the seismic cycle. In order to do this, it is necessary to document geological evidence that constrains the likely fluctuations in fluid pressure that occur as well as the ways in which different parts of the overall fault network (e.g. low-angle fault core and high-angle footwall faults) may mutually interact through time. Ultimately this will lead to important advances in fault and earthquake mechanics, particularly along enigmatic structures such as low-angle normal faults.

Acknowledgements

S.A.F.S. is funded by a University of Durham Doctoral Fellowship. Fieldwork was supported by grants from The Geological Society of London, the American Association of Petroleum Geologists, the Geologists Association, the Mineralogical Society of Great Britain and Ireland, the Edinburgh Geological Society, and the John Ray Trust. Discussions with Nicola De Paola, and comments from Tom Blenkinsop, proved very helpful. Dougal Jerram provided useful advice on using ImageTool® software. Nick Oliver and an anonymous reviewer are thanked for helping us to clarify our arguments and significantly improve the quality of the manuscript. Tom Blenkinsop is also thanked for his editorial handling of the manuscript.

References

Agterberg, F.P., 1974. Geomathematics: Mathematical Background and Geoscience Applications. Elsevier, Amsterdam.

Anderson, E.M., 1942. The Dynamics of Faulting and Dyke Formation with Application to Britain. Oliver & Boyd, Edinburgh.

Axen, G.J., 2004. Mechanics of low-angle normal faults. In: Karner, G.D., Morris, J.D., Driscoll, N.W., Silver, E.A. (Eds.), Rheology and Deformation of the Lithosphere at Continental MarginsMARGINS Theoretical and Experimental Earth Science Series, Chapter 3. Columbia University Press, pp. 46–91.

Axen, G.J., 2007. Research focus: significance of large-displacement, low-angle normal faults. Geology 35, 287–288.

Baas, J.H., 2000. EZ-ROSE: a computer program for equal-area circular histograms and statistical analysis of two-dimensional vectorial data. Computers & Geosciences 26, 153–166.

Bagnold, R.A., 1954. Experiments on a gravity-free dispersion of large solid spheres in a Newtonian fluid under shear. Proceedings of the Royal Society London, Series A 225, 49–63.

Barchi, M.R., Minelli, G., Pialli, G., 1998. The CROP 03 profile: a synthesis of results on deep structures of the Northern Apennines. Memorie della Societa Geologica Italiana 52, 383–400.

Boncio, P., Brozetti, F., Ponziani, F., Barchi, R.M., Lavecchia, G., Pialli, G., 1998. Seismicity and extensional tectonics in the northern Umbria-Marches Apennines. Memorie della Societa Geologica Italiana 52, 539–555.

Boncio, P., Brozetti, F., Lavecchia, G., 2000. Architecture and seismotectonics of a regional low-angle normal fault in central Italy. Tectonics 19, 1038–1055.

Boorman, S.J., McGuire, J.B., Boudreau, A.E., Kruger, F.J., 2003. Fluid overpressure in layered intrusions: formation of a breccia pipe in the eastern Bushveld Complex, Republic of South Africa. Mineralium Deposita 38, 356–369.

Bortolotti, V., Fazzuoli, M., Pandeli, E., Principi, G., Babbini, A., Corti, S., 2001. Geology of central and Eastern Elba island, Italy. Ofioliti 26, 97–150.

Bos, B., Spiers, C.J., 2002. Frictional-viscous flow of phyllosilicate-bearing fault rock: microphysical model and implications for crustal strength profiles. Journal of Geophysical Research 107 (B), 2028, doi:10.1029/2001JB000301.

Brune, J.N., Brown, S., Johnson, P.A., 1993. Rupture mechanism and interface separation in foam rubber models of earthquakes: a possible solution to the heat flow paradox and the paradox of large overthrusts. In: Tectonophysics, 218 59–67.

Chiaraluce, L., Chiarabba, C., Collettini, C., Piccinini, D., Cocco, M., 2007. The architecture and mechanics of an active low angle normal fault: the Alto Tiberina Fault, northern Apennines, Italy. Journal of Geophysical Research 112, doi:10.1029/2007JB005015 B10310.

Chiodini, G., Cioni, R., 1989. Gas geobarometry for hydrothermal systems and its application to various Italian geothermal areas. Applied Geochemistry 4, 465–472.

Chiodini, G., Cardellini, C., Amato, A., Boschi, E., Caliro, S., Frondini, F., Ventura, G., 2004. Carbon dioxide Earth degassing and seismogenesis in central and southern Italy. Geophysical Research Letters 31, doi:10.1029/2004GL019480 L07615.

Cladouhos, T.T., 1999. Shape-preferred orientations of survivor grains in fault gouge. Journal of Structural Geology 21, 419–436.

Clark, C., James, P., 2003. Hydrothermal brecciation due to fluid pressure fluctuations: examples from the Olary Domain, South Australia. Tectonophysics 366, 187–206.

Collettini, C., Barchi, M.R., 2002. A low-angle normal fault in the Umbria region (central Italy): a mechanical model for the related microseismicity. Tectonophysics 359, 97–115.

Collettini, C., Holdsworth, R.E., 2004. Fault zone weakening processes along low-angle normal faults: insights from the Zuccale fault, Isle of Elba, Italy. Journal of the Geological Society 161, 1039–1051.

Collettini, C., Sibson, R.H., 2001. Normal faults, normal friction? Geology 29, 927–930.

Collettini, C., De Paola, N., Goulty, N.R., 2006a. Switches in the minimum compressive stress direction induced by overpressure beneath a low-permeability fault zone. Terra Nova 18, 224–231.

Collettini, C., De Paola, N., Holdsworth, R.E., Barchi, M.R., 2006b. The development and behavior of low-angle normal faults during Cenozoic asymmetric extension in the Northern Apennines, Italy. Journal of Structural Geology 28, 333–352.

Cowan, D.S., 1999. Do faults preserve a record of seismic slip? A field geologists opinion. Journal of Structural Geology 21, 995–1001.

Cox, S.F., 1995. Faulting processes at high fluid pressures: an example of fault-valve behavior from the Wattle Gully Fault, Victoria, Australia. Journal of Geophysical Research 100, 12841–12859.

Davis, J.C., 2002. Statistics and Data Analysis in Geology, third ed. John Wiley & Sons.

Dini, A., Innocenti, F., Rocchi, S., Tonarini, S., Westerman, D.S., 2002. The magmatic evolution of the late Miocene laccolith-pluton-dyke granitic complex of Elba Island, Italy. Geological Magazine 139, 257–279.

Elter, P., Giglia, G., Tongiorgi, M., Trevisan, L., 1975. Tensional and contractional areas in recent Tortonian to present evolution of the Northern Apennines. Bollettino di Geofisica Teorica ed Applicata 17, 1975.

Eichhubl, P., Boles, J.R., 2000. Rates of fluid flow in fault systems – evidence for episodic rapid fluid flow in the Miocene Monterey Formation, coastal California. American Journal of Science 300, 571–600.

Famin, V., Hebert, R., Philippot, P., Jolivet, L., 2005. Ion probe and fluid inclusion evidence for co-seismic fluid infiltration in a crustal detachment. Contributions to Mineralogy and Petrology 150, 354–367.

Faulkner, D.R., Rutter, E.H., 1998. The gas permeability of clay-bearing fault gouge at 20 °C. In: Jones, G., Fisher, Q.J., Knipe, R.J. (Eds.), Faulting, Fault Sealing and Fluid Flow in Hydrocarbon Reservoirs. Special Publications, vol. 147. Geological Society, London, pp. 147–156.

Faulkner, D.R., Rutter, E.H., 2000. Comparisons of water and argon permeability in natural clay-bearing fault gouge under high-pressure at 20 °C. Journal of Geophysical Research 105 (B7), 16415–16426.

Gagnevin, D., Daly, J.S., Poli, G., 2004. Petrographic, geochemical and isotopic constraints on magma dynamics and mixing in the Miocene Monte Capanne monzogranite (Elba Island, Italy). Lithos 78, 157–195.

Gratier, J.P., Gueydan, F., 2007. Deformation in the presence of fluids and mineral reactions: effects of fracturing and fluid-rock interaction on seismic cycles. In: Handy, M.R., Hirth, G., Hovius, N. (Eds.), Tectonic Faults: Agents of Change on a Dynamic Earth, Dahlem Workshop Reports. The MIT Press, pp. 319–356.

Han, R., Shimamoto, T., Ando, J., Ree, J.H., 2007a. Seismic slip record in carbonate-bearing fault zones: an insight from high-velocity friction experiments on siderite gouge. Geology 35, 1131–1134.

Han, R., Shimamoto, T., Hirose, T., Ree, J.H., Ando, J., 2007b. Ultralow friction of carbonate faults caused by thermal decomposition. Science 316, 878–881.

Hayman, N.W., Housen, B.A., Cladouhos, T.T., Livi, K., 2004. Magnetic and clast fabrics as measurements of grain-scale processes within the Death Valley shallow crustal detachment faults. Journal of Geophysical Research 109, doi:10.1029/2003JB002902 B05409.

Henderson, I.H.C., McCaig, A.M., 1996. Fluid pressure and salinity variations in shear zone related veins, central Pyrenees, France: implications for the fault-valve model. Tectonophysics 262, 321–348.

Hickman, S., Sibson, R.H., Bruhn, R., 1995. Introduction to special section: Mechanical involvement of fluids in faulting. Journal of Geophysical Research 100, 12831–12840.

Jackson, J.A., White, N.J., 1989. Normal faulting in the upper continental crust: observations from regions of active extension. Journal of Structural Geology 11, 15–36.

Jolivet, L., Faccannena, C., Goffe, B., Mattei, M., Rossetti, F., Brunet, C., Storti, F., Funicielallo, R., Cadet, J.P., D'Agostino, N., Parra, T., 1998. Midcrustal shear zones in postorogenic extension: examples from the northern Tyrrhenian Sea. Journal of Geophysical Research 103, 12123–12160.

Keller, J.V.A., Pialli, G., 1990. Tectonics of the island of Elba: a reappraisal. Bollettino della Societa Geologica Italiana 109, 413–425.

Keller, J.V.A., Coward, M.P., 1996. The structure and evolution of the northern Tyrrhenian Sea. Geological Magazine 133, 1–16.

Le Guen, Y., Renard, F., Hellmann, R., Brosse, E., Collombet, M., Tisserand, D., Gratier, J.P., 2007. Enhanced deformation of limestone and sandstone in the presence of high PCO_2 fluids. Journal of Geophysical Research 112, doi:10.1029/2006JB004637.

Maineri, C., Benvenuti, M., Costaglioli, P., Dini, A., Lattanzi, P., Ruggieri, G., Villa, I.M., 2003. Sericitic alteration at the La Crocceta deposit (Elba Island, Italy): interplay between magmatism, tectonics and hydrothermal activity. Mineralium Deposita 38, 67–86.

Miller, S.A., Collettini, C., Chiaraluce, L., Cocco, M., Barchi, M.R., Kaus, B., 2004. Aftershocks driven by a high pressure CO_2 source at depth. Nature 427, 724–727.

Minissale, A., 2004. Origin, transport and discharge of CO_2 in central Italy. Earth-Science Reviews 66, 89–141.

Minissale, A., Magro, G., Martinelli, G., Vaselli, O., Tassi, G.F., 2000. Fluid geochemical transect in the Northern Apennines (central-northern Italy): fluid genesis and migration and tectonic implications. Tectonophysics 319, 199–222.

Montone, P., Mariucci, M.T., Pondrelli, S., Amato, A., 2004. An improved stress map for Italy and surrounding regions (central Mediterranean). Journal of Geophysical Research 109, doi:10.1029/2003JB002703 B10410.

Monzawa, N., Otsuki, K., 2003. Comminution and fluidization of granular fault materials: implications for fault slip behaviour. Tectonophysics 367, 127–143.

Mort, K., Woodcock, N.H., 2008. Quantifying fault breccia geometry: Dent Fault, NW England. Journal of Structural Geology, doi:10.1016/j.jsg.2008.02.005.

Nguyen, P.T., Cox, S.F., Harris, L.B., Powell, C.M., 1998. Fault-valve behavior in optimally oriented shear zones: an example at Revenge gold mine, Kambalda, Western Australia. Journal of Structural Geology 20, 1625–1640.

Nostro, C., Cocco, M., Belardinelli, M.E., 1997. Static stress changes in extensional regimes: an application to southern Apennines (Italy). Bulletin of the Seismological Society of America 87, 234–248.

Numelin, T., Marone, C., Kirby, E., 2007. Frictional properties of natural fault gouge from a low-angle normal fault, Panamint Valley, California. Tectonics 26, doi:10.1029/2005TC001916 TC2004.

Oliver, N.H.S., 1996. Review and classification of structural controls on fluid flow during regional metamorphism. Journal of Metamorphic Geology 14, 477–492.

Oliver, N.H.S., Rubenach, M.J., Fu, B., Baker, T., Blenkinsop, T.G., Cleverley, J.S., Marshall, L.J., Ridd, P.J., 2006. Granite-related overpressure and volatile release in the mid-crust: fluidized breccias from the Cloncurry district, Australia. Geofluids 6, 346–358.

Otsuki, K., Monzawa, N., Nagase, T., 2003. Fluidization and melting of fault gouge during seismic slip: identification in the Nojima fault zone and implications for focal earthquake mechanisms. Journal of Geophysical Research 108 (B4), doi:10.1029/2001JB001711 2192.

Parry, W.T., Bruhn, R.L., 1990. Fluid pressure transients on seismogenic normal faults. Tectonophysics 179, 335–344.

Pascucci, V., Merlini, S., Martini, I.P., 1999. Seismic stratigraphy in the Miocene-Pleistocene sedimentary basins of the Northern Tyrrhenian Sea and western Tuscany (Italy). Basin Research 11, 337–356.

Pauselli, C., Federico, C., 2002. The brittle/ductile transition along the CROP03 seismic profile: relationship with the geological features. Bollettino della Societa Geologica Italiana 1, 25–35.

Pauselli, C., Barchi, M.R., Federico, C., Magnani, M.B., Minelli, G., 2006. The crustal structure of the northern Apennines (Central Italy): an insight by the CROP03 seismic line. American Journal of Science 306, 428–450.

Person, M., Baumgartner, L.P., Bos, B., Connolly, J.A.D., Gratier, J.P., Gueydan, F., Miller, S.A., Rosenberg, C.L., Urai, J.L., Yardley, B., 2007. Group report: Fluids, geochemical cycles, and mass transport in fault zones. In: Handy, M.R., Hirth, G., Hovius, N. (Eds.), Tectonic Faults: Agents of Change on a Dynamic Earth. The MIT Press, pp. 403–425. Dahlem Workshop Reports.

Reynolds, S.J., Lister, G.S., 1987. Structural aspects of fluid–rock interactions in detachment zones. Geology 15, 362–366.

Rossetti, F., Tecce, F., Billi, A., Brilli, M., 2007. Patterns of fluid flow in the contact aureole of the Late Miocene Monte Capanne pluton (Elba Island, Italy): the role of structures and rheology. Contributions to Mineralogy and Petrology 153, 743–760.

Rowe, C.D., Moore, J.C., Meneghini, F., McKeirnan, A.W., 2005. Large-scale pseudotachylytes and fluidized cataclasites from an ancient subduction thrust fault. Geology 33, 937–940.

Sheldon, H.A., Ord, A., 2005. Evolution of porosity, permeability and fluid pressure in dilatant faults post-failure: implications for fluid flow and mineralization. Geofluids 5, 272–288.

Sibson, R.H., 1989. Earthquake faulting as a structural process. Journal of Structural Geology 11, 1–14.

Sibson, R.H., 1990. Conditions for fault-valve behavior. In: Knipe, R.J., Rutter, E.H. (Eds.), Deformation Mechanisms, Rheology and Tectonics. Special Publications, vol. 54. Geological Society, London, pp. 15–28.

Sibson, R.H., 1992. Implications of fault-valve behavior for rupture nucleation and recurrence. Tectonophysics 18, 1031–1042.

Sibson, R.H., 2000. Fluid involvement in normal faulting. Journal of Geodynamics 29, 469–499.

Sibson, R.H., 2007. An episode of fault-valve behavior during compressional inversion? The 2004 M(J)6.8 Mid-Niigata Prefecture, Japan, earthquake sequence. Earth and Planetary Science Letters 257, 188–199.

Smith, S.A.F., Holdsworth, R.E., Collettini, C., Imber, J., 2007. Using footwall structures to constrain the evolution of low-angle normal faults. Journal of the Geological Society London 164, 1187–1191.

Taylor, H.P., Turi, B., 1979. High-^{18}O igneous rocks from the Tuscan magmatic province, Italy. Contributions to Mineralogy and Petrology 55, 33–54.

Tenthorey, E., Cox, S.F., 2006. Cohesive strengthening of fault zones during the interseismic period: an experimental study. Journal of Geophysical Research, Solid Earth 111 (B9) B09202.

Trevisan, L., Marinelli, G., Barberi, F., Giglia, G., Innocenti, F., Raggi, G., Squarci, P., Taffi, L., Ricci, C.A., 1967. Carta Geologica dell'Isola d'Elba. Scala 1:25.000. Consiglio Nazionale delle Ricerche, Gruppo di Ricerca per la Geologia dell'Appennino centro-settentrionale e della Toscana. Pisa, Italy.

Ujiie, K., Yamaguchi, A., Kimura, G., Toh, S., 2007. Fluidization of granular material in a subduction thrust at seismogenic depths. Earth and Planetary Science Letters 259, 307–318.

Ujiie, K., Yamaguchi, A., Taguchi, S., 2008. Stretching of fluid inclusions in calcite as an indicator of frictional heating on faults. Geology 36, 111–114.

Wernicke, B., 1995. Low-angle normal faults and seismicity: a review. Journal of Geophysical Research 100, 20159–20174.

Appendix III – Geological map and cross section of the footwall of the Zuccale fault at Spiagge Nere

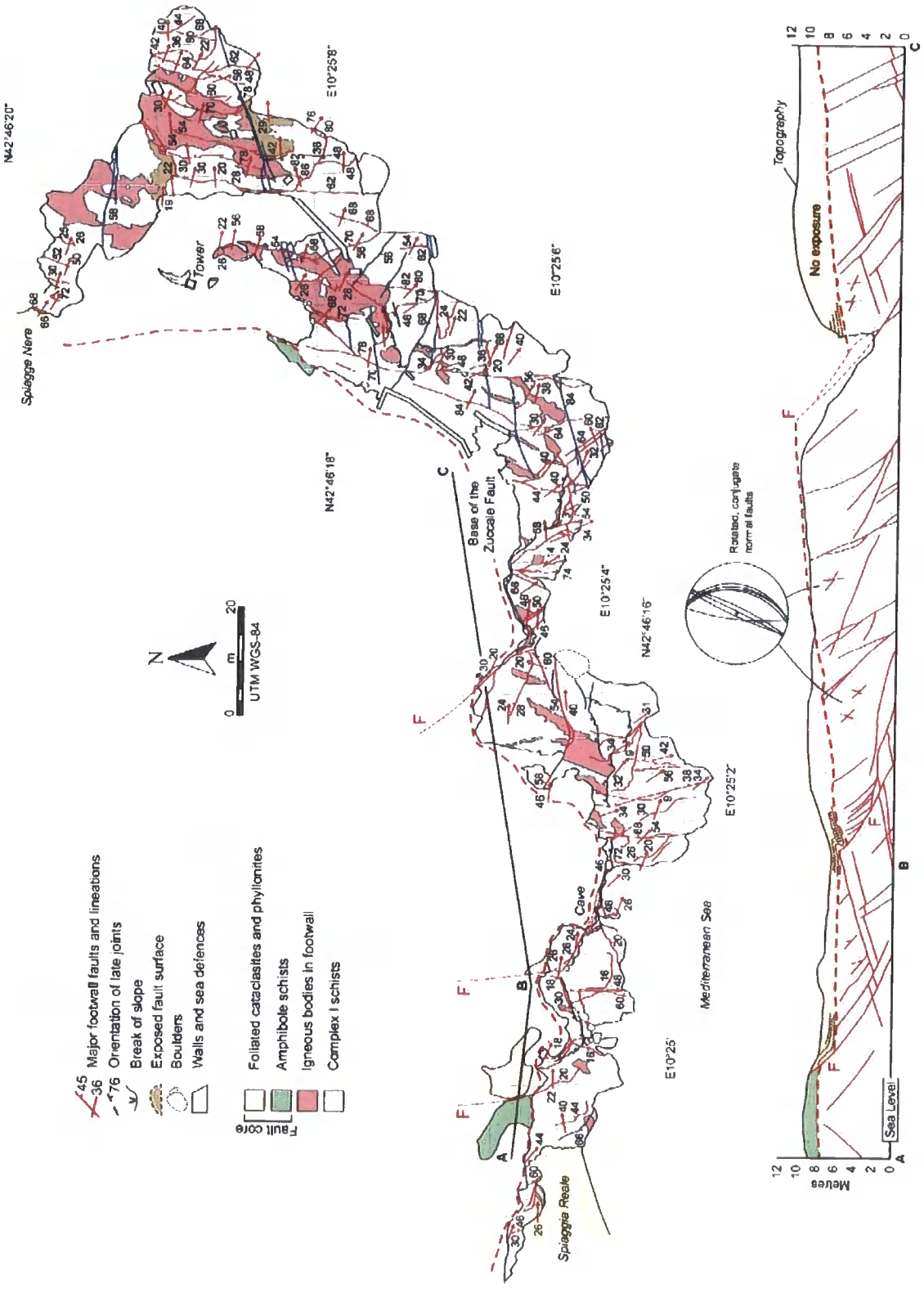

Detailed geological map and cross section to illustrate faulting patterns in the immediate footwall of the Zuccale fault between Spiaggia Reale and Spiagge Nere. The location of this outcrop is shown in Figure 4.2b. Also shown on the map is the basal trace of the Zuccale fault, and the distribution of fault rocks within the central core of the Zuccale fault. Footwall faults and later exhumation joints are hosted in Complex I quartz-mica schists, which are intruded by a network of igneous dykes and sills related to the Porto Azzurro pluton (not shown on the cross section). The density of footwall faulting in this area is high: magnitudes of extension locally exceed 60% over distances of 25 metres or less. The cross section highlights the presence of sub-horizontal and east-dipping footwall faults discussed in the text of Chapter 4. In this area, some of the larger east-dipping faults displace the lower margin of the fault core, resulting in 'back-rotation' of the fault core and footwall in to a series of shallowly west-dipping segments. The stereonet shows the orientation of minor conjugate pairs of normal faults which suggest values of back-rotation of around 15-20°.

Appendix IV

Paper submitted to *Geology* in November 2008

The development of interconnected talc networks and weakening of continental low-angle normal faults

Cristiano Collettini[1], Cecilia Viti[2], Steven A.F. Smith[3] & Robert E. Holdsworth[3]

[1]*Geologia Strutturale e Geofisica, Dipartimento di Scienze della Terra Università degli Studi di Perugia,Italy.*
[2]*Dipartimento di Scienze della Terra Università degli Studi di Siena, Italy.*
[3]*Reactivation Research Group, Department of Earth Sciences, University of Durham, Durham, DH1 3LE, U.K.*

Abstract

Fault zones which slip when oriented at high angles to the maximum compressive stress, i.e. weak faults, represent a significant mechanical problem. Here we document fault weakening induced by dissolution of dolomite and subsequent precipitation of calcite + abundant talc along a low-angle normal fault. Within the fault core, talc forms an interconnected foliated network that deforms by frictional sliding along 50-200 nm thick talc lamellae. The frictional properties of talc can explain both slip on low-angle normal faults and the absence of strong earthquakes along these structures. Given the relative abundance of carbonates in the upper continental crust the formation of talc along fault zones may be widespread, leading to profound and long-term fault weakness.

Introduction

Why and in which way do some faults move when theory predicts that they should be inactive? Slip on unfavourably oriented faults with respect to a remotely applied stress implies that faults such as the San Andreas fault [*Zoback et al.*, 1987] and low-angle normal faults, LANF, [*Holdsworth*, 2004, *Numelin et al.*, 2007] are weak when compared to laboratory-measured frictional strength [*Byerlee*, 1978]. The recent discovery of the mineral talc in borehole cuttings from ~3km depth along the San Andreas fault has been invoked to explain the apparent weakness of this structure [*Moore and Rymer*, 2007]. However, the relatively minor amounts of talc found here and along other weak faults like oceanic detachments [*Escartin et al.*, 2003, *Boschi et al.*, 2006b] has led to doubts concerning whether talc can widely influence crustal fault mechanics.

In a stretching crust where the maximum compressive stress trajectories are typically subvertical, the standard friction coefficient values determined for faults in the laboratory, $0.6<\mu_s<0.85$ [*Byerlee*, 1978], predict that normal faults should cease to slip at dips of 30°-40° [*Sibson*, 1985]. This mechanical prediction is consistent with the absence of moderate-to-large seismic ruptures on continental LANF [*Jackson and White*, 1989, *Collettini and Sibson*, 2001]. In marked contrast, widespread geological data [*Hayman et al.*, 2003, *Axen*, 2004] and seismic reflection profiles [*Wernicke*, 1995, *Floyd et al.*, 2001] show that LANF have accommodated significant regional displacements. Furthermore, in some cases, slip on LANF may occur by some combination of microseismicity and aseismic creep [*Rigo et*

al., 1996, *Boncio et al.*, 2000, *Chiaraluce et al.*, 2007]. For frictional sliding under upper crustal conditions, one of the few minerals capable of absolute fault weakening is talc, which has a friction coefficient between ~0.05-0.23, depending on the temperature, pressure, fluid conditions and applied strain rate [*Escartin et al.*, 2008, *Moore and Lockner*, 2008]. In this paper we document the development of a large amount of talc along a continental LANF, and discuss the implications that this has for the mechanics of such structures.

Tectonic setting

In the Northern Apennines of Italy, the CROP03 seismic reflection profile has shown that a significant amount of extension in the upper crust is accommodated by a set of LANF [*Barchi et al.*, 1998, *Boncio et al.*, 2000] with the locus of extension migrating with time from west to east (Fig. 1). In the actively extending area, a LANF (the Altotiberina Fault) is characterized by microseismicity between 4-16 km depth in a regional stress field with a vertical maximum compressive stress [*Boncio et al.*, 2000, *Chiaraluce et al.*, 2007]. To understand the mechanisms which allow slip to occur along such faults at depth, we have studied the Zuccale fault, an ancient exhumed LANF belonging to the same regional fault system exposed on the Isle of Elba, Italy (Fig. 1). Fault rocks presently exposed at the surface preserve evidence for deformation processes which occurred at <8 km depth, with a total fault offset in the range of 6-8 km [*Keller and Coward*, 1996, *Collettini and Holdsworth*, 2004]. Geological data demonstrate that the fault accommodated extension as a gently dipping structure [*Collettini and Holdsworth*, 2004, *Smith et al.*, 2007]. The fault zone is characterized by an intensely foliated and lithologically heterogeneous fault core several meters thick. The adjacent hangingwall and footwall rocks deformed predominantly by brittle cataclastic processes. Within the fault core a significant amount of extension was accommodated within a carbonate- and phyllosilicate-rich basal horizon up to 5 m thick [*Collettini and Holdsworth*, 2004]. These rocks formed in the early stages of fault activity [*Smith et al.*, 2007] and were derived from a protolith sequence dominated by carbonates (Complexes II-IV, Fig. 1B).

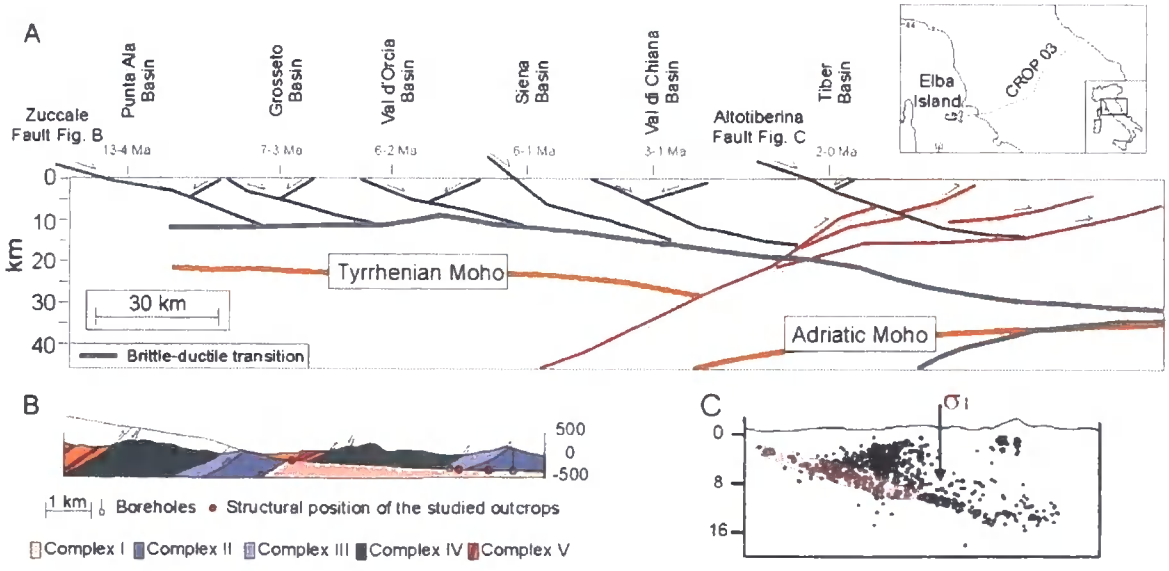

Figure 1) Low-angle normal faults and crustal extension in the Northern Apennines. A, Schematic representation of the CROP03 deep seismic reflection profile [*Barchi et al.*, 1998] showing the

east-dipping low-angle normal faults of the Northern Apennines . Extension migrated with time from west to east as documented by the age of the syn-tectonic basins bounded by the normal faults [*Collettini et al.*, 2006b]. Therefore, the ancient structures exposed at the surface and the seismicity recorded along active faults represent complementary datasets that provide insights of the same deformation processes. B, Geological cross section through central and eastern Elba showing the geometry of the Zuccale fault [*Collettini and Holdsworth*, 2004]. Complex I: Palaeozoic basement schists; Complex II: Tuscan metamorphic sequence; Complex III: Tuscan limestone sequence; Complex IV: Ligurian ophiolite sequence; Complex V: Cretaceous foredeep deposits. Dolostones are present at the base of the sedimentary sequences in Complexes II and III and at the top of the basement of Complex I. C, In the area of currently active extension, the Altotiberina fault is characterized by microseismicity (about 3 events per day with ML<2.3). Inversion of focal mechanisms suggests a stress field characterized by vertical maximum compressive stress trajectories [*Chiaraluce et al.*, 2007]. The pink area schematically represents where dolostone rocks have been documented in the hanging-wall and/or footwall of the fault trace from boreholes and the interpretation of seismic reflection profiles [*Collettini et al.*, 2006b].

Talc development along the Zuccale Fault

Textural relationships and microstructures from the basal foliated horizon have been studied using optical microscopy, supplemented by use of X-Ray Diffraction, XRD, Scanning Electron Microscopy, SEM (back-scattered electron images, BSE), and Transmission Electron Microscopy, TEM, equipped with X-ray energy dispersive spectrometry, EDS.

In the less deformed regions of the basal foliated horizon (Fig. 2), the protolith is preserved and it is composed of a fine-grained, 100-200 μm, dolostone. The dolostone is extensively fractured, and calcite replaces dolomite grains along grain boundaries and intragranular fractures (1 in Fig. 2B). Wide fractures are filled by syn-tectonic calcite and talc lamellae, 50-200 nm thick (2 in Fig. 2B). Quartz is also present in small veins or along calcite grain boundaries (3 in Fig. 2B). The boundaries between dolomite and calcite grains are sharp, but irregular and lobate in shape (4 in Fig. 2B). TEM images show that dolomite contains numerous stress-induced dislocations, whilst calcite is dislocation free (4 in Fig. 2b). Electron diffraction and TEM/EDS show that adjacent dolomite and calcite have unrelated crystallographic orientations and sharp chemical boundaries. Collectively, these microstructural observations suggest fracturing and fluid circulation, followed by stress-induced dissolution of the dolomite and precipitation of calcite and talc in the presence of silica-rich fluids. The calcite and talc forming reaction is:

$$3\ MgCa(CO_3)_2 + 4\ SiO_2 + H_2O = Mg_3Si_4O_{10}(OH)_2 + 3\ CaCO_3 + 3\ CO_2$$
dolomite silica talc calcite

The silica-rich fluids were most likely related to widespread granitic magmatism that occurred broadly contemporaneously with movements along the Zuccale fault [*Dini et al.*, 2002]. In highly deformed regions (Fig. 2C), which dominate the basal foliated horizon, calcite occurs as dispersed elongate sigmoids, surrounded by a foliated matrix of strongly aligned talc lamellae (1 in Fig 2c), 1-2 μm in length. The calcite sigmoids are truncated against the surrounding talc matrix (2 in Fig. 2c). Talc is the main phase in the foliated matrix, but it also develops within calcite sigmoids, at grain boundaries, along intragranular fractures, and in numerous strain shadows (3 in Fig. 2c). Talc formation is also contemporaneous with the development of foliation-parallel calcite veins characterized by crack-and-seal textures, demonstrating that cyclic build-ups in fluid

pressure occurred during fault activity. Collectively, these observations suggest that fluid-assisted dissolution and precipitation of carbonates, and authigenic growth of talc, was both syn-tectonic and continuous throughout the history of these particular fault rocks. Ultimately, these processes resulted in the development of a talc-rich foliation, which forms an interconnected framework in high-strain domains (e.g. 1 Fig. 2c). TEM images and electron diffraction patterns indicate that talc lamellae, up to 200 nm thick, are aligned parallel to the foliation (4 in Fig. 2c) and are affected by stacking disorders, with translation and rotation of the (001) talc layers. Interlayer delaminations are common, resulting in talc grain size reduction, down to 50 nm in thickness, and providing an infinite number of possible sliding surfaces. Kinking and layer bending of talc are rare.

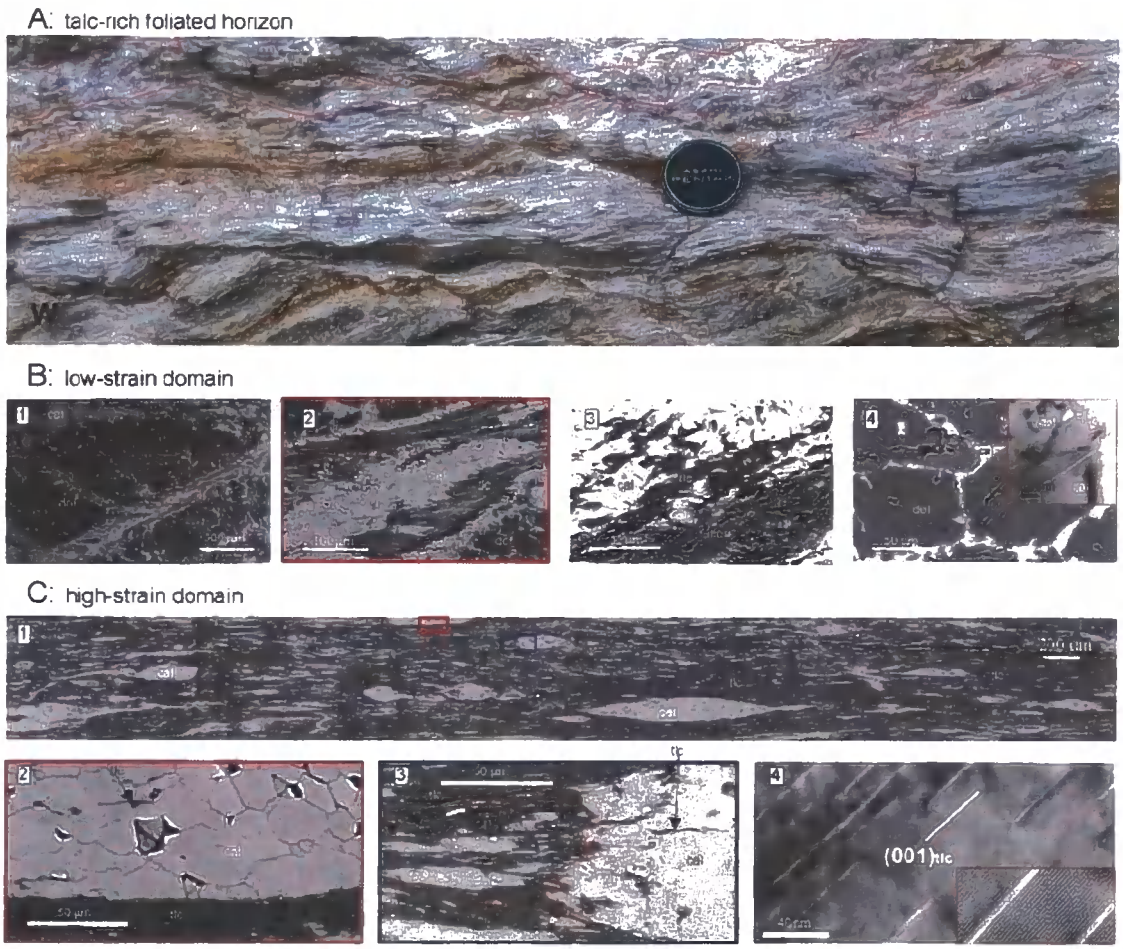

Figure 2) Talc development along the Zuccale fault. A, Outcrop photograph of the basal foliated horizon. Red lines highlight the low-strain domains surrounded by strongly foliated high-strain domains. B, Fault rocks in the low-strain domains. SEM/BSE image (1) of fractured dolomite (dol) with calcite (cal) development at grain boundaries and along fractures. Close-up image (2) of a syntectonic vein filled with calcite and talc (tlc). SEM/BSE image (3) showing silica deposition along a fracture surrounded by talc and calcite. SEM/BSE image (4) of the sharp boundaries between dolomite and calcite. TEM detail (inset) shows highly strained dolomite, closely associated with dislocation-free calcite; TEM/EDS and electron diffraction (not shown here) indicate that the boundary between the two carbonates is chemically sharp and lacks any crystallographic continuity. C, Fault rocks in the high-strain domains. SEM/BSE image (1) of the foliated microstructure comprising calcite sigmoids, enclosed within a talc-rich interconnected network; the red and blue boxes show the location of images (2) and (3) respectively. (2) Sharp

boundary between calcite sigmoid and talc-rich foliation, with truncated calcite crystals, suggesting fluid-assisted dissolution-precipitation processes. (3) Talc occurs along sigmoid strain shadows (outlined in red), grain boundaries and intragrain fractures. TEM image (4) of talc (001) lamellae, oriented parallel to foliation. Talc lamellae are affected by stacking disorders (with rotation and translation of talc layers) and by frequent interlayer delaminations. The inset shows the 9 Å-spaced (001) lattice fringes of talc, with an interlayer delamination.

Discussion

The abundance of talc and its development as an interconnected network, taken together with the TEM nanotextural evidence, suggest that deformation in the Zuccale fault core was accommodated by frictional slip along talc (001) planes. In such a fault zone, the low friction coefficient of talc means that in an extending crust characterized by vertical maximum stress trajectories, frictional sliding can occur on normal faults dipping close to zero degrees (Fig. 3). Moderate-to-large earthquakes on talc-bearing LANF would not be expected to occur, because the velocity strengthening behavior of talc [*Moore and Lockner*, 2008] favors stable sliding and fault creep. However it is worth noting that even within faults with very low-friction coefficients, reactivation close to the frictional lock-up angle requires some fluid overpressure (Fig. 3).

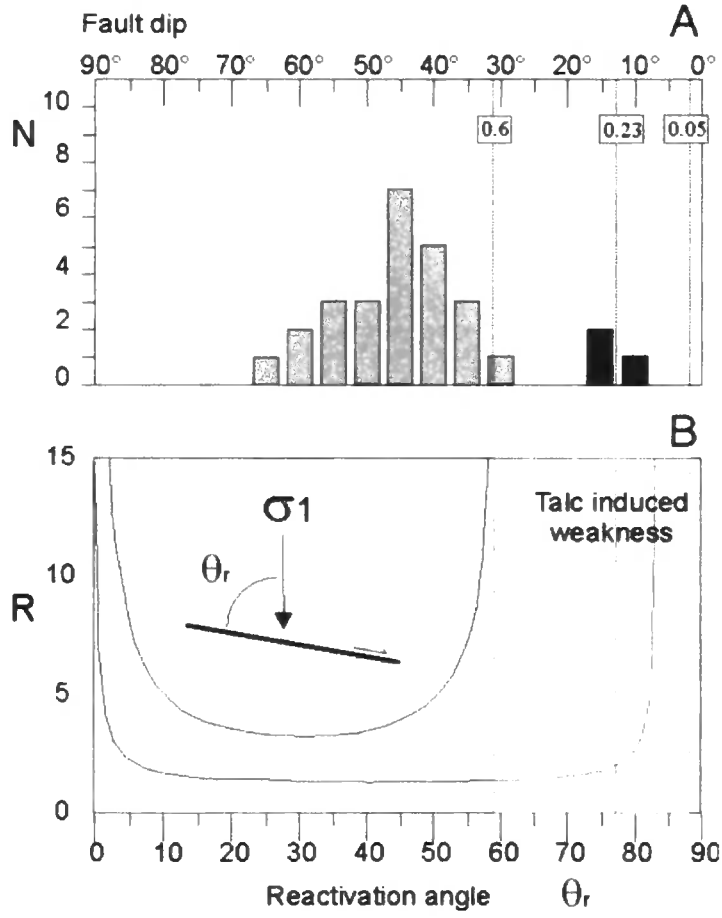

Figure 3) Implications of talc for the mechanics of low-angle normal faults. A, Dip distribution of unambiguously identified normal fault ruptures, M>5.5 (grey bins), plotted in terms of reactivation angle, θr, as inferred for a vertical maximum compressive stress [*Collettini and Sibson*, 2001]. The peak at 45° could be the result of normal faults formed at 45° in the ductile crust and then exhumed

in the brittle field, and/or domino rotation during extension and/or extensional reactivation of inherited reverse faults. Average dip (black bins) of the Zuccale fault (15°), the Altotiberina fault (15°) and the Radicofani fault (10°). These faults are part of the Northern Apennines LANF system they cut Mg-rich carbonates within the upper crust. B, Conditions for frictional fault reactivation. For the two dimensional case, where an existing cohesionless fault containing the intermediate principal stress axis lies at a reactivation angle θ_r to the maximum compressive stress, Amonton's law, $\tau=\mu_s\sigma'_n$, may be written in terms of effective principal stresses as:

$$R = \frac{\sigma'1}{\sigma'3} = \frac{(\sigma1 - Pf)}{(\sigma3 - Pf)} = \left(\frac{1 + \mu s \cot \theta r}{1 - \mu s \tan \theta r}\right)$$

where σ'_n is the effective normal stress, σ_1 and σ_3 are the maximum and minimum principal stresses, P_f is the pore fluid pressure and μ_s is the friction coefficient [*Sibson*, 1985]. Frictional lock-up occurs when the function goes to infinity. In extensional environments, under the assumptions of vertical principal stress trajectories, the absence of moderate-to-large earthquakes on low-angle normal faults is consistent with frictional lock-up for μ_s~0.6, at the bottom of the Byerlee range [*Collettini and Sibson*, 2001]. By using the coefficient of friction for talc, $0.05<\mu_s<0.23$ [*Moore and Lockner*, 2008], the lock-up angle expands to the range, $78°<\theta_r<87°$, and reactivation can occur on normal faults dipping even close to zero degrees.

The Zuccale fault belongs to a regionally recognized suite of LANF developed across the northern Apennines of Italy (Fig. 1) that cut extensive magnesium-rich carbonate sequences of Mesozoic age [*Collettini et al.*, 2006b]. The development of talc by a process such as that documented in the Zuccale fault provides a plausible explanation for the creeping behavior of the currently active Altotiberina fault [*Chiaraluce et al.*, 2007] since dolostones are widespread in the hangingwall of the fault down to 8-10 km depth. Like the northern Apennines, many other documented LANF [*Manatschal and Bernoulli*, 1999] are developed in pre-existing fold and thrust belts formed in shallow marine passive margin sequences dominated by carbonates.

The talc-forming processes proposed here may be applicable to other types of faults (thrusts, strike-slip faults) cutting carbonate sequences within many areas of the upper continental crust. This process should be particularly effective in areas characterized by low-strain rates [*Niemeijer and Spiers*, 2005], where chemical dissolution of Mg-rich carbonates would be more efficient, and at the relatively shallow depths of 4-8 km, where other temperature-activated weakening processes are less likely to occur, [e.g. *Wibberley*, 2007]. Following fracturing and fluid rock interaction, the development of an interconnected phyllosilicate-rich network, like that documented along the Zuccale fault, is a weakening mechanism that may be active along many faults within the upper crust.

References

Abers, G. A. (1991), Possible seismogenic shallow-dipping normal faults in the Woodlark-D'Entrecasteaux extensional province, Papua New Guinea, *Geology*, *19*, 1205-1208.

Acocella, V. (2000), Space accommodation by roof lifting during pluton emplacement at Amiata (Italy), *Terra Nova*(12), 149-155.

Acocella, V. and F. Rossetti (2002), The role of extensional tectonics at different crustal levels on granite ascent and emplacement: an example from Tuscany (Italy), *Tectonophysics*, *354*(1-2), 71-83.

Agosta, F., M. Prasad and A. Aydin (2007), Physical properties of carbonate fault rocks, fucino basin (Central Italy): implications for fault seal in platform carbonates, *Geofluids*, *7*(1), 19-32.

Agterberg, F. P. (1974), *Geomathematics: Mathematical background and geoscience applications*, Elsevier.

Allard, P., P. Jean-Baptiste, P. D'Alessandro, F. Parello, B. Parisi and C. Flehoc (1997), Mantle-derived helium and carbon in groundwaters and gases of Mount Etna, Italy, *Earth and Planetary Science Letters*, *148*, 501-516.

Alvarez, W. (1972), Rotation of Corsica-Sardinia Microplate, *Nature*, *235*(58), 103-105.

Anders, M. H., N. Christie-Blick and C. D. Walker (2006), Distinguishing between rooted and rootless detachments: A case study from the Mormon Mountains of southeastern Nevada, *Journal of Geology*, *114*(6), 645-664.

Anderson, E. M. (1942), *The dynamics of faulting and dyke formation with application to Britain*, Oliver & Boyd, Edinburgh.

Anderson, R. E. (1971), Thin Skin Distension in Tertiary Rocks of Southeastern Nevada, *Geological Society of America Bulletin*, *82*(1), 43-58.

Andreani, M., A. M. Boullier and J. P. Gratier (2005), Development of schistosity by dissolution-crystallization in a Californian serpentinite gouge, *Journal of Structural Geology*, *27*(12), 2256-2267.

Axen, G. J. (1988), The Geometry of Planar Domino-Style Normal Faults above a Dipping Basal Detachment, *Journal of Structural Geology*, *10*(4), 405-411.

Axen, G. J. (1992), Pore Pressure, Stress Increase, and Fault Weakening in Low-Angle Normal Faulting, *Journal of Geophysical Research-Solid Earth*, *97*(B6), 8979-8991.

Axen, G. J. and J. M. Bartley (1997), Field tests of rolling hinges: Existence, mechanical types, and implications for extensional tectonics, *Journal of Geophysical Research-Solid Earth*, *102*(B9), 20515-20537.

Axen, G. J. (1999), Low-angle normal fault earthquakes and triggering, *Geophysical Research Letters*, *26*(24), 3693-3696.

Axen, G. J. (2004), Mechanics of Low-Angle Normal Faults, *Rheology and Deformation of the Lithosphere at Continental Margins, MARGINS theoretical and Experimental Earth Sceince Series*, 46-91.

Axen, G. J. (2007), Research Focus: Significance of large-displacement, low-angle normal faults, *Geology*, *35*(3), 287-288.

Baas, J. H. (2000), EZ-ROSE: a computer program for equal-area circular histograms and statistical analysis of two-dimensional vectorial data, *Computers & Geosciences*, *26*, 153-166.

Bagnold, R. A. (1954), Experiments on a gravity-free dispersion of large solid spheres in a Newtonian fluid under shear, *Proc. R. Soc. London, Ser. A.*, *225*, 49-63.

Barchi, M. R., R. Minelli and G. Pialli (1998), The CROP 03 profile: A synthesis of results on deep structures of the northern Apennines, *Mem. Soc. Geol. It.*, *52*, 383-400.

Barnhoorn, A., M. Bystricky, L. Burlini and K. Kunze (2004), The role of recrystallisation on the deformation behaviour of calcite rocks: large strain torsion experiments on Carrara marble, *Journal of Structural Geology*, *26*(5), 885-903.

Beeler, N. M., T. E. Tullis, M. L. Blanpied and J. D. Weeks (1996), Frictional behaviour of large displacement experimental faults, *Journal of Geophysical Research*, *101*(B4), 8697-8715.

Bestmann, M., K. Kunze and A. Matthews (2000), Evolution of a calcite marble shear zone complex on Thassos Island, Greece: microstructural and textural fabrics and their kinematic significance, *Journal of Structural Geology*, *22*, 1789-1807.

Bestmann, M. and D. J. Prior (2003), Intragranular dynamic recrystallisation in naturally deformed calcite marble: diffusion accommodated grain boundary sliding as a result of subgrain rotation recrystallisation, *Journal of Structural Geology*, *25*, 1597-1613.

Blanpied, M. L., D. A. Lockner and J. D. Byerlee (1995), Frictional slip of granite at hydrothermal conditions, *Journal of Geophysical Research*, *100*, 13045-13064.

Blenkinsop, T. G. and E. H. Rutter (1986), Cataclastic deformation of quartzite in the Moine thrust zone, *Journal of Structural Geology*, *8*(6), 669-681.

Boncio, P., F. Brozetti, F. Ponziani, R. M. Barchi, G. Lavecchia and G. Pialli (1998), Seismicity and extensional tectonics in the northern Umbria-Marches Apennines, *Mem. Soc. Geol. Ital.*, *52*, 539-555.

Boncio, P., F. Brozetti and G. Lavecchia (2000), Architecture and seismotectonics of a regional low-angle normal fault in central Italy, *Tectonics*, *19*, 1038-1055.

Boorman, S. L., J. B. McGuire, A. E. Boudreau and F. J. Kruger (2003), Fluid overpressure in layered intrusions: formation of a breccia pipe in the Eastern Bushveld Complex, Republic of South Africa, *Mineralium Deposita*, *38*(3), 356-369.

Bortolotti, V., M. Fazzuoli, E. Pandeli, G. Principi, A. Babbini and S. Corti (2001a), Geology of Central and Eastern Elba Island, Italy, *Ofioliti*, *26* ((2a)), 97-150.

Bortolotti, V., E. Pandeli and G. Principi (2001b), The geology of the Elba Island: An historical introduction, *Ofioliti*, *26* (2a), 79-96.

Bos, B. and C. J. Spiers (2000), Effect of phyllosilicates on fluid-assisted healing of gouge-bearing faults, *Earth and Planetary Science Letters*, *184*(1), 199-210.

Bos, B. and C. J. Spiers (2001), Experimental investigation into the microstructural and mechanical evolution of phyllosilicate-bearing fault rock under conditions favouring pressure solution, *Journal of Structural Geology*, *23*(8), 1187-1202.

Bos, B. and C. J. Spiers (2002), Frictional-viscous flow of phyllosilicate-bearing fault rock: Microphysical model and implications for crustal strength profiles, *Journal of Geophysical Research*, *107*(B2), 2028, doi:2010.1029/2001JB000301.

Boschi, C., G. L. Fruh-Green, A. Delacour, J. A. Karson and D. S. Kelley (2006a), Mass transfer and fluid flow during detachment faulting and development of an oceanic core complex, Atlantis Massif (MAR 30 degrees N), *Geochemistry Geophysics Geosystems*, *7*, Q01004, doi:01010.01029/02005GC001074.

Boschi, C., G. L. Fruh-Green and J. Escartin (2006b), Occurrence and significance of serpentinite-hosted, talc- and amphibole-rich fault rocks in modern oceanic settings and ophiolite complexes: An overview, *Ofioliti*, *31*(2), 129-140.

Bottinga, Y. (1968), Calculation of fractionation factors for carbon and oxygen isotopic exchange in the system calcite-carbon dioxide-water, *Journal of Physical Chemistry*, *72*, 800-808.

Bouillin, J. P., J. L. Bouchez, P. Lespinasse and A. Pecher (1993), Granite Emplacement in an Extensional Setting - an Ams Study of the Magmatic Structures of Monte-Capanne (Elba, Italy), *Earth and Planetary Science Letters*, *118*(1-4), 263-279.

Branca, M. and M. Voltaggio (1993), Erosion rate in badlands of central Italy: Estimation by radiocaesium isotope ration from Chernobyl nuclear accident, *Applied Geochemistry*, *8*, 347-445.

Brichau, S., U. Ring, A. Carter, P. Monie, R. Bolhar, D. Stockli and M. Brunel (2007), Extensional faulting on Tinos island, Aegean sea, Greece: How many detachments?, *Tectonics*, *26*, TC4009, doi:4010.1029/2006TC001969.

Brogi, A., A. Lazzarotto, D. Liotta and G. Ranalli (2005), Crustal structures in the geothermal areas of southern Tuscany (Italy): Insights from the CROP 18 deep seismic reflection lines, *Journal of Volcanology and Geothermal Research*, *148*, 60-80.

Bruhn, R. L., W. T. Parry, W. A. Yonkee and T. Thompson (1994), Fracturing and Hydrothermal Alteration in Normal-Fault Zones, *Pure and Applied Geophysics*, *142*(3-4), 609-644.

Brune, J., S. Brown and P. A. Johnson (1993), Rupture mechanism and interface separation in foam rubber models of earthquakes: a possible solution to the heat flow paradox and the paradox of large overthrusts, *Tectonophysics*, *218*, 59-67.

Brunet, C., P. Monie, L. Jolivet and J. P. Cadet (2000), Migration of compression and extension in the Tyrrhenian Sea, insights from Ar^{40}/Ar^{39} ages on micas along a transect from Corsica to Tuscany, *Tectonophysics*, *321*(1), 127-155.

Buck, W. R. (1988), Flexural rotation of normal faults, *Tectonics*, *7*, 959-973.

Buick, I. S. (1991), The Late Alpine Evolution of an Extensional Shear Zone, Naxos, Greece, *Journal of the Geological Society*, *148*, 93-103.

Burchfiel, B. C., B. Wernicke, J. H. Willemin, G. J. Axen and C. S. Cameron (1982), A New Type of Decollement Thrusting, *Nature*, *300*(5892), 513-515.

Burke, W. H., R. E. Denison, E. A. Hetherington, R. B. Koepnick, H. F. Nelson and J. B. Otto (1982), Variation of Sea-Water $^{87}Sr/^{86}Sr$ Throughout Phanerozoic Time, *Geology*, *10*(10), 516-519.

Burkhard, M. (1993), Calcite twins, their geometry, appearance and significance as stress–strain markers and indicators of tectonic regime: a review, *Journal of Structural Geology*, *15*, 351-368.

Byerlee, J. (1978), Friction of Rocks, *Pure and Applied Geophysics*, *116*(4-5), 615-626.

Caine, J. S., J. P. Evans and C. B. Forster (1996), Fault zone architecture and permeability structure, *Geology*, *24*(11), 1025-1028.

Cann, J. R., D. K. Blackman, D. K. Smith, E. McAllister, B. Janssen, S. Mello, E. Avgerinos, A. R. Pascoe and J. Escartin (1997), Corrugated slip surfaces formed at ridge-transform intersections on the Mid-Atlantic Ridge, *Nature*, *385*(6614), 329-332.

Carmignani, L. and R. Kligfield (1990), Crustal Extension in the Northern Apennines - the Transition from Compression to Extension in the Alpi Apuane Core Complex, *Tectonics*, *9*(6), 1275-1303.

Cemen, I., O. Tekeli, G. Seyitoglu and V. Isik (2005), Are turtleback fault surfaces common structural elements of highly extended terranes?, *Earth-Science Reviews*, *73*(1-4), 139-148.

Chester, F. and N. G. Higgs (1992), Multimechanism friction constitutive model for ultrafine quartz gouge at hypocentral conditions, *Journal of Geophysical Research*, *97*, 1859-1870.

Chester, F. M., M. Friedman and J. M. Logan (1985), Foliated Cataclasites, *Tectonophysics*, *111*(1-2), 139-146.

Chester, F. M. and J. M. Logan (1987), Composite planar fabric of gouge from the Punchbowl fault, California, *Journal of Structural Geology*, *9*, 621-634.

Chester, F. M. and J. S. Chester (1998), Ultracataclasite structure and friction processes of the Punchbowl fault, San Andreas system, California, *Tectonophysics*, *295*(1-2), 199-221.

Chester, F. M. and J. S. Chester (2000), Stress and deformation along wavy frictional faults, *Journal of Geophysical Research-Solid Earth*, *105*(B10), 23421-23430.

Chester, F. M., J. S. Chester, D. L. Kirschner, S. E. Schulz and J. P. Evans (2004), Structure of large-displacement, strike-slip fault zones in the brittle continental crust, in *Rheology and deformation in the lithosphere at Continental Margins*, edited by G. D. Karner, B. Taylor, N. W. Driscoll and D. L. Kohlstedt, Columbia University Press, New York.

Chiaraluce, L., A. Amato, M. Cocco, C. Chiarabba, G. Selvaggi, M. Di Bona, D. Piccinini, A. Deschamps, L. Margheriti, F. Courboulex and M. Ripepe (2004), Complex normal faulting in the Apennines thrust-and-fold belt: The 1997 seismic sequence in central Italy, *Bulletin of the Seismological Society of America*, *94*(1), 99-116.

Chiaraluce, L., C. Chiarabba, C. Collettini, D. Piccinini and M. Cocco (2007), Architecture and mechanics of an active low-angle normal fault: Alto Tiberina Fault, northern Apennines, Italy, *Journal of Geophysical Research-Solid Earth*, *112*(B10), B10310, doi: 10310.11029/12007JB005015.

Childs, C., J. Watterson and J. J. Walsh (1996), A model for the structure and development of fault zones, *Journal of the Geological Society*, *153*, 337-340.

Chiodini, G. and R. Cioni (1989), Gas geobarometry for hydrothermal systems and its application to various Italian geothermal areas, *Applied Geochemistry*, *4*, 465-472.

Chiodini, G., F. Frondini, D. M. Kerrick, J. Rogie, F. Parello, L. Peruzzi and A. R. Zanzari (1999), Quantification of deep CO_2 fluxes from Central Italy. Examples of carbon balance for regional aquifers and of soil diffuse degassing, *Chemical Geology*, *159*(1-4), 205-222.

Chiodini, G., F. Frondini, C. Cardellini, F. Parello and L. Peruzzi (2000), Rate of diffuse carbon dioxide Earth degassing estimated from carbon balance of regional aquifers: The case of central Apennine, Italy, *Journal of Geophysical Research-Solid Earth*, *105*(B4), 8423-8434.

Chiodini, G., C. Cardellini, A. Amato, E. Boschi, S. Caliro, F. Frondini and G. Ventura (2004), Carbon dioxide Earth degassing and seismogenesis in central and southern Italy, *Geophysical Research Letters*, *31*(7), L07615, doi:07610.01029/02004GL019480.

Cichanski, M. (2000), Low-angle, range-flank faults in the Panamint, Inyo, and Slate ranges, California: Implications for recent tectonics of the Death Valley region, *Geological Society of America Bulletin*, *112*(6), 871-883.

Cladouhos, T. T. (1999a), A kinematic model for deformation within brittle shear zones, *Journal of Structural Geology*, *21*(4), 437-448.

Cladouhos, T. T. (1999b), Shape preferred orientations of survivor grains in fault gouge, *Journal of Structural Geology*, *21*(4), 419-436.

Clark, C. and P. James (2003), Hydrothermal brecciation due to fluid pressure fluctuations: examples from the Olary Domain, South Australia, *Tectonophysics*, *366*(3-4), 187-206.

Cocco, M., P. Montone, M. R. Barchi, G. Dresen, M. D. Zoback, M. Mariucci and S. Pierdominici (2007), The MOLE Drilling Project: Laboratory at Depth on an Active Fault in Central Italy, paper presented at AGU, Fall. Meeting Supp., San Francisco.

Collettini, C., M. Barchi, C. Pauselli, C. Federico and G. Pialli (2000), Seismic expression of active extensional faults in northern Umbria (Central Italy), *Journal of Geodynamics*, *29*(3-5), 309-321.

Collettini, C. and R. H. Sibson (2001), Normal faults, normal friction?, *Geology*, *29*(10), 927-930.

Collettini, C. (2002), Hypothesis for the mechanics and seismic behaviour of low-angle normal faults: the example of the Altotiberina fault Northern Apennines, *Annals of Geophysics*, *45*(5), 683-698.

Collettini, C. and M. R. Barchi (2002), A low-angle normal fault in the Umbria region (Central Italy): a mechanical model for the related microseismicity, *Tectonophysics*, *359*(1-2), 97-115.

Collettini, C. and R. E. Holdsworth (2004), Fault zone weakening and character of slip along low-angle normal faults: insights from the Zuccale fault, Elba, Italy, *Journal of the Geological Society*, *161*, 1039-1051.

Collettini, C., L. Chiaraluce, S. Pucci, M. R. Barchi and M. Cocco (2005), Looking at fault reactivation matching structural geology and seismological data, *Journal of Structural Geology*, *27*(5), 937-942.

Collettini, C., N. De Paola and N. R. Goulty (2006a), Switches in the minimum compressive stress direction induced by overpressure beneath a low-permeability fault zone, *Terra Nova*, *18*(3), 224-231.

Collettini, C., N. De Paola, R. E. Holdsworth and M. R. Barchi (2006b), The development and behaviour of low-angle normal faults during Cenozoic asymmetric extension in the Northern Apennines, Italy, *Journal of Structural Geology*, *28*(2), 333-352.

Coney, P. J. (1980), Cordilleran metamorphic core complexes: a review, in *Cordilleran metamorphic core complexes*, edited by M. D. Crittenden, P. J. Coney and G. H. Davis, pp. 7-31, Geological Society of America, Memoirs.

Corry, C. E. (1988), *Laccoliths – Mechanisms of emplacement and growth*, 110 pp.

Cottle, J. M., M. J. Jessup, D. L. Newell, M. P. Searle, R. D. Law and M. S. A. Horstwood (2007), Structural insights into the early stages of exhumation along an orogen-scale detachment: The South Tibetan Detachment system, Dzakaa Chu section, eastern Himalaya, *Journal of Structural Geology*, *29*(11), 1781-1797.

Cowan, D. S. (1999), Do faults preserve a record of seismic slip? A field geologist's opinion, *Journal of Structural Geology*, *21*(8-9), 995-1001.

Cowan, D. S., T. T. Cladouhos and J. K. Morgan (2003), Structural geology and kinematic history of rocks formed along low-angle normal faults, Death Valley, California, *Geological Society of America Bulletin*, *115*(10), 1230-1248.

Cox, S. F. and M. S. Paterson (1991), Experimental Dissolution-Precipitation Creep in Quartz Aggregates at High-Temperatures, *Geophysical Research Letters*, *18*(8), 1401-1404.

Cox, S. F. (1995), Faulting Processes at High Fluid Pressures - an Example of Fault Valve Behavior from the Wattle Gully Fault, Victoria, Australia, *Journal of Geophysical Research-Solid Earth*, *100*(B7), 12841-12859.

Crawford, B. R., D. R. Faulkner and E. H. Rutter (2008), Strength, porosity, and permeability development during hydrostatic and shear loading of synthetic quartz-clay fault gouge, *Journal of Geophysical Research-Solid Earth*, *113*(B3), B03207, doi:03210.01029/02006JB004634.

Cruden, A. R. (1998), On the emplacement of tabular granites, *Journal of the Geological Society of London*, *155*, 852-862.

Cruden, A. R. and K. J. W. McCaffrey (2001), Growth of plutons by floor subsidence: Implications for rates of emplacement, intrusion spacing and melt-extraction mechanisms, *Physics and Chemistry of the Earth Part a-Solid Earth and Geodesy*, *26*(4-5), 303-315.

Daniel, J. M. and L. Jolivet (1995), Detachment Faults and Pluton Emplacement - Elba Island (Tyrrhenian Sea), *Bulletin De La Societe Geologique De France*, *166*(4), 341-354.

Davis, G. A. (1980), Structural characteristics of metamorphic core complexes, southern Arizona, in *Cordilleran metamorphic core complexes*, edited by M. D. Crittenden, P. J. Coney and G. H. Davis, pp. 35-77, Geological Society of America, Memoirs.

Davis, G. A., G. S. Lister and S. J. Reynolds (1986), Structural Evolution of the Whipple and South Mountains Shear Zones, Southwestern United-States, *Geology*, *14*(1), 7-10.

Davis, G. A. (1987), A shear-zone model for the structural evolution of metamorphic core complexes in southeastern Arizona, in *Continental extensional tectonics*, edited by M. P. Coward, J. F. Dewey and P. L. Hancock, pp. 247-266, The Geological Society of London, London.

Davis, G. A., T. K. Fowler, K. M. Bishop, T. C. Brudos, S. J. Friedmann, D. W. Burbank, M. A. Parke and B. C. Burchfiel (1993), Pluton Pinning of an Active Miocene Detachment Fault System, Eastern Mojave Desert, California, *Geology*, *21*(7), 627-630.

Davis, G. H. (1983a), Shear zone model for the origin of metamorphic core complexes, *Geology*, *11*, 342-347.

Davis, G. H. (1983b), A shear zone model for the structural evolution of metamorphic core complexes in southeastern Arizona, in *Continental extensional tectonics*, edited by M. P. Coward, J. F. Dewey and P. L. Hancock, pp. 247-266, Geological Society of London, Special Publications, London.

Davis, G. H. and G. S. Lister (1988), Detachment faulting in continental extension: Perspectives from the southwestern US Cordillera, in *Processes in continental lithospheric deformation*, edited by S. P. Clark, B. C. Burchfiel and J. Suppe, pp. 133-159, Geological Society of America, Special Papers.

Davis, J. C. (2002), *Statistics and data analysis in geology*, 3 ed., John Wiley & Sons.

de Bresser, J. H. P., J. H. Ter Heege and C. J. Spiers (2001), Grain size reduction by dynamic recrystallisation: can it result in major rheological weakening?, *International Journal of Earth Sciences*, *90*, 28-45.

De Meer, S., M. R. Drury, J. H. P. De Bresser and G. M. Pennock (2002), Current issues and new developments in deformation mechanisms, rheology and tectonics, in *Deformation Mechanisms, Rheology and Tectonics: Current Status and Future Perspectives*, edited by S. De Meer, M. R. Drury, J. H. P. De Bresser and G. M. Pennock, pp. 1-27, The Geological Society of London, London.

Decandia, F. A., A. Lazzarotto, D. Liotta, L. Cernobori and R. Nicolich (1998), The CROP 03 traverse: insights on the post-collisional evolution of the northern Apennines, *Mem. Soc. Geol. It.*, *52*, 413-425.

Deines, P. (2002), The carbon isotope geochemistry of mantle xenoliths, *Earth-Science Reviews*, *58*(3-4), 247-278.

Di Toro, G., D. L. Goldsby and T. E. Tullis (2004), Friction falls towards zero in quartz rock as slip velocity approaches seismic rates, *Nature*, *427*(6973), 436-439.

Dieterich, J. H. (1979), Modelling of rock friction: 1. Experimental results and constitutive equations, *Journal of Geophysical Research*, *84*, 2161-2168.

Dini, A., F. Innocenti, S. Rocchi, S. Tonarini and D. S. Westerman (2002), The magmatic evolution of the late Miocene laccolith-pluton-dyke granitic complex of Elba Island, Italy, *Geological Magazine*, *139*(3), 257-279.

Dini, A., G. Gianelli, M. Puxeddu and G. Ruggieri (2005), Origin and evolution of Pliocene–Pleistocene granites from the Larderello geothermal field (Tuscan Magmatic Province, Italy), *Lithos*, *81*, 1–31.

Dini, A., F. Farina, F. Innocenti, S. Rocchi and D. S. Westerman (2007), Monte Capanne pluton revisited 40 years after Giglia's contributions, *Rend. Soc. Geol. It*, *5*, 126-128.

Dini, A., F. Mazzarini, G. Musumeci and S. Rocchi (2008), Multiple hydro-fracturing by boron-rich fluids in the Late Miocene contact aureole of eastern Elba Island (Tuscany, Italy), *Terra Nova*, *20*(4), 318-326.

Doglioni, C., P. Harabaglia, S. Merlini, F. Mongelli, A. Peccerillo and C. Piromallo (1999), Orogens and slabs vs. their direction of subduction, *Earth Science Reviews*, *45*(3-4), 167-208.

Douglas, T. A., C. P. Chamberlain, M. A. Poage, M. Abruzzese, S. Shultz, J. Henneberry and P. Layer (2003), Fluid flow and the Heart Mountain fault: a stable isotopic, fluid inclusion, and geochronologic study, *Geofluids*, *3*(1), 13-32.

Duenkel, I., J. Kuhlemann and U. Nohlen (2003), Iron ore formation and neotectonic evolution in Elba (Tuscany, Italy) during Messinian plutonism, *Neues Jahrbuch Fur Geologie Und Palaontologie-Abhandlungen*, *230*(2-3), 391-407.

Duranti, S., R. Palmeri, P. C. Pertusati and C. A. Ricci (1992), Geological evolution and metamorphic petrology of the basal sequences of eastern Elba (complex II), *Acta Vulcanologica*, *2*, 213-229.

Ebert, A., M. Herwegh and A. Pfiffner (2007), Cooling induced strain localization in carbonate mylonites within a large-scale shear zone (Glarus thrust, Switzerland), *Journal of Structural Geology*, *29*, 1164-1184.

Eichhubl, P. and J. R. Boles (2000), Rates of fluid flow in fault systems-evidence for episodic rapid fluid now in the miocene monterey formation, coastal California, *American Journal of Science*, *300*(7), 571-600.

Elter, P., G. Giglia, M. Tongiorgi and L. Trevisan (1975), Tensional and compressional areas in recent (Tortonian to present) evolution of the northern Apennines, *Bollettino di Geofisica Teorica e Applicata*, *17*, 3-18.

Escartin, J., C. Mevel, C. J. MacLeod and A. M. McCaig (2003), Constraints on deformation conditions and the origin of oceanic detachments: The Mid-Atlantic Ridge core complex at 15 degrees 45 ' N, *Geochemistry Geophysics Geosystems*, *4*(8), 1067, doi:1010.1029/2002GC000472.

Escartin, J., M. Andreani, G. Hirth and B. Evans (2008), Relationships between the microstructural evolution and the rheology of talc at elevated pressures and temperatures, *Earth and Planetary Science Letters*, *268*(3-4), 463-475.

Evans, J. P. (1988), Deformation Mechanisms in Granitic-Rocks at Shallow Crustal Levels, *Journal of Structural Geology*, *10*(5), 437-443.

Evans, J. P. (1990), Thickness Displacement Relationships for Fault Zones, *Journal of Structural Geology*, *12*(8), 1061-1065.

Evans, J. P. and F. M. Chester (1995), Fluid-Rock Interaction in Faults of the San-Andreas System - Inferences from San-Gabriel Fault Rock Geochemistry and Microstructures, *Journal of Geophysical Research-Solid Earth*, *100*(B7), 13007-13020.

Famin, V., R. Hebert, P. Philippot and L. Jolivet (2005), Ion probe and fluid inclusion evidence for co-seismic fluid infiltration in a crustal detachment, *Contributions to Mineralogy and Petrology*, *150*(3), 354-367.

Famin, V. and S. Nakashima (2005), Hydrothermal fluid venting along a seismogenic detachment fault in the Moresby rift (Woodlark basin, Papua New Guinea), *Geochemistry Geophysics Geosystems*, *6*, Q12003, doi:12010.11029/12005GC001112.

Faulkner, D. R. and E. H. Rutter (2000), Comparisons of water and argon permeability in natural clay-bearing fault gouge under high pressure at 20 degrees C, *Journal of Geophysical Research-Solid Earth*, *105*(B7), 16415-16426.

Faulkner, D. R. and E. H. Rutter (2001), Can the maintenance of overpressured fluids in large strike-slip fault zones explain their apparent weakness?, *Geology*, *29*(6), 503-506.

Faulkner, D. R., A. C. Lewis and E. H. Rutter (2003), On the internal structure and mechanics of large strike-slip fault zones: field observations of the Carboneras fault in southeastem Spain, *Tectonophysics*, *367*(3-4), 235-251.

Faulkner, D. R. and E. H. Rutter (2003), The effect of temperature, the nature of the pore fluid, and subyield differential stress on the permeability of phyllosilicate-rich fault gouge, *Journal of Geophysical Research-Solid Earth*, *108*(B5), 2227, doi:2210.1029/2001JB001581.

Faulkner, D. R. (2004), A model for the variation in permeability of clay-bearing fault gouge with depth in the brittle crust, *Geophysical Research Letters*, *31*(19), L19611, doi:19610.11029/12004GL020736.

Faulkner, D. R., T. M. Mitchell, D. Healy and M. J. Heap (2006), Slip on 'weak' faults by the rotation of regional stress in the fracture damage zone, *Nature*, *444*(7121), 922-925.

Faure, M., M. Bonneau and J. Pons (1991), Ductile deformation and syntectonic granite emplacement during the late Miocene extension of the Aegea (Greece), *Bulletin de la Societe Geologique de France*, *162*, 3-11.

Fellin, M. G., P. W. Reiners, M. T. Brandon, E. Wuthrich, M. L. Balestrieri and G. Molli (2007), Thermochronometric evidence for the exhumational history of the Alpi Apuane metamorphic core complex, northern Apennines, Italy, *Tectonics*, *26*.

Ferrill, D. A., A. P. Morris, M. A. Evans, M. Burkhard, R. H. J. Groshong and C. M. Onasch (2004), Calcite twin morphology: a low-temperature deformation geothermometer, *Journal of Structural Geology*, *26*, 1521-1529.

Floyd, J. S., J. C. Mutter, A. M. Goodliffe and B. Taylor (2001), Evidence for fault weakness and fluid flow within an active low-angle normal fault, *Nature*, *411*(6839), 779-783.

Fossen, H. and E. Rykkelid (1992), The Interaction between Oblique and Layer-Parallel Shear in High-Strain Zones - Observations and Experiments, *Tectonophysics*, *207*(3-4), 331-343.

Gagnevin, D., J. S. Daly and G. Poli (2004), Petrographic, geochemical and isotopic constraints on magma dynamics and mixing in the Miocene Monte Capanne monzogranite (Elba Island, Italy), *Lithos*, *78*(1-2), 157-195.

Gans, P. B., G. A. Mahood and E. R. Schermer (1989), Synextensional magmatism in the Basin and Range province; a case study from the eastern Great Basin, in *Geological Society of America, Special Papers*, edited, pp. 1-53.

Garces, M. and J. S. Gee (2007), Paleomagnetic evidence of large footwall rotations associated with low-angle faults at the Mid-Atlantic Ridge, *Geology*, *35*(3), 279-282.

Garfagnoli, F., F. Menna, E. Pandeli and G. Principi (2005), The Porto Azzurro Unit (Mt. Calamita promontory, south-eastern Elba Island, Tuscany): Stratigraphic, tectonic and metamorphic evolution, *Bollettino Della Societa Geologica Italiana*, 119-138.

Giger, S. B., S. F. Cox and E. Tenthorey (2008), Slip localization and fault weakening as a consequence of fault gouge strengthening - Insights from laboratory experiments, *Earth and Planetary Science Letters, In Press*.

Gordon, T. M. and H. J. Greenwood (1970), The reaction: Dolomite + Quartz + Water = Talc + Calcite + Carbon Dioxide, *American Journal of Science, 268*, 225-242.

Gratier, J. P. and F. Gueydan (2007), Deformation in the presence of fluids and mineral reactions: Effects of fracturing and fluid-rock interaction on seismic cycles, in *Dahlem Workshop Reports, Tectonic Faults: Agents of change on a dynamic earth*, edited by M. R. Handy, G. Hirth and N. Hovius, pp. 319-356, The MIT Press.

Gueydan, F., Y. M. Leroy, L. Jolivet and P. Agard (2003), Analysis of continental midcrustal strain localization induced by microfracturing and reaction-softening, *Journal of Geophysical Research-Solid Earth, 108*(B2), 2064, doi:2010.1029/2001JB000611.

Hadizadeh, J. and E. H. Rutter (1983), The low-temperature brittle-ductile transition in a quartzite and the occurrence of cataclastic flow in nature, *Geologische Rundschau, 72*(2), 493-509.

Hammond, K. J. and J. P. Evans (2003), Geochemistry, mineralization, structure, and permeability of a normal-fault zone, Casino mine, Alligator Ridge district, north central Nevada, *Journal of Structural Geology, 25*(5), 717-736.

Han, R., T. Shimamoto, T. Hirose, J. H. Ree and J. Ando (2007a), Ultralow friction of carbonate faults caused by thermal decomposition, *Science, 316*(5826), 878-881.

Han, R. H., T. Shimamoto, J. I. Ando and J. H. Ree (2007b), Seismic slip record in carbonate-bearing fault zones: An insight from high-velocity friction experiments on siderite gouge, *Geology, 35*(12), 1131-1134.

Hawkesworth, C. J. and R. Vollmer (1979), Crustal contamination versus enriched mantle: $^{143}Nd/^{144}Nd$ and $^{87}Sr/^{86}Sr$ evidence from the Italian volcanics, *Contributions to Mineralogy and Petrology, 69*, 151-165.

Hayman, N. W., J. R. Knott, D. S. Cowan, E. Nemser and A. M. Sarna-Wojcicki (2003), Quaternary low-angle slip on detachment faults in Death Valley, California, *Geology, 31*(4), 343-346.

Hayman, N. W., B. A. Housen, T. T. Cladouhos and K. Livi (2004), Magnetic and clast fabrics as measurements of grain-scale processes within the Death Valley shallow crustal detachment faults, *Journal of Geophysical Research-Solid Earth, 109*(B5), B05409, doi:05410.01029/02003JB02902.

Hayman, N. W. (2006), Shallow crustal fault rocks from the Black Mountain detachments, Death Valley, CA, *Journal of Structural Geology, 28*(10), 1767-1784.

Hecht, L., R. Freiberger, H. Albert Gilg, G. Grundmann and Y. A. Kostitsyn (1999), Rare earth element and isotope (C, O, Sr) characteristics of hydrothermal carbonates: genetic implications for dolomite-hosted talc mineralization at Gopfersgrun (Fichtelgebirge, Germany), *Chemical Geology, 155*, 115-130.

Henderson, I. H. C. and A. M. Mccaig (1996), Fluid pressure and salinity variations in shear zone related veins, central Pyrenees, France: Implications for the fault valve model, *Tectonophysics*, *262*, 321-348.

Herwegh, M. and K. Kunze (2002), The influence of nano-scale second-phase particles on deformation of fine grained calcite mylonites, *Journal of Structural Geology*, *24*, 1463-1478.

Hickman, S. and B. Evans (1995), Kinetics of pressure solution at halite-silica interfaces and intergranular clay films, *Journal of Geophysical Research*, *100*(B7), 13113-13132.

Hickman, S., R. Sibson and R. Bruhn (1995), Introduction to Special Section - Mechanical Involvement of Fluids in Faulting, *Journal of Geophysical Research-Solid Earth*, *100*(B7), 12831-12840.

Hirth, G. and J. Tullis (1992), The brittle-plastic transition in experimentally deformed quartz aggregates, *Journal of Geophysical Research*, *99*, 11731-11747.

Hoefs, J. (1987), *Stable isotope geochemistry*, 3rd edition ed., Springer-Verlag, Berlin.

Holdsworth, R. E., R. A. Strachan, J. Magloughlin and R. J. Knipe (Eds.) (2001), *The Nature and Tectonic Significance of Fault Zone Weakening*, Geological Society of London, London.

Holdsworth, R. E. (2004), Weak faults - Rotten cores, *Science*, *303*(5655), 181-182.

Holm, D. K. (1985), Relation of deformation and multiple intrusion in the Death Valley extended region, California, with implications for magma entrapment mechanism, *Journal of Geophysical Research*, *100*, 10495-10505.

Holness, M. B. (1997), Fluid flow paths and mechanisms of fluid infiltration in carbonates during contact metamorphism: the Beinn an Dubhaich aureole, Skye, *Journal of Metamorphic Geology*, *15*, 59-70.

Hubbert, M. K. and W. W. Rubey (1959), Role of fluid overpressure in mechanics of overthrust faulting, *Geological Society of America Bulletin*, *70*, 583-586.

Hunstad, I., G. Selvaggi, N. D'Agostino, P. England, P. Clarke and M. Pierozzi (2003), Geodetic strain in peninsular Italy between 1875 and 2001, *Geophysical Research Letters*, *30*(4), 1181, doi: 1110.1029/2002GL016447.

Ildefonse, B., D. K. Blackman, B. E. John, Y. Ohara, D. J. Miller and C. MacLoed (2007), Oceanic core complexes and crustal accretion at slow spreading ridges, *Geology*, *35*, 623-626.

Imber, J., R. E. Holdsworth, C. A. Butler and G. E. Lloyd (1997), Fault-zone weakening processes along the reactivated Outer Hebrides Fault Zone, Scotland, *Journal of the Geological Society*, *154*, 105-109.

Imber, J., R. E. Holdsworth, C. A. Butler and R. A. Strachan (2001), A reappraisal of the Sibson-Scholz fault zone model: The nature of the frictional to viscous ("brittle-ductile")

transition along a long-lived, crustal-scale fault, Outer Hebrides, Scotland, *Tectonics*, *20*(5), 601-624.

Imber, J., R. E. Holdsworth, S. A. F. Smith, S. P. Jefferies and C. Collettini (2008), Frictional-viscous flow, seismicity and the geology of weak faults: a review and future directions, in *The Internal Structure of Fault Zones: Implications for Mechanical and Fluid Flow Properties*, edited by C. A. J. Wibberley, W. Kurz, J. Imber, R. E. Holdsworth and C. Collettini, pp. 151-173, The Geological Society of London, London.

Jackson, J. A. and N. J. White (1989), Normal Faulting in the Upper Continental-Crust - Observations from Regions of Active Extension, *Journal of Structural Geology*, *11*(1-2), 15-36.

Jaeger, J. G. and N. G. W. Cook (1979), *Fundamentals of rock mechanics*, 3rd edition ed., Chapman and Hall, London.

Jefferies, S. P., R. E. Holdsworth, T. Shimamoto, H. Takagi, G. E. Lloyd and C. J. Spiers (2006a), Origin and mechanical significance of foliated cataclastic rocks in the cores of crustal-scale faults: Examples from the Median Tectonic Line, Japan, *Journal of Geophysical Research-Solid Earth*, *111*(B12), B12303, doi:12310.11029/12005JB004205.

Jefferies, S. P., R. E. Holdsworth, C. A. J. Wibberley, T. Shimamoto, C. J. Spiers, A. R. Niemeijer and G. E. Lloyd (2006b), The nature and importance of phyllonite development in crustal-scale fault cores: an example from the Median Tectonic Line, Japan, *Journal of Structural Geology*, *28*(2), 220-235.

Jessell, M. W. (1987), Grain-boundary migration microstructures in a naturally deformed quartzite, *Journal of Structural Geology*, *9*, 1007-1014.

John, B. E. (1987), Geometry and evolution of a mid-crustal extensional fault system: Chemehuevi Mountains, southeastern California, in *Continental Extensional Tectonics*, edited by M. P. Coward, J. F. Dewey and P. L. Hancock, pp. 313-336, Geological Society of London, London.

Jolivet, L., C. Faccenna, B. Goffe, M. Mattei, F. Rossetti, C. Brunet, F. Storti, R. Funiciello, J. P. Cadet, N. d'Agostino and T. Parra (1998), Midcrustal shear zones in postorogenic extension: Example from the northern Tyrrhenian Sea, *Journal of Geophysical Research-Solid Earth*, *103*(B6), 12123-12160.

Kapp, P., M. Taylor, D. Stockli and L. Ding (2008), Development of active low-angle normal fault systems during orogenic collapse: Insight from Tibet, *Geology*, *36*(1), 7-10.

Karson, J. A., G. L. Fruh-Green, D. S. Kelley, E. A. Williams, D. R. Yoerger and M. Jakuba (2006), Detachment shear zone of the Atlantis Massif core complex, Mid-Atlantic Ridge, 30N, *Geochemistry Geophysics Geosystems*, *7*, Q06016, doi:06010.01029/02005GC001109.

Keller, J. V. A. and G. Pialli (1990), Tectonics of the island of Elba: a reappraisal, *Boll. Geol. Soc. It.*, *109*, 413-425.

Keller, J. V. A., G. Minelli and G. Pialli (1994), Anatomy of Late Orogenic Extension - the Northern Apennines Case, *Tectonophysics*, *238*(1-4), 275-294.

Keller, J. V. A. and M. P. Coward (1996), The structure and evolution of the Northern Tyrrhenian Sea, *Geological Magazine*, *133*(1), 1-16.

Kennedy, L. A. and J. C. White (2001), Low-temperature recrystallisation in calcite: Mechanisms and consequences, *Geology*, *29*(11), 1027-1030.

Kerrick, D. M. (2001), Present and past nonanthropogenic CO_2 degassing from the solid Earth, *Reviews of Geophysics*, *39*(4), 565-585.

Knipe, R. J. (1989), Deformation Mechanisms - Recognition from Natural Tectonites, *Journal of Structural Geology*, *11*(1-2), 127-146.

Kopf, A., J. H. Behrmann, A. Deyhle, S. Roller and H. Erlenkeuser (2003), Isotopic evidence (B, C, O) of deep fluid processes in fault rocks from the active Woodlark Basin detachment zone, *Earth and Planetary Science Letters*, *208*(1-2), 51-68.

Krabbendam, M., J. L. Urai and L. J. van Vliet (2003), Grain size stabilisation by dispersed graphite in a high-grade quartz mylonite: an example from Naxos (Greece), *Journal of Structural Geology*, *25*, 855-866.

Kumerics, C., U. Ring, S. Brichau, J. Glodny and P. Monie (2005), The extensional Messaria shear zone and associated brittle detachment faults, Aegean Sea, Greece, *Journal of the Geological Society*, *162*, 701-721.

Lachenbruch, A. H. and J. H. Sass (1980), Heat-Flow and Energetics of the San-Andreas Fault Zone, *Journal of Geophysical Research*, *85*(Nb11), 6185-6222.

Le Guen, Y., F. Renard, R. Hellmann, E. Brosse, M. Collombet, D. Tisserand and J. P. Gratier (2007), Enhanced deformation of limestone and sandstone in the presence of high P-CO_2 fluids, *Journal of Geophysical Research-Solid Earth*, *112*(B5), doi:10.1029/2006JB004637.

Lister, G. S. (1984), Metamorphic Core Complexes of Cordilleran Type in the Cyclades, Aegean Sea, Greece, *Geology*, *12*(4), 221-225.

Lister, G. S. and G. A. Davis (1989), The Origin of Metamorphic Core Complexes and Detachment Faults Formed during Tertiary Continental Extension in the Northern Colorado River Region, USA, *Journal of Structural Geology*, *11*(1-2), 65-94.

Lister, G. S. and S. L. Baldwin (1993), Plutonism and the Origin of Metamorphic Core Complexes, *Geology*, *21*(7), 607-610.

Little, T. A., S. L. Baldwin, P. G. Fitzgerald and B. Monteleone (2007), Continental rifting and metamorphic core complex formation ahead of the Woodlark spreading ridge, D'Entrecasteaux Islands, Papua New Guinea, *Tectonics*, *26*(1), TC1002, doi:1010.1029/2005TC001911.

Llana-Funez, S. and E. H. Rutter (2008), Strain localization in direct shear experiments on Solnhofen limestone at high-temperature - Effects of transpression, *Journal of Structural Geology*, *30*, 1372-1382.

Logan, J. M., M. Friedman, N. Higgs, C. Dengo and T. Shimamoto (1979), Experimental studies of simulated gouge and their application to studies of natural fault zones, 79-1239 pp, U.S. Geological Survey Open-File Report

Logan, J. M. and K. A. Rauenzahn (1987), Frictional dependence of gouge mixtures of quartz and montmorillonite on velocity, composition and fabric, *Tectonophysics*, *144*, 87-108.

Losh, S., D. Purvance, R. Sherlock and E. C. Jowett (2005), Geologic and geochemical study of the Picacho gold mine, California: gold in a low-angle normal fault environment, *Mineralium Deposita*, *40*(2), 137-155.

Maineri, C., M. Benvenuti, P. Costagliola, A. Dini, P. Lattanzi, G. Ruggieri and I. M. Villa (2003), Sericitic alteration at the La Crocetta deposit (Elba Island, Italy): interplay between magmatism, tectonics and hydrothermal activity, *Mineralium Deposita*, *38*(1), 67-86.

Mair, K. and C. Marone (1999), Friction of simulated fault gouge for a wide range of velocites and normal stresses, *Journal of Geophysical Research*, *104*(B12), 28899-28914.

Malinverno, A. and W. B. F. Ryan (1986), Extension in the Tyrrhenian Sea and Shortening in the Apennines as Result of Arc Migration Driven by Sinking of the Lithosphere, *Tectonics*, *5*(2), 227-245.

Manatschal, G. (1999), Fluid- and reaction-assisted low-angle normal faulting: evidence from rift-related brittle fault rocks in the Alps (Err Nappe, eastern Switzerland), *Journal of Structural Geology*, *21*(7), 777-793.

Manatschal, G. and D. Bernoulli (1999), Architecture and tectonic evolution of non-volcani margins: Present-day Galicia and ancient Adria, *Tectonics*, *18*, 1099-1119.

Manatschal, G., D. Marquer and G. L. Fruh-Green (2000), Channelized fluid flow and mass transfer along a rift-related detachment fault (Eastern Alps, southeast Switzerland), *Geological Society of America Bulletin*, *112*(1), 21-33.

Mancktelow, N. S. and T. L. Pavlis (1994), Fold-Fault Relationships in Low-Angle Detachment Systems, *Tectonics*, *13*(3), 668-685.

Mancktelow, N. S. and G. Pennacchioni (2005), The control of precursor brittle fracture and fluid-rock interaction on the development of single and paired ductile shear zones, *Journal of Structural Geology*, *27*(4), 645-661.

Marone, C. (1998), Laboratory-derived friction laws and their application to seismic faulting, *Annual Review of Earth and Planetary Sciences*, *26*, 643-696.

Mattey, D., D. Lowry and C. Macpherson (1994), Oxygen-Isotope Composition of Mantle Peridotite, *Earth and Planetary Science Letters*, *128*(3-4), 231-241.

Matthews, A. and A. Katz (1977), Oxygen isotope fractionation during dolomitization of calcium carbonate, *Geochimica Et Cosmochimica Acta*, *41*, 1431-1438.

Maurin, J. C. and B. Niviere (2000), Extensional forced folding and decollement of the pre-rift series along the Rhine graben and their influence on the geometry of the syn-rift

sequences, in *Forced folds and fractures*, edited by J. W. Cosgrove and M. S. Ameen, pp. 73-86, Geological Society of London, Special Publications.

McCaffrey, K. J. W., C. F. Miller, K. E. Karlstrom and C. Simpson (1999), Synmagmatic deformation patterns in the Old Woman Mountains, SE California, *Journal of Structural Geology*, *21*(3), 335-349.

Means, W. D. (1995), Shear zones and rock history, *Tectonophysics*, *247*, 157-160.

Mehl, C., L. Jolivet and O. Lacombe (2005), From ductile to brittle: Evolution and localization of deformation below a crustal detachment (Tinos, Cyclades, Greece), *Tectonics*, *24*(4), TC4017, doi:4010.1029/2004TC001767.

Miller, M. B. and T. L. Pavlis (2005), The Black Mountains turtlebacks: Rosetta stones of Death Valley tectonics, *Earth-Science Reviews*, *73*(1-4), 115-138.

Miller, M. G. (1992), Brittle Faulting Induced by Ductile Deformation of a Rheologically Stratified Rock Sequence, Badwater Turtleback, Death-Valley, California, *Geological Society of America Bulletin*, *104*(10), 1376-1385.

Miller, S. A., C. Collettini, L. Chiaraluce, M. Cocco, M. Barchi and B. J. P. Kaus (2004), Aftershocks driven by a high-pressure CO_2 source at depth, *Nature*, *427*(6976), 724-727.

Minissale, A., M. G., M. G., V. O. and T. G.F. (2000), Fluid geochemical transect in the Northern Apennines (central-northern Italy): fluid genesis and migration and tectonic implications, *Tectonophysics*, *319*, 199–222.

Minissale, A. (2004), Origin, transport and discharge of CO_2 in central Italy, *Earth-Science Reviews*, *66*, 89–141.

Mitchell, T. M. (2006), Fluid flow properties of fault damage zones, Unpublished PhD thesis, University of Liverpool, Liverpool.

Mitchell, T. M. and D. R. Faulkner (2008), Experimental measurements of permeability evolution during triaxial compression of initially intact crystalline rocks and implications for fluid flow in fault zones, *Journal of Geophysical Research, In Press*.

Miyashiro, A. (1973), *Metamorphism and metamorphic belts*, John Wiley, New York.

Mizoguchi, K., M. Takahashi, W. Tanikawa, K. Masuda, S.-R. Song and W. Soh (2008), Frictional strength of fault gouge in Taiwan Chelungpu fault obtained from TCDP Hole B, *Tectonophysics*, *460*(1-4), 198-205.

Montone, P., M. T. Mariucci, S. Pondrelli and A. Amato (2004), An improved stress map for Italy and surrounding regions (central Mediterranean), *Journal of Geophysical Research-Solid Earth*, *109*(B10), B10410, doi:10410.11029/12003JB002703.

Monzawa, N. and K. Otsuki (2003), Comminution and fluidization of granular fault materials: implications for fault slip behavior, *Tectonophysics*, *367*(1-2), 127-143.

Moore, D. E., D. A. Lockner, S. L. Ma, R. Summers and J. D. Byerlee (1997), Strengths of serpentinite gouges at elevated temperatures, *Journal of Geophysical Research-Solid Earth*, *102*(B7), 14787-14801.

Moore, D. E. and D. A. Lockner (2004a), Crystallographic controls on the frictional behavior of dry and water-saturated sheet structure minerals, *Journal of Geophysical Research-Solid Earth*, *109*(B3), -.

Moore, D. E. and D. A. Lockner (2004b), Crystallographic controls on the frictional behavior of dry and water-saturated sheet structure minerals, *Journal of Geophysical Research-Solid Earth*, *109*(B3), B03401, doi:03410.01029/02003JB002582.

Moore, D. E. and M. J. Rymer (2007), Talc-bearing serpentinite and the creeping section of the San Andreas fault, *Nature*, *448*(7155), 795-797.

Moore, D. E. and D. A. Lockner (2008), Talc friction in the Temperature Range 25°-400°C: Relevance for Fault-Zone Weakening, *Tectonophysics*, *449*(1-4), 120-132.

Morrison, J. and J. L. Anderson (1998), Footwall refrigeration along a detachment fault: Implications for the thermal evolution of core complexes, *Science*, *279*(5347), 63-66.

Morrow, C. A., L. Q. Shi and J. D. Byerlee (1982), Strain-Hardening and Strength of Clay-Rich Fault Gouges, *Journal of Geophysical Research*, *87*(Nb8), 6771-6780.

Morrow, C. A., D. E. Moore and D. A. Lockner (2000), The effect of mineral bond strength and adsorbed water on fault gouge frictional strength, *Geophysical Research Letters*, *27*(6), 815-818.

Mort, K. and N. H. Woodcock (2008), Quantifying fault breccia geometry: Dent Fault, NW England, *Journal of Structural Geology*, *30*(6), 701-709.

Nguyen, P. T., S. F. Cox, L. B. Harris and C. M. Powell (1998), Fault-valve behaviour in optimally oriented shear zones: an example at the Revenge gold mine, Kambalda, Western Australia, *Journal of Structural Geology*, *20*(12), 1625-1640.

Niemeijer, A. R. and C. J. Spiers (2005), Influence of phyllosilicates on fault strength in the brittle-ductile transition: insights from rock analogue experiments, in *High Strain Zones: Structure and Physical Properties*, edited by R. Bruhn and L. Burlini, pp. 303-327, The Geological Society of London, London.

Northrop, D. A. and R. N. Clayton (1966), Oxygen isotope fractionations in systems containing dolomite, *Journal of Geology*, *74*, 174-196.

Nostro, C., M. Cocco and M. E. Belardinelli (1997), Static stress changes in extensional regimes: An application to southern Apennines (Italy), *Bulletin of the Seismological Society of America*, *87*(1), 234-248.

Numelin, T., C. Marone and E. Kirby (2007), Frictional properties of natural fault gouge from a low-angle normal fault, Panamint Valley, California, *Tectonics*, *26*(2), TC2004, doi:2010.1029/2005TC001916.

O'Neil, J. R., R. N. Clayton and T. K. Mayeda (1969), Oxygen isotope fractionation in divalent metal carbonates, *Journal of Chemical Physics*, *51*, 5547-5558.

Oesterling, N., R. Heilbronner, H. Stunitz, A. Barnhoorn and G. Molli (2007), Strain dependent variation of microstructure and texture in naturally deformed Carrara marble, *Journal of Structural Geology*, *29*(4), 681-696.

Ohmoto, H. and R. O. Rye (1979), Isotopes of sulfur and carbon, in *Geochemistry of hydrothermal ore deposits*, edited by H. L. Barnes, pp. 509-561, John Wiley & Sons.

Oliver, N. H. S. (1996), Review and classification of structural controls on fluid flow during regional metamorphism, *Journal of Metamorphic Geology*, *14*, 477-492.

Oliver, N. H. S., M. J. Rubenach, B. Fu, T. Baker, T. G. Blenkinsop, J. S. Cleverley, L. J. Marshall and P. J. Ridd (2006), Granite-related overpressure and volatile release in the mid crust: fluidized breccias from the Cloncurry District, Australia, *Geofluids*, *6*(4), 346-358.

Otsuki, K., N. Monzawa and T. Nagase (2003), Fluidization and melting of fault gouge during seismic slip: Identification in the Nojima fault zone and implications for focal earthquake mechanisms, *Journal of Geophysical Research-Solid Earth*, *108*(B4), 2192, doi:2110.1029/2001JB001711.

Parry, W. T. and R. L. Bruhn (1990), Fluid Pressure Transients on Seismogenic Normal Faults, *Tectonophysics*, *179*(3-4), 335-344.

Pascucci, V., S. Merlini and I. P. Martini (1999), Seismic stratigraphy of the Miocene-Pleistocene sedimentary basins of the Northern Tyrrhenian Sea and western Tuscany (Italy), *Basin Research*, *11*(4), 337-356.

Passchier, C. W. and R. A. J. Trouw (2005), *Microtectonics*, 2 ed., Springer, Berlin.

Paterson, M. S. and T. F. Wong (2005), *Experimental Rock Deformation: The Brittle Field*, 2 ed., 348 pp., Springer.

Pauselli, C. and C. Federico (2002), The brittle/ductile transition along the CROP03 seismic profile: relationship with the geological features, *Boll. Soc. Geol. It.* , *1*, 25-35.

Pauselli, C., M. R. Barchi, C. Federico, M. B. Magnani and G. Minelli (2006), The crustal structure of the Northern Apennines (central Italy): An insight by the CROP03 seismic line, *American Journal of Science*, *306*(6), 428-450.

Pavlis, T. L. (1996), Fabric development in syn-tectonic intrusive sheets as a consequence of melt-dominated flow and thermal softening of the crust, *Tectonophysics*, *253*(1-2), 1-31.

Pennacchioni, G., G. Di Toro, P. Brack, L. Menegon and I. M. Villa (2006), Brittle-ductile-brittle deformation during cooling of tonalite (Adamello, Southern Italian Alps), *Tectonophysics*, *427*(1-4), 171-197.

Person, M., L. P. Baumgartner, B. Bos, J. A. D. Connolly, J. P. Gratier, F. Gueydan, S. A. Miller, C. L. Rosenberg, J. L. Urai and B. Yardley (2007), Group report: Fluids, geochemical cycles, and mass transport in fault zones, in *Dahlem Workshop Reports,*

Tectonic Faults: Agents of change on a dynamic earth, edited by M. R. Handy, G. Hirth and N. Hovius, pp. 403-425, The MIT Press.

Perugini, D. and G. Poli (2007), Tourmaline nodules from Capo Bianco aplite (Elba Island, Italy): an example of diffusion limited aggregation growth in a magmatic system, *Contributions to Mineralogy and Petrology*, *153*(5), 493-508.

Prior, D. J., A. P. Boyle, F. Brenker, M. C. Cheadle, A. Day, G. Lopez, L. Peruzzo, G. J. Potts, S. Reddy, R. Spiess, N. E. Timms, P. Trimby, J. Wheeler and L. Zetterstrom (1999), The application of electron backscatter diffraction and orientation contrast imaging in the SEM to textural problems in rocks, *American Mineralogist*, *84*(11-12), 1741-1759.

Proffett, J. M. (1977), Cenozoic geology of the Yerington district, Nevada, and implications for the nature and origin of Basin and Range faulting, *Geological Society of America Bulletin*, *88*, 247-266.

Putnis, A. (2002), Mineral replacement reactions: from macroscopic observations to microscopic mechanisms, *Mineralogical Magazine*, *66*(5), 689-708.

Putnis, A. and C. V. Putnis (2007), The mechanism of reequilibration of solids in the presence of a fluid phase, *Journal of Solid State Chemistry*, *180*, 1783-1786.

Rawling, G. C. and L. B. Goodwin (2003), Cataclasis and particulate flow in faulted, poorly lithified sediments, *Journal of Structural Geology*, *25*, 317-331.

Regenauer-Lieb, K., R. F. Weinberg and G. Rosenbaum (2006), The effect of energy feedbacks on continental strength, *Nature*, *442*(7098), 67-70.

Reinen, L. A., J. D. Weeks and T. E. Tullis (1994), The Frictional Behavior of Lizardite and Antigorite Serpentinites - Experiments, Constitutive Models, and Implications for Natural Faults, *Pure and Applied Geophysics*, *143*(1-3), 317-358.

Reynolds, S. J. and G. S. Lister (1987), Structural Aspects of Fluid-Rock Interactions in Detachment Zones, *Geology*, *15*(4), 362-366.

Rice, J. R. (1992), Fault Stress States, Pore Pressure Distributions, and the Weakness of the San Andreas Fault, in *Fault Mechanics and Transport Properties of Rocks*, edited by B. Evans and T. F. Wong, pp. 475-503, Academic Press, London.

Rice, J. R. (2006), Heating and weakening of faults during earthquake slip, *Journal of Geophysical Research-Solid Earth*, *111*(B5), B05311, doi:05310.01029/02005JB004006.

Rigo, A., H. Lyon-Caen, R. Armijo, A. Deschamps, D. Hatzfeld, K. Makropoulos, P. Papadimitrou and I. Kassaras (1996), A microseismic study in the western Gulf of Corinth (Greece): Implications for large-scale normal faulting mechanisms, *Geophysical Journal International*, *126*, 663-688.

Ring, U. and A. S. Collins (2005), U-Pb SIMS dating of synkinematic granites: timing of core-complex formation in the northern Anatolide belt of western Turkey, *Journal of the Geological Society*, *162*, 289-298.

Rocchi, S., D. S. Westerman, A. Dini, F. Innocenti and S. Tonarini (2002), Two-stage growth of laccoliths at Elba Island, Italy, *Geology*, *30*(11), 983-986.

Rocchi, S., A. Dini, F. Mazzarini, D. S. Westerman and M. Gemelli (2008), Field guidebook, paper presented at LASI III: Physical Geology of Subvolcanic Systems: Laccoliths, Sills and Dykes, University of Pisa, Italy, Elba, Italy.

Rollinson, H. (1993), *Using Geochemical Data: Evaluation, Presentation, Interpretation*, Pearson Prentice Hall, Harlow.

Rosenbaum, G. and G. S. Lister (2004), Neogene and Quaternary rollback evolution of the Tyrrhenian Sea, the Apennines, and the Sicilian Maghrebides, *Tectonics*, *23*(1), TC1013, doi 1010.1029/2003TC001518.

Rosenbaum, G., K. Regenauer-Lieb and R. Weinberg (2005), Continental extension: From core complexes to rigid block faulting, *Geology*, *33*(7), 609-612.

Rossetti, F., C. Faccenna, L. Jolivet, R. Funiciello, F. Tecce and C. Brunet (1999), Syn-versus post-orogenic extension: the case study of Giglio Island (Northern Tyrrhenian Sea, Italy), *Tectonophysics*, *304*(1-2), 71-93.

Rossetti, F., F. Tecce, A. Billi and M. Brilli (2007), Patterns of fluid flow in the contact aureole of the Late Miocene Monte Capanne pluton (Elba Island, Italy): the role of structures and rheology, *Contributions to Mineralogy and Petrology*, *153*(6), 743-760.

Rossetti, F., F. Balsamo, I. M. Villa, M. Bouybaouenne, C. Faccenna and R. Funiciello (2008), Pliocene-Pleistocene HT-LP metamorphism during multiple granitic intrusions in the southern branch of the Lardarello geothermal field (southern Tuscany, Italy), *Journal of the Geological Society*, *165*, 247-262.

Rowe, C. D., J. C. Moore, F. Meneghini and A. W. McKeirnan (2005), Large-scale pseudotachylytes and fluidized cataclasites from an ancient subduction thrust fault, *Geology*, *33*(12), 937-940.

Ruina, A. L. (1983), Slip instability and state variable friction laws, *Journal of Geophysical Research*, *88*, 10359-10370.

Rutter, E. H. (1976), Kinetics of rock deformation by pressure solution, *Philosophical Transactions of the Royal Society of London Series a-Mathematical Physical and Engineering Sciences*, *283*(1312), 203-219.

Rutter, E. H. (1986), On the nomenclature of mode of failure transitions in rocks, *Tectonophysics*, *122*(3-4), 381-387.

Rutter, E. H., R. H. Maddock, S. H. Hall and S. H. White (1986), Comparitive microstructures of natural and experimentally produced clay-bearing fault gouges, *Pure and Applied Geophysics*, *124*, 3-30.

Rutter, E. H. (1995), Experimental study of the influence of stress, temperature, and strain on the dynamic recrystallization of Carrara marble, *Journal of Geophysical Research-Solid Earth*, *100*(B12), 24651-24663.

Rutter, E. H., D. R. Faulkner, K. H. Brodie, R. J. Phillips and M. P. Searle (2007), Rock deformation processes in the Karakoram fault zone, Eastern Karakoram, Ladakh, NW India, *Journal of Structural Geology*, *29*(8), 1315-1326.

Saffer, D. M., K. M. Frye, C. Marone and K. Mair (2001), Laboratory results indicating complex and potentially unstable frictional behavior of smectite clay, *Geophysical Research Letters*, *28*(12), 2297-2300.

Saupe, F., C. Marignac, B. Moine, J. Sonet and J. L. Zimmermann (1982), K/Ar and Rb/Sr Dating of Rocks from the Eastern Part of Elba Island (Province of Livorno, Italy), *Bulletin De Mineralogie*, *105*(3), 236-245.

Scholz, C. H. (2000), Evidence for a strong San Andreas fault, *Geology*, *28*(2), 163-166.

Scholz, C. H. (2002), *The Mechanics of Earthquakes and Faulting*, 2 ed., 471 pp., Cambridge University Press, Cambridge.

Serri, G., F. Innocenti and P. Manetti (1993), Geological and petrological evidence of the subduction of delaminated Adriatic continental lithosphere in the genesis of the Neogene-Quaternary magmatism of central Italy, *Tectonophysics*, *223*, 117-147.

Shea, W. T. and A. K. Kronenberg (1993), Strength and anisotropy of foliated rock with varied mica contents, *Journal of Structural Geology*, *15*, 1097-1121.

Sheldon, H. A. and A. Ord (2005), Evolution of porosity, permeability and fluid pressure in dilatant faults post-failure: implications for fluid flow and mineralization, *Geofluids*, *5*(4), 272-288.

Sheldon, H. A. and S. Micklethwaite (2007), Damage and permeability around faults: Implications for mineralization, *Geology*, *35*(10), 903-906.

Sheppard, S. M. F. (1986), Characterization and isotopic variations in natural waters, in *Stable isotopes in high temperature geological processes*, edited by V. J.W., T. H.P. and O. N. J.R., pp. 165-183, Mineralogical Society of America.

Sibson, R. H. (1977), Fault rocks and fault mechanisms, *Journal of the Geological Society, London*, *133*, 191-213.

Sibson, R. H. (1985), A Note on Fault Reactivation, *Journal of Structural Geology*, *7*(6), 751-754.

Sibson, R. H. (1989), Earthquake Faulting as a Structural Process, *Journal of Structural Geology*, *11*(1-2), 1-14.

Sibson, R. H. (1990), Conditions for fault-valve behaviour, in *Deformation mechanisms, rheology, and tectonics*, edited by R. J. Knipe and E. H. Rutter, Geological Society of London, Special Publications, London.

Sibson, R. H. (1992), Fault-Valve Behavior and the Hydrostatic Lithostatic Fluid Pressure Interface, *Earth-Science Reviews*, *32*(1-2), 141-144.

Sibson, R. H. (2000), Fluid involvement in normal faulting, *Journal of Geodynamics*, *29*(3-5), 469-499.

Sibson, R. H. (2007), An episode of fault-valve behaviour during compressional inversion? The 2004 M(J)6.8 Mid-Niigata Prefecture, Japan, earthquake sequence, *Earth and Planetary Science Letters*, *257*(1-2), 188-199.

Smalley, P. C., A. C. Higgins, R. J. Howarth, H. Nicholson, C. E. Jones, N. H. M. Swinburne and J. Bessa (1994), Seawater Sr Isotope Variations through Time - a Procedure for Constructing a Reference Curve to Date and Correlate Marine Sedimentary-Rocks, *Geology*, *22*(5), 431-434.

Smith, D. K., J. R. Cann and J. Escartin (2006), Widespread active detachment faulting and core complex formation near 13 degrees N on the Mid-Atlantic Ridge, *Nature*, *442*(7101), 440-443.

Smith, S. A. F., R. E. Holdsworth, C. Collettini and J. Imber (2007), Using footwall structures to constrain the evolution of low-angle normal faults, *Journal of the Geological Society*, *164*, 1187-1191.

Smith, S. A. F., C. Collettini and R. E. Holdsworth (2008), Recognizing the seismic cycle along ancient faults: CO_2-induced fluidization of breccias in the footwall of a sealing low-angle normal fault, *Journal of Structural Geology*, *30*, 1034-1046.

Steffen, K., J. Selverstone and A. J. Brearley (2001), Episodic weakening and strengthening during synmetamorphic deformation in a deep-crustal shear zone in the Alps, in *The Nature and Tectonic Significance of Fault Zone Weakening*, edited by R. E. Holdsworth, R. A. Strachan, J. F. Magloughlin and R. J. Knipe, pp. 141-156, The Geological Society of London, London.

Stewart, M., R. E. Holdsworth and R. A. Strachan (2000), Deformation processes and weakening mechanisms within the frictional-viscous transition zone of major crustal-scale faults: insights from the Great Glen Fault Zone, Scotland, *Journal of Structural Geology*, *22*(5), 543-560.

Takahashi, M. and T. Shimamoto (1998), Velocity dependence of flow and friction behaviors of clay gouges, in *Japan Geoscience Union Meeting*, edited, p. 339.

Takahashi, M., K. Mizoguchi, K. Kitamura and K. Masuda (2007), Effects of clay content on the frictional strength and fluid tranport property of faults, *Journal of Geophysical Research*, *112*, B08206, doi:08210.01029/02006JB004678.

Tanelli, G., M. Benvenuti, P. Costagliola, A. Dini, P. Lattanzi, C. Maineri, I. Mascaro and G. Ruggieri (2001), The iron mineral deposits of Elba Island: State of the art, *Ofioliti*, *26*(2A), 239-247.

Taylor, H. P. and B. Turi (1976), High-O^{18} Igneous Rocks from Tuscan-Magmatic-Province, Italy, *Contributions to Mineralogy and Petrology*, *55*(1), 33-54.

Taylor, H. P. and S. M. F. Sheppard (1986), Igneous rocks: 1. Processes of isotopic fractionation and isotope systematics, in *Stable isotopes in high-temperature geological*

processes, edited by J. W. Valley, H. P. Taylor and J. R. O'Neil, pp. 227-271, Mineralogical Society of America.

Tenthorey, E. and S. F. Cox (2006), Cohesive strengthening of fault zones during the interseismic period: An experimental study, *Journal of Geophysical Research-Solid Earth*, *111*(B9), B09202, doi:09210.01029/02005JB004122.

ter Heege, J. H., J. H. P. de Bresser and C. J. Spiers (2002), The influence of dynamic recrystallisation on the grain size distribution and rheological behaviour of Carrara marble deformed in axial compression, in *Deformation Mechanisms, Rheology, and Tectonics: Current Status and Future Perspectives*, edited by S. de Meer, M. R. Drury, J. H. P. de Bresser and G. M. Pennock, pp. 331-354, The Geological Society of London, London.

Touret, J. L. R. (2001), Fluids in metamorphic rocks, *Lithos*, *55*, 1-25.

Townend, J. and M. D. Zoback (2000), How faulting keeps the crust strong, *Geology*, *28*(5), 399-402.

Tracy, R. J. and B. R. Frost (1991), Phase equilibria and thermobarometry of calcareous, ultramafic and mafic rocks, and iron formations, in *Contact Metamorphism*, edited by D. M. Kerrick, pp. 207-290, BookCrafters Inc., Michigan.

Trevisan, L., G. Marinelli, F. Barberi, G. Giglia, F. Innocenti, G. Raggi, P. Squarci, L. Taffi and C. A. Ricci (1967), Carta Geologica dell'Isola d'Elba, Consiglio Nazionale delle Ricerche, Gruppo di Ricerca per la Geologia dell'Appennino centro-settentrionale e della Toscana, Pisa.

Trullenque, G., K. Kunze, R. Heilbronner, H. Stunitz and S. M. Schmid (2006), Microfabrics of calcite ultramylonites as records of coaxial and non-coaxial deformation kinematics: Examples from the Rocher de l'Yret shear zone (Western Alps), *Tectonophysics*, *424*(1-2), 69-97.

Tullis, T. E., R. Burgmann, M. Cocco, G. Hirth, G. C. P. King, O. Oncken, K. Otsuki, J. R. Rice, A. M. Rubin, P. Segall, S. A. Shapiro and C. A. J. Wibberley (2007), Group Report: Rheology of Fault Rocks and Their Surroundings, in *Tectonic Faults: Agents of change on a dynamic Earth*, edited by M. R. Handy, G. Hirth and N. Hovius, pp. 183-204, The MIT Press, Cambridge, Massachusets.

Turi, B. and H. P. Taylor (1976), Oxygen Isotope Studies of Potassic Volcanic-Rocks of Roman Province, Central Italy, *Contributions to Mineralogy and Petrology*, *55*(1), 1-31.

Twiss, R. J. and E. M. Moores (1992), *Structural geology*, 532 pp., W.H. Freeman and Company, New York.

Ujiie, K., H. Yamaguchi, A. Sakaguchi and S. Toh (2007), Pseudotachylytes in an ancient accretionary complex and implications for melt lubrication during subduction zone earthquakes, *Journal of Structural Geology*, *29*(4), 599-613.

Ujiie, K., A. Yamaguchi and S. Taguchi (2008), Stretching of fluid inclusions in calcite as an indicator of frictional heating on faults, *Geology*, *36*(2), 111-114.

Valley, J. W. and D. R. Cole (Eds.) (2001), *Stable Isotope Geochemistry*, 662 pp., Mineralogical Society of America.

Veizer, J. and J. Hoefs (1976), The nature of O^{18}–O^{16} and C^{13}-C^{12} secular trends in sedimentary carbonate rocks, *Geochimica Et Cosmochimica Acta*, *40*, 1387-1395.

Viola, G., N. S. Mancktelow and J. A. Miller (2006), Cyclic frictional-viscous slip oscillations along the base of an advancing nappe complex: Insights into brittle-ductile nappe emplacement mechanisms from the Naukluft Nappe Complex, central Namibia, *Tectonics*, *25*(3), TC3016, doi:3010.1029/2005TC001939.

Vrolijk, P. and B. A. Van der Pluijm (1999), Clay gouge, *Journal of Structural Geology*, *21*, 1039-1048.

Walker, C. D., M. H. Anders and N. Christie-Blick (2007), Kinematic evidence for downdip movement on the Mormon Peak detachment, *Geology*, *35*(3), 259-262.

Watts, L. M., R. E. Holdsworth, J. A. Sleight, R. A. Strachan and S. A. F. Smith (2007), The movement history and fault rock evolution of a reactivated crustal-scale strike-slip fault: the Walls Boundary Fault Zone, Shetland, *Journal of the Geological Society*, *164*, 1037-1058.

Weeks, J. D. and T. E. Tullis (1985), Frictional Sliding of Dolomite: A Variation in Constitutive Behaviour, *Journal of Geophysical Research*, *90*(B9), 7821-7826.

Wernicke, B. (1981), Low-Angle Normal Faults in the Basin and Range Province - Nappe Tectonics in an Extending Orogen, *Nature*, *291*(5817), 645-648.

Wernicke, B. and G. J. Axen (1988), On the Role of Isostasy in the Evolution of Normal-Fault Systems, *Geology*, *16*(9), 848-851.

Wernicke, B. (1995), Low-Angle Normal Faults and Seismicity - a Review, *Journal of Geophysical Research-Solid Earth*, *100*(B10), 20159-20174.

Westaway, R. (1999), The mechanical feasibility of low-angle normal faulting, *Tectonophysics*, *308*(4), 407-443.

Westerman, D. S., F. Innocenti, S. Tonarini and G. Ferrara (1993), The Pliocene intrusions of the Island of Giglio, *Mem. Soc. Geol. It.*, *49*, 345-363.

Wibberley, C. A. J. (1999), Are feldspar-to-mica reactions necessarily reaction-softening processes in fault zones?, *Journal of Structural Geology*, *21*, 1219-1227.

Wibberley, C. A. J. and T. Shimamoto (2003), Internal structure and permeability of major strike-slip fault zones: the Median Tectonic Line in Mie Prefecture, Southwest Japan, *Journal of Structural Geology*, *25*(1), 59-78.

Wibberley, C. A. J. and T. Shimamoto (2005), Earthquake slip weakening and asperities explained by thermal pressurization, *Nature*, *436*(7051), 689-692.

Wibberley, C. A. J. (2007), Talc at fault, *Nature*, *448*, 756-757.

Wibberley, C. A. J., G. Yielding and G. Di Toro (2008), Recent advances in the understanding of fault zone internal structure: a review, in *The Internal Structure of Fault Zones: Implications for Mechanical and Fluid Flow properties*, edited by C. A. J. Wibberley, W. Kurz, J. Imber, R. E. Holdsworth and C. Collettini, pp. 5-33, The Geological Society of London, London.

Wickham, S. M., M. T. Peters, H. C. Fricke and J. R. Oneil (1993), Identification of Magmatic and Meteoric Fluid Sources and Upward-Moving and Downward-Moving Infiltration Fronts in a Metamorphic Core Complex, *Geology*, *21*(1), 81-84.

Wintsch, R. P. (1975), Feldspathization as a Result of Deformation, *Geological Society of America Bulletin*, *86*(1), 35-38.

Wintsch, R. P., R. Christoffersen and A. K. Kronenberg (1995), Fluid-Rock Reaction Weakening of Fault Zones, *Journal of Geophysical Research-Solid Earth*, *100*(B7), 13021-13032.

Withjack, M. O. and S. Callaway (2000), Active normal faulting beneath a salt layer: An experimental study of deformation patterns in the cover sequence, *Aapg Bulletin-American Association of Petroleum Geologists*, *84*(5), 627-651.

Wright, L. A., J. Otten and B. W. Troxel (1974), Turtleback fault surfaces of Death Valley viewed as a phenomenon of extension, *Geology*, *2*, 53-54.

Yin, A. (1989), Origin of Regional, Rooted Low-Angle Normal Faults - a Mechanical Model and Its Tectonic Implications, *Tectonics*, *8*(3), 469-482.

Yin, A. (1991), Mechanisms for the Formation of Domal and Basinal Detachment Faults - a 3-Dimensional Analysis, *Journal of Geophysical Research-Solid Earth and Planets*, *96*(B9), 14577-14594.

Zoback, M. D., M. L. Zoback, V. S. Mount, J. Suppe, J. P. Eaton, J. H. Healy, D. Oppenheimer, P. Reasenberg, L. Jones, C. B. Raleigh, I. G. Wong, O. Scotti and C. Wentworth (1987), New Evidence on the State of Stress of the San-Andreas Fault System, *Science*, *238*(4830), 1105-1111.

Zoback, M. D. (2000), Strength of the San Andreas, *Nature*, *405*, 31-32.